



Towards quantum optics experiments with single flying electrons in a solid state system

Tobias Bautze

► To cite this version:

Tobias Bautze. Towards quantum optics experiments with single flying electrons in a solid state system. Physics [physics]. Université de Grenoble, 2014. English. NNT : 2014GRENY059 . tel-01367013

HAL Id: tel-01367013

<https://theses.hal.science/tel-01367013>

Submitted on 15 Sep 2016

HAL is a multi-disciplinary open access archive for the deposit and dissemination of scientific research documents, whether they are published or not. The documents may come from teaching and research institutions in France or abroad, or from public or private research centers.

L'archive ouverte pluridisciplinaire **HAL**, est destinée au dépôt et à la diffusion de documents scientifiques de niveau recherche, publiés ou non, émanant des établissements d'enseignement et de recherche français ou étrangers, des laboratoires publics ou privés.

THÈSE

Pour obtenir le grade de

DOCTEUR DE L'UNIVERSITÉ DE GRENOBLE

Spécialité : **Nanophysique**

Arrêté ministériel : 7 août 2006

Présentée par

Tobias Bautze

Thèse dirigée par **Christopher Bäuerle**

préparée au sein de l'**Institut Néel - CNRS**
et de l'**École doctorale de Physique**

Towards quantum optics experiments with single flying electrons in a solid state system

Thèse soutenue publiquement le **19 décembre 2014**,
devant le jury composé de :

D. Feinberg

Directeur de recherches, Institut Néel - CNRS, Grenoble, Président

H. Buhmann

Prof. Dr., Universität Würzburg, Rapporteur

C. Texier

Maître de conférences, LPTMS, Université Paris-Sud, Rapporteur

G. Fève

Professeur, ENS-LPA, Paris, Examineur

X. Waintal

Ingénieur-Chercheur, CEA/INAC/SPSMS, Grenoble, Examineur

C. Bäuerle

Directeur de recherches, Institut Néel - CNRS, Grenoble, Directeur de thèse



Abstract

Tobias Bautze

Towards quantum optics experiments with single flying electrons in a solid state system.

This thesis contains the fundamental study of nano-electronic systems at cryogenic temperatures. We made use of ballistic electrons in a two-dimensional electron gas in a GaAs/AlGaAs heterostructure to form a real two-path electronic interferometer and showed how the phase of the electrons and hence their quantum state can be controlled by means of electrostatic gates. The device represents a promising candidate of a flying qubit. We developed a sophisticated numerical tight-binding model based on ballistic quantum transport, which reproduces all experimental findings and allows to gain profound knowledge about the subtle experimental features of this particular device. We proposed further measurements with this flying qubit system. With the ultimate goal of building a single electron flying qubit, we combined the single electron source that has been developed in our lab prior to this manuscript with an electronic beam splitter. The electrons are injected from static quantum dots into a train of moving quantum dots. This moving potential landscape is induced in the piezoelectric substrate of GaAs by surface acoustic waves from interdigital transducers. We studied and optimized all key components, which are necessary to build a single electron beam splitter and built up a reliable local fabrication process. The device is capable of studying electron interactions on the single electron level and can serve as a measurement platform for quantum optics experiments in electronic solid state systems. Finally, we developed a powerful tool capable of calculating the potential landscapes of any surface gate geometry, which can be used as a fast feedback optimization tool for device design and proposed an optimized prototype for the single electron beam splitter.

Ce travail de thèse porte sur l'étude fondamentale de systèmes nano-électroniques, mesurés à très basse température. Nous avons réalisé des interféromètres électroniques à deux chemins à partir d'électrons balistiques obtenus dans un gaz 2D d'électrons d'une hétéro-structure GaAs/AlGaAs. Nous montrons que la phase des électrons, et ainsi leur état quantique, peut être contrôlée par des grilles électrostatiques. Ces dispositifs se révèlent être des candidats prometteurs pour la réalisation d'un qubit volant. Nous avons développé une simulation numérique évoluée d'un modèle de liaisons fortes à partir de transport quantique ballistique qui décrit toutes les découvertes expérimentales et nous apporte une connaissance approfondie sur les signatures expérimentales de ces dispositifs particuliers. Nous proposons des mesures complémentaires de ce système de qubit volants. Pour atteindre le but ultime, à savoir un qubit volant à un électron unique, nous avons assemblé la source à électron unique précédemment développée dans notre équipe à un beam splitter électronique. Les électrons sont alors injectés depuis une boîte quantique à un train de boîtes quantiques en mouvement. Ce potentiel électrostatique en mouvement est généré par des ondes acoustiques de surface créées par des transducteurs inter-digités sur le substrat GaAs piézo-électrique. Nous avons étudié et optimisé chacun de ces composants fondamentaux nécessaires à la réalisation d'un beam splitter à électron unique et développé un procédé local et fiable de fabrication. Ce dispositif nous permet

d'étudier les interactions électroniques pour des électrons isolés et pourra servir de base de mesure pour des expériences d'optique quantiques sur un système électronique de l'état condensé. Enfin, nous avons développé un outil puissant de simulation du potentiel électrostatique à partir de la géométrie des grilles. Ceci permet d'optimiser la conception des échantillons avant même leur réalisation. Nous proposons ainsi un prototype optimisé de beam splitter à électron unique.

Key words: nano-electronics, quantum dot, single electron, surface acoustic wave (SAW), beam splitter, flying qubit, electrostatic potential, single electron source, kwant, python, design optimization, tight-binding model

Contents

Résumé en français	1
1 Introduction	9
2 Background	13
2.1 Two-dimensional electron gas	13
2.2 Landauer-Büttiker formalism	15
2.3 Coherent scattering theory	19
2.4 Tight-binding model	21
3 Numerical simulations	25
3.1 Kwant	25
3.2 Real units	30
3.3 Electrostatic gates	30
3.4 Magnetic field	37
3.5 Examples	38
3.6 Simulation interface	43
4 The flying qubit	47
4.1 Introduction	47
4.2 The electrical two-path interferometer	51
4.3 Analytical model	57
4.4 Semi-analytical analysis	63
4.5 Numerical simulations	71
5 Experiments	85
5.1 The single electron beam splitter	85
5.1.1 Quantum dots	88
5.1.2 Surface acoustic waves	91
5.2 Device fabrication	99
5.3 Experimental set-up	104
6 Experimental results and outlook	107
6.1 Surface acoustic wave characterization	108

6.2	SAW current measurement	113
6.3	SAW influence on a quantum dot	116
6.4	Stability diagrams	120
6.5	Single electron regime and metastable states	122
6.6	Comparison and outlook	128
7	Conclusion	139
	Bibliography	143
	Appendix	163
A	Appendix	163
A.1	Leads	163
A.2	Analytical model	165
	Publications	167

Résumé en français

Introduction

Le 20^{ème} siècle a été très fructueux pour la science et la technologie. Parmi les centaines d'inventions qui ont irrévocablement changé les habitudes humaines, une en particulier a considérablement modifié la société humaine et initié un boom technologique toujours en cours. Il s'agit de l'invention du transistor en décembre 1947 par BRATTAIN, BARDEEN et SHOCKLEY qui a donné naissance à l'industrie des semi-conducteurs d'aujourd'hui et a permis la miniaturisation toujours plus poussée des ordinateurs très miniaturisés qui peuvent aujourd'hui être portés dans la poche de tout le monde. Bien que ce premier transistor était assez grand pour être assemblé à la main, l'état de l'art des transistors disponibles sur le marché est qu'ils sont désormais aussi petits que quelques nanomètres¹. Pour donner une idée de l'ordre de grandeur, l'assemblage de 100 millions de ces transistors peut tenir sur une tête d'épingle. Le processus de miniaturisation suit ce qui est communément connu comme la loi de Moore et les dispositifs atteignent des dimensions où la physique classique n'est plus valide.

À ces échelles, le comportement des transistors est alors gouverné par la nature ondulatoire des électrons, décrite par les lois de la mécanique quantique moderne. Au lieu de contourner ces effets quantiques dans ces dispositifs de plus en plus petits, un nouveau domaine de recherche, la *nanoélectronique quantique*, utilise ces effets quantiques et propose de nouvelles façons de manipuler l'information. Avec les transistors classiques, l'information peut simplement être codé par la présence ou l'absence d'un courant électrique, en d'autres termes par un état binaire des transistors, *on* ou *off*. Un ensemble de n ($n \in \mathbb{N}$) bits classiques représente alors 2^n états différents, mais ne peut occuper qu'un état à la fois. Un bit quantique (qubit) profite maintenant de ce qui appelé une superposition d'états qui diffère fondamentalement de l'image classique d'un état. L'information qui est stockée dans un système de n -qubit nécessiterait 2^n bits classiques différents pour stocker les 2^n coefficients complexes qui décrivent un seul état quantique. Un système avec n -qubit peut contenir de façon exponentielle plus d'information qu'un système de n -bits classiques. En plus du codage de l'information, un ordinateur quantique bénéficie également d'une accélération exponentielle du calcul par rapport à un système

¹ En septembre 2013, Intel a présenté lors de l'Intel Developer Forum à San Francisco, la génération *Broadwell* de micro-processeurs où la dimension des transistors est de 14 nm.

classique. En simplifiant à l'extrême cette question plutôt subtile, nous pouvons dire que nous ne pouvons effectuer qu'une opération classique à la fois sur un ensemble de bits. Au contraire, les opérations quantiques travaillent sur la superposition complète de l'état d'un ensemble de qubits. Dit autrement, faire une opération quantique est équivalent à un nombre exponentiel d'opérations classiques en même temps.

Le concept de l'utilisation de ce que l'on appelle le parallélisme quantique a été introduit en 1982 par Richard FEYNMAN [1]. Il a proposé qu'une machine qui utilise le parallélisme quantique devrait être capable de simuler efficacement un système quantique, alors qu'une machine classique subirait un ralentissement exponentielle en raison du grand nombre d'états possibles. C'est une énorme motivation pour construire réellement un ordinateur quantique car les systèmes quantiques vont jouer un rôle de plus en plus important dans le développement et l'étude de nombreuses formes de la nanotechnologie et dans notre compréhension de la nanomachinerie de molécules biologiques [2].

Sans doute la tâche la plus connue pour un ordinateur quantique est l'algorithme quantique de Shor pour la factorisation de grands nombres [3]. Notre système de cryptographie moderne repose sur la très grande complexité pour factoriser un grand nombre entier en nombres premiers avec un algorithme classique. Les meilleurs algorithmes nécessitent un temps de calcul qui augmente exponentiellement avec la taille du nombre à factoriser, alors que l'algorithme quantique n'évolue que de façon linéaire avec la taille du nombre à factoriser et est donc également intéressant pour un public plus large.

« *L'idée d'un ordinateur quantique est simple, même si sa réalisation ne l'est pas.* » [4]

De nombreux matériaux sont à l'étude pour atteindre cet objectif technologique très ambitieux. Plusieurs réalisations de qubits ont été imaginées : avec la plus petite forme de la matière comme un atome isolé, qui peut par exemple être capturé dans un piège à ions [5], ou créés artificiellement à partir de composants électroniques, comme c'est le cas dans les systèmes supraconducteurs par exemple [6–8]. En principe, tout système à deux niveaux qui peut être préparé dans une superposition de ses deux états peut servir comme qubit. Dans ce manuscrit, nous allons nous concentrer sur des qubits qui sont construits à partir d'hétérostructures semi-conductrices et réalisés par nanofabrication.

Dans un premier temps, nous étudierons les caractéristiques générales partagées par les différents types de qubits. Probablement, l'aspect le plus important, c'est qu'un ordinateur quantique doit être isolé de son environnement. Il est alors primordial de déterminer la dynamique des interactions avec l'environnement extérieur pour réaliser des calculs quantiques. Cette interaction avec l'extérieur provoque des *fuites d'informations* et perturbe les états quantiques du qubit, c'est ce qu'on appelle la décohérence [9]. L'information quantique est très fragile comparée à l'information classique. Une fois la cohérence quantique perdue, les effets d'interférence ne peuvent plus être observés et la phase qui porte l'information dans un système quantique est perdue. L'exigence d'avoir des temps de décohérence longs et pertinents est depuis connu comme un des critères de DiVincenzo [4]. En tout, un ensemble de cinq critères ont été proposés, qui doivent être

satisfaits pour la réalisation physique de traitement quantique de l'information. Tout d'abord, un système physique qui contient une collection de qubits est nécessaire. Leurs états doivent être intriqués, ce qui signifie que leur état total ne peut pas être écrit comme un simple produit des états de qubits individuels. On peut aussi aller plus loin et dire que la croissance exponentielle de l'espace de Hilbert quand des qubits sont ajoutés ne doivent pas s'accompagner d'un coût exponentiel des ressources telles que le temps, l'espace ou l'énergie [2]. En même temps, les qubits individuels doivent être bien caractérisés. Les paramètres physiques doivent être connus exactement. Parmi eux, nous mentionnons les états propres de l'énergie du qubit, les couplages à d'autres états du qubit, les interactions avec d'autres qubits et les couplages possibles aux champs externes.

Deuxièmement, il faut pouvoir initialiser l'état des qubits avec une grande fidélité. L'initialisation signifie ici la préparation d'un état quantique comme par exemple la polarisation d'un spin dans son état fondamental. C'est d'une part important car les registres de qubits doivent être connues avant un calcul et d'autre part, ce qu'on appelle des mécanismes de corrections d'erreur quantique exigent des copies de l'état initial. Ces mécanismes sont nécessaires car aucun système n'est totalement exempt de décohérence mais différentes techniques peuvent permettre de compenser de petites quantités de décohérence. Pour plus de détails sur ces schémas, nous référons le lecteur intéressé à [10].

Étroitement liée à l'initialisation est la nécessité d'une capacité de mesure spécifique au qubit. De toute évidence, le résultat du calcul doit être mesuré, mais la mesure du qubit spécifique doit aussi être projective. Le qubit mesuré restera dans le même état après la mesure même après avoir répété les mesures.

Enfin, pour un ordinateur quantique, il y a la nécessité d'un *ensemble universel* de grilles quantiques. Comme dans un ordinateur classique, nous devons être capable de manipuler les états de qubits. Dans un ordinateur quantique, ceci est équivalent à dire que nous devons avoir accès à l'espace de Hilbert complet du système. Il a été montré que ce qu'on appelle les rotations simples de qubits combinés avec des opérations à deux qubits peuvent être utilisées pour créer des grilles universelles quantiques [11]. Ces exigences doivent être satisfaites pour la mise en œuvre pratique d'un ordinateur quantique.

Cet objectif très ambitieux expérimentalement de faire un ordinateur quantique qui fonctionne est encore loin d'être atteint. Plusieurs approches sont poursuivies par différents groupes de recherche dans le monde entier, mais il est impossible de prévoir quel système va satisfaire à tous ces critères.

Nous avons choisi d'étudier les systèmes à état solide et en particulier les systèmes électroniques de basse dimensionnalité. Les qubits qui seront présentés ici sont des prototypes de qubits possibles et nous allons étudier comment leurs états quantiques peuvent être manipulés. Ces structures permettent également l'étude fondamentale des interactions électrons comme nous le verrons plus tard. Le système physique que nous utilisons est l'hétérostructure de semi-conducteurs GaAs/AlGaAs. Dans ce système, les qubits peuvent être réalisés avec des boîtes quantiques [12–15]. Ces boîtes quantiques correspondent à une région de l'espace où les électrons sont confinés dans toutes les dimensions spatiales. Les degrés de liberté d'un tel électron isolé, c'est-à-dire sa charge

ou son spin, peuvent maintenant servir comme un système quantique à deux niveaux. La mesure de l'état de charge est devenue une technologie bien établie dans le domaine [16–18], tandis que le degré de liberté de spin peut également être obtenu grâce à la conversion spin-charge [19]. Le degré de liberté de spin a été largement étudiée par rapport à son application à l'informatique quantique [20, 21]. Pour une compréhension plus approfondie de ce sujet spécifique de qubits de spin dans les boîtes quantiques, nous renvoyons le lecteur intéressé à cette excellente revue [22]. Comme les boîtes quantiques sont des régions bien confinées dans l'espace, les qubits sont stationnaires et il reste notamment une question ouverte : combien de ces qubits peuvent être couplés pour échanger de l'information quantique de manière cohérente, étape nécessaire pour faire des calculs quantiques complexes. On pourrait imaginer la manipulation locale de systèmes de qubits multiples avec l'état de l'art de la technologie disponible, mais la connexion des différents qubits est encore un problème non résolu.

Cette thèse se concentre désormais pour faire progresser cet aspect de *solid state* qubits. Deux idées générales seront étudiées. À l'opposé de manipulations sur des qubits stationnaires, nous pouvons également imaginer de définir un qubit et réaliser ces opérations pendant son vol. Dans ce but, nous allons utiliser la nature ondulatoire des électrons. Les trajets électroniques que les électrons suivent, ainsi que la phase de l'onde électronique peut être utilisés comme porteur d'information quantique. Comme la longueur de cohérence de phase de l'onde électronique est grande par rapport à la taille de notre système, nous pouvons produire des effets d'interférence entre les différents trajets électroniques, semblables à des interféromètres optiques [23]. Les trajets que les électrons suivent, peuvent être créés de deux manières différentes. Tout d'abord, on peut confiner les électrons dans les états de bord de l'effet Hall quantique [24–29] et obtenir des effets d'interférence par analogie avec un interféromètre de Mach-Zehnder optique. Deuxièmement, il est possible de confiner les électrons balistiques dans des canaux unidimensionnels définis par un champ de potentiel électrique [23]. C'est l'approche que nous allons suivre et détailler plus tard, dans le chapitre 4. Dans un tel système, nous pouvons définir des états logiques $|0\rangle$ et $|1\rangle$ par la présence d'électrons dans des trajets différents [23] et la combinaison de plusieurs canaux unidimensionnels via des barrières tunnel permet, en principe, de créer un ensemble universel de grs quantiques.

Des interféromètres balistiques similaires ont été étudiés avant ce manuscrit [30, 31] et nous allons montrer ici comment un interféromètre électronique balistique couplé à un fil avec une barrière tunnel [32, 33] peut être mis en œuvre comme un *solid state* qubit volant [34].

Dans le chapitre 4 nous allons développer le cadre théorique pour décrire la physique du système et effectuer des calculs numériques sophistiqués pour reproduire les données obtenues expérimentalement. Les simulations numériques sont effectuées avec Kwant qui est un logiciel de simulation numérique de transport quantique développé par nos collaborateurs X. WAIN TAL *et al.* [35]. Les résultats de ce chapitre ont été publiés [36].

Une autre approche pour transporter de l'information quantique est la suivante :

On peut considérer la manipulation locale de l'état quantique d'un électron dans un boîte quantique standard. Au lieu de coupler le système à un autre système quantique pour transporter l'information quantique, on peut aussi transférer l'électron lui-même, contenant l'information quantique. Dans ce but, nous utilisons des boîtes quantiques volantes [37] (*sic.*), qui peuvent être créées par une onde acoustique de surface. En plaçant des boîtes quantiques sur les côtés d'injection et réception d'un canal électronique unidimensionnel, nous avons pu montrer qu'il est possible d'isoler un électron unique de son environnement et de le transférer à une vitesse d'environ 3000 m/s sur une distance de l'ordre de 3 μm [38]. Cette approche est étudiée en détail dans notre groupe [39, 40] et forme une source fiable d'électrons uniques.

Dans le chapitre expérimental de ce manuscrit, nous allons viser à combiner cette source d'électrons uniques avec un *beam-splitter* électronique, similaires à ce que nous avons mis en place au préalable pour le qubit volant. La combinaison de deux sources d'électrons uniques distinctes avec un *beam-splitter* électronique permettra de réaliser des expériences de tunneling avec les électrons uniques volants. Il ouvrira également la possibilité d'étudier les interactions entre deux électrons isolés pendant le vol et peut servir de plateforme pour les expériences d'optique quantique avec des électrons à l'avenir. Nous allons élaborer les démarches nécessaires pour atteindre cet objectif expérimental très ambitieux et caractériser les caractéristiques principales de tous les ingrédients nécessaires.

Conclusion

De nombreux éléments de base sont nécessaires pour construire un ordinateur quantique et la communauté se rapproche de la réalisation de cet objectif expérimentalement très ambitieux. Cependant, être capable de contrôler de manière fiable et d'utiliser l'information quantique pour le calcul, serait une autre percée dans l'informatique similaire à la mise au point du transistor, ce qui a conduit à des progrès technologiques alors inimaginables en moins d'un siècle de temps. Les physiciens d'aujourd'hui sont confrontés au défi de l'exploitation de tout système possible à deux niveaux qui peut servir comme porteur de l'information quantique. Les états quantiques doivent être préparés de manière fiable, leur évolution temporelle doit être contrôlée et leur mesure doit être conçue attentivement. En dehors du stockage et de la manipulation de tels qubits, la question de l'échange d'informations cohérent, c'est-à-dire coupler des états cohérents à d'autres états cohérents a été posée et est activement débattue. L'échange d'information peut être fait en couplant des systèmes différents par l'échange de particule, comme des photons ou des paires de Cooper ou directement par le transport de la particule qui porte l'information quantique d'un endroit à un autre.

L'objectif de cette thèse est d'étudier et de manipuler des électrons, pendant qu'ils se propagent à travers une structure spécialement conçue et d'acquérir des connaissances au sujet de leur état quantique.

Nous avons poursuivi deux approches différentes.

Tout d'abord, la manipulation d'électrons balistiques dans un interféromètre à deux

trajets électronique et d'autre part, la combinaison d'une source d'électrons unique avec un beam-splitter électronique. Le premier projet a été réalisé en collaboration avec l'université de Tokyo. Nous avons pu montrer que l'interféromètre Aharonov-Bohm couplé à une barrière tunnel est un véritable interféromètre à deux chemins et que la phase de l'électron peut être entièrement contrôlé par des grilles électrostatiques. Ce dispositif est ainsi très prometteur pour l'étude d'un qubit électronique volant. L'absence et la présence des électrons dans le deux trajets haut et bas de l'interféromètre définit un état quantique, qui peut être manipulé pendant le vol, simplement en ajustant de l'environnement électrostatique des électrons, c'est-à-dire la modification des tensions de grilles électrostatiques. Nous avons développé un modèle numérique approfondi pour comprendre tous les effets subtils qui se déroulent dans cette structure. Cette analyse a été possible grâce aux progrès de nos collaborateurs du CEA dans le domaine du transport quantique numérique, qui nous a permis d'augmenter considérablement la taille de l'échantillon numérique et de simuler les conditions expérimentales précises à l'aide d'un cluster de calcul. Avec l'aide de ces calculs, nous avons réussi de comprendre le principe du fonctionnement du qubit volant en détail et de reproduire l'ensemble des résultats expérimentaux. Nous avons compris que les fils couplés avec la barrière tunnel ne contrôlent pas seulement la répartition des électrons entre les chemins du haut et du bas, mais aussi la propagation des modes électroniques à l'interface entre l'anneau d'Aharonov-Bohm et les fils couplés. En fonction de la barrière tunnel, deux régimes expérimentaux peuvent être obtenus. Dans le premier régime, le signal est principalement renvoyé dans la branche de l'anneau Aharonov-Bohm opposée, des trajectoires électroniques encerclant l'anneau sont créées et l'interférence entre les deux chemins est brouillée. Nous avons pu montrer que, dans le deuxième régime, cette rétrodiffusion est fortement supprimée et le dispositif peut être utilisé comme un qubit volant. Dans ce régime, il est possible de régler la phase des électrons dans l'anneau Aharonov-Bohm, simplement en changeant la tension d'une grille de l'anneau qui permet de contrôler la potentiel de confinement. En outre, les fils couplés avec la barrière tunnel permettent de séparer les électrons balistiques entre le trajet du haut et du bas des fils couplés. Ces deux caractéristiques permettent d'accéder à tous les états sur la sphère du Bloch du qubit volant en ajustant attentivement les tensions de grille. Nous constatons que, même si nous avons négligé l'interaction de Coulomb, les résultats expérimentaux peuvent bien être reproduits, mais plus de recherches et de calculs sont nécessaires pour une meilleure connaissance du rôle des interactions de Coulomb dans un tel système. Nous avons proposé une mesure supplémentaire avec le qubit volant, qui est l'augmentation de la surface effective due à la présence des fils tunnel couplés, qui pourront être étudiés dans un avenir proche. Le dispositif convient ainsi à une grande variété de mesures, comme la mesure de la phase de transmission d'une boîte quantique dans le régime Kondo, placé à l'intérieur de l'un des bras de l'interféromètre Aharonov-Bohm et sera probablement utilisé pour étudier *spin-flip scattering* dans l'avenir.

Le deuxième projet de cette thèse est la combinaison d'une source d'électrons uniques avec les ondes acoustiques de surface (SAW), qui a été développée dans notre laboratoire avant cette thèse et sa combinaison avec le même beam-splitter électronique, que nous

avons utilisé dans le fil de tunnel couplé du qubit volant. Comme un seul électron interagit avec le fil couplé par tunnel, la visibilité des événements tunnel devrait être proche de 100 %. Une fois que la barrière tunnel est réglée comme un beam-splitter, c'est-à-dire 50 % de probabilité pour un électron d'être mesuré dans le canal en haut et 50 % de probabilité d'être mesuré dans le canal en bas, le dispositif peut servir comme plateforme de mesure pour les expériences d'optique quantique avec des électrons, c'est-à-dire on peut envoyer deux électrons simultanément sur le beam-splitter et d'étudier leurs interactions. La structure peut être considérée comme une double boîte quantique volante et pourrait également être utilisée pour étudier le transport de spin de l'électron, similaire à ce que notre groupe poursuit dans les structures de simple boîtes quantiques volant, mais nous avons omis la discussion du spin de l'électron dans ce manuscrit. Nous avons été capable d'étudier les techniques requises pour construire d'un tel dispositif.

Nous avons caractérisé avec succès et optimisé les transducteurs interdigités (IDT), qui sont nécessaires pour créer des boîtes quantiques volants dans notre structure. Nous pourrions comparer l'IDT avec des doigts simple et avec des doigts double en termes de potentiel électrique induit et trouver étonnamment que les deux designs ont des performances comparables en termes d'amplitude. Néanmoins, la bande passante de l'IDT avec des doigts double est plus grande, qui donne un temps de montée de l'onde acoustique de surface plus élevé. Pour améliorer encore la fabrication IDT, nous proposons l'utilisation de nano-lithographie pour les transducteurs interdigités car il améliore nettement la qualité du dispositif, ouvrant la voie à des applications SAW haute fréquence. Les grilles de surface dans des hétérostructures GaAs/AlGaAs ainsi que le confinement des électrons uniques dans le 2DEG est une technologie bien établie dans notre domaine. Cependant, les structures de grille conçues ont eu le plus grand nombre de contacts électriques jusqu'à présent dans notre laboratoire. Le premier prototype doit être considéré comme une preuve de principe que même ces structures très denses sont réalisables. Et avec les progrès constants de la nano-fabrication, il est envisageable de réaliser des structures encore plus complexes. Le nombre important de contacts électriques a également nécessité une refonte fastidieuse du câblage du cryostat à dilution Mélusine utilisé pour ces expériences.

D'autres technologies sont également étudiées par la communauté pour réduire le nombre de connexions électriques à l'aide de techniques de multiplexage. Le deuxième prototype fut développé en ce sens. Toutefois des problèmes récurrents avec le masker électroniques l'ont sans cesse retardé et il n'a pu être réalisée avant la fin de ce manuscrit.

Le logiciel développé pour étudier les propriétés de transport du qubit volant a eu des retombées positives pour l'équipe : le développement fut poussé pour permettre aux utilisateurs non familiers de la simulation numérique de calculer rapidement le potentiel électrostatique pour différentes configurations simplement à partir du dessin des grilles de surface. Cela devrait en principe aider à optimiser le développement de l'échantillon pour tous les différents types d'expériences. Un troisième prototype avec une structure de grilles légèrement moins dense a été développée guidée par ce code et nous espérons inspirer les générations futures d'étudiants à poursuivre ce travail. Le beam-splitter

d'électrons unique pour les expériences d'optique quantique dans les systèmes de l'état solide à la base de ce qui a été présenté dans cette thèse est de toute façon possible et d'autres expériences sont en cours de réalisation.

CHAPTER 1

Introduction

The 20th century has been very fruitful for science and technology. Among hundreds of inventions that have changed humane habits irrevocably, one in particular has altered the human society tremendously and initiated a still ongoing technological boom. The invention of the transistor in December 1947 by Brattain, Bardeen and Shockley gave birth to today's semiconductor industry and started the development of highly miniaturized computers that can nowadays be carried around in everyone's pocket. While this first transistor was large enough to be assembled by hand, commercially available state-of-the art transistors are as small as several nanometers ¹. To give an idea about the order of magnitude, 100 million of such transistors could fit onto the head of a needle pin. The miniaturization process follows what is commonly known as Moore's Law and the devices are pushing forward into length scales where classical physics is no longer valid. At these scales, the behaviour of the transistors is governed by the wave nature of the electrons, described by the laws of modern quantum mechanics. Apart from trying to circumvent this quantum effects in even smaller devices, a new field of research, namely the field of quantum nanoelectronics, is taking advantage of these quantum effects and is proposing new ways of manipulating information. With a classical transistor information can simply be encoded into the presence or absence of an electrical current, in other words into the transistors state being *on* or *off*. An array of n ($n \in \mathbb{N}$) classical bits can represent 2^n different states but can only occupy one state at a time. A quantum bit (qubit) now takes advantage of what is called a superposition of states which differs fundamentally from the classical picture of a state. The information that is stored in a n -qubit system would require 2^n different classical bits to store the 2^n complex coefficients that describe the single quantum state. One n -qubit system can hold exponentially more 'classical' information than one 'classical' n -bit system. Apart from the information content, a quantum computer also benefits from an exponential speed-up compared to a classical system. Oversimplifying this rather subtle issue, we can say that classically we can only perform one operation at a time on a given set of bits. Quantum operations

¹ In September 2013, Intel demonstrated a 14nm Broadwell CPU at the Intel Developer Forum in San Francisco.

(quantum **gates**), by contrast, work on the complete superposition of states of one set of qubits at the same time. Putting it differently, doing one quantum operation is equivalent to doing an exponential number of classical operations at the same time. The concept of using this so-called quantum parallelism was first introduced in 1982 by Richard Feynman [1]. He proposed that a machine that utilizes quantum parallelism should be able to efficiently simulate any quantum system, when a classical machine would suffer an exponential slowdown due to the large number of possible superposed states. This is a huge motivation for actually building a quantum computer since quantum systems will play an ever more important role in the development and study of many forms of nanotechnology and in our understanding of the nanomachinery of biological molecules [2]. Perhaps the most widely known task for a quantum computer is Shor's quantum algorithm for factoring large numbers [3]. Our modern cryptographic system relies heavily on the fact that for conventional computers it is practically impossible to factorize a large number into its respective prime numbers. The computational time needed scales exponentially with the number of digits of the input number. A quantum computer however only scales linearly with this respect and is hence also interesting for a broader public audience.

'The idea of a quantum computer is simple, even if its realization is not.' [4]. Many materials are under consideration to achieve this highly ambitious technological goal. Qubits are usually imagined to be built up of the smallest form of matter like an isolated atom, that can for example be caught in an ion trap [5], but they may also be artificially created from larger electronic components, as is the case in superconducting systems for example [6–8]. In principle, every two-level system that can be prepared in a superposition of its two states can serve as a qubit. In this manuscript we will later focus on qubits which are constructed from semiconductor heterostructures and engineered by nanofabrication. Let us first have a look at the features that all different kinds of qubits have in common. Perhaps the most important aspect is that a quantum computer has to be isolated from its environment. It is hence crucial to study the dynamics of the interactions with the external environment to realize a quantum computer. This *information leakage* disturbs the quantum states of the qubit and causes what is known as decoherence [9]. Quantum information is very fragile compared to classical information. Once quantum coherence is lost, interference effects can no longer be observed and the phase that carries the information in a quantum system is lost. The requirement of having long relevant decoherence times has become known as one of the DiVincenzo criterions [4]. In total, a set of five criteria have been proposed, which have to be satisfied for the physical realization of quantum information processing. A physical system is needed that contains a collection of qubits. Their states have to be entangled, meaning that their total state cannot be written as a product of the states of individual qubits. One can also go one step further and state that the exponential growth of the Hilbert space when adding qubits must not come along with an exponential cost in resources such as time, space or energy [2]. At the same time, the individual qubits have to be well characterized. The physical parameters should be accurately known. Among them we mention the energy eigenstates of the qubit, the couplings to other states of the qubit, interactions with other qubits and possible couplings to external fields. Furthermore,

one needs the ability to initialize the state of the qubits with high fidelity. Initialization here means the ability to prepare a quantum state like for example the polarization of a spin in its ground state. On the one hand, this is important since the qubit registers should be known prior to a computation. On the other hand, so-called quantum error corrections schemes require copies of the initialized state. These schemes are needed since no system is completely free of decoherence but various techniques can allow for compensation of small amounts of decoherence. For further details on these schemes we refer the interested reader to [10]. Closely related to the initialization is the need for a qubit-specific measurement capability. Obviously, the result of the computation has to be measured, but the measurement of the specific qubit has also to be projective. The measured qubit will remain in the same state after measurement even after repeating measurements. At last, a quantum computer needs a *universal* set of quantum gates. As in a classical computer, we have to be able to manipulate the states of qubits. In a quantum computer this is equivalent to saying that we have to have access to the complete Hilbert space of the system. It has been shown that so-called single qubit rotations combined with two-qubit operations can be used to create universal quantum gates [11]. These requirements have to be fulfilled for the practical implementation of a quantum computer.

This highly ambitious goal of actually building a working quantum computer is still far from being reached. A variety of approaches is pursued by different research groups worldwide, yet it is impossible to predict, which system is going to fulfill all needed requirements in the future. We have chosen to study solid state systems and in particular low-dimensional electronic systems. The qubits that will be presented here are prototypes of possible qubit candidates and we will investigate how their quantum states can be manipulated. These structures also allow the fundamental study of electron interactions as we will see later on. The material system that we are using is the GaAs / AlGaAs semiconductor heterostructure. In this system, qubits can be realized by so-called quantum dots [12–15]. Quantum dots in this sense are a region of space where electrons are confined along all spacial dimensions. The degrees of freedom of such an isolated electron, i.e. its charge or spin can now serve as a two-level quantum system. The read-out of the charge state has become a well-established technology in the field [16–18], while the spin degree of freedom can also be accessed via spin-to-charge conversion [19]. The spin degree of freedom has been widely studied with respect to its application to quantum computing [20, 21]. For a deeper insight into this specific subject of electron spin qubits in quantum dots we refer the interested reader to this excellent review [22]. As the quantum dots are well confined regions in space, the qubits are stationary and an open question remains, how many of such qubits can be coupled in order to exchange quantum information coherently, and to do elaborate quantum computations. One could imagine to locally manipulate multiple qubit systems with the available state-of-the-art technology but the connection of the different qubits is still an outstanding problem.

This thesis now focuses in advancing this aspect of solid state qubits. Two general ideas will be investigated: In contrast to performing stationary qubit manipulations, we

can also envision to define a qubit, which can be operated on-the-fly. For this purpose we will make use of the wave nature of ballistic electrons. The electronic path which the electrons are following as well as the phase of the electronic wave can be used as the quantum information carrier. Since the phase coherence length of the electrons for our devices is large compared to our system size, we can produce interference effects between different electronic paths similar to optical interferometers [23]. The electronic paths can in turn be created in two different ways. Firstly, one can confine the electrons into quantum Hall edge states [24–29] and achieve interference effects analog to an optical Mach-Zehnder interferometer. Secondly, it is possible to confine ballistic electrons into one-dimensional channels by carefully shaping the potential landscape seen by the electrons [23]. This is the approach that we are going to follow and detail later-on in chapter 4. In such a system we can define logical states $|0\rangle$ and $|1\rangle$ by the presence of electrons in different paths [23] and combination of multiple one-dimensional channels via tunnel barriers in principle allows to create a universal set of quantum gates. Similar ballistic interferometers have been studied prior to this manuscript [30, 31] and we here will show how a ballistic electronic interferometer coupled to a tunnel-coupled wire [32, 33] can be implemented as a solid state flying qubit [34]. In chapter 4 we will develop a theoretical framework to describe the ongoing physics and carry out sophisticated numerical calculations to reproduce the experimentally obtained data. The numerical simulations will be carried out with Kwant, which is a software package for numerical quantum transport developed by our collaborators X. Waintal et al. [35]. The results of this chapter have been published [36].

Another approach for the coherent transport of quantum information is the following: One can think of locally manipulating the quantum state of an electron in a *standard* quantum dot. Instead of coupling this system now to another quantum system to transport the quantum information, one can also transfer the electron itself, containing the quantum information. For this purpose, we make use of so-called moving quantum dots [37] which can be created by a surface acoustic wave. Placing quantum dots at the injection and reception side of an one-dimensional electronic channel, we could show that it is feasible to isolate a single electron from its environment and to transfer it at a speed of approximately 3000 m/s over a distance of around 3 μm [38]. This approach is studied in detail in our group [39, 40] and forms a reliable single electron source. In the experimental chapter of this manuscript (Chap. 5) we will now aim at combining this single electron source with an electronic beam splitter, similar to what we have introduced above for the flying qubit device. The combination of two distinct single electron sources with an electron beam splitter will allow to perform tunneling experiments on single propagating electrons. It will also open up the possibility to study the interactions of two isolated electrons on-the-fly and can serve as a platform for quantum optics experiments with electrons in the future. We will elaborate the necessary steps towards this highly ambitious experimental goal and characterize the key features of all necessary ingredients.

CHAPTER 2

Background

Nowadays, almost every semiconductor device relies on the use of interfaces. Connecting two different materials creates new possibilities for generating novel electronic systems with unique electronic properties. Here we will concentrate on structures where the electronic behaviour is essentially two-dimensional. This means that the motion of charge carriers is restricted in the third spacial direction and thus quantized. In such structures with charge carrier densities ranging from $(10^{10} - 10^{12}) \text{ cm}^{-2}$ it is possible to achieve high mobilities exceeding $1 \times 10^7 \text{ cm}^2 \text{ V}^{-1} \text{ s}^{-1}$ at low temperature. High mobilities accompanied by long mean free paths have been essential for the discovery of the quantum Hall effect [41] and are indispensable for the study of coherent low-dimensional systems. Here we will focus on a two-dimensional electron gas (2DEG) formed in a GaAs / AlGaAs heterostructure. This material system has been used for the so-called *flying qubit*, a low-dimensional electronic interferometer (see chapter 4 for the details), as well as for single electron transport experiments (see chapter 5 for further information). In the first part of this chapter we will elaborate the necessary background that is needed to understand the physics of a two-dimensional electron gas (2DEG). The Landauer-Büttiker scattering formalism, which has been extremely successful for the description of quantum transport in 2DEGs will be presented, followed by a discussion of the general properties of the scattering matrix in the coherent scattering theory. We will then introduce the tight-binding model, which will form the basis of the simulations that will be carried out in chapter 3 concerning the flying qubit.

2.1 Two-dimensional electron gas

A two-dimensional electron gas can be obtained by growing different semiconductor materials with different band gaps on top of each other. In our case we use a silicon doped GaAs / AlGaAs heterostructure. This superlattice has been grown by means of molecular beam epitaxy by our collaborator A.D. Wieck from the Ruhr-University Bochum, Germany. The specific layer stacking, which is depicted in figure 2.1(a), will lead to a band structure that confines the electrons in the growth direction of the superlattice in a triangular quantum well, which can be seen in figure 2.1(b). A layer of undoped $\text{Al}_{0.34}\text{Ga}_{0.66}\text{As}$ (spacer) with a band gap of 1.86 eV is grown on a pure GaAs substrate with a band gap of 1.52 eV. This is followed by Si-delta doping [42] and a subsequent

$\text{Al}_{0.34}\text{Ga}_{0.66}\text{As}$ layer capped by GaAs. The Silicon acts as a n-dopant by replacing the Aluminum atoms.

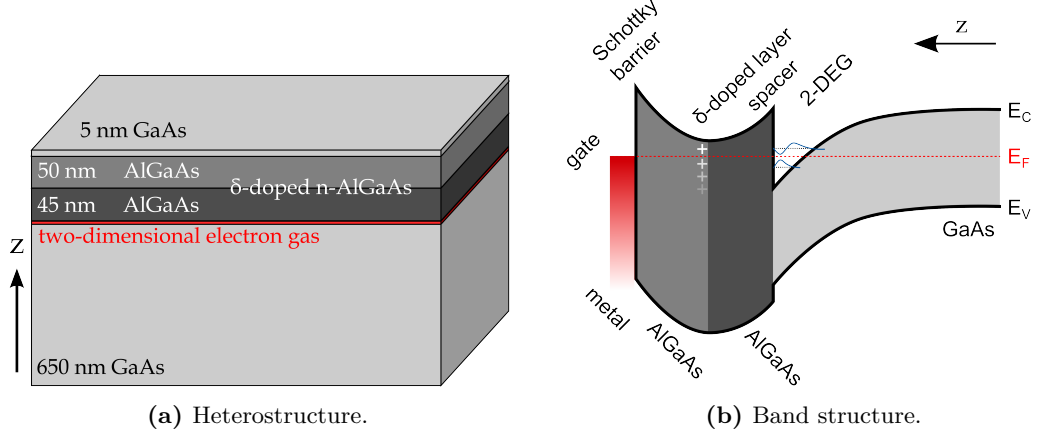


Figure 2.1: GaAs/AlGaAs heterostructure with band structure. Different layers of GaAs/AlGaAs have been grown by molecular beam epitaxy (panel a). Due to their difference in band structure (panel b), a quantum well is forming at the interface of the GaAs and the AlGaAs. This forms the two-dimensional electron gas (2DEG) as charge transport is quantized in z -direction.

Due to the difference in the band gaps, a quantum well is formed. At cryogenic temperatures, the well electrons only occupy the lowest energy level and are confined in the z -direction but are free to move in the x - y plane, which in our case is buried around 90 nm below the structure's surface. This forms the so-called two-dimensional electron gas. The spacing layer separates the 2DEG from ionized impurities which leads to a reduced impurity scattering potential felt by the electrons in the 2DEG and hence increases the carrier mobility. General transport properties of such a system can be obtained with the so-called Van der Pauw method [43, 44]. This allows to determine the charge carrier density, which in our case is $n_e = 2.7 \times 10^{11} \text{ cm}^{-2}$ and the mobility, which is $\mu = 1 \times 10^6 \text{ cm}^2 \text{ V}^{-1} \text{ s}^{-1}$. From this we can estimate the mean free path of an electron to $l_e = 8.6 \mu\text{m}$. This is the average distance an electron travels before scattering elastically off an impurity. We can also deduce the Fermi energy of the system via

$$E_F = \frac{\pi \hbar^2}{m^*} n_e, \quad (2.1)$$

with $m^* = 0.067 \times m_e$ being the effective band mass of an electron in bulk GaAs and m_e the rest mass of the electron, to 9.6 meV. The corresponding Fermi wavelength can be calculated from the electron density as well via

$$\lambda_F = \sqrt{\frac{2\pi}{n_e}} \quad (2.2)$$

to approximately 50 nm. This gives rise to the order of magnitude at which the wave nature of electrons plays an important role. Electric manipulation of the potential that

is seen by the 2DEG is done via metallic surface gates. These gates form a Schottky barrier at the metal-semiconductor interface, which provides a high enough barrier such that no charges can leak from the gates into the 2DEG. A detailed description of the potential engineering that can be performed is postponed to the simulation section (see section 3.3) and further details about the handling of the 2DEG to the fabrication part of this thesis (see section 5.2). Let us now turn to the transport properties of a 2DEG. We will first introduce the quantum transport regime from both, a conceptual and an experimental point of view, and then present the Landauer-Büttiker formalism that can be used to describe this regime.

2.2 Landauer-Büttiker formalism

Conductivity in solid state systems is essentially limited by the scattering events of the charge carriers. These can be divided into several categories, each associated with a specific length scale due to the specific scattering process. The transition from a classical transport regime to a quantum transport regime can be well characterized by these length scales. To begin with, electrons can scatter off the lattice vibrations of a crystal, called phonons. The energy of the electron in such a collision is not conserved, the scattering is inelastic. We can define a characteristic inelastic scattering length

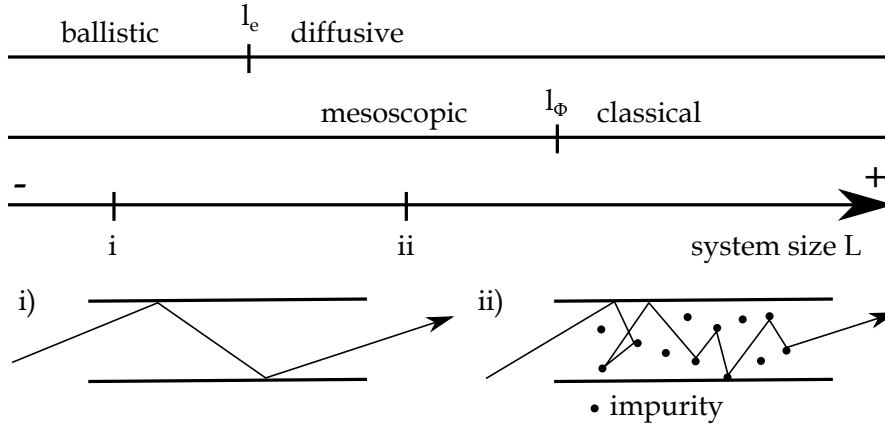


Figure 2.2: Definition of different transport regimes. A system with a system size L smaller than the mean free path l_e and smaller than the phase coherence length l_ϕ ($L < l_e < l_\phi$) is in the ballistic quantum regime (i), whereas a system with $l_e < L < l_\phi$ (ii) is called diffusive. Systems which do not preserve the phase coherence of the electrons ($L > l_\phi$) are considered classical, systems that preserve are called mesoscopic. The two bottom subfigures show possible electron trajectories of (i) and (ii).

l_{ie} that has to be larger than the sample size in order to be in the quantum regime. Furthermore, electrons can also scatter off other electrons in the crystal. This is an extremely important inelastic process since it is responsible for the thermalisation of the electrons at very low temperatures (< 1 K), where the electron-phonon coupling is inefficient. In addition, the electrons can scatter elastically from impurities. The donors that have been mentioned above as well as lattice defects and surface states fall into this category of elastic scatterers. The associated length scale is the mean free path l_e . In

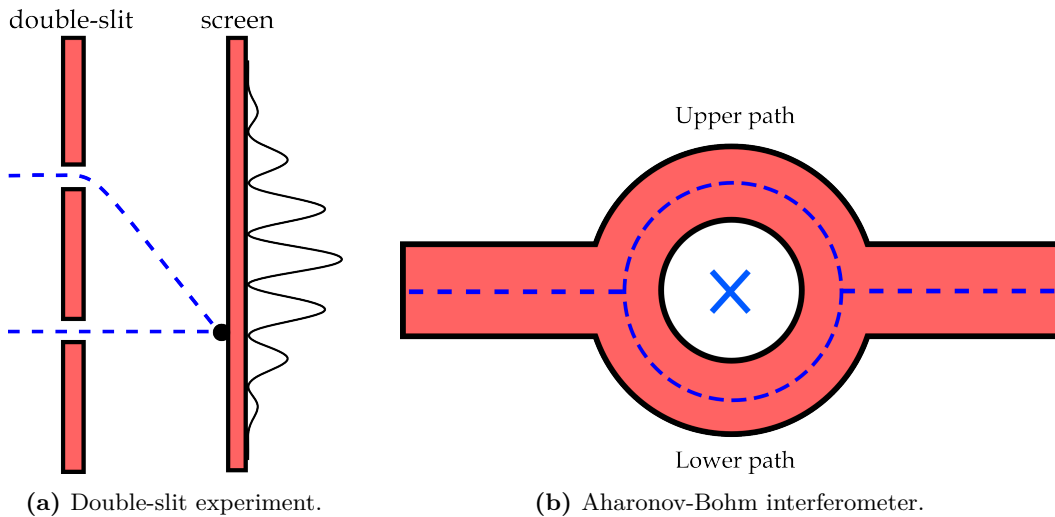
order to observe quantum interference effects it is important that the wave functions have a well defined phase relation. The distance over which the wave functions keep a well-defined phase relation is called the phase coherence length $l_\phi \sim l_{ie}$. This length scale hence sets the condition whether quantum effects can be observed. Altogether, these length scales now provide a powerful tool to distinguish between different transport regimes as we have depicted in figure 2.2.

In a classical circuit, transport can be described well by Ohm's law and Kirchhoff's law. Resistance arises due to the fact that electrons are losing their energy during the transfer. Energy is absorbed by the phonons and as a consequence, the temperature of the crystal is increased. Equivalently we can say that the sample size is much bigger than the inelastic scattering length. The transport regime of interest is the mesoscopic transport regime. The first important characteristic is that the energy of the charge carriers remains unaltered. No inelastic scattering events are taking place. Elastic scattering events only affect the initial momentum of the charge carriers and therefore do not change the phase of the electrons. Coherence can be guaranteed by decreasing the sample size accordingly to the phase coherence length. With the help of the different length scales that we have introduced above, we can summarize these conditions by

$$l_{in}, l_\phi > L > l_e, \quad (2.3)$$

where L is the actual sample size. These conditions are met in the high quality, high mobility heterostructures that we are using. Modern nanofabrication technology allows to scale down the sample size to these length scales and transport in the mesoscopic transport regime can be achieved. Here, the wave nature of the electrons is governing the transport properties and quantum effects can be observed and coherently manipulated. Let us introduce some simple examples along with experimental manifestations of this coherent behaviour of electrons before turning to a deeper theoretical description.

The simplest way to prove coherent quantum effects is to employ interference phenomena. The first observed electron interference dates back to 1925, when C. Davisson and L.H. Germer bombarded a crystal of nickel atoms with a beam of electrons [45, 46]. They observed interference fringes of the scattered electrons and their associated wavelength was found to be in good agreement with the hypothesis of Louis de Broglie from 1924 [47]. Another milestone was the demonstration of the famous Young's double slit experiment from optics with electrons in 1961 by Jönsson and coworkers [48, 49], who measured single, double and multiple slit electron diffraction in vacuum. A sketch of the double slit experiment is depicted in figure 2.3(a). Their experiment has been performed with a huge ensemble of electrons. Thereinafter, in two separate experiments, interference patterns were created using individual electrons. Pozzi et al. studied statistical aspects of electron interference phenomena in 1974 [50] whereas 15 years later Tonomura et al. performed another realization of the Young's double slit experiment from optics with single electrons [51]. They have shown experimentally that single electrons, which are successively passing through a so-called *electron biprism* [52] - a device equivalent to a set of double slits - show an interference pattern when measured on a screen behind. We show their experimentally obtained data in figure 2.4. After a sufficient number of



(a) Double-slit experiment.

(b) Aharonov-Bohm interferometer.

Figure 2.3: Electronic interference experiments. Panel a) shows an oversimplified cartoon of the Young's double-slit experiment. A coherent wave, in our case an electron wave, passes through both slits on the left (blue dotted line) and interferes on the screen on the right. The depicted situation shows a destructive interference of the two electron trajectories. The resulting interference pattern is indicated on the right side of the screen. Panel b) depicts a sketch of an Aharonov-Bohm interferometer. The incoming electron wave separates into the upper and lower arm and interferes when the two trajectories are recombining. The resulting interference pattern here depends on the magnetic field (blue center cross) which the two paths are encircling.

electrons having passed one-by-one through the double-slit, an interference pattern is clearly visible. This is '[...] a phenomenon impossible, absolutely impossible to explain in any classical way, and has in it the heart of quantum mechanics', Feynman [53]. The fact that any classical theory fails to explain its experimental outcome, renders this example perfect for a proof of quantum mechanical behaviour. A classical particle-like picture cannot explain the arising interference phenomenon. Quantum mechanically, one could naively state that the electron has passed through both slits simultaneously and interfered with itself, however it is more convenient to specify that the probability amplitude, the actual quantum wave has passed through both slits. The interference arises due to the difference of the geometrical paths of the two trajectories, which is equivalent to phase difference of the probability wave in the two different paths. Nevertheless, looking at the experimental data in figure 2.4, one might object that the actual detection of an individual electron is a point on the detector screen and thus particle-like. This can be understood, that when the electron strikes the screen, there is no longer an ambiguity about its location. Striking on the screen, the electronic wave function collapses on the impact point. Quantum mechanics does not explicitly say that an electron is a wave, but rather that its probability of being found anywhere in space is determined from a wave function. Putting it differently, we can say, that the lack of information, which slit the electrons have passed gives rise to the interference phenomenon.

The measurement of such interference patterns is a direct manifestation of the wave

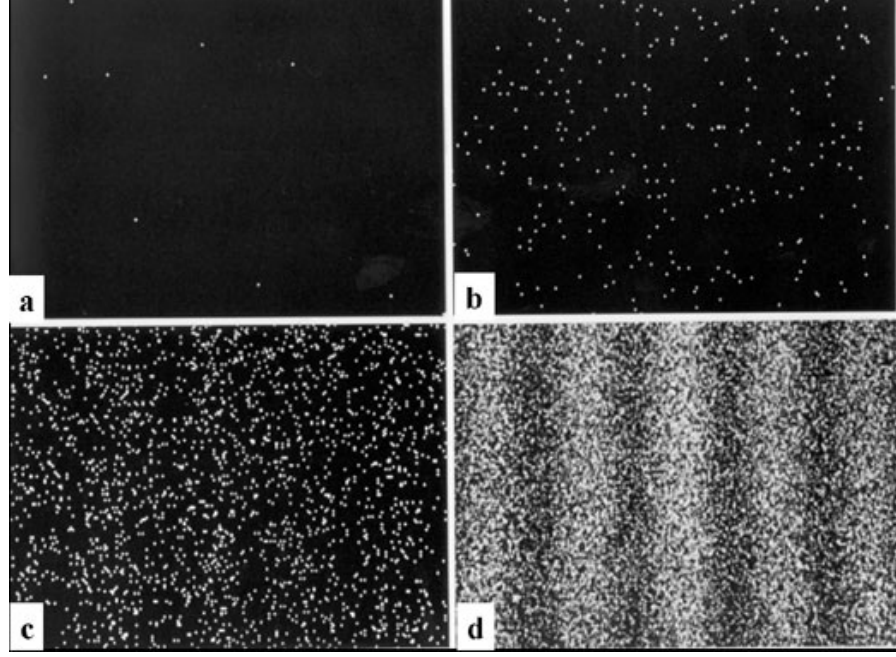


Figure 2.4: Tonomura experiment. Single electrons in vacuum are passing successively through a double slit set-up. The different panels show a time sequence of images with an increasing number of electrons, each arriving separately on the screen. a) 10 electrons, b) 100 electrons, c) 20000 electrons, d) 70000 electrons. An interference pattern is clearly visible after a sufficient number of electrons, revealing the wave nature of the electrons.

nature of particle waves and of their coherence. In our electronic system, such interference patterns can not only be created with a geometrical path difference, but can also be observed with respect to magnetic flux. It has been shown that a magnetic field changes the phase of two electron beams that are encircling a magnetic flux. This is commonly known as the Aharonov-Bohm effect [54] and the pioneering experimental work has been done with electrons in vacuum by Tonomura et al. [55], whereas the first solid state experiment was conducted by Webb et al. in a metallic ring structure [56]. The Aharonov-Bohm phase can be expressed using the following formula:

$$\phi = \oint \vec{k} d\vec{l} + \frac{e}{\hbar} \int B dS, \quad (2.4)$$

where $k = 2\pi/\lambda$ is the wave vector, λ the corresponding wavelength, B the magnetic field, S the surface area of the Aharonov-Bohm ring and ϕ the phase difference of the two encircling paths. Depending on the latter, the recombination of the two trajectories leads to destructive or constructive interference patterns. The first term in equation 2.4 corresponds to a geometrical path difference whereas the second term corresponds to the phase due to the magnetic field and the surface area of the Aharonov-Bohm ring. These electronic wave phenomena are extremely similar to the interference effects that are observed in optics. Apart from the obvious one-to-one correspondence of a path difference

in such interferometers, the trajectories can also be influenced by the wave vector k (first term in equation 2.4). In an optical interferometer, this can be achieved by slowing down a coherent beam of light in one arm of the interferometer. A difference in the diffractive indices of the materials in the two arms can serve this purpose. Similarly, the propagation speed of electrons can be influenced by changing the confinement potential of the respective arm and hence the respective eigenenergies of the propagating electrons. As we will verify for the flying qubit later-on (see paragraph around figure 4.29), this can be done by simply changing the gate voltages of the confinement gates.

Keeping these rather elegant examples of the manifestation of the wave nature of electrons in mind, we can now turn to a theoretical description of the quantum transport regime. Let us introduce the key features of the Landauer-Büttiker approach, which has proven very successful in the description of mesoscopic transport. In 1957, Landauer proposed a new point of view that transport should be viewed as a 'consequence of incident carrier flux' [57, 58]. The general idea behind is to write the current through a conductor as a probability of an electron being able to transmit through the conductor. He has derived a formula that relates the linear response conductance to the transmission probability through a region of elastic scatterers between two temperature baths. This was followed by a more complete discussion in 1970 [59], where he has treated the conductor as a single scattering center that lies in between two dissipative reservoirs. The role of the reservoirs is to inject electrons into a state defined by their chemical potential and to absorb electrons that are leaving the conductor into a reservoir. All dissipative phenomena are taking place in the reservoirs, in particular, an electron that enters a reservoir, loses its phase coherence and in addition, two electrons emitted from different reservoirs are incoherent. His approach has been extended to the case of multiple-terminal measurements with multiple quantum channels [60, 61] and derived from linear response theory [62, 63]. Without going into a detailed derivation, we can write the zero-temperature multi-channel Landauer-Büttiker formula [64]:

$$G = \frac{2e^2}{h} \text{Tr}(\hat{t}\hat{t}^\dagger) = \frac{2e^2}{h} \sum_n T_n, \quad (2.5)$$

where \hat{t} is the transmission matrix which contains the transmission amplitudes $t_{\alpha\beta}$ from channel β to channel α . Tr is the *Trace* operator. T_n are the eigenvalues of the matrix $\hat{t}\hat{t}^\dagger$, or in other words the transmission probability associated to the n -th transmission eigenmode. The actual transmission coefficients can be obtained from the scattering matrix which will be introduced in the following section.

2.3 Coherent scattering theory

Scattering experiments have always played an eminent role in nuclear and atomic physics, like the discovery of the nucleus by Rutherford [65] or the discovery of sub-atomic particles such as quarks [66, 67]. In low energy physics, scattering phenomena provide information about the solid state system like information from neutron, electron or x-ray scattering. In transport physics, scattering theory provides a powerful tool to get insights into the details that are governing the quantum phenomena that are arising

at small length scales. Here we restrict ourselves to a simple example of the coherent scattering formalism by introducing the scattering of a single electronic mode on a tunnel barrier. This example will point out the general properties of the scattering matrix. The explicit calculation of the scattering matrix elements will be done for a tunnel-coupled wire in the simulation section (see 4.3). For a more complex system, the calculation of the scattering matrix can be quite cumbersome. In this case, a numerical approach is very useful and we will conduct these kind of calculations with the aid of the open source package Kwant (see 3.1).

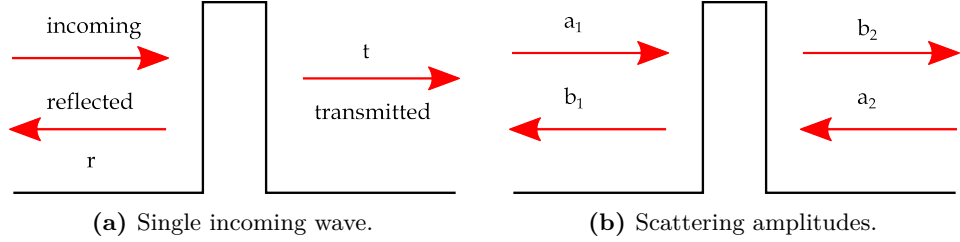


Figure 2.5: Scattering matrix of a wave at a tunnel barrier. Panel a) shows a single incoming wave that is transmitted and reflected at the tunnel barrier with corresponding transmission and reflection coefficients t and r . Panel b) shows the wave amplitudes of incoming and outgoing waves as they have been defined in equation 2.7.

Panel a) in figure 2.5(a) shows an incoming one-dimensional wave with wave vector k_x that is partially transmitted at a tunnel barrier with the transmission coefficient t and partially reflected with the reflection coefficient r . The scattering state can be described via

$$\Psi_{inc}(x) = e^{ik_x x} \quad \Psi_{ref}(x) = r e^{-ik_x x} \quad \Psi_{tra}(x) = t e^{ik_x x} \quad (2.6)$$

whereas the complete scattering matrix for the tunnel barrier reads

$$\begin{pmatrix} b_1 \\ b_2 \end{pmatrix} = \begin{pmatrix} r & t' \\ t & r' \end{pmatrix} \begin{pmatrix} a_1 \\ a_2 \end{pmatrix} \quad (2.7)$$

where a_i and b_i are the amplitudes of the incoming and outgoing waves, respectively, as depicted in panel b) of 2.5(b). The scattering matrix has to be unitary, since the current has to be conserved:

$$s^\dagger s = 1. \quad (2.8)$$

Multiple scattering events can be calculated by multiplying the individual scattering matrices. The scattering matrix can be calculated analytically for some explicit cases [68], solving the time-independent Schroedinger equation with appropriate boundary conditions, whereas more complicated systems have to be approximated, for instance by using the WKB-method [69]. Let us now study the influence of the magnetic field on the transmission coefficient of the scattering matrix for this simple two-terminal device. We

rewrite equation 2.7 to

$$\begin{pmatrix} b_1 \\ b_2 \end{pmatrix} = s(B) \begin{pmatrix} a_1 \\ a_2 \end{pmatrix}. \quad (2.9)$$

This equation remains invariant if we reverse the momenta and the magnetic field:

$$\begin{pmatrix} a_1^* \\ a_2^* \end{pmatrix} = s(-B) \begin{pmatrix} b_1^* \\ b_2^* \end{pmatrix}, \quad (2.10)$$

which leads us to

$$s(B)s^*(-B) = 1 \quad (2.11)$$

and after some algebra to a condition for the transmission coefficient

$$T(B) = T(-B), \quad (2.12)$$

which, combined with equation 2.5, tells us that the conductance of a two-terminal device has to be an even function of the magnetic field.

$$G(B) = G(-B) \quad (2.13)$$

This is commonly known as the Onsager relation and in our context referred to as phase rigidity. For a two-terminal device it is obvious from equation 2.13 that the conductance has to be a symmetric function with respect to the magnetic field. As a consequence, the phase at zero magnetic field can only take multiples of 0 or π and is hence called rigid. We will come back in greater detail to this fundamental effect when discussing the different regimes of the flying qubit.

The Landauer-Büttiker-formalism together with the scattering approach provides a powerful toolkit to calculate the transport properties in mesoscopic conductors. The formalism has proven itself in a multitude of applications [70, 71] and will be used in chapter 4 to describe the main features of the flying qubit. As briefly mentioned above, the calculation of the scattering matrix of complex systems can be quite difficult, even impossible, analytically. For this reason we now introduce a tight-binding approach that allows to describe complex systems numerically and furthermore, together with the concepts that will be introduced in section 3.1, to compute their respective scattering matrices.

2.4 Tight-binding model

A common approach for the calculation of the electronic band structure of a crystal is the so-called tight-binding model [72]. It is most appropriate when the electrons move through the crystal slowly and are in some sense tightly bound to an atom or *site* from where they can tunnel or *hop* to adjacent neighbors. The model is not easily applicable to free electrons in a metal but works rather well for the description of semiconductors or insulators. The electronic wave function is calculated similarly to the

atomic orbitals of the free atom and the atom itself is treated non-interacting with the neighboring atoms. The atomic potential is assumed to be strong. The tight-binding approximation deals with the case where the overlap of these atomic wave functions is large enough to require corrections to the picture of isolated atoms. Here, we will concentrate on the treatment of a two-dimensional electronic system.

The general tight-binding Hamiltonian for systems in second quantization reads [73]

$$\hat{H} = \sum_{i \neq j}^N t_{ij} c_i^\dagger c_j + \sum_{i=1}^N \varepsilon_i c_i^\dagger c_i \quad (2.14)$$

where c_i (c_i^\dagger) denotes the annihilation (creation) operator of an electron on site i . t_{ij} is the hopping from site i to site j and ε is the energy of site i . The site index i commonly stands for the position in space although it can also include other possible degrees of freedom like any combination of spin or atomic orbital. Hamiltonians of this form can directly arise from an approximate atomic description of a physical system or alternatively from a finite-size discretization of a continuum Hamiltonian which will result in a tight-binding Hamiltonian.

Let us turn to our specific case of a two-dimensional electron gas and consider the Schrödinger equation in two dimensions:

$$-\frac{\hbar^2}{2m^*} \Delta \Psi(x, y) + V(x, y) \Psi(x, y) = E \Psi(x, y). \quad (2.15)$$

m^* denotes the effective mass of the electron, $V(x, y)$ the potential in the two-dimensional electron gas induced by surface gates or impurities. We discretize the Laplace-operator Δ in two dimensions via

$$\partial_x^2 + \partial_y^2 = \lim_{a \rightarrow 0} \frac{\Psi(x+a, y) + \Psi(x-a, y) + \Psi(x, y+a) + \Psi(x, y-a) - 4\Psi(x, y)}{a^2}, \quad (2.16)$$

with a being the discretization or lattice constant. This allows to map the Schrödinger equation onto a discrete lattice. The prefactor 4 in the last term comes from the simple fact that we consider only nearest neighbour hoppings on a square lattice and that each site has four sites. We define the discrete wave function $\phi_{i,j} \equiv \Psi(ia, ja)$ and the potential $V_{i,j} \equiv V(ia, ja)$. The variable change for the wave function has been made for clarity to distinguish between the discrete and the continuous case. This leads us to the discrete two-dimensional Schrödinger equation

$$-\frac{\hbar^2}{2m^* a^2} (\phi_{i+1,j} + \phi_{i-1,j} + \phi_{i,j+1} + \phi_{i,j-1} - 4\phi_{i,j}) + V_{i,j} \phi_{i,j} = E \phi_{i,j}. \quad (2.17)$$

We can identify the hopping integral from one site to an adjacent site

$$t = \frac{\hbar^2}{2m^* a^2} \quad (2.18)$$

with a being the lattice constant. With the hopping we can then identify the term $4 \times t$ in equation 2.17, which will be referred to as the onsite energy. In figure 2.6 we show such a tight-binding lattice.

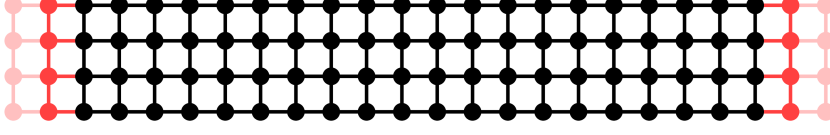


Figure 2.6: Tight-binding square lattice. Sites are represented by black dots and hoppings by lines connecting the sites. The lattice constant is the distance between two of such sites. Two leads (fading red) are connected to each side of the structure.

Sites are represented by the black dots and hoppings by the black lines connecting them. The lattice constant a is the distance between two of such sites. For this specific case, the mesoscopic region is connected to two contacts (fading red). These contacts are modeled by infinite leads, which can be represented as finite objects due to their translational invariance. The general form of the wave function in them is a superposition of plane waves. Additional information about the leads can be found in the appendix (see A.1). Let us already note at this point, that it is crucial to consider the potential landscape at the transition region between a lead contact and the scattering region. In order to avoid parasitic backscattering, one must not to introduce a spurious jump in the potential at the contact. In the case, which is depicted in figure 2.6 one should apply the potential $V_{i,j}$ of the leftmost (rightmost) site i on the left (right) lead contact as well. Following this procedure assures that no backscattering occurs at the connection of the system to the leads. This goes along with the fact, that the number of available channels in the semi-infinite electrodes is equivalent to the number of channels at the system's borders. We will come back to this point later-on in section 4.5.

For the numerical implementation of the tight-binding model and for the numerical simulations of our desired structures, we have been using the open source package Kwant that is under active development by our collaborators X. Waintal and co-workers [35] which will be detailed and used in the following section.

CHAPTER 3

Numerical simulations

As we have mentioned in the introduction, an important part of this thesis has been devoted to the understanding of the flying qubit experiments through numerical simulations. In this chapter we will outline the basic principles of Kwant, which forms the basis of the numerical simulations that have been performed throughout this thesis. After a general introduction, we will detail, how to create a tight-binding system using the Kwant system builder. We will then elaborate step by step everything that is necessary to simulate the complete flying qubit, such as SI-units in a two-dimensional tight-binding system, electrostatic surface gates and the implementation of the magnetic field. The theoretical background will be explained as much as needed whereas the developed tools will be tested on well-established examples. In the end of this chapter we will comment on the software architecture that has been written around Kwant.

3.1 Kwant

Numerical simulations have always played an important role in mesoscopic quantum transport [74–76]. The most popular recursive Green’s function (RGF) algorithm has been developed and became a valuable tool to check and extend analytical calculations, although it is restricted to quasi-one-dimensional geometries. Another important step has been the development of the non-equilibrium green function (NEGF) formalism [77, 78], which has been derived from the Keldysh formalism [79] and provided a simple route to compute the physical observables from a microscopic model. It has become a sophisticated numerical approach with a variety of applications in physics [80–83]. The NEGF formalism relies in its core on the calculation of retarded Green functions and hence on the direct inversion of the Hamiltonian which restricts its application to a few thousand sites. The RGF algorithm allows the computation of systems of a few million sites but had first to be generalized for arbitrary geometries and an arbitrary number of terminals. This so-called knitting algorithm [73] is now one of the cornerstones of the Kwant solver libraries. At the same time Kwant includes a new set of algorithms, which is known as the wave function approach. This kind of algorithm is associated with the Landauer-Büttiker scattering formalism and generally speaking performs wave-matching between individual parts of the system. For piecewise smooth potentials and potentials with at most a finite step discontinuity at the matching point, matching two wave functions means to

adjust both, their values and their derivatives at the matching point. Continuity of the wave function requires the value left and right of the matching point to be identical, smoothness of the wave function requires the derivative of the total wave function left and right of the matching point to be identical. The framework has recently been shown to be mathematically equivalent to the NEGF algorithms in the dissipation-less case [62, 64, 84] and offers an enormous speed-up compared to conventional solvers. Kwant is designed such that it automatically chooses the best solver for a given problem, which already indicates that Kwant has been developed for a broader audience without the need to have a profound knowledge about all the mathematical subroutines that are taking place. In fact, userfriendliness has been one of the key aims of the Kwant-project. Kwant is a Python package for numerical quantum transport calculations. It is a powerful tool for the simulation of any physical system that can be described by a tight-binding model. The choice of Python as a high-level interface offers an extremely powerful and yet simple way for system definitions and calculations of the transport properties like conductance, noise, scattering matrix, dispersion relations, modes, wave functions and charge or current densities. Apart from its solvers, Kwant contains a generic tight-binding system builder that allows to easily define lattices, Hamiltonians and the degrees of freedom like charge or spin. Kwant allows to easily map the Hamiltonians to their corresponding sparse matrices and does not require the user to be concerned with all the mathematical details. This saves a lot of time, which can be spent more conveniently

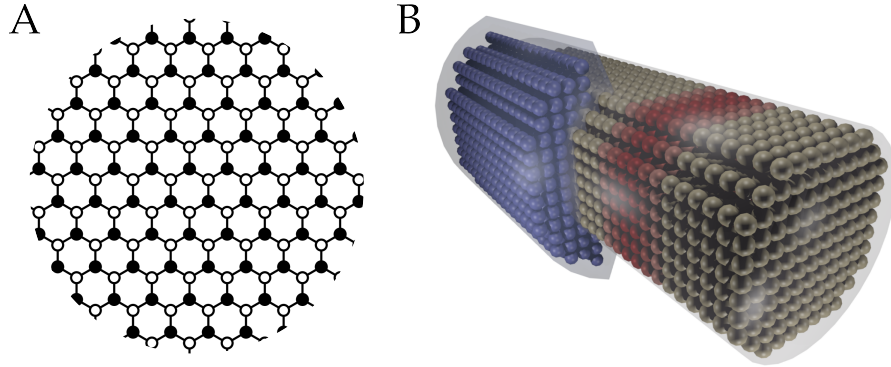


Figure 3.1: Examples of different tight-binding lattices. Kwant allows to create a variety of different tight-binding lattices like for example a honeycomb lattice (panel A) as it can be found in Graphene. 3-dimensional lattices are feasible as well and we show a 3D model of a semiconducting quantum wire in panel B. The semiconductor is gray, whereas the red region corresponds to a tunnel barrier and the blue region is superconducting. The latter image has been taken from [35].

on physics. A common usage of Kwant can be divided into four steps. One first defines a system, calculates the observables, analyses the data and plots the results.

In the following we will elaborate this process first for simple systems and then complicate it step by step, by introducing real units, electrostatic gates, magnetic fields, multiple contacts and apply it in the end to the study of a solid-state implementation of a flying qubit. We will restrict the discussion to two-dimensional electron gases throughout this chapter although any other lattice type can be described by Kwant within the same

approach. Figure 3.1 shows two different tight-binding systems that have been realized with Kwant. Panel A is a honeycomb lattice that can be used to calculate properties of Graphene and panel B is a more advanced three-dimensional lattice combining a semiconducting wire, a tunnel barrier and a superconductor.

Let us now consider the simple case of a quasi one-dimensional wire connected to two terminals. Here we will show how to create the precise square lattice that has already served as an example in the previous chapter (see figure 2.6 for comparison). The lattice that we will create in the following is 20 sites long, 4 sites wide and connected to one lead at both sides. We take advantage of the Kwant tight-binding model builder and define a Kwant - Builder object using

```
1 sys = kwant.Builder()
```

and define its lattice to be a square lattice

```
1 lattice = kwant.lattice.square()
```

The Builder object does not yet contain any sites. In order to add sites to the system, in this case to create a one-dimensional wire, we define a specific geometry and hence the number of sites. We specify their onsite energy (see equation 2.17) at the same time.

```
1 sys[(x,y) for x in arange(20) and y in arange(4)] = 4 * t
```

t is the hopping integral from equation 2.18. The term in the square bracket is a so-called generator that generates 20 sites in x-direction and 4 sites in y-direction. Generators are Python-specific and allow to create iterable functions without the need of storing iterable lists in the computer's memory. The definition of the hopping Hamiltonian matrix elements between nearest neighbors is done by the command

```
1 sys[lattice.neighbors()] = - t
```

Since we want to study transport properties of the structure, we have to add at least two electrodes to the system. These electrodes are semi-infinite leads and hence characterized by their translational invariance. They can be represented with a Builder object

```
1 lead_symmetry = kwant.TranslationalSymmetry([-1, 0])
2 lead = kwant.Builder(lead_symmetry)
3 lead[(lattice(0, y) for y in range(4))] = 4 * t
4 lead[lattice.neighbors()] = - t
```

In the first line, we define the translation symmetry via the vector $[-1,0]$. Line 2 creates the Builder object similar to the system definition above, however here we make use of the translational symmetry. For this reason, we only need to specify the y-direction of the lead as it is done in line 3. Line 4 defines the nearest neighbor hoppings in the lead. Finally, the lead is attached to the scattering region.

```
1 sys.attach_lead(lead)
```

A second lead on the other side of the wire can be created by simply inverting the vector that points in the direction of the translational symmetry. To convert this tight-binding model into a form suitable for efficient numerical calculations, we finalize it via

```
1 sys = sys.finalized()
```

This is the common procedure to create tight-binding models using the system Builder from the Kwant library. Builder objects contain the sites with their corresponding degrees of freedom, information about the lattice type, spacial symmetries, connection to leads and hermiticity of the system. The *finalization* converts the created tight-binding system to a low-level system. This procedure becomes clearer looking at figure 3.2. Here we give the one to one correspondence between a tight-binding system and the corresponding low-level system.

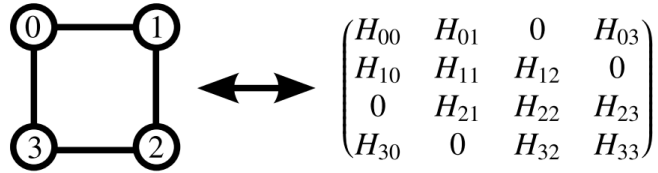


Figure 3.2: Low-level tight-binding system. The tight-binding degrees of freedom correspond to nodes and are the diagonal matrix elements, whereas off-diagonal elements connect different sites via hoppings. The figure has been taken from [35]

Tight-binding degrees of freedom (H_{ii}) correspond to a node of a graph, whereas every non-zero hopping matrix element H_{ij} to an edge connecting nodes i and j . For further details and benchmarks we refer to [35].

These systems can now be passed on to one of the solvers of Kwant. The system that we have created with the above algorithm is indeed the system that is depicted in figure 2.6. Let us first calculate the scattering matrix of the system that we have just created as a function of the energy of the incoming modes.

```
1 smatrix = kwant.solvers.default.smatrix(sys, energy)
```

Together with equation 2.5 we can compute the conductance which is depicted in figure 3.3.

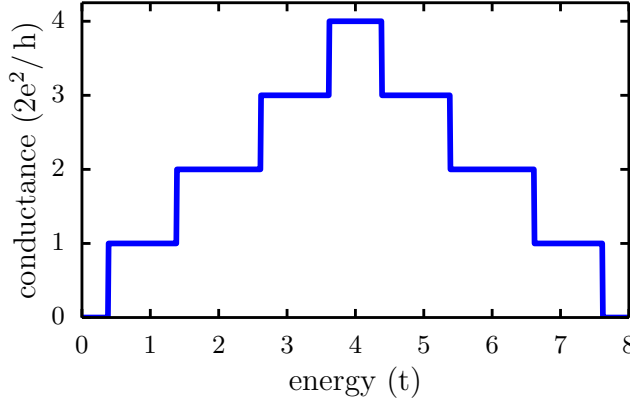


Figure 3.3: Conductance as a function of energy. As we increase the energy of a tight-binding system, in this case a system with 4 parallel chains of sites, the conductance increases until each chain carries one quantum of conductance. The tight-binding approximation is limited to energies below four times the hopping t . Above this energy, the conductance decreases.

At zero energy, the conductance of the system is zero. When increasing the energy of the system, more and more channels can be occupied and the total conductance is increasing stepwise. In a real physical system, we would expect the conductance to increase incessively with increasing energy. In this simple numerical system, we however observe a maximum conductance when the energy reaches $4 \times t$. This maximum is given by the maximum width (y-direction) of the wire, which in our case is 4. Each *chain* (number of sites in y-direction) carries one conductance channel in this case. Above an energy of $4 \times t$, the conductance decreases. This effect is a band effect and reflects the tight-binding nature of our calculation. The elsewise parabolic dispersion relation is approximated by the cosine potential

$$E = -2t \cos(k_x a) - 2t \cos(k_y a) + 4t \quad (3.1)$$

which is displayed in figure 3.4. The red curve shows the parabolic dispersion relation whereas the black curve shows the tight-binding approximation. The approximation is valid at small energies.

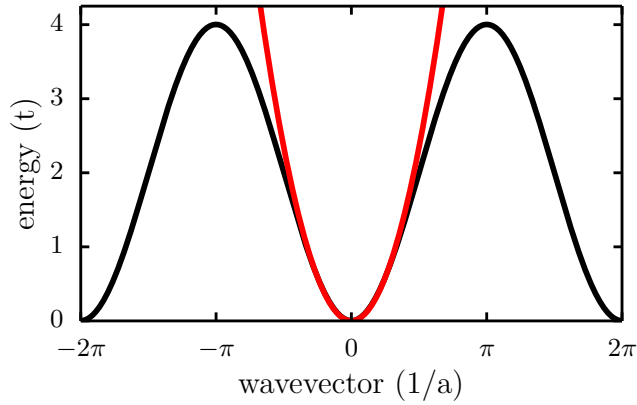


Figure 3.4: Dispersion relation. The tight-binding dispersion relation is sinusoidal (black curve) and hence 2π -periodic. This is an approximation of the otherwise parabolic dispersion relation (red curve).

3.2 Real units

In order to simulate a real 2DEG, it is much more convenient to change from an arbitrary unit system to real physical values. This allows to build the structures with the actual nanofabricated size and to confront the simulations quantitatively to the experimental conditions. From the charge carrier density of the wafer, we can calculate the Fermi energy at which the conductance of the system will be calculated (see equation 2.1). The hoppings depend on the choice of the lattice constant a and can be calculated from equation 2.18. The choice of the lattice constant is crucial for the simulations. A too large lattice constant will lead to parasitic discretization effects and has hence to be avoided. We will investigate this in greater detail, when introducing the quantum point contact as a first example, by doing a so-called convergence test. This will help us to choose an appropriate lattice constant and prove that our simulations are in the continuum limit. A too small lattice constant however, is of no use due to simulation time limitations. We can already anticipate here that it will be of the order of several nanometers. Our algorithm has been designed such that the sample geometry stays fix, but we are still able to vary the lattice constant. The code will directly calculate the corresponding number of sites for a given sample depending on the choice of a . All simulations are carried out in SI-units, with the exception of the energy, which we scale with the electron charge to eV. On the one side, this circumvents being limited by the precision of *doubles* in Python and on the other side it is a practical unit for low-temperature experimentalists.

3.3 Electrostatic gates

In experiments it is common practice to pattern the 2DEG with metallic surface gates. The gates have different properties. Obviously, the gates have a certain size (commonly nanometer scale) and a certain shape (commonly rectangular or triangular). Apart from this, they are spatially separated from the 2DEG, since they are sitting on the wafer's surface, typically at a distance of around 100 nm. Although it is possible to approximate

the potential landscape that is created by such kind of gates via empirical functions, we have chosen a different approach in our simulations. We would like to stay as close as possible to a specific sample design but at the same time keep the algorithm as universal as possible for different sample designs. Python is a highly object-oriented programming language and we have therefore chosen to create gate objects, which have the same properties as the nanofabricated gates: they can be adjusted in shape and size and can be placed at a certain distance above the *numerical* 2DEG. We can calculate the potential of an individual gate analytically starting from Poisson equation following reference [85]. We limit ourselves to triangular and rectangular shapes since these are sufficient for modeling any arbitrary shape of gates. The electrostatic potential Φ of a finite rectangle can be calculated via

$$\frac{\Phi(\vec{r}, d)}{V_g} = g(x - L, y - B) + g(x - L, T - y) + g(R - x, y - B) + g(R - x, T - y). \quad (3.2)$$

This rectangle is defined by $L < x < R$ and $B < y < T$ (Left, Right, Bottom, Top). It is a

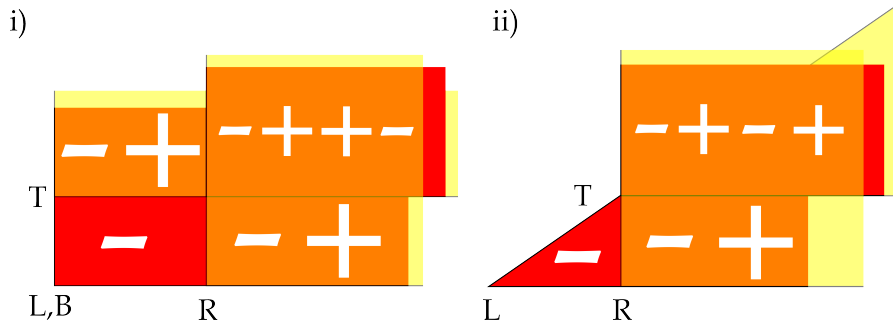


Figure 3.5: Electrostatic gate definition. Finite gates can be built with semi-infinite rectangles and infinite triangles. Rectangles are infinite to the top and to the right, whereas triangles are infinite in the direction of their opening opposite to their anchor point. The red (yellow) color illustrates a negatively (positively) charged infinite gate. Panel i) (ii) shows the construction of a rectangular (triangular) gate. To create the red negatively charged rectangular gate (L, T, R, B), we place negative semi-infinite rectangles at LB and TR and positive semi-infinite rectangles at BR and TL.

linear combination of four semi-infinite rectangles with their vertices on the four corners. These rectangles have borders on the bottom and on the left side, whereas they are infinite in the other two directions. For clarity, we illustrate this in panel i) of figure 3.5. The first gate on (B, L) carries a negative voltage $-V_G$ (red color). To obtain the top border, we place a positive gate $+V_G$ at (B, T) (yellow color). This gate cancels out the surface above T (red (negative) + yellow (positive) = orange (neutral)). The right border is built by placing a positively charged rectangle at (L, R). The contributions add up in the top right quadrant and we have to place a negatively charged gate at (T, R) to finally obtain a single finite rectangular gate with borders defined by (B, L) and (T, R).

The potential of one semi-infinite rectangular gate is given by

$$g(u,v) = \frac{1}{2\pi} \arctan \frac{uv}{dR}. \quad (3.3)$$

d denotes the depth of the 2DEG and u,v the spatial coordinates of the sites. Following the exact same line of thought, panel ii) of figure 3.5 shows how to create a finite triangle out of infinite gate objects. We can now use these gates to shape the potential landscape that is seen by the electrons in our 2DEG. Since any polygon can be sliced into a finite number of triangles, we are now able to implement any shape of gates. To simplify the work flow, we have developed an algorithm that converts the binary GDS II format, which we commonly use to design our nanostructures, into python-friendly gate objects. This allows to study and optimize our gate structures. The python-interface is designed such that no profound knowledge of the implementation is necessary and is hence user-friendly. GDS II files can be imported directly and the corresponding potential landscape is automatically calculated. Let us now take advantage of what we have elaborated so far and turn to a specific example.

One interesting case is the situation of a quantum point constriction. When the width of a constriction is of the order of the Fermi wavelength, the effect of conductance quantization arises. Pioneering work has been done by two groups [71, 86] who showed that such short and narrow constrictions in a 2DEG can indeed form a so-called *quantum point contact* (QPC). The quantization arises due the quantization of the transverse momentum of the charge carriers. In an ideal quasi-one-dimensional channel with a square-well confinement of width W , the allowed states have quantized values for $k_y = \pm n\pi/W$ and continuous values for k_x . These quantized subbands lead to a quantized conductance of

$$G = \frac{2e^2}{h} N, \quad (3.4)$$

where

$$N = k_F W / \pi \quad (3.5)$$

is the integer number of channels and can be evaluated from the Fermi wavevector k_F and the width W of the constriction. The factor of '2' comes from the spin degeneracy. A lot of effort has been undertaken to describe the subtle details of such quantum point contacts [87, 88]. With our gate implementation we are able to study the conductance properties of different QPC geometries numerically. Let us start by defining the gate structure as it is depicted in the left panel of figure 3.6. We place two gates symmetrically in the center of a tight-binding lattice that is connected to one lead on each side of the structure. The square lattice is $1 \mu\text{m}^2$ large. We choose a lattice constant of $a = 5 \text{ nm}$, which leads us to 40000 sites in the square lattice. The rectangular gates in this example are $w = 30 \text{ nm}$ wide and separated by $h = 150 \text{ nm}$. In the right panel of figure 3.6, we switch on the two gates and exemplify a potential landscape for a certain gate voltage that is seen by the electrons 90 nm below the sample's surface. The blue color corresponds to a high negative voltage, while red is the onsite energy at zero gate voltage. Such a structure

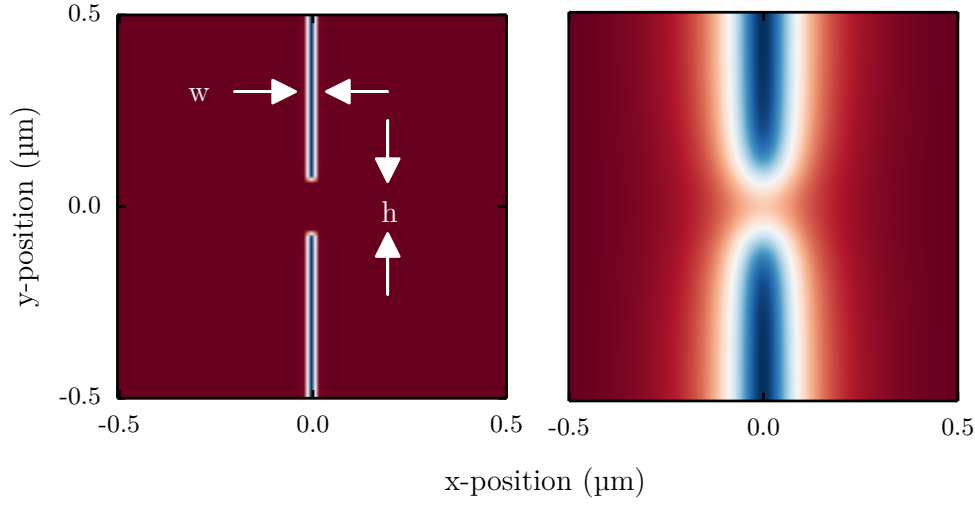


Figure 3.6: Quantum point contact gates. The quantum point contact is formed by two rectangular gates that are separated by $h=150$ nm and are $w=30$ nm wide. The left figure shows the position of these two surface gates (blue with white frame) on top of the 2DEG and the right figure shows the potential that is seen by the electrons in the 2DEG 90 nm below the surface in arbitrary units (blue: high potential, red: low potential).

allows us to reproduce the behaviour of a quantum point contact. When increasing the negative gate voltage of the two gates, we deplete the electron gas that is underneath the gates and form the one-dimensional constriction. Further increase of the negative gate voltage pushes the channels consecutively above the Fermi energy, which in our case is simply fixed at 9.6 meV (electron density $n_e = 2.7 \times 10^{11} \text{ cm}^{-2}$) and results in conductance steps as it is seen in figure 3.7. On the left side, we show a simulated

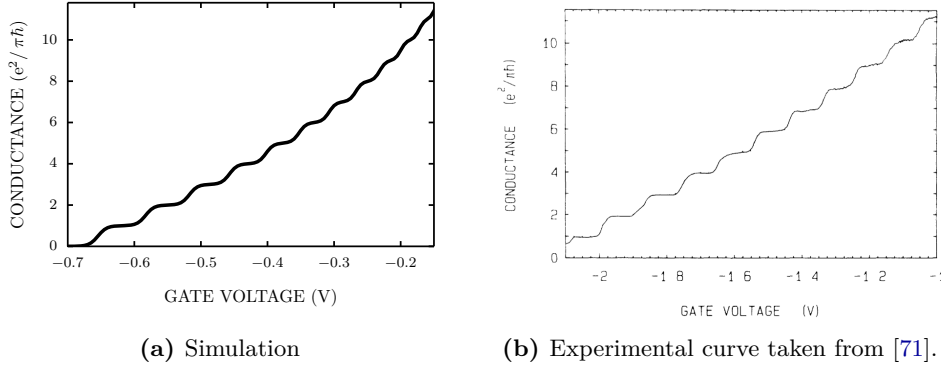


Figure 3.7: Quantum point contact: simulation vs. experiment. In the left panel we show a simulated pinch-off of a quantum point contact. The conductance drops stepwise as the energy levels are pushed above the Fermi energy when increasing the gate voltage. In the right panel we show experimental data from the original experiment [71] for comparison.

pinch-off curve, while on the right side we confront it to actual experimental data taken

from [71]. The resemblance is quite remarkable, although the gate voltage values differ by a factor of three. We will come back to this difference later on. Let us take advantage of what we have introduced so far. With the help of these gate objects, we are able to simulate any arbitrary gate shape and to check the potential landscape created by these gates. This provides a powerful tool to check different geometries and to optimize a given sample design before even setting one foot into a cleanroom. In support of this idea, let us investigate the behaviour of the just introduced example of a quantum point contact and change its geometry. The results of this numerical experiment is shown in figure

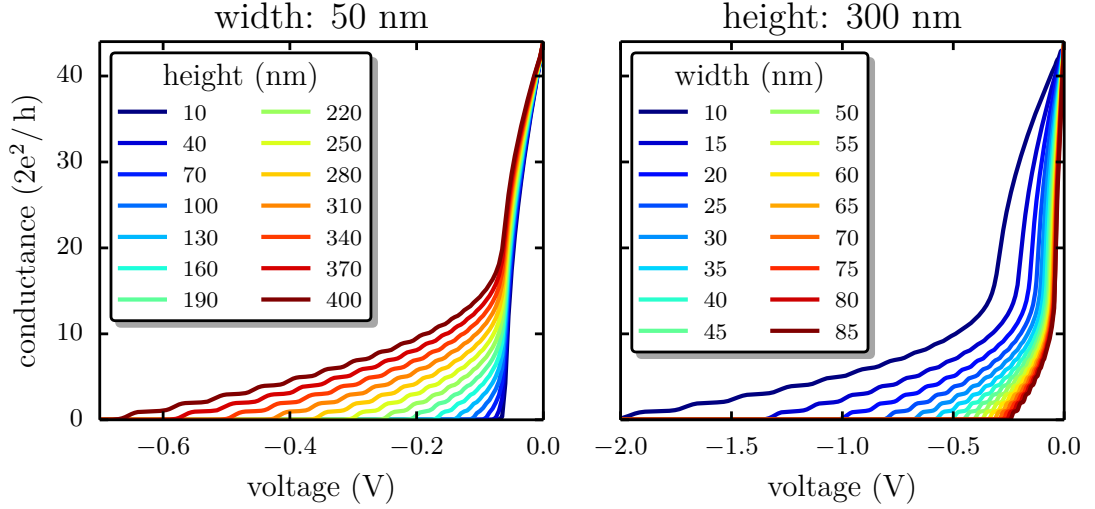


Figure 3.8: Quantum point contact geometries. Pinch-off curves for quantum point contacts with fixed width (left panel) and fixed height (right panel). All curves have the first sharp descent in common, which is due to the depletion of the electrons in the 2DEG below the gates. The change in the slopes indicates that the transport is governed by the one-dimensional constriction and quantization effects start appearing. The bigger the distance between the contacts (larger height), the more conductance steps are visible and the wider the contacts the fewer are the number of steps.

3.8. Besides their geometrical difference, the general shape of all the pinch-off curves is very similar. The first sharp descent is the so-called *2D pinch-off*. The electrons are pushed away from beneath the gates, more precisely they are scattered back from the gate potential, starting at the point where the gates have the strongest influence. This is obviously right below the gates. Once, all conductance channels are backscattered in this manner, the two-dimensional electron gas below is depleted and conduction from the left to the right side is only possible through the quantum point contact. This is where all pinch-off curves change their slope and quantization effects start appearing. In the left panel of figure 3.8, we have fixed the width w (see figure 3.6) to 50 nm. We vary the distance between the two gates (color scale). If the constriction is too narrow, we are not able to observe conductance steps and all the conductance channels are pinched directly after the 2D pinch-off. For an increased distance, we observe more and more conductance steps as equation 3.5 suggests. In theory we can in principle increase this

distance to infinity and still observe a complete pinch between these two gates. On the contrary, this size is limited by the maximum voltage that can be applied on the gate without breaking the Schottky-barrier between the metallic gate and the semi-conductor. For the wafer that we will use in the experimental part of this thesis, the gate voltage should not exceed -2.5 V. The voltages of a simulated pinch and a real pinch have to be scaled by a factor of around 20 due to screening effects. In the right panel of figure 3.8 we do a complementary experiment, fix the distance between the two gates and change its width. For a very thin gate, one needs a quite large voltage to completely pinch the channel. The thinner the gate, the further is the 2D pinch-off shifted to more negative gate voltages. Our simulations are conducted at zero temperature, but the shape of the conductance steps is already rounded, which we therefore associate to the smoothness of the electrostatic potential.

For the above simulations we have chosen a lattice constant of $a = 5$ nm and quietly assumed the continuum limit where discretization effects are negligible in our simulations. To verify that this is indeed the case, we now pinch curves of the structure presented above for different lattice constants. The results are depicted in figure 3.9. For large lattice constants, we observe noisy curves that rather poorly resemble a common pinch-off curve, as it can be seen in the top panel. This is due to the fact that the important length scale of our system, which is the Fermi wave length $\lambda_F \approx 50$ nm is comparable to the lattice constant. For even bigger a , our simulations would yield zero for any system or gate structure. Decreasing the lattice constant leads to a converge of the curves. This convergence becomes clearer, looking at the difference of the conductances with respect to the smallest lattice constant of $a = 3$ nm, as it is depicted in the bottom panel. On the one hand, this figure shows that the algorithm that we have designed works properly and on the other hand that we can safely assume the continuum limit with lattice constants smaller than 5 nm. On a theoretical level, the computation time scales with $O(L^3)$ and the memory usage with $O(L^2 \log L)$. For the case of a square lattice the number of sites increases by a factor of 4 when dividing the lattice constant by 2. To give an example, we table this circumstance for the simulation of the quantum point contact that we have presented above using a single processor. It is important to note, that one can use multiple CPUs and work in parallel to increase the simulation speed. To present this scaling behaviour clearly and understandably, we assume that computing the scattering matrix with a lattice constant of 10 nm takes exactly one second and refer to table 3.1.

Table 3.1: Comparison of different lattice constants

lattice constant	number of sites	computation time	sweep (240 pts)
10 nm	10000	1 s	4 min
5 nm	40000	64 s	4 h
4 nm	62500	244 s	16 h
2 nm	250000	1562 s	4.3 d

As a result of the above discussion, we have chosen to work with a lattice constants of 10 nm for common calibrations and quick simulations and to decrease it usually to 5 nm

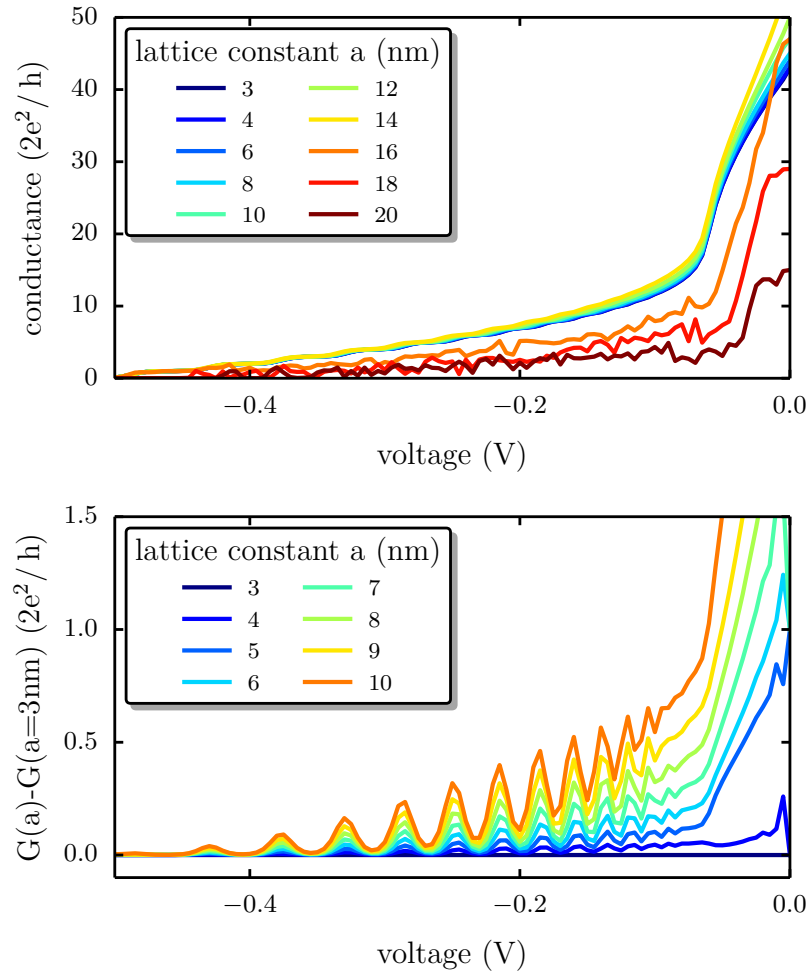


Figure 3.9: Quantum point contact: convergence test. Pinches of a quantum point contact for different lattice constants. Huge lattice constants lead to numerical noise as can be seen in the top panel. The curves converge for a sufficient small lattice constant. In the lower panel, we display the difference of the conductance with respect to the smallest used lattice constant.

for real simulations.

3.4 Magnetic field

We now turn to the implementation of the magnetic field. The vector potential alters the phase of the electrons and can hence be expressed as a phase factor for the electrons that are hopping from one site to another. The magnetic flux can be expressed as multiples of the magnetic flux quantum h/e in one unit cell via

$$\Phi = \frac{e}{h} a^2 B \quad (3.6)$$

where B is the magnetic field and a^2 is the surface of the unit cell in a square lattice with lattice constant a . Since the physical properties of our system are not influenced by the specific choice of gauge, we can choose the Landau gauge

$$\vec{A} = By\hat{e}_x \quad (3.7)$$

and compute the phase Φ_{ij} between two sites i, j to

$$\Phi_{ij} = -\frac{e}{h} B(x_i - x_j) \frac{y_i + y_j}{2}. \quad (3.8)$$

This phase corresponds to $\int d\vec{r} \vec{A}$, where the integral is calculated along the straight line between the two sites i and j . We identify the additional phase factor

$$t_{ij} = te^{2\pi i \Phi_{ij}}, \quad (3.9)$$

where t_{ij} is the hopping from site i to j and site i has the coordinates (x_i, y_i) . This implementation now allows to apply a magnetic field to our simulations. As a first example we compute the local density of states for the quantum point contact that has been discussed above. Panel A in figure 3.10 shows the sum of the squared wave functions of the modes that are injected into the system via the left lead. The system is tuned such that a total of two channels is transmitted through the constriction. Most of the electrons are reflected from the potential that is created by the gates and form an interference pattern. The color scale is logarithmic to put an emphasis on the transmitted signal through the constriction. This kind of behaviour has been beautifully demonstrated by [89, 90], where the actual wave function of such a quantum point contact has been measured with the help of an atomic force microscope. If we now turn on the magnetic field in our simulations, we observe that the density of states gets quantized and the well-known Quantum Hall Effect [41] appears. Here we display the mode with filling factor $\nu = 1$ at $B = 2.6$ T and tune the gates such that 50% of the edge state is transmitted and 50% of the edge state is reflected by the constriction. Quantum point contacts that work in such a beamsplitter configuration in the Quantum Hall regime have recently attracting a lot of interest, since they can be used to study interference effects of single electronic wave packages [91, 92].

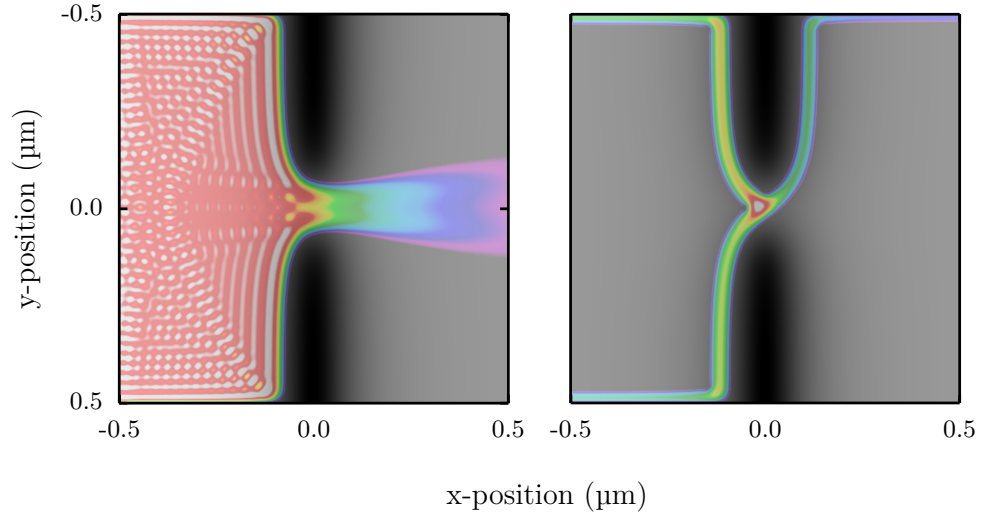


Figure 3.10: Quantum point contact wave functions. Panel A shows the sum of the squared wave functions of all incoming modes from the left. Two channels are being transmitted through the quantum point contact. Panel B shows a quantum Hall edge channel at filling factor $\nu = 1$ that is partially reflected from the quantum point contact (transmission $T=0.5$).

3.5 Examples

In the following we give a few examples that can be easily implemented with Kwant, following the approaches that we have introduced above. These examples will help us to verify that our simulations work properly when confronting the numerical results to the physical expectations. As we have mentioned above, a typical example of coherent

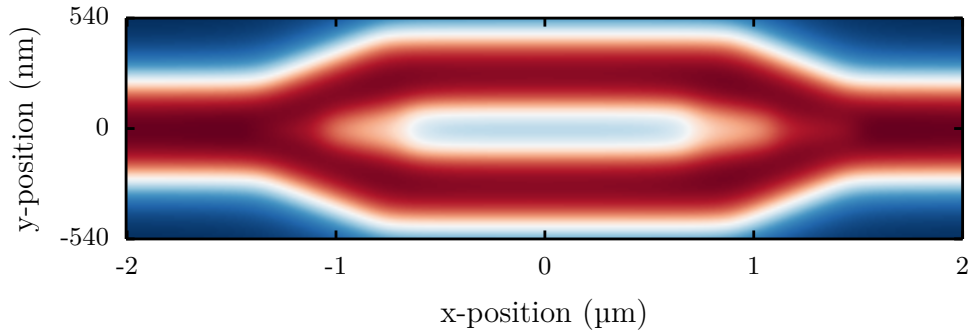


Figure 3.11: Realistic implementation of an Aharonov-Bohm interferometer. The electrostatic potential has been defined using the gates from the previous section. The structure is connected to one lead contact on each side. Electrons follow the red paths (low potential), whereas the 2DEG is depleted below the blue color (high potential). Changing the magnetic field will change the phase of the two electron trajectories.

electron transport in the ballistic regime is the Aharonov-Bohm interferometer. Let us directly simulate a realistic electronic implementation using our gates from the previous

section. The potential landscape of the sample is shown in figure 3.11. The structure is connected to one lead on each side. Red indicates the electron paths, whereas blue indicates the depleted region of the 2DEG. The phase difference between two electron paths will depend on the actual surface of the center gate. Without knowing the precise electron trajectories it is difficult to estimate the precise size of the center island of the Aharonov-Bohm ring. We can however estimate a maximum and a minimum surface

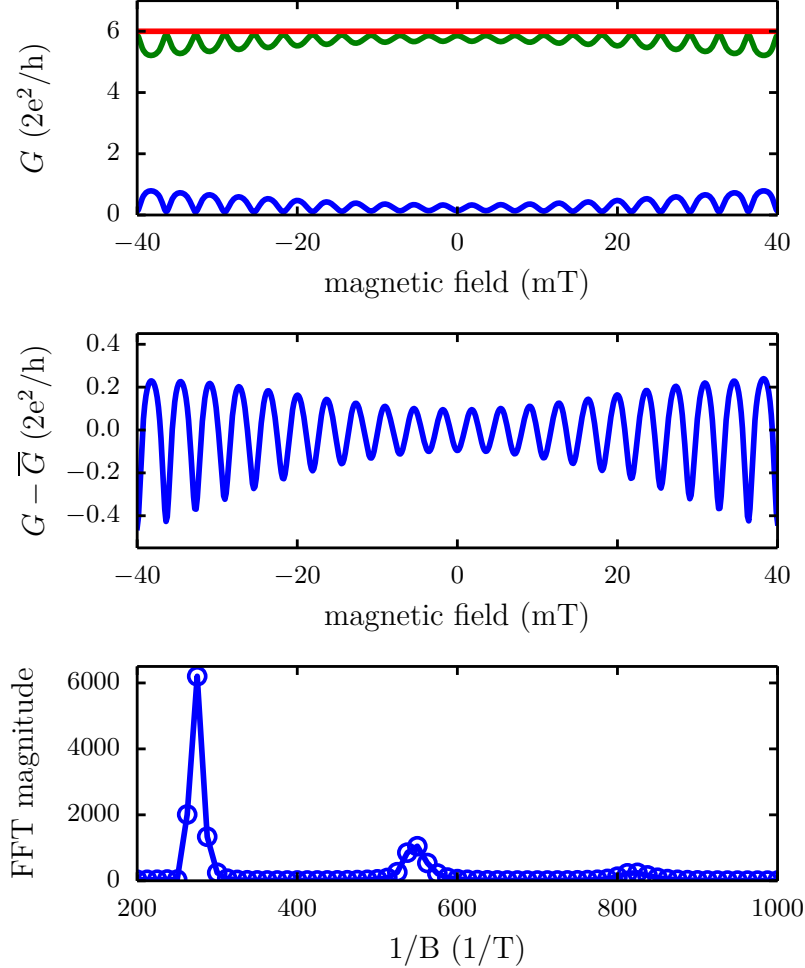


Figure 3.12: Aharonov-Bohm oscillations. The top panel shows the simulated data as a function of magnetic field, leading to interference between the upper and the lower electron trajectory. In the center panel, we have removed a linear background for better visibility. The bottom panel shows the calculated FFT. The first peak corresponds to the direct interference between the upper and lower electron trajectory. The higher order peaks correspond to trajectories that encircle the Aharonov-Bohm ring multiple times, the peak amplitude is decreasing due to the diminished probability for these long trajectories.

area from the sample design. Geometrical considerations lead us to a surface between $2 \times 10^{-12} \text{m}^2$ and $6 \times 10^{-13} \text{m}^2$. We now pinch all the gates such that a total of six channels

is transmitted through the structure and sweep the magnetic field symmetrically around zero. Electron interference arises due to the phase that the electrons acquire in one path relative to the other (see equation 2.4). The numerical result is displayed in figure 3.12. In the top panel we find that the transmitted signal (blue) oscillates as a function of the magnetic field. This is the typical feature of the Aharonov-Bohm effect. Here we display the total number of modes (red) and the backscattered signal (green). Most of the channels are backscattered. Already from this curve, we can draw several conclusions. Since the backscattered signal is oscillating with the magnetic field, there exist electron trajectories that encircle the Aharonov-Bohm ring and come back into the injecting lead on the left. Most of the injected modes are backscattered.

In general, there are different possible mechanisms for backscattering. First of all, modes that see a potential barrier with an energy higher than their eigenenergy are commonly scattered back, although a small portion of the wave function may also extend into the region behind the potential barrier, depending on its thickness. Secondly, the backscattering depends on the speed with which the potential barrier grows. One could in principle assign a wave impedance for every distinct translational invariant region and calculate the amount of backscattered signal due to an impedance mismatch. Or in other words, if we for example double the width of a quantum channel, a part of the wave function will be backscattered at this channel opening due to the change in width. In the example that is presented above, most backscattering occurs at the entrance of the Aharonov-Bohm ring, where any symmetric wave function would hit the *peak* of the potential of the center island with its anti-node. We detail this circumstance in figure 3.13: the potential landscape of figure 3.11 is displayed in black and white (high and low electrostatic potential) in the background of both panels. As can be seen in the top panel, the first symmetric mode (mode 0), shows interference in the most left region due to the backscattering, which is happening at the entrance of the Aharonov-Bohm ring at around $-1\text{ }\mu\text{m}$. This image corroborates our above statement. In contrast, the first anti-symmetric mode (mode 1) does not show such interference due to its node at the onset of the potential peak. This figure nicely shows the backscattering that is happening at the entrance of the Aharonov-Bohm ring, however it is hard to estimate the amount of backscattered signal at the exit of the Aharonov-Bohm ring, which shows magnetic field dependence. In order to get more information about this signal, which encircles the Aharonov-Bohm ring multiple times, we subtract a linear background from the transmitted signal (top panel of figure 3.12) and display it in the center panel. We note that this curve is symmetric with respect to the magnetic field as its symmetry is bound to Onsager relations (see equation 2.13 for comparison). To further analyze the data and to extract the actual surface of the center island, we perform a Fast Fourier Transformation (FFT), which is displayed in the bottom panel. The first harmonic corresponds to an interference of the electrons that are propagating in the upper and lower arm of the interferometer and are directly forward scattered to the right lead contact. These trajectories do not encircle the center island multiple times. This peak position is directly related to one times the surface of the Aharonov-Bohm ring, which we extract to $1.16 \times 10^{-12}\text{m}^2$. This is in agreement with the geometrical boundaries that we have discussed above. The second and third harmonic is due to electron trajectories

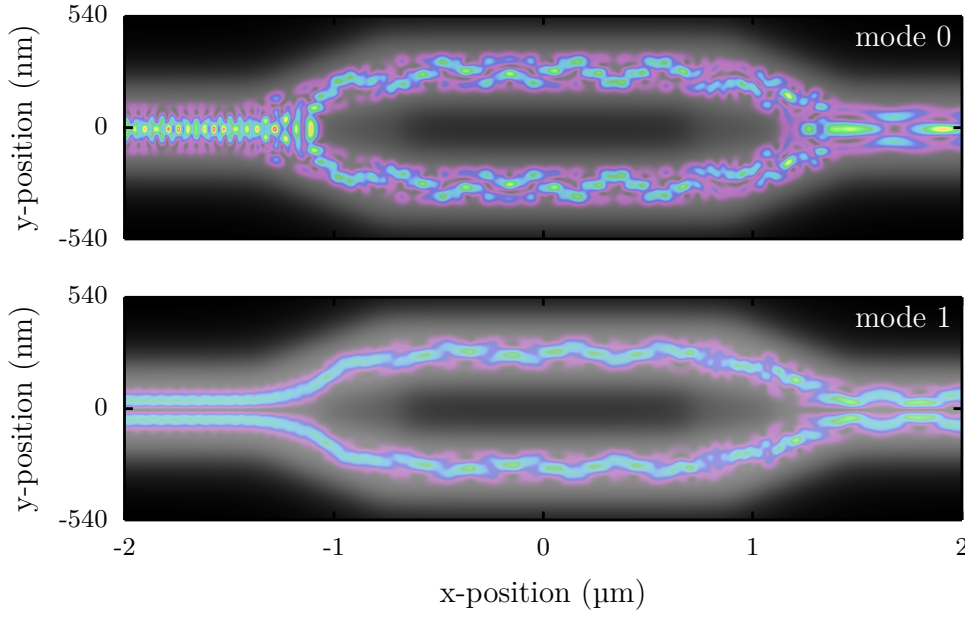


Figure 3.13: First two propagating modes in the Aharonov-Bohm ring. The electrostatic potential of figure 3.11 is displayed in black (high potential) and white (low potential) in the background of both panels. Electron modes are injected from the left and follow the regions of low potential in white. In the top panel we see the first symmetric mode (mode 0) inside the structure. Most backscattering occurs at the entrance of the Aharonov-Bohm ring which leads to interference effects and a complex pattern for the transmitted wave. The first anti-symmetric mode (mode 1) is displayed in the bottom panel. Only minimal backscattering occurs at the entrance of the Aharonov-Bohm ring due to the node of the mode at $y=0$.

that encircle the center island multiple times due to backscattering at the exit of the Aharonov-Bohm ring. Since the probability of doing so is diminished simply by the length of the trajectory, the amplitude of the FFT decreases with increasing number of loops. The second example that we will discuss is a double quantum point contact as displayed in figure 3.14. This structure forms an electronic cavity which resembles a Fabry-Perot interferometer. The transmission through such a system is governed by the resonant tunneling effect. Each time an energy level of the localized states in between those two quantum point contacts is aligned with the Fermi energy, we can observe an increase of the conductance. The shape of these conductance peaks is Lorentzian and the transmission coefficient $t(E)$ of such a resonant tunneling event can be described as a function of energy E by [93, 94]

$$t(E) = \frac{\Gamma_L \Gamma_R}{(E - E_r)^2 + \frac{1}{4}(\Gamma_L + \Gamma_R)^2}, \quad (3.10)$$

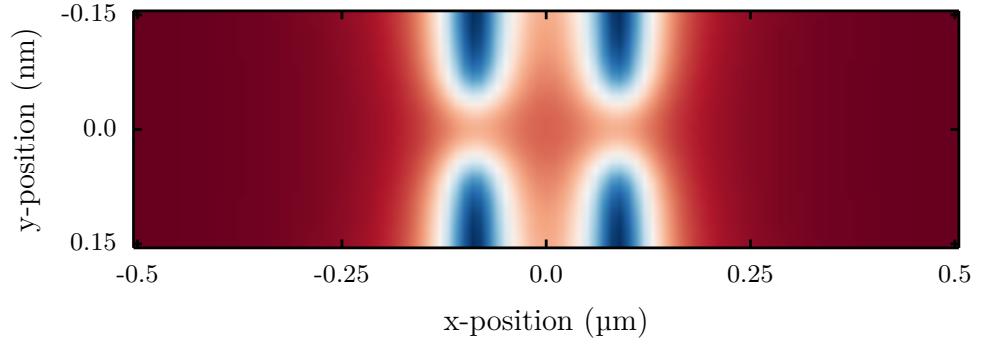


Figure 3.14: Two quantum point contacts in series form a cavity for the electrons. The gates are 25 nm wide and separated by 80 nm. Transport through such a structure will lead to Fabry-Perot resonances.

where E_r is the energy of the localized state and Γ the leak rate of an electron from the localized state to the **L**eft and **R**ight electrodes. This transmission has a maximum when the two barriers are symmetric. This effect has been observed experimentally [95, 96] as

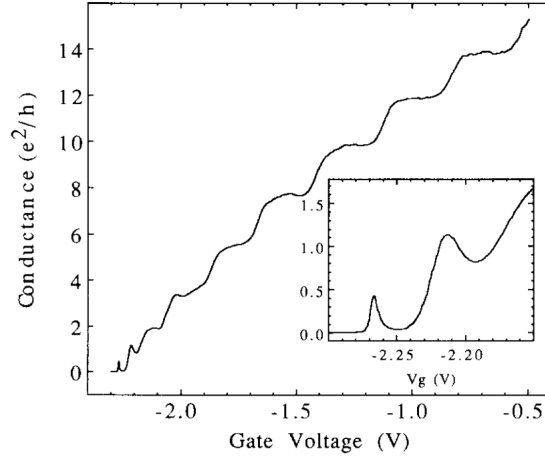


Figure 3.15: Resonant tunneling effect observed by [95]. The Lorentzian shaped conductance peaks on top of the pinch-off curve are associated to the formation of a Fabry-Perot cavity due to an impurity that is situated close to a quantum point contact.

we show the obtained experimental data of the latter reference in figure 3.15. McEuen et al associate the feature to a neutral impurity that is situated in their quantum point constriction. This effect is also commonly observed in our experiments. If we now pinch our numerical structure symmetrically, we expect to find these resonances on the top of the pinch-off curve. The numerical result is shown in figure 3.16. Indeed we find the Fabry-Perot resonances on top of our pinch-off curve. Let us focus on the very left peak and check what happens if we introduce an asymmetry between the two tunnel barriers. To do so, we fix the voltage on the right quantum point contact and sweep the left quantum point contact through the resonance. The center peak in the top panel

has the highest amplitude and corresponds to the situation where the two barriers are symmetric. When increasing (decreasing) the voltage on the right quantum point contact, the right tunnel barrier increases (decreases), the peak is decreasing in amplitude and shifting to the right (left). A more positive voltage on one gate has to be compensated by a more negative voltage of the other gate.

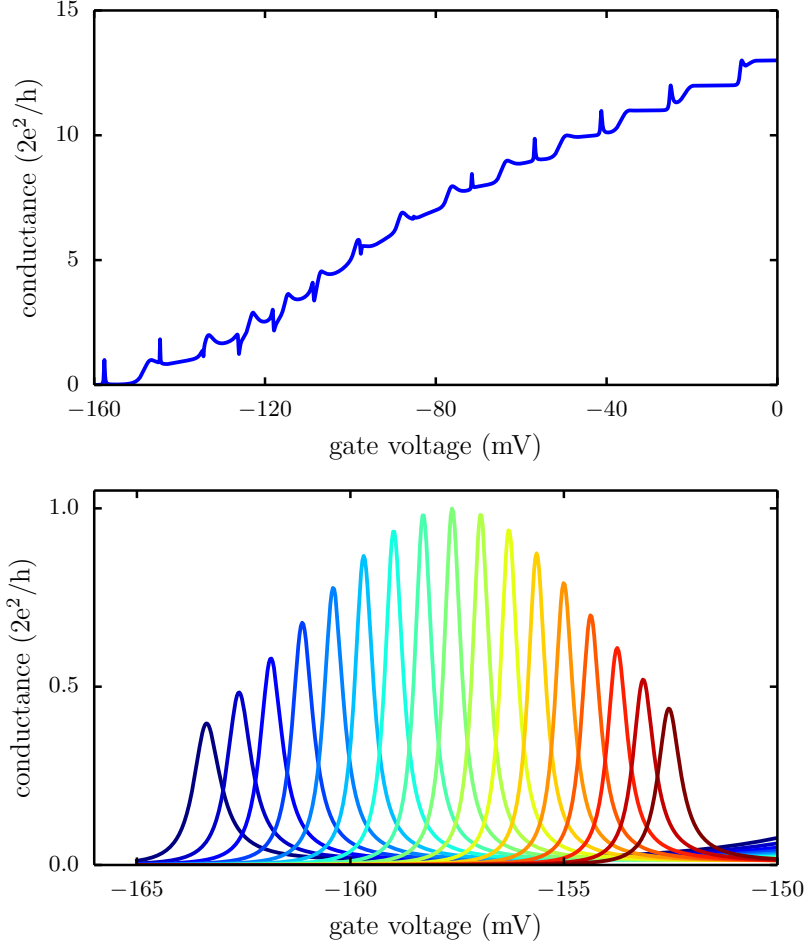


Figure 3.16: Simulated Fabry-Perot resonances. The top panel shows the pinch-off curve which is governed by Fabry-Perot resonances. All four gates are swept simultaneously. The bottom panel is a zoom on the left peak from the top panel. The right pair of gates is stepped whereas the left pair is swept. The highest peak in the center corresponds to the situation where both barriers are symmetric. When decreasing (increasing) the right tunnel barrier, the peaks are shifting to the right (left).

3.6 Simulation interface

An important part of this thesis has been the development of the simulation interface that has been used for the numerical simulations. Here we detail the software architecture of the framework that has been written around Kwant to give an idea of how it can be

used.

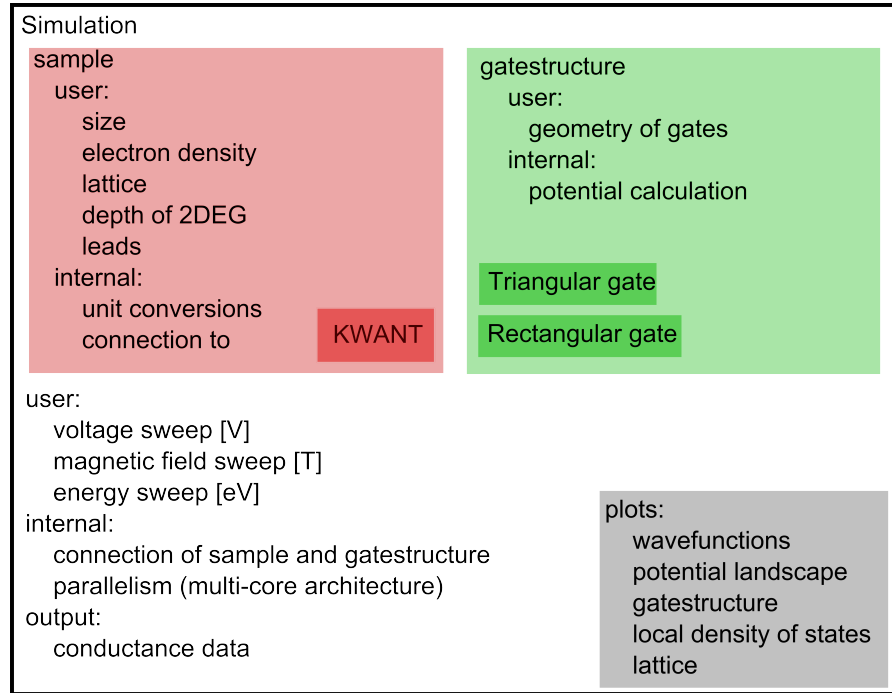


Figure 3.17: Software architecture that has been written around Kwant. The software interface has been written as user-friendly as possible. A common work flow can be summarized as follows: the user defines a numerical sample by defining size, electron density, lattice type, depth of the 2DEG and the number and position of the lead contacts. On top of the 2DEG, he places the gates that have been designed with a standard gdsii editor. From this, the program can automatically calculate the potential landscape seen by the electrons in the 2DEG. The user has now access to the complete parameter space given by every single electrostatic gate and can also change magnetic fields. A variety of functions for plotting and parallel computing has been developed as well.

An abstract overview of the program can be found in figure 3.17. Working with a numerical sample is basically equivalent to working with a real sample. The sample class is similar to the mesa that has been etched on a given wafer. The user chooses the size of his sample, the electron density of his wafer, the type of the lattice, the depth of the 2DEG and how many leads are connected to the sample. This sample object takes care of every necessary unit conversion and handles the connection to the Kwant libraries. The gates that are fabricated on top of a structure can be defined via the gatestructure object which allows to create any shape of gates in any size. One can use predefined triangular and rectangular gate objects or any custom function to do so. It is also possible to directly convert gdsii gate designs into such a pythonic gatestructure object. The sample and the gatestructure objects are given to the sweep object that forms the main workspace for the user. Here one can change or sweep any gate voltage, apply an magnetic field or change the energy of the system. It automatically handles samples and

gatestructures and computes transport properties. The sweep object supports parallelism and the calculations can be easily distributed over multiple CPUs to gain computational time. The data is automatically collected and stored in a single measurement file. A plotting class is also available that allows to check the wave functions, the potential landscape, the gatestructure, the local density of states and the tight-binding lattice. This architecture in principle allows to be implemented into a graphical user interface.

CHAPTER 4

The flying qubit

4.1 Introduction

Any practical quantum computer requires that quantum information is coherently transferred over large distances. Apart from being able to manipulate the quantum information locally in qubits, scalability imposes that distant qubits, which are individually used to perform the calculations, are coupled coherently, i.e. without loss of the information of the quantum state. One idea is to use photons as information carriers, since photons have long coherence times and can easily be transferred. The coupling between a single photon and a qubit is extensively studied, for example in a superconducting two-level system coupled to a cavity [97]. At present, there are many different systems under development. Another promising candidate is the so-called nitrogen vacancy (NV) center in diamond [98]. It has been shown recently that the spin of two NV-center qubits, separated by three meters, can be entangled via coupling the spin to a photon [99]. The same approach can be applied to semiconductor quantum dots [100, 101]. A further possibility is to use the electrons as information carriers and to transport them directly without encoding the information in photons. Such electron transport between distant quantum dots has been recently achieved with the aid of acoustic phonons [38, 102]. We will concentrate on this aspect in greater detail in the chapter 5.

Another complementary idea is to use a ballistic system for the electron transport and to build an interferometer out of it. In such an electronic system, it will be possible to define and manipulate a qubit state while it is being transferred, as we will see shortly. This so-called flying qubit stands in the center of the discussion of this chapter. We will use an electronic two-path interferometer, similar to the Mach-Zehnder interferometer. After conceptually introducing how the interferometer works, we will detail the main experimental results and put them into the above context of quantum information theory. We will develop a minimalistic analytical description to grasp its main characteristics. Numerical calculations will then be used to emphasize the main points of our analytical model and afterwards a complete simulation of the experimental system will be carried out. The numerical results will be confronted to experimental data and a few predictions for further measurements will be given. The main results of this chapter have been

published [36].

Let us start by discussing the Mach-Zehnder interferometer. As can be seen in figure

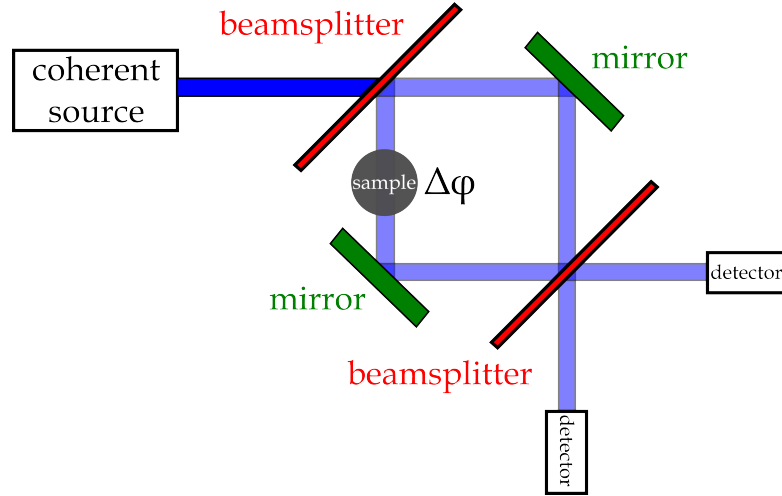


Figure 4.1: Mach-Zehnder interferometer. A coherent signal is sent onto a 50-50 beam splitter and equally partitioned into the upper and lower path of the interferometer. The phase φ is altered in one arm due to the presence of a phase shifter and the arising interference pattern measured using two detectors after a second beam splitter.

4.1, such a device first of all contains a coherent source. In optics it is common to use the photons of a coherent laser beam, whereas in our case, we will use an electrical current. Photons interact rarely with their environment, have long coherence times and such an interferometer is effectively not limited by its length scale. However, in our system, we have to consider the phase coherence length of the electron beam, which is of the order of several tens of micrometers and adjust the sample size accordingly by means of nanofabrication. This coherent beam is then sent onto a 50-50 beam splitter, which in its simplest form consists of two triangular glass prisms glued together. We will come back to the realization of a beam splitter in an electronic system shortly. The beam is equally partitioned into the upper and lower path of the interferometer. One can now alter the phase of the beam in one arm of the interferometer. This can be done by simply changing the position of one mirror and hence the length of one arm. Another possibility is to employ a sample in one arm, for example a piezoelectric transducer. The two trajectories are then recombined with a second beam splitter and its outputs are measured using one detector for each output. In optics this is commonly done with photo diodes, in electronics this is done by measuring the current with the help of current amplifiers.

In electronics, there exist two major approaches to build a beam splitter. The first approach makes use of the quantum point contact that we have introduced in section 3.3. Similar to modern optical beam splitters, the electrical one can be tuned to repartition a certain percentage of the electrons in the upper or lower path. Following this idea, Ji and co-workers have fabricated the first electronic analogue of an optical Mach-Zehnder interferometer, which we will detail briefly. In figure 4.2 we display the schematic of this interferometer taken from [24]. Electrons are injected into one quantum Hall

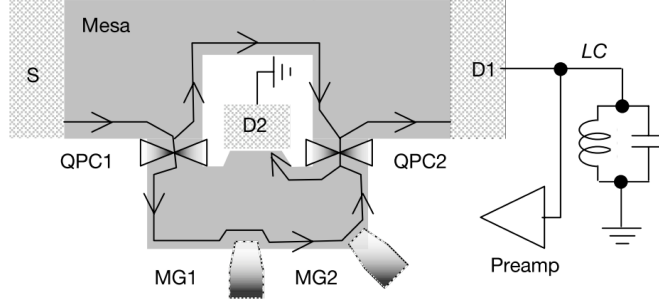


Figure 4.2: Electronic Mach-Zehnder interferometer from Ji and co-workers [24]. Edge states are formed in a high, perpendicular, magnetic field. The incoming edge state from S is split by QPC1 into two paths; one moves along the inner edge, and the other along the outer edge, of the device. The two paths meet again at QPC2, interfere, and result in two complementary currents in D1 and D2. By changing the contours of the outer edge state and thus the enclosed area between the two paths, the modulation gates (MGs) tune the phase difference between the two paths via the Aharonov-Bohm effect.

edge channel from the source contact (S). Both QPCs are tuned such that 50 % of an incoming edge channel is reflected and 50 % is transmitted. The resulting electron paths are indicated in figure 4.2. They encircle a surface area, before being measured at the drain contact (D1). A phase difference between the two paths can be introduced via the Aharonov-Bohm effect. In figure 4.3 we display the experimental findings from

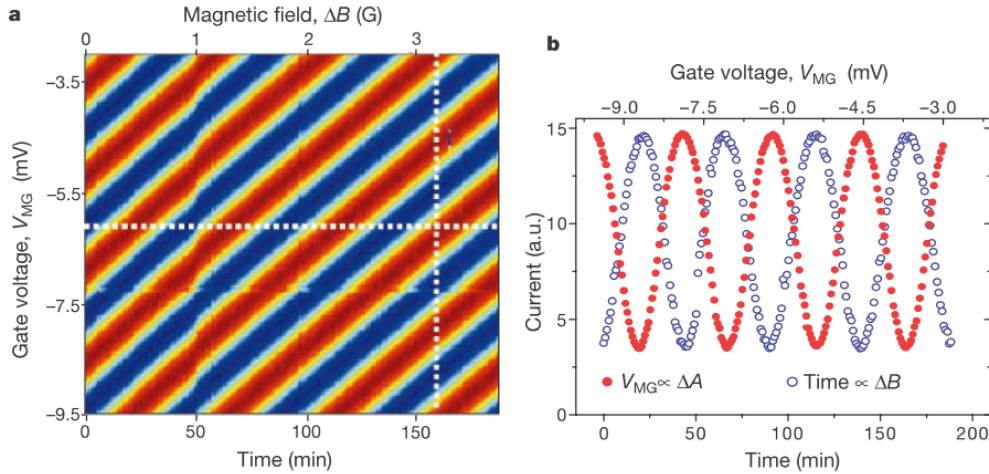


Figure 4.3: Interference pattern of electrons in a Mach-Zehnder interferometer taken from Ji and co-workers [24]. **a**, two-dimensional colour plot of the current collected by D1 as a function of magnetic field and gate voltage. The magnet was set in its persistent current mode with a decay rate of some 0.12 mT/hour, hence time appears on the abscissa. Both QPCs were set to transmission $T_1 = T_2 = 0.5$. **b**, the current collected by D1 is plotted as a function of the voltage on the modulation gate, V_{MG} (red plot), and as a function of the magnetic field, B (blue plot) - along the white dotted lines shown in **a**.

[24]. In panel b), we can see that a modulation of the gate voltage V_{MG} (red curve)

changes the phase between the two paths. This can be explained by the fact that this gate (MG1 in figure 4.2) pushes the edge state further away from the sample's border, changes the length of the lower path and hence the phase difference between the two paths. Furthermore they show that it is possible to change the phase by changing the magnetic field that penetrates the encircled surface area. The blue curve of panel b) shows the evolution of the transmitted current as a function of time. In their experiment, the magnetic field is created by a superconducting coil in persistent current mode. The circulating current is subject to continuous resistive losses and every 50 minutes, the magnetic field has dropped by a value corresponding to one flux quantum in the ring. This also alters the phase difference between the two paths as can be seen in the blue curve of panel b) of figure 4.3. In panel a) we can nicely see the linear phase shift as a function of the magnetic field and of the gate voltage V_{MG} as a color plot. Red (blue) stands for high (low) current. This experiment has paved the way for a variety of experiments [26, 29, 103–106]. Similar experimental set-ups could be used to study the interactions between counter-propagating edge states [103, 107] and to realize interference between two indistinguishable electrons from independent sources [104]. In the latter paper, Neder and co-workers connected two separate Mach-Zehnder interferometers in the quantum Hall regime and studied the cross-correlations between two output currents that led to the observation of two-particle interference in an electron stream. Another important experiment has been the experimental determination of a phase coherence length for edge states by studying the temperature dependence of the visibility of the interference patterns for different interferometer sizes [26, 27]. More recently, this kind of interferometer has been combined with a single electron source [108] and used to study the interference of single-electron wave packages in quantum Hall edge channel [91, 109]. We will come back to this experiment later on in chapter 5.

A second possibility to build such a beam splitter is to employ a tunnel barrier separating a quantum wire into two distinct channels [32, 33, 110]. This will be referred to as the *tunnel-coupled wire* in the following. The tunnel-coupled wire will be coupled to an Aharonov-Bohm ring and we therefore start by focusing on Aharonov-Bohm type interferometers. One difference between such a device and devices presented above is the magnetic field range where each one can be operated. In the quantum Hall regime (high magnetic field), it is rather straightforward to create an interferometer where exactly two paths are interfering. An important detail, which we have not yet mentioned is the Ohmic contact D2 in figure 4.2. It prevents that the edge channel, which is reflected from QPC2 contributes to the interference pattern of the two electron trajectories. Such multiple path contributions are cumbersome to handle at low magnetic fields. In the quantum Hall regime, backscattering is absent [70], whereas at low magnetic fields, backscattering can lead to multiple path contributions. Another problem is that a two-terminal Aharonov-Bohm interferometer suffers from phase rigidity [111]. The phase of the conductance through such a structure is pinned to 0 or π at zero magnetic field. This poses a severe problem when attempting to measure for example the transmission phase of an artificial atom [30, 31], similar to what has been done in optics [112]. One solution has been to increase the number of terminals [113], which lifted this rigidity and allowed to measure the transmission phase of a quantum dot. Additional terminals have

been used to suppress the amount of backscattered signal with the drawback that the amount of transmitted signal has been reduced as well and hence the visibility of the interference has been decreased. Such multi-terminal Aharonov-Bohm interferometers have been widely studied in literature [114–118] and we refer the interested reader to [119, 120]. Here we will concentrate on the tunnel-coupled wire and show that in a device, where a tunnel-coupled wire is connected to an Aharonov-Bohm interferometer, the phase rigidity can be lifted, multiple path contributions can be suppressed and that such an interferometer works as a real two-path interferometer. In contrast to high magnetic field Mach-Zehnder interferometers, Aharonov-Bohm-type interferometers give access to physics at smaller magnetic fields, like the Kondo effect [121, 122]. Furthermore, this device can be interpreted as a flying qubit, as we have motivated in the beginning of this chapter.

So far, we have conceptually introduced electronic interferometers, discussed different approaches and commented on the occurring problems for the different designs. We will now turn to the explicit design of our electronic two-path interferometer and discuss the experimental features of the device. This project has been carried out in collaboration with the group of S. Tarucha from the University of Tokyo and in particular with M. Yamamoto [34].

4.2 The electrical two-path interferometer

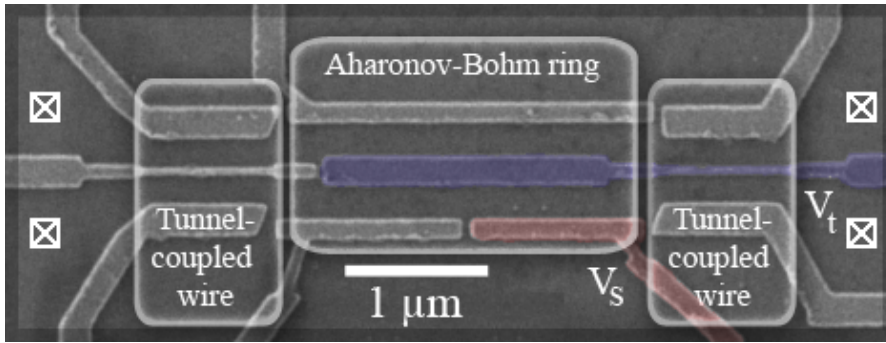


Figure 4.4: Electron beam micrograph of the electrical two-path interferometer. Two tunnel-coupled wires are connected to the central Aharonov-Bohm ring. The four white crossed boxes represent Ohmic contacts. Current is usually injected into one of the left contacts and recorded on both contacts on the right side.

In figure 4.4 we show an electron beam micrograph of the two-path interferometer. The device is connected to four lead contacts which are represented by the crossed boxes. In most cases that we will discuss here, the top left contact is floating and a bias voltage is applied to the bottom left contact. This injects a current into the device. It first arrives at the left tunnel-coupled wire. This will serve as the beam splitter that repartitions the electrons into the upper and lower arm of the Aharonov-Bohm region that follows. In this region, the upper and lower arm of the ring are completely decoupled, yet the electrons in each arm acquire a phase depending on the magnetic field that is penetrating the center island (see equation 2.4). The bottom two confinement gates in this region are separated

such that they can be addressed individually. These gates allow to modulate the wave vector of the electrons in this arm, as we will detail later. V_S denotes the side gate voltage of the red gate on the right. Afterwards, the electrons enter another tunnel-coupled wire, which serves as the second beam splitter. The current is now measured in the two right contacts with two current amplifiers (not depicted here). The top (bottom) right contact will be referred to as the upper (lower) current. In order to serve as a real two-path interferometer, it is obvious, though crucial that only two distinct paths are interfering. Electrons that encircle the Aharonov-Bohm ring multiple times before being measured in one of the right outputs have to be suppressed, which is not at all trivial, in contrast to the quantum Hall edge states. Indeed, we will show how we can differ between two regimes of the device, one where such contributions govern its behaviour and another one where we can clearly see the suppression of these encircling electron trajectories. Let us now describe the different regimes that the sample undergoes when we apply a voltage to the right tunnel gate labeled V_t in figure 4.4. Current is injected into the

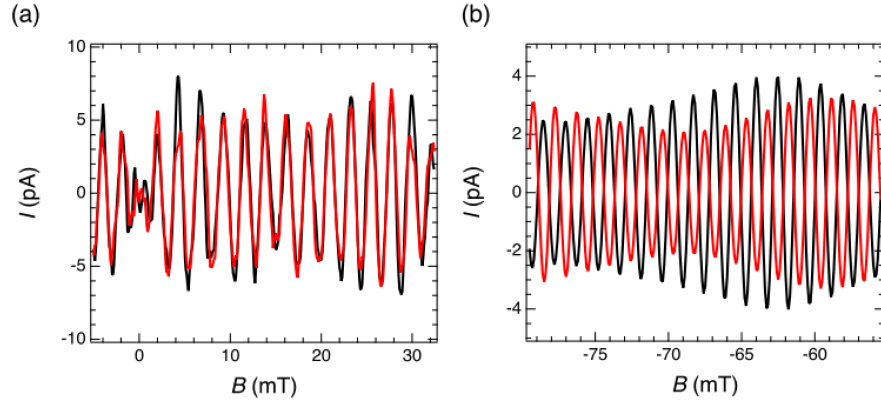


Figure 4.5: Magnetic field dependence of the upper (black) and lower (red) output current. The flying qubit shows in-phase oscillations in the Strong Coupling Regime (SCR) in panel (a) and anti-phase oscillations in the Weak Coupling Regime (WCR) in panel (b). The two different experimental regimes are due to a different configuration of the tunnel-coupled wire and explained in detail in the text. The data has been taken from [119].

structure from the bottom left contact and its path is provided by the outer gates, which deplete the electrons beneath them. We first apply a relatively small voltage V_t on the right tunnel gate and leave the left tunnel gate at zero voltage. The left tunnel gate will not be used in the following discussion. The current is equally repartitioned into both arms of the Aharonov-Bohm ring. In this first regime, the center island will be depleted, but essentially no tunnel barrier will be formed in the tunnel-coupled wire region on the right side as it is depicted in panel i) of figure 4.6. For this reason, this regime is called the Strong Coupling Regime (SCR). The system behaves as an effective two-terminal device and the currents in the upper and lower path are identical as shown in panel (a) of figure 4.5. This behaviour is rather natural since the two measurement probes on the right side are essentially on the same spot and one could imagine replacing both of them by a single contact. In the Strong Coupling Regime (SCR) the upper and lower currents

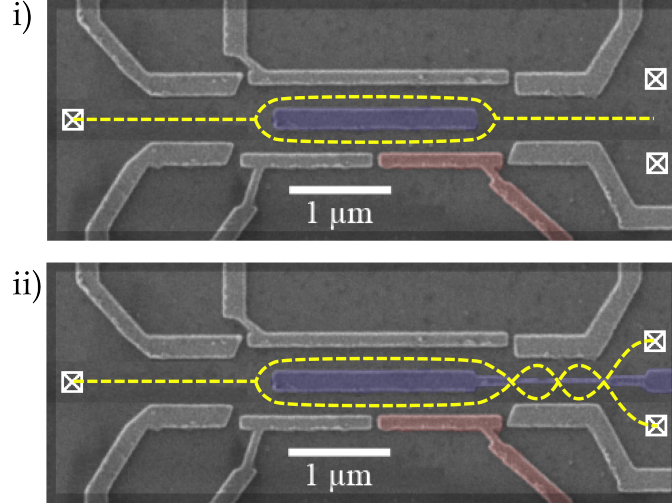


Figure 4.6: Electron trajectories in the different experimental regimes. In the Strong Coupling Regime (panel i), only the center island is depleted and the device behaves as a common Aharonov-Bohm interferometer. Both Ohmic contacts on the right side show a similar behaviour, the device is effectively two-terminal and the currents in both contacts on the right side oscillate in-phase. In the Weak Coupling Regime (panel ii), a tunnel barrier is present in the right tunnel-coupled wire leading to a real three terminal device. The currents in the upper and lower contact on the right side now oscillate anti-phase.

are oscillating in-phase with respect to the magnetic field. This oscillation is a common Aharonov-Bohm oscillation, whereas its period corresponds to the surface area of the Aharonov-Bohm center island. Since the device is an effective two-terminal device, the symmetry of these oscillations is bound to the Onsager relations as we have mentioned above (see equation 2.13). In this regime it is impossible to alter the phase of one arm of the Aharonov-Bohm ring since it is pinned to multiples of 0 and π at zero magnetic field (phase rigidity). We can imagine to change the confinement potential of the electrons that are propagating in the lower arm of the structure using the red side gate labeled V_S in figure 4.4. Increasing its negative voltage confines the electrons further. Since the total energy of the propagating electrons has to be conserved, an increase of the confinement energy (transversal energy) leads to a decrease of their longitudinal energy. In other words, the electrons are slowing down when increasing their transversal energy. Changing the longitudinal energy changes the longitudinal wave vector and would hence (after equation 2.4) change the phase linearly. On the contrary, experimentally, this will lead to phase jumps when changing the confinement potential of one arm, as the phase rigidity is pinning the phase to 0 or π . This behaviour can be seen in the left panel of figure 4.7.

Another peculiarity is that from this measurement, we can deduce that the electrons are encircling the Aharonov-Bohm ring multiple times. Let us remind that the total conductance is quantized and has to be a sum of the total transmitted signal plus the backscattered signal. Since the upper and lower currents are oscillating in-phase, their sum will also oscillate in the same manner. From this it is obvious, that the backscattered

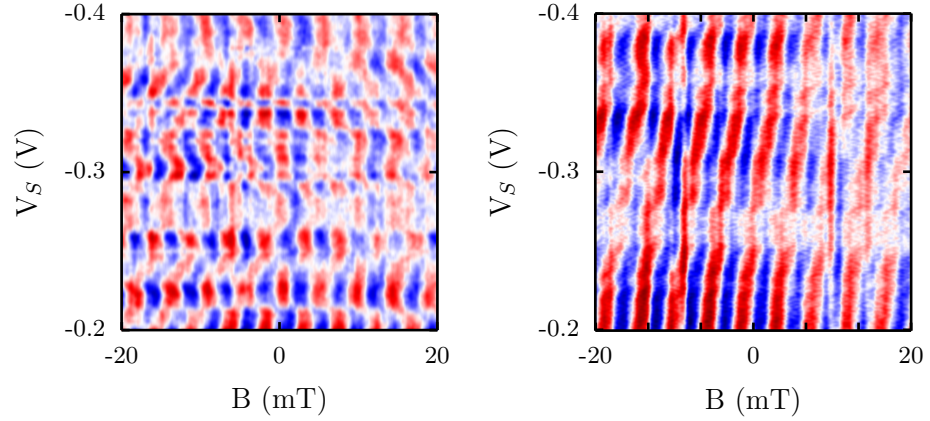


Figure 4.7: In the Strong Coupling Regime (SCR), the phase is pinned to multiples of 0 and π at zero magnetic field due to Onsager relations for a two-terminal device and phase jumps appear (left panel). In the Weak Coupling Regime (WCR), the phase can be shifted linearly (right panel), as Onsager relation only accounts for the sum of upper and lower current.

signal also shows an oscillating behaviour, which can only be the case, if the backscattered electrons are also encircling the Aharonov-Bohm ring.

Let us now increase the right tunnel gate voltage V_t further. The device undergoes a transition and the in-phase oscillations turn surprisingly out-of-phase as one is entering the so-called Weak Coupling Regime (WCR). Corresponding electron trajectories are shown in panel ii) of figure 4.6. The tunnel barrier in the tunnel-coupled wire is no longer negligible and governs the device's behaviour. We have displayed the corresponding experimental data in figure 4.5, panel (b). Following the same argumentation line as above we can sum up the two output currents and find that the backscattered signal does basically not show oscillations with respect to the magnetic field. This is a clear indication that the backscattered signal, which encircles the Aharonov-Bohm ring has been suppressed and that the device behaves as a true two-path interferometer in this configuration. Furthermore, the device no longer acts as a two-terminal but rather a three terminal device. In this regime, the phase rigidity is lifted and the phase in one arm of the interferometer can be shifted linearly, as we have envisioned above. Corresponding experimental data is shown in the right panel of figure 4.7. The requirement that the conductance has to be an even function of the magnetic field does not apply for the individual currents in the upper and lower branch, but to their sum. Here, the phase of an electron trajectory can be changed by altering the wave vector of the electrons inside this path. We will come back to this feature later on in section 4.5, where we will elaborate all underlying details of this rather subtle process. Apart from the application as a flying qubit that we envision in this manuscript, this experimental set-up, specifically in the WCR also allows other interesting measurements. A quantum dot could be fabricated in the center of the lower arm of the interferometer and as it has recently been shown by our collaborators, the device can be used to reliably measure the transmission phase of a

quantum dot. We refer the interested reader to [122].

The last but probably most important experimental observation has been that both currents oscillate as a function of applied tunnel gate voltage V_t . Changing V_t changes

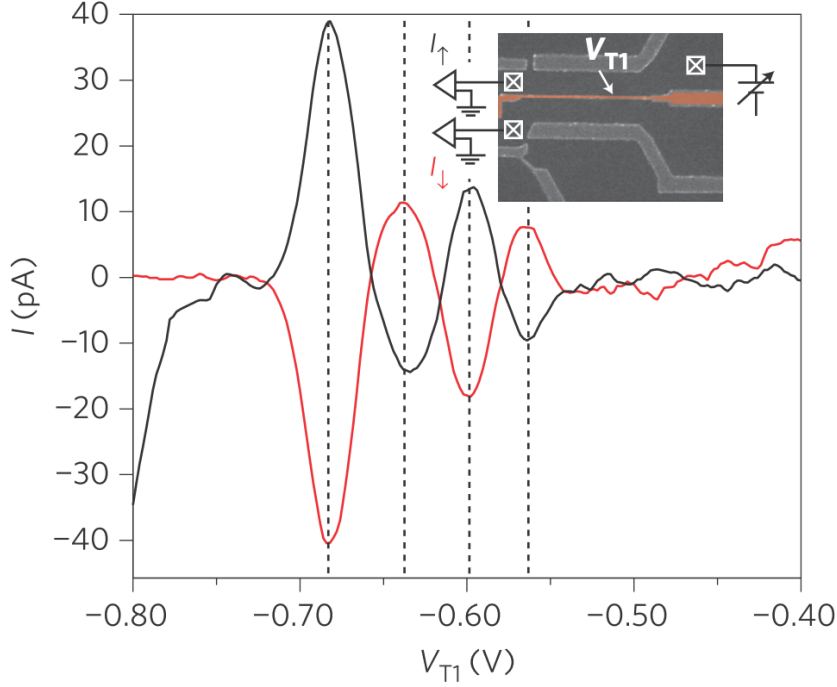


Figure 4.8: Anti-phase oscillations as a function of the tunnel gate voltage. Changing the tunnel gate voltage changes the tunneling rate of the electrons towards the upper and lower arm in the tunnel-coupled wire and allows therefore to repartition the current between the upper and lower arm. This allows to tune the tunnel-coupled wire into beam splitter conditions, where we have equal probability of measuring the current in the lower and in the upper current contact. The plot has been taken from [34]

the tunnel barrier in the tunnel-coupled wire and hence the probability of the current to be measured in the upper or lower path. In figure 4.8 we display the oscillating parts of the currents that are measured in the upper (black) and lower (red) channels while injecting the current into the upper right branch as shown in the inset. The tunnel gate V_{T1} controls the tunneling events between the upper and lower part. One oscillation corresponds hence to a complete rotation of 2π around the x-axis of the Bloch sphere (see equation 4.3). A total rotation of 3π can be observed. With the help of this controllable tunnel barrier one can now tune the device into a configuration where the current is equally divided. This is the case for a $\pi/2$ rotation and occurs at the zero-crossings of the two oscillation currents of figure 4.8. In this condition the tunnel-coupled wire serves as a 50-50 beam splitter for electrons and forms one of the building blocks for quantum optics experiments with electrons. We postpone the discussion of the underlying effects to the following sections. Increasing V_t beyond -0.7 V decouples the two channels and is hence not of interest for our discussion.

From what we have presented so far, we can get a grasp of the physics behind the flying

qubit. Before going more into detail by developing an analytical model of this two-path interferometer, we will now interpret the experimentally observed features in terms of quantum information language and see how one can define a qubit state and how we can use the described features to manipulate this state on-the-fly. We start with defining the basis of the qubit by the presence of a traveling electron in the upper $|\uparrow\rangle$ or lower $|\downarrow\rangle$ path of the interferometer. The qubit state $|\Psi\rangle$ can be expressed in the basis

$$|\Psi\rangle = \alpha |\uparrow\rangle + \beta |\downarrow\rangle, \quad (4.1)$$

where $|\alpha|^2 + |\beta|^2 = 1$ are normalized complex numbers. In the center part of the flying qubit, the phase difference between \uparrow and \downarrow can be manipulated via the Aharonov-Bohm flux (see equation 2.4). As mentioned above, the phase difference can be induced by a magnetic field but it can also be altered by changing the wave vector k in one path of the interferometer in the WCR. Changing the magnetic field is inconvenient since the timescale where it can be manipulated is slow compared to the timescale for changing a gate voltage. The WCR regime is hence the regime of main interest for the qubit operation, since here a side gate can be used to alter the wave vector and hence the phase. In the language of quantum information controlling this phase can be interpreted as a rotation of the qubit state around the z-axis.

$$R_z(\phi) = \begin{pmatrix} e^{i\phi/2} & 0 \\ 0 & e^{-i\phi/2} \end{pmatrix} \quad (4.2)$$

The simplest and probably most illustrating representation of the qubit state of a two-level system is the Bloch sphere (see figure 4.9). In our case, the north and the south pole represent the eigenbasis $|\uparrow\rangle$ and $|\downarrow\rangle$ of our interferometer, respectively. The left and right side of the Bloch sphere are the symmetric (+) and anti-symmetric (-) combination of the latter two eigenstates and form a second basis for this particular qubit. In the Aharonov-Bohm region, this can be used as an eigenbasis, since the states $|\uparrow\rangle$ and $|\downarrow\rangle$ are completely decoupled and their respective eigenenergies are degenerate. A rotation around the z-axis is equivalent to a vector rotating between those two states as it is shown in figure 4.9(a). The blue dots indicate the rotation (equation 4.2) when initialized in the state represented by the blue vector. To have full access to every point on the sphere, i.e. to every state of the qubit, one needs a second rotation, perpendicular to the rotation around the z-axis. In the flying qubit, the tunnel-coupled wire that is coupled to the Aharonov-Bohm interferometer can be used for such a rotation. There, the electrons can tunnel from the upper to the lower state, when the tunnel-coupling is non-zero. This is equivalent to a rotation around the x-axis of the Bloch sphere (see figure 4.9(b)). The rotation angle can be controlled by the tunnel gate voltage V_t .

$$R_x(\Theta) = \begin{pmatrix} \cos \Theta/2 & -i \sin \Theta/2 \\ -i \sin \Theta/2 & \cos \Theta/2 \end{pmatrix} \quad (4.3)$$

With these two rotations, every state on the Bloch sphere can be accessed and the qubit's state can be manipulated. Arbitrary rotations are possible by simultaneously controlling the tunnel coupling and the difference of the transmission phase between the two paths.

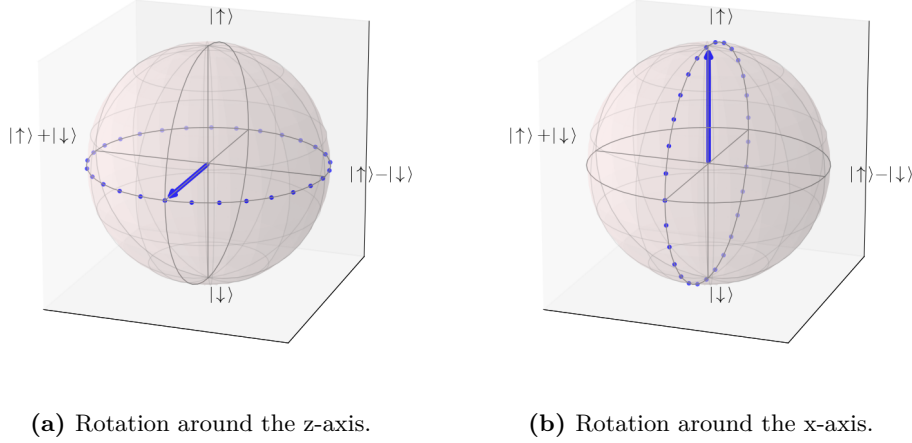


Figure 4.9: Qubit rotations. The dots indicate the rotation, whereas the blue vector indicates the initial state. The north (south) pole of the sphere corresponds to the $|\uparrow\rangle$ ($|\downarrow\rangle$) state of the qubit, whereas the left (right) state to a symmetric (anti-symmetric) combination of these states.

Having introduced the main experimental features and interpreted them in terms of a flying qubit, we will now elaborate an analytical model based on the coherent scattering formalism to explain these findings and to gain a deeper understanding of the governing processes behind.

4.3 Analytical model

Let us first simplify the sample presented in 4.4 by drawing a schematic, which is depicted in figure 4.10. On the left, we have replaced the two contacts by a single contact which has no influence on the discussed physics. A fourth contact only shifts the Aharonov-Bohm oscillations by a phase. For the same reason, we have omitted the left tunnel-coupled wire. It can be used to partition the current into the upper and lower arm of the Aharonov-Bohm ring and can simply be expressed by a phase factor. This will become clearer later on when discussing figure 4.12. For the discussion, we divide the structure into several distinct regions: the injection region on the left, the central Aharonov-Bohm region, the tunnel-coupled wire and the projection region. Each distinct region can be modeled by their respective scattering matrices, S_{inj} , S_{ab} , S_{tw} and S_p . In our calculations, we restrict ourselves to the case where a single channel is propagating in each arm of the interferometer. However, this simplification will be relaxed later on in the numerical section of the flying qubit (section 4.5). We begin by discussing the structure of the different scattering matrices. S_{inj} is rather arbitrary. It is described by the transmission amplitude a_\uparrow (a_\downarrow) for an electron to be injected from the left into the

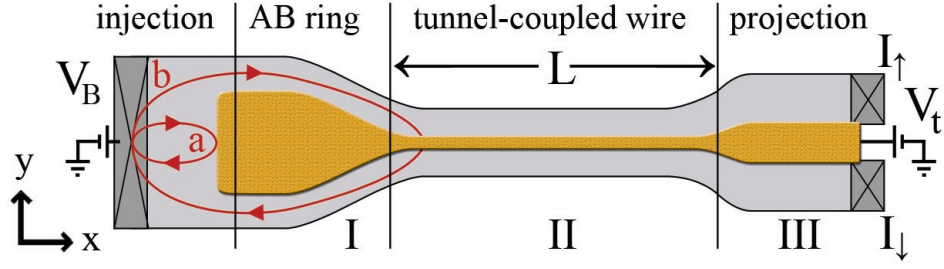


Figure 4.10: Schematic of the flying qubit system. We divide the sample into several regions: the injection region on the left, the central Aharonov-Bohm ring, the tunnel-coupled wire on the right and the projection region. A bias V_B is applied on the left Ohmic contact. The tunnel-coupled wire can further be split into three regions I, II and III: the two wires are coupled only in region II and decoupled upon entering in region I or III. The coupling can be controlled via the tunnel gate voltage V_T . a), b) correspond to two possible backscattered electron trajectories that could, in principle, contribute to the reflection amplitude. Electron trajectory b) has to be prohibited in order to work the interferometer as a real two-path interferometer.

upper (lower) channel. The amplitude a_{bs} for an electron to be backscattered into the injecting lead can be obtained from the current conservation law

$$|a_{bs}|^2 + |a_{\uparrow}|^2 + |a_{\downarrow}|^2 = 1. \quad (4.4)$$

The backscattering mainly depends on the width of the injection region compared to the width of the arms. A good rule of thumb to prevent backscattering is to design the interferometer such that the width of the injection region is twice the size of the individual arms, which are supposed to be symmetric. Nevertheless, the reduction of the arm width at the transition will inevitably lead to backscattering since all symmetric modes will have an anti-node at the position of the potential at the center (y-direction) of the system. We will come back to this issue in greater detail afterwards. The backscattered electron path is illustrated by the red trajectory labeled a in figure 4.10. The Aharonov-Bohm region is translation invariant along the x-direction. Equivalently we can say, that the confinement potential does not change along the path of the propagating electrons. This prevents backscattering in this region and the electrons are simply transmitted by forward scattering. However, we need to account for the Aharonov-Bohm effect. The electrons in the lower arm pick up a phase $e^{i2\pi\Phi/\Phi_0}$ with respect to the upper arm, where $\Phi_0 = h/e$ is the flux quantum and Φ , following equation 2.4, is the magnetic flux through the Aharonov-Bohm ring. The projection region is translation invariant as well and both arms in this region are completely decoupled due to a quasi infinite tunnel barrier in between both arms. More subtle physics is taking place in the tunnel-coupled wire region. It is important to consider the signal that is backscattered at the transition region between the Aharonov-Bohm ring and the tunnel-coupled wire. One representative path is indicated by the red trajectory labeled b in figure 4.10. The phase of the electrons gets easily scrambled when the electrons are encircling the ring multiple times [34].

Experimentally, it is a rather complicated task to extract the desired phase information in the case of encircling paths. Encircling paths travel a longer distance and can lose their coherence. This adds more incoherent background to the measurements. Generally speaking, this behaviour causes the quantum information carried by the electrons to be lost and has hence to be avoided. For our simplified analytical model we ignore these electron trajectories for the following reason: We argue that the potential at the entrance of the tunnel-coupled wire is such that for a propagating electron it is difficult to be scattered back into the opposite arm of the Aharonov-Bohm ring. Apart from this purely geometrical consideration we can also argue that when a tunnel barrier is present in the tunnel-coupled wire, the characteristic time it takes the electron to tunnel to the opposite arm is longer than the time that it stays in the transition region. From [33, 123, 124] we can get an upper theoretical limit of the inter-well coupling energy $\Delta E = 10 \text{ meV}$ for the case of a symmetric double quantum well. The time required for half an oscillation is

$$t_T = \frac{h}{2\Delta E} \quad (4.5)$$

and as a lower limit, we can estimate a timescale of 2 ps, which leads us with the Fermi velocity of $v_F = 2.2 \times 10^5 \text{ m/s}$ to a length scale of $l_T = 440 \text{ nm}$. This supports the above argument. We hence assume that the modes from the arms of the Aharonov-Bohm ring can be matched to their respective eigenenergies when entering the tunnel-coupled wire. The suppression of these amplitudes is crucial to obtain working conditions for the flying qubit. When conducting numerical simulations of the complete structure in section 4.5, we will come back to this point and verify that the assumption is valid with respect to the actual experiment. Keeping this in mind, we can parametrize the scattering matrix

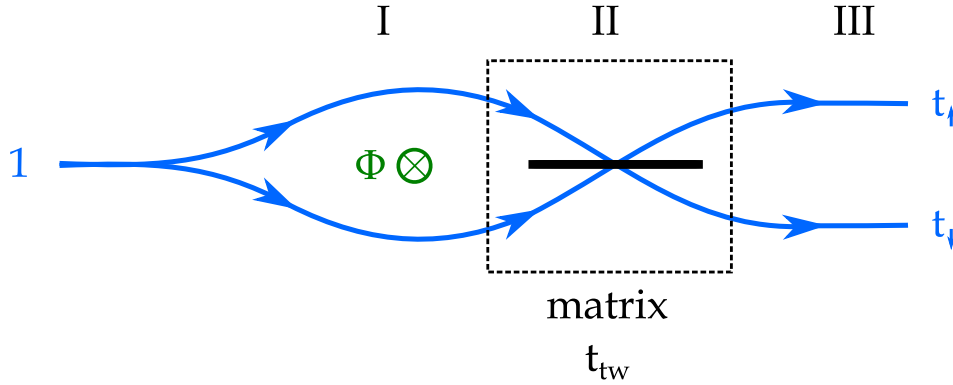


Figure 4.11: Electron trajectories in the tunnel-coupled wire. The Roman numbers correspond to the three different regions of the tunnel-coupled wire from figure 4.10. The black horizontal line depicts the beam splitter, whereas the dotted box represents the scattering matrix of the tunnel-coupled wire as it is calculated in the text. t_\uparrow/t_\downarrow is the total amplitude for an electron injected from the left to be transmitted to the upper/lower right electrode.

of the tunnel-coupled wire:

$$t_{tw} = \begin{pmatrix} t_{\uparrow\uparrow} & t_{\uparrow\downarrow} \\ t_{\downarrow\uparrow} & t_{\downarrow\downarrow} \end{pmatrix} \quad (4.6)$$

with $t_{tw}t_{tw}^\dagger = 1$ (current conservation). We show a graphical representation of this scattering matrix in figure 4.11. The transfer matrix t_{tw} connects the incoming electrons from the Aharonov-Bohm region (I) with the tunnel-coupled wire (region II) and the projection region (III). To calculate the amplitude for the electrons to be measured in the upper or lower state, we sum up all the probability amplitudes for the different paths and arrive at a Mach-Zehnder like expression

$$t_\uparrow = t_{\uparrow\uparrow}a_\uparrow + e^{i2\pi\Phi/\Phi_0}t_{\uparrow\downarrow}a_\downarrow \quad (4.7a)$$

$$t_\downarrow = t_{\downarrow\uparrow}a_\uparrow + e^{i2\pi\Phi/\Phi_0}t_{\downarrow\downarrow}a_\downarrow \quad (4.7b)$$

where $t_{\uparrow/\downarrow}$ is the total amplitude for an electron injected from the left to be transmitted in the upper/lower right electrode. The corresponding currents are given by the Landauer formula (see equation 2.5)

$$\frac{dI_{\uparrow(\downarrow)}}{dV_b} = \frac{2e^2}{h}T_{\uparrow(\downarrow)}. \quad (4.8)$$

Here $T_{\uparrow/\downarrow} = |t_{\uparrow/\downarrow}|^2$ is the total transmission probability from the left to the right upper (lower) electrode. V_b is the applied bias voltage between the source and the drain contacts. We will now propose a model for the transmission matrix t_{tw} . The tunnel barrier at the entrance and exit of the tunnel-coupled wire (see region I and III of figure 4.10 and 4.11) is infinitely high and accordingly, the two wires are fully decoupled and their energies are degenerate. In the central region (region II), the coupling is finite and we solve the two-dimensional Schrödinger equation:

$$\left[-\frac{\hbar^2}{2m^*}\Delta + V(y)\right]\Psi_\alpha(x,y) = E_F\Psi_\alpha(x,y) \quad (4.9)$$

where m^* is the effective mass of the electrons in the 2DEG, $V(y)$ describes the symmetric double well confinement potential in the two wires in y -direction, E_F is the Fermi energy of the system, and α labels the different modes. Since the transversal part of the wave function is independent of the longitudinal part due to translation invariance, we can separate the variables:

$$\Psi(x,y) = e^{ik_x x} \Psi(y) \quad (4.10)$$

After some algebra, this leads us to

$$\left[-\frac{\hbar^2}{2m^*}\frac{\partial^2}{\partial y^2} + V(y)\right]\Psi_\alpha(y) = E\Psi_\alpha(y), \quad (4.11)$$

where we have defined $E = E_F - \frac{\hbar^2}{2m^*} k_x^2$. The two-dimensional equation has hence been reduced to a one-dimensional equation and simplified the problem. We consider the first two propagating modes which will be labeled symmetric (S) and anti-symmetric (A) with respect to the two wires. In region I, the two modes $|S_I\rangle$ and $|A_I\rangle$ are degenerate due to the infinite tunnel barrier and can also be rewritten as combinations of the modes that propagate in the upper $|\uparrow\rangle$ or lower $|\downarrow\rangle$ parts:

$$|S_I\rangle = (|\uparrow\rangle + |\downarrow\rangle)/\sqrt{2}; |A_I\rangle = (|\uparrow\rangle - |\downarrow\rangle)/\sqrt{2} \quad (4.12)$$

We can now obtain the transmission matrix t_{tw} by the following adiabatic argument: We initialize the system in region I in state

$$|\uparrow\rangle = (|S_I\rangle + |A_I\rangle)/\sqrt{2} \quad (4.13)$$

The wave function evolves smoothly into region II and follows the basis change adiabatically:

$$(|S_{II}\rangle + |A_{II}\rangle)/\sqrt{2} \quad (4.14)$$

It picks up a mode-dependent phase while propagating through the tunnel-coupled wire and has evolved towards the end of region II to

$$(e^{ik_S L} |S_{II}\rangle + e^{ik_A L} |A_{II}\rangle)/\sqrt{2}, \quad (4.15)$$

where L is the total length of region II. Lastly, the wave function is smoothly transformed into region III and can be reexpressed as

$$|\xi\rangle \equiv (e^{ik_S L} [|\uparrow\rangle + |\downarrow\rangle] + e^{ik_A L} [|\uparrow\rangle - |\downarrow\rangle])/2 \quad (4.16)$$

From this expression we can calculate the scattering matrix elements

$$\begin{aligned} t_{\uparrow\uparrow} &= \langle \uparrow | \xi \rangle \\ &= \frac{1}{2} (\exp(ik_S L) + \exp(ik_A L)) \\ &= \frac{1}{2} (\cos(k_S L) + \cos(k_A L)) + \frac{1}{2} i (\sin(k_S L) + \sin(k_A L)) \\ &= \cos\left(\frac{k_S - k_A}{2} L\right) \left(\cos\left(\frac{k_S + k_A}{2} L\right) + i \sin\left(\frac{k_S + k_A}{2} L\right) \right) \\ &= \cos\left(\frac{k_S - k_A}{2} L\right) \exp\left(i \frac{k_S + k_A}{2} L\right) \end{aligned} \quad (4.17)$$

$t_{\uparrow\downarrow}, t_{\downarrow\uparrow}, t_{\downarrow\downarrow}$ can be calculated following the same procedure as presented above, which in the end leads to

$$t_{tw} = \exp\left(i \frac{k_S + k_A}{2} L\right) \begin{pmatrix} \cos\left(\frac{k_A - k_S}{2} L\right) & i \sin\left(\frac{k_S - k_A}{2} L\right) \\ i \sin\left(\frac{k_S - k_A}{2} L\right) & \cos\left(\frac{k_A - k_S}{2} L\right) \end{pmatrix} \quad (4.18)$$

As pointed out by C. Texier, this equation can also be obtained more elegantly. The calculation is presented in the appendix A.2. Putting everything together, the Landauer formula provides after a little exercise in linear algebra:

$$\begin{aligned} \frac{dI_{\uparrow(\downarrow)}}{dV_b} = \frac{2e^2}{h} & \left[\frac{|a_{\uparrow}|^2 + |a_{\downarrow}|^2}{2} \pm \frac{|a_{\uparrow}|^2 - |a_{\downarrow}|^2}{2} \cos[(k_A - k_S)L] \right. \\ & \left. \pm |a_{\uparrow}a_{\downarrow}| \sin[(k_A - k_S)L] \cos(2\pi\Phi/\Phi_0 + \phi) \right] \end{aligned} \quad (4.19)$$

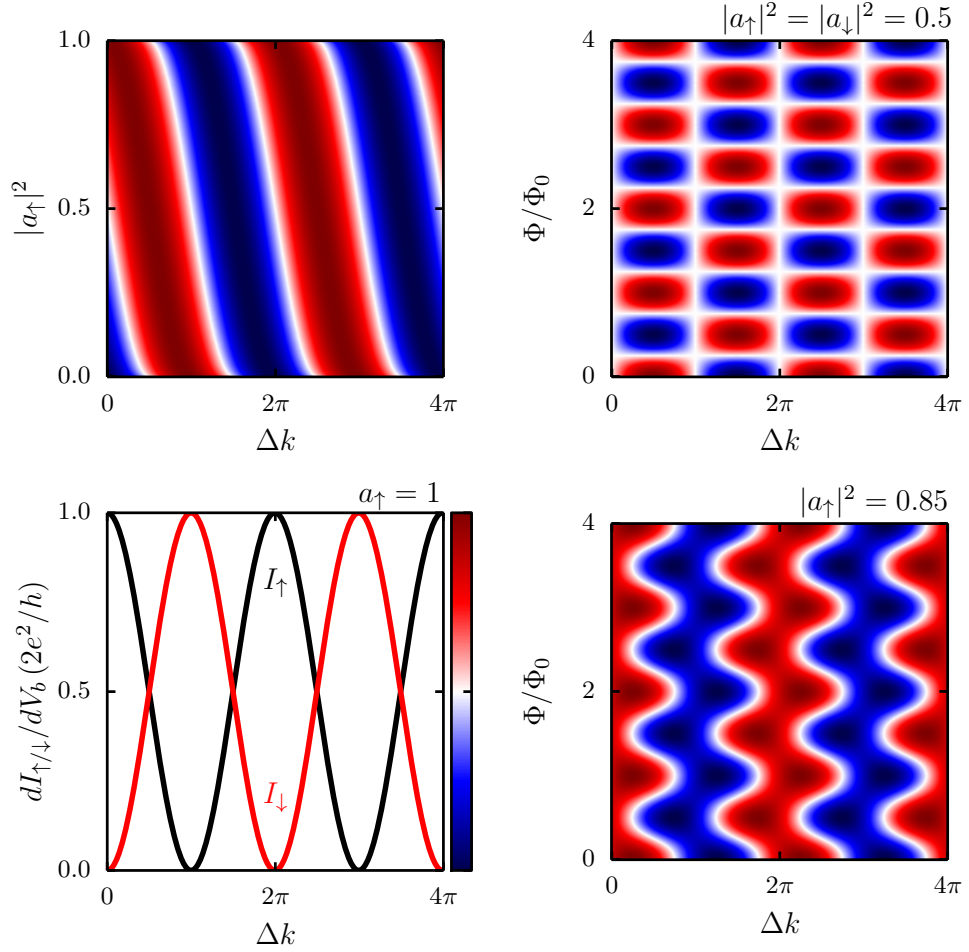


Figure 4.12: Graphical representation of equation 4.19. Top left: phase shift induced by an asymmetric injection. Top right: symmetric oscillations as a function of magnetic flux and Δk for a symmetric injection ($|a_{\uparrow}|^2 = |a_{\downarrow}|^2 = 0.5$). Bottom left: anti-phase oscillations vs. Δk for $a_{\uparrow} = 1$ and $a_{\downarrow} = 0$. Black (red) corresponds to the current I_{\uparrow} (I_{\downarrow}). Bottom right: asymmetric oscillations as a function of magnetic flux and Δk for an asymmetric injection ($|a_{\uparrow}|^2 = 0.85$). Blue (red) corresponds to low (high) conductance, whereas its precise scale is shown in the bottom left panel.

Equation 4.19 now provides a general analytical description of the interferometer. In

order to understand this equation more intuitively, let us plot it for different configurations of variables and discuss it with the help of figure 4.12. We define $\Delta k = k_A - k_S$ for simplicity. The simplest case that we can consider is to inject the current into the upper arm of the interferometer only. This situation ($a_\uparrow = 1, a_\downarrow = 0$) is shown in the bottom left panel. The conductance of the upper and lower channel is oscillating in perfect anti-phase as a function of $\Delta k L$ and this oscillation does not depend on the magnetic field since the last term in equation 4.19 cancels. The equation has reduced to a simple split-wire without an Aharonov-Bohm ring. This already explains the anti-phase oscillations in the WCR as a function of $\Delta k L$ that have been discussed above, although we need to connect the experimental parameters to the difference of the wave vectors of the symmetric and anti-symmetric states Δk . Δk depends on the eigenenergies of the two propagating modes in the tunnel-coupled wire and will hence depend on the tunnel gate voltage V_t . It furthermore depends on the magnetic field, since the electrons are experiencing a Lorentz force while propagating under the influence of a magnetic field. Both dependencies will be detailed in the following section. Changing the amplitudes $|a_\uparrow|^2$ and $|a_\downarrow|^2$ allows to control the symmetry of the injected wave function. This is reflected in a phase change of π as can be seen in the top left figure, where the amplitudes $|a_\uparrow|^2 = 1 - |a_\downarrow|^2$ are altered. The red (blue) color corresponds to a maximum (minimum) of the upper current. The color scale of the conductance is shown in the bottom left panel. These amplitudes can be controlled by the left tunnel-coupled wire. For an even injection into the upper and lower Aharonov-Bohm arm (top right panel, $|a_\uparrow|^2 = |a_\downarrow|^2 = 0.5$), we can see that the conductance is oscillating symmetrically as a function of magnetic field and Δk . Altering the symmetry of the injected wave function changes the amplitude and the phase of the oscillations depending on the choice of flux or Δk . This can be seen in the bottom right panel for a value of $|a_\uparrow|^2 = 0.85$.

In summary, this straightforward analysis already shows that the currents in the upper and lower branch oscillate anti-phase as a function of $\Delta k = k_A - k_S$. Changing the tunnel gate voltage V_t induces a change Δk and hence explains the experimentally observed oscillations with respect to V_t . In a similar way, for a given Δk the two output currents have opposite sign and will also oscillate anti-phase as a function of magnetic field. We will now elaborate this in detail in the following section.

4.4 Semi-analytical analysis

Equation 4.19 mainly depends on Δk and we would like to get a deeper insight into the physics of the split-wire by calculating the exact dependence of Δk on the tunnel gate voltage V_t and on the magnetic field B . This can be done by numerically solving the Schrödinger equation (Eq. 4.11) in the split-wire. We will calculate the band structure of the propagating electron states in the split-wire and its evolution as a function of the experimental parameters. For this purpose we use the Kwant solver

```
1 kwant.physics.Bands
```

that allows to calculate band structures of infinite systems. We create a translational invariant Kwant-Builder object and calculate the potential in the split-wire using the gate objects that have been introduced in section 3.3. We postpone a detailed discussion

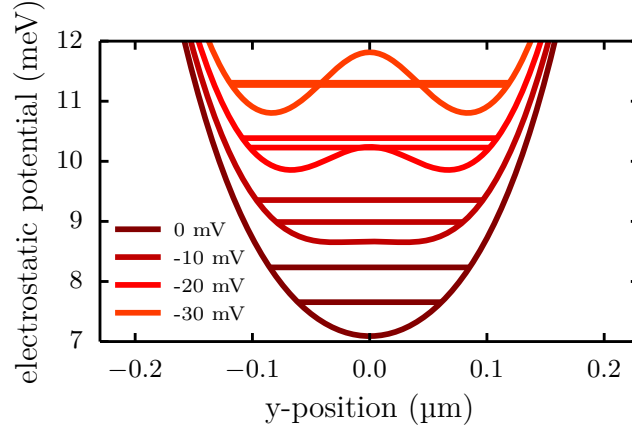


Figure 4.13: Electrostatic potential in the split-wire seen by the 2DEG 90 nm below the surface. The confinement gates stay fix for each calculation and we plot the dependence of the potential on different tunnel gate voltages. The first two eigenstates in each double-well potential are shown as horizontal lines.

of the used gate structure geometry (see figure 4.21 for comparison), however we display the obtained potential landscape of the split-wire along the y -direction as it is seen by the electrons of the 2DEG 90 nm below the surface for different tunnel gate voltages in figure 4.13. The tunnel gate that is used here is 55 nm wide. These potentials (figure 4.13) can now be injected into the Schrödinger equation (Eq. 4.11) to calculate the band structures. With this, let us first calculate the actual wave function of the symmetric

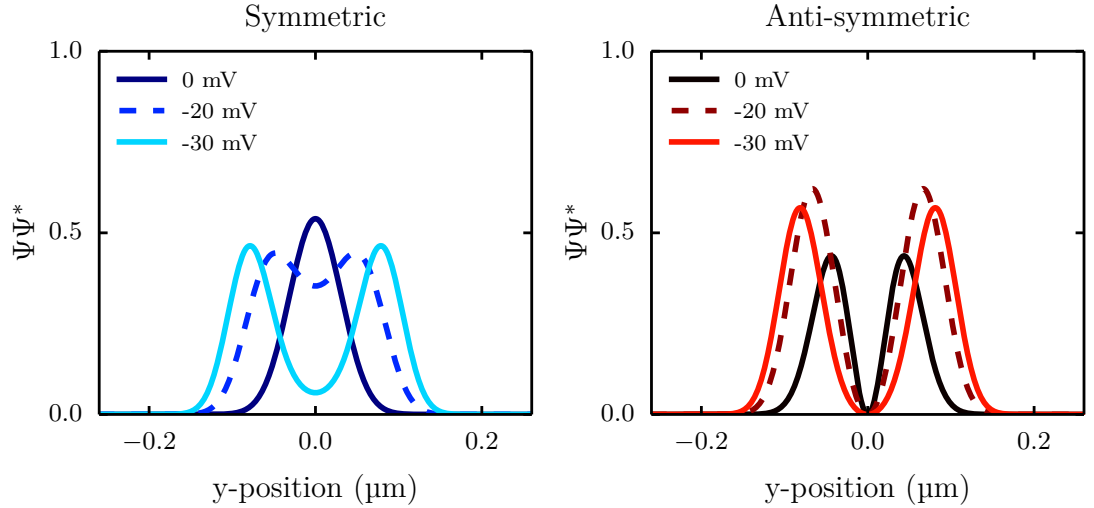


Figure 4.14: Normalized wave function probability of the symmetric (left) and anti-symmetric (right) state in the symmetric double well potential for different tunnel gate voltages.

and anti-symmetric state as displayed in figure 4.14. The weight of the symmetric state is pinned to the center of the wire whereas the anti-symmetric state lies within each tunnel-coupled wire. Increasing the tunnel barrier affects the symmetric state stronger and displaces it from the center. By further increasing the tunnel gate voltage, the two wave functions converge and become degenerate when the two wires are completely decoupled. We now calculate the dispersion relation of the infinite wire for each potential as it is displayed in figure 4.15. Here we show the dispersion relation for zero tunnel gate voltage and zero magnetic field. For a fixed Fermi-energy (black dotted line) we can

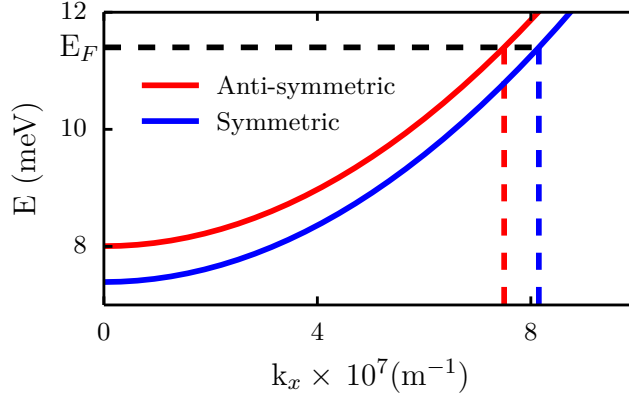


Figure 4.15: Dispersion relations for the symmetric (anti-symmetric) state in blue (red) at zero magnetic field and zero tunnel gate voltage. The wave vectors in propagation direction have been extracted at the Fermi energy as indicated by the dashed lines.

extract the wave vector in propagation direction k_x for both states and calculate k_y via energy conservation

$$k_F^2 = k_x^2 + k_y^2 \quad (4.20)$$

and the corresponding energies via

$$E_i = \frac{\hbar^2 k_i^2}{2m^*}, \quad (4.21)$$

with $i=(x,y)$. The Fermi energy in our case is $E_F = 11.4$ meV, set by the charge carrier density of the 2DEG. The confinement energy for different values of V_t of the symmetric and anti-symmetric state at zero magnetic field is displayed in panel a) of figure 4.16. At zero tunnel gate voltage, the energy difference is simply the energy separation of the two lowest energy states created by the confinement potential of the outer electrostatic gates, which is approximately harmonic. Upon increasing the tunnel barrier, the energy difference becomes smaller until the two minima in the split-wire are decoupled and their respective energies are degenerate. The absolute energy values of the two states move higher in energy as the confinement potential is rising due to the strong influence of the tunnel barrier and will eventually cross the Fermi energy. From the dispersion relations, we can evaluate the values for $\Delta k = k_A - k_S$ from equation 4.20 which is

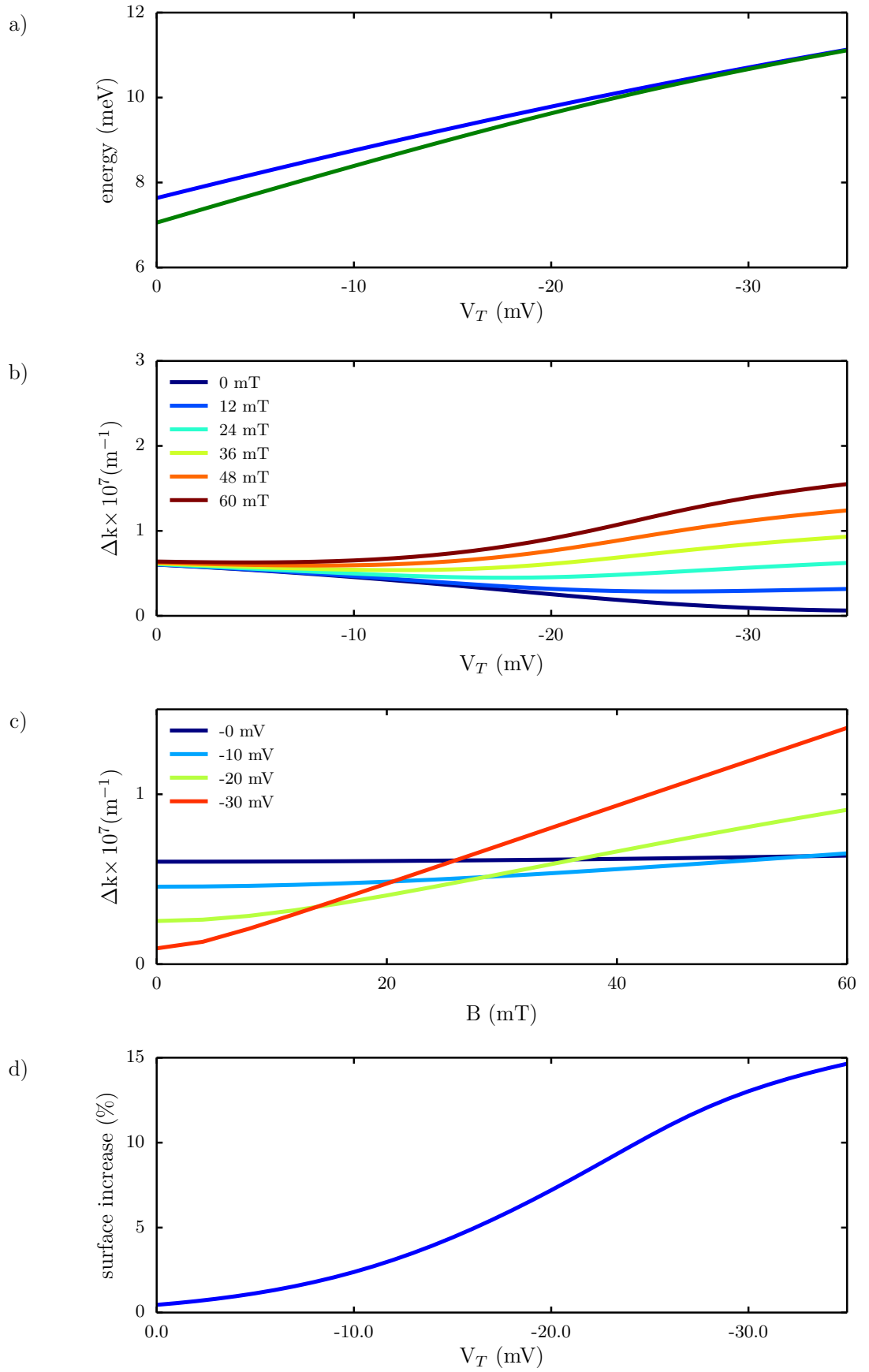


Figure 4.16: a) energy dependence of the symmetric (green) and anti-symmetric (blue) state as a function of tunnel gate voltage for $B = 0$ T. b) tunnel gate voltage dependence of Δk for different magnetic fields. c) magnetic field dependence of Δk for different tunnel gate voltages. d) surface area increase with respect to the Aharonov-Bohm ring calculated using the results of c).

displayed in panel b) of figure 4.16. The energy bands are affected by the tunnel coupling (x-axis) as well as by the magnetic field (color scale). For zero magnetic field, Δk is decreasing when increasing the negative tunnel gate voltage as shown by the blue curve of panel b). This is equivalent to the curve of panel a) and can be intuitively explained by the degeneracy of the two states at high tunnel gate voltage. A different behaviour, is observed when applying a magnetic field. We will come to this point shortly. Let us first consider the simple case at zero magnetic field before describing the rather subtle magnetic field dependence in detail. We have calculated the evolution of the wave vectors of the symmetric and anti-symmetric state as a function of the tunnel gate voltage. We are hence able to plot equation 4.19 as a function of tunnel gate voltage. As a simplification we assume that the electrons are injected into the upper arm of the interferometer only ($a_{\uparrow} = 1$ and $a_{\downarrow} = 0$). This leads us to figure 4.17, which reproduces

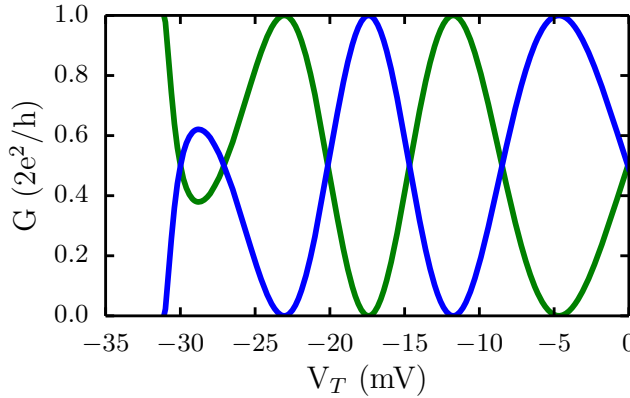


Figure 4.17: Conductance of the upper/lower channel (blue/green curve) as a function of the tunnel gate voltage as given by Eq.(4.19). The mapping between V_T and Δk was performed numerically.

nicely the experimental features. Our semi-analytical calculation yields that the two output currents oscillate anti-phase with respect to the tunnel gate voltage. The two currents are equal at zero tunnel gate voltage since we fix the phase of $\Delta k \times L$ in equation 4.19 to $\pi/2$ by adjusting the length of the wire to about $L = 2.7 \mu\text{m}$. This is reasonable, since in the experiment, the strong coupling between the upper and lower channel is responsible for the two output currents to be equal at zero tunnel gate voltage, and in theory we have to compensate for this artifact, which arises due to the simplifications of our model. We will see later on that our full numerical simulations can nicely reproduce this experimental feature as well. The decoupling of the two channels takes place above -30 mV. Since we are injecting into the upper lead only, the conductance in the lower branch goes to zero when the system is decoupled whereas the upper branch shows opposite behaviour. In the light of the motivation as a flying qubit, this curve is of importance. Tuning the tunnel gate voltage allows to reach full electrical control of the repartition of the two output currents into the two branches. In particular, the tunnel-coupled wire can also be tuned into a perfect beam splitter where the two output

currents are equal.

Let us now turn back to the subtle field dependence of Δk . In panel b) of figure 4.16 we observe that $k_a - k_s$ is increasing when increasing the negative tunnel gate voltage at a magnetic field of 60 mT. In order to understand this property, we have to take a closer look at the Schrödinger equation 4.11 considering the magnetic field as well. The Schrödinger equation now reads:

$$\frac{(i\hbar\vec{\nabla} - e\vec{A})^2}{2m}\Psi(x,y) = (E - V(y))\Psi(x,y), \quad (4.22)$$

where \vec{A} is the vector potential. We can again separate the x - and y - component of the wave function (eq. 4.10), insert the vector potential in the Landau gauge (eq. 3.7) and carry out the calculation. We arrive at

$$[\hbar^2 k_x^2 + 2e\hbar B y k_x + e^2 B^2 y^2 - \hbar^2 \Delta + V(y)]\Psi(y) = E\Psi(y) 2m^* \quad (4.23)$$

In this equation we can identify three spatially dependent terms: $V(y)$ denotes the electrostatic potential in the tunnel-coupled wire created by the surface gates (see figure 4.13). The quadratic term increases the parabolic confinement symmetrically, whereas the second term induces a tilt in the potential landscape which is linear in y , B and k_x . Due to the dependence on k_x , the electrons will see a different effective potential landscape depending on their state. We display the effective tilted potential for the

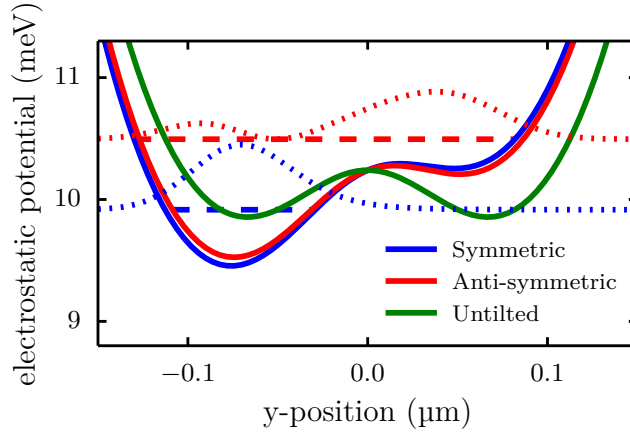


Figure 4.18: Effective confinement potential under a magnetic field of 60 mT. Blue (red) solid line corresponds to the symmetric (anti-symmetric) state. The dashed lines show their respective eigenenergies. Green solid line shows the confinement potential for $B = 0$ T for comparison. The blue (red) dotted curves correspond to the symmetric (anti-symmetric) wave function under magnetic field.

symmetric and anti-symmetric state in figure 4.18 for a magnetic field of 60 mT. The blue (red) solid curve shows the potential for the symmetric (anti-symmetric) state, the dashed lines, their respective eigenenergies. The untilted potential at zero magnetic field

is drawn in green for comparison. The bigger k_x , the faster the electrons propagate, the higher is the tilt of the potential. This is effectively a manifestation of the Lorentz force. Furthermore, the dotted lines show the corresponding wave functions of the two states. We also note that the coupling between the two wave functions is rather small for the situation that is depicted here. This will lead to a decreased visibility of the oscillations. Depending on the value of the magnetic field, this tilt of the potential modifies the intuitive dependence of Δk on the tunnel gate voltages as seen in panel b) of figure 4.16. We can also look at this data set in a different way. Instead of plotting Δk as a function of V_t for different magnetic fields, we transpose the data set and plot slices in y-direction of panel b) for different values of the tunnel gate voltage. This is depicted in panel c) of figure 4.16. The stronger the tunnel barrier, the stronger is the increase $\partial\Delta k/\partial B$. For a completely decoupled wire the slope of Δk finally saturates with respect to the magnetic field. There is no direct measure of Δk in an experimental system, however, starting from here it is possible to determine a measurable quantity. $\Delta k \times L$, where L is the length of the split-wire, is the phase difference acquired between the symmetric and anti-symmetric state propagating in the split-wire. This phase can be interpreted as a surface area. Let us reconsider the Aharonov-Bohm ring that has been mentioned above. It shows oscillations with respect to the magnetic field, with a period which correspond to the surface area of the Aharonov-Bohm loop. We now predict that this surface area will depend on the presence of the tunnel-coupled wire and will change proportionally to Δk . We reinterpret the acquired phase $\Delta k \times L$ inside the split-wire as a surface area by writing

$$\int \Delta k(V_t, B) dl \stackrel{!}{=} \frac{e}{\hbar} \int B dS \quad (4.24)$$

We carry out the integration on the left hand side and write

$$\frac{\hbar}{e} \int \frac{\partial \Delta k(V_t, B)}{\partial B} L dB = BS \quad (4.25)$$

The partial derivative can be written in front of the integral since it is constant over the magnetic field range of interest. In panel c) of figure 4.16 we find that this is case between 20 mT and 60 mT, in agreement to the field range that is usually measured in experiments [34, 119, 122]. We arrive at the expression

$$\frac{\hbar}{e} \frac{\partial \Delta k(V_t, B)}{\partial B} L = S \quad (4.26)$$

This surface S corresponds to the additional surface area that is acquired due to the presence of the split-wire. For each value of the tunnel gate we now take a linear fit in this range and calculate the effective surface area increase which is displayed in panel d) of figure 4.16. The surface is normalized to the surface area of the Aharonov-Bohm ring, which is connected to the tunnel-coupled wire. In this plot, we see that the surface area of the Aharonov-Bohm ring coupled to the tunnel-coupled wire increases about 15% when increasing the tunnel gate voltage, before the two wires decouple.

Since our calculations omit screening effects [72], we also investigate different geometries of our split-wire. This allows us to obtain different potential landscapes, which should be closer to the real screened potential. We can therefore check the influence of different potentials on the surface area increase and get an idea of the importance of screening effects on this surface area increase. In our simulations, we can change the width of the wire and place the 2DEG artificially closer to the tunnel gate. This increases the influence of the tunnel gate while decreasing the actual width of the tunnel barrier. We display different potential landscapes for different configurations in figure 4.19. We have chosen to put the tunnel gate at three different distances, i.e. 90, 40 and 20 nm, while varying the size down to the limits what is possible with common lithography technology.

All potentials are plotted at a tunnel gate voltage of $V_t = -20$ mV for comparison.

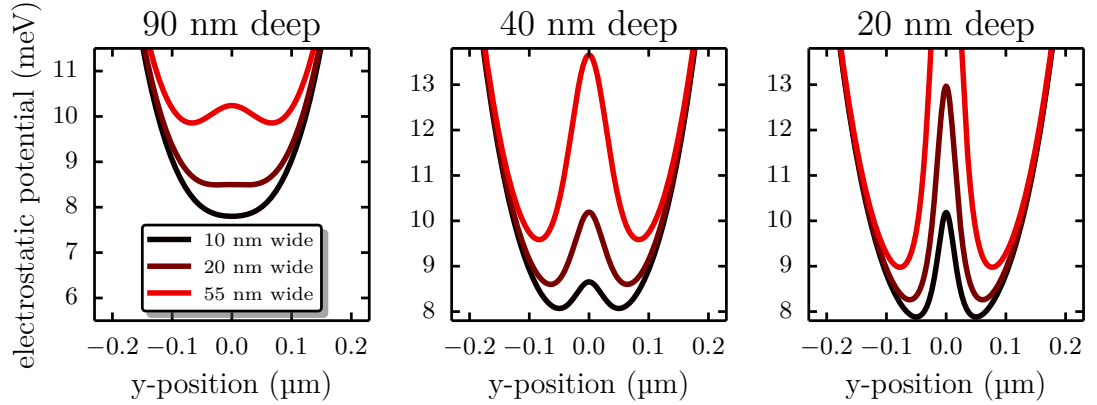


Figure 4.19: Potential landscape in the split-wire for different geometries. Putting the split-wire closer to the 2DEG by decreasing its depth, we artificially increase the influence of the tunnel gate and decrease the width of the tunnel barrier. All plots are done for $V_t = -20$ mV.

For each combination of depth and width, we carry out the same calculations, which are summarized by figure 4.16 and plot the obtained surface area increase in figure 4.20. Taken together, these calculations do not differ tremendously from our first result. The maximum surface area increase that we can obtain is about 20%. We observe two different slopes in the curves of figure 4.19. We associate the first steep rise to a regime where the tunnel gate only affects the very bottom of the potential landscape, but effectively no tunnel barrier is formed. Already in this regime, the influence of the tunnel gate is sufficient to turn the in-phase oscillations out-of phase and to govern the device's behaviour as will be seen in the numerical simulation in section 4.5. Our calculations suggest that out-of phase oscillations could already be obtained in a single wire, when carefully shaping its confinement potential, obviously without the same amount of tunability due to the tunnel gate. The *real* tunneling regime is associated with the second less steep slope. It is easier to reach such a regime, when the tunnel barrier is thinner and closer to the 2DEG. It is difficult to distinguish experimentally between those two regimes, since both regimes behave similarly. An experimental demonstration

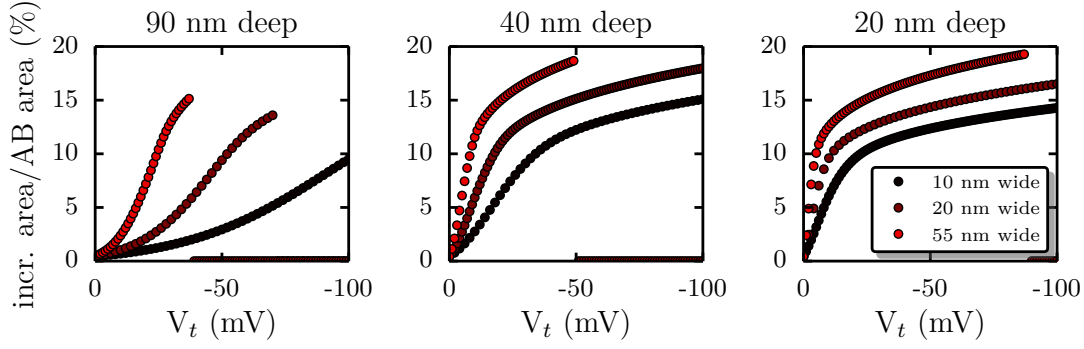


Figure 4.20: Surface area increase for the different geometries discussed in figure 4.19. The surface area increase drops to zero when the two states are above the Fermi-energy. We find a maximum surface area increase of 20%.

would require to transit from on to the other regime. One could envision to control the charge carrier density in the 2DEG by means of a back gate similar to what is done in undoped 2DEG structures [125]. This would allow to control screening effects and hence to influence the shape of the potential landscape formed by the tunnel gate. Nevertheless, the surface area increase can be verified experimentally and we will come back to this point in the end of the next section.

So far we have been able to explain the magnetic field dependence and the tunnel gate dependence of Δk which helped us understand the underlying physics of the split-wire. We will now concentrate on the distinction between the SCR and WCR as we have introduced them above and check that we can reproduce the phase jumps and the linear phase shift in these two regimes. For our simplified theoretical model we have assumed that only a single mode is propagating in each arm of the interferometer and that only forward scattering occurs. These assumptions will be relaxed in the following. In the end of the next section, we will also take a closer look on the additional surface area and strengthen the arguments that have been presented above. For this purpose, we will carry out a complete numerical simulation with a sample, that resembles the actually fabricated device.

4.5 Numerical simulations

With the calculations that have been carried out so far, we have been able to understand the underlying physics of the Aharonov-Bohm interferometer coupled to a tunnel-coupled wire. As shown in the previous section, a simplified analytical model that has been complemented with a numerical calculation of the mapping between V_t and B to Δk helped to understand the experimental findings to a certain extent. However, the model relies on the assumption that encircling paths induced by backscattering are fully suppressed and was restricted to a single propagating mode in each arm of the Aharonov-Bohm interferometer. For this reason we now turn to more elaborate microscopic simulations to confirm that we can indeed suppress the encircling paths in the WCR by correctly choosing the device configuration. Furthermore we investigate and reproduce the effect of

phase rigidity in the SCR and the linear phase shift in the WCR. Experimental data in the different regimes will also be presented. In spite of neglecting screening and Coulomb interactions, we will find that for a certain parameter range, both the conductance and the visibility of the magnetic field oscillations can be tuned remarkably close to what is observed in the experiments.

To begin with, we define a gate structure that resembles the actual nanofabricated gate structure of figure 4.4 using the gate objects that have been introduced above. We display a schematic of the gates in figure 4.21. The size of the total structure is $1 \times 7 \mu\text{m}^2$,

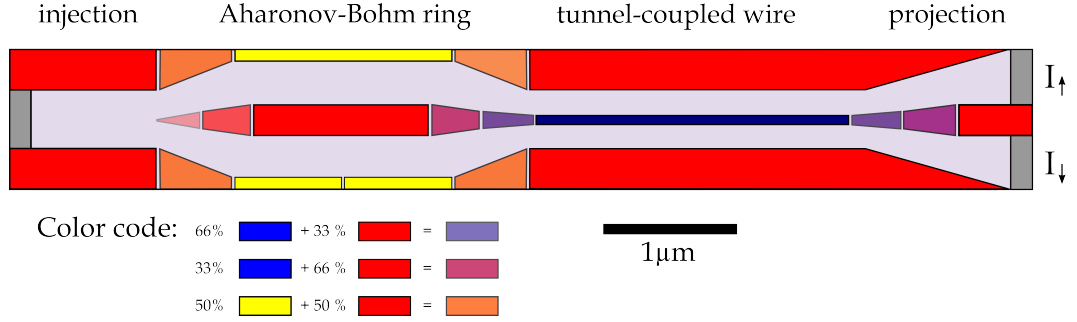


Figure 4.21: Gate structure that has been used to implement the flying qubit from figure 4.4. Red, blue and yellow gates could be accessed individually, whereas the voltage on intermediate gates has been calculated following the color code in the legend. The sample is connected to one lead on the left and two leads on the right, namely the upper and lower contact.

which leads to a total number of sites of 280000 with a lattice constant of $a = 5 \text{ nm}$. For most simulations that will be presented in the following, a lattice constant of $a = 5 \text{ nm}$ has been chosen. The number of sites is then automatically calculated by the simulation engine as presented above. It should be noted that the lattice constant has been adopted such that no influence of discretisation on the transport properties could be observed and that we can safely assume that we are in the continuum limit. For calibrations, the lattice constant has been varied, although such kind of preliminary curves will not be displayed here. To give an idea, calibrations in such simulations are necessary to save computation time. Computing the scattering matrix for a total of 280000 sites takes around 30s for a single point on a single CPU (2.4 GHz) after finalizing the system. For calibrations, this time can easily be decreased to 1s per point by increasing the lattice constant. Such preliminary computations are extremely useful to delimit the parameter range of sweeps before simulating interesting parameter spaces in greater detail. The tight-binding lattice (not displayed here) is connected to three lead contacts (gray rectangles), one injection lead on the left and two leads on the right side of the sample, namely the upper and lower contact. The voltage of the gates could be adjusted for each gate (rectangle/triangle/polygon) individually, except for the gates with intermediate colors (see the color code of figure 4.21 for comparison). The voltage of these gates was calculated as a percentage of the voltage of its adjacent gates. To guarantee smoothness of the injection and the projection we also apply a potential to the boundaries of the system. More precisely, we apply the potential that is seen by the outermost sites to adherent

leads as well. This ensures that no parasitic backscattering is taking place at the entrance or exit of the system and more precisely that the number of available channels in the semi-infinite electrodes is equivalent to the number of channels in the system's borders. To furthermore minimize unwanted backscattering in the projection region, we create a triangular shaped opening on the right side towards the upper and lower lead contact. This ensures that the density of states in the projection region is larger than the one in the tunnel-coupled wire and that every incoming mode can be matched into this region.

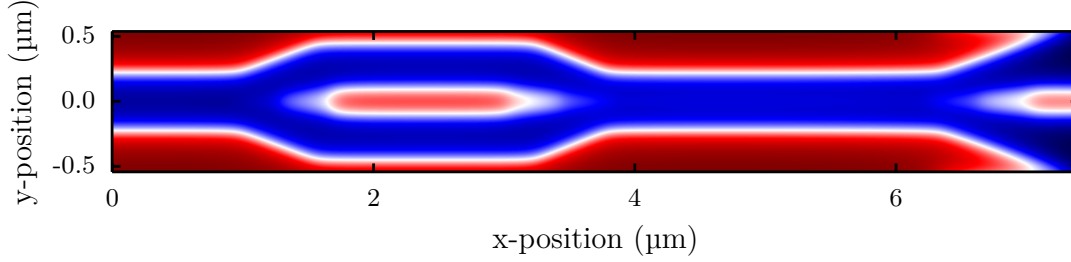


Figure 4.22: Potential landscape of the complete structure calculated using the gate structure from figure 4.21. Red (blue) corresponds to high (low) potential.

In figure 4.22 we depict an example of the calculated potential landscape of one typical gate voltage configuration. The red color corresponds to a high potential, whereas blue corresponds to a low potential and hence to the path that injected electrons can follow. All addressable gates are fixed at a value of -40 mV, which is a typical value used for the following simulations. For convenience, we have separated the right tunnel-coupled wire from the middle island such that its voltage can be swept independently. In experiments this can also be done by connecting the center Aharonov-Bohm island with a bridge, although nanofabricating such a sample is a bit more involved. This allows to separately investigate the influence of the tunnel-coupled wire on the Aharonov-Bohm oscillation frequency and to confront this to our semi-analytical calculations.

In order to tune our system we have adopted a standard procedure. We start by sweeping the outer gates of the structure to obtain a conductance that is similar to the one of the experiment. This defines a certain parameter range for the outer gates within which we now sweep the desired parameters. For the physics discussed it is sufficient to restrict ourselves to sweeping the tunnel gate, the side gate and the magnetic field. Let us first focus on the SCR.

We apply a finite gate voltage of around -40 mV on the center island and on the confinement gates in order to form an Aharonov-Bohm ring and then sweep the magnetic field. Corresponding data is depicted in the left panel of figure 4.23. The total conductance (cyan) is exactly five channels, as we can easily see, when summing up the individual conductances of the upper (blue) and lower (green) contact plus the signal that is backscattered (red) into the injection contact. The tunnel gate voltage in this configuration is zero and we remark that first of all, the two channels are nicely oscillating in-phase, since the upper and lower contacts are strongly coupled. Secondly, we find that the backscattered signal is strongly oscillating with the magnetic field. This clearly indicates

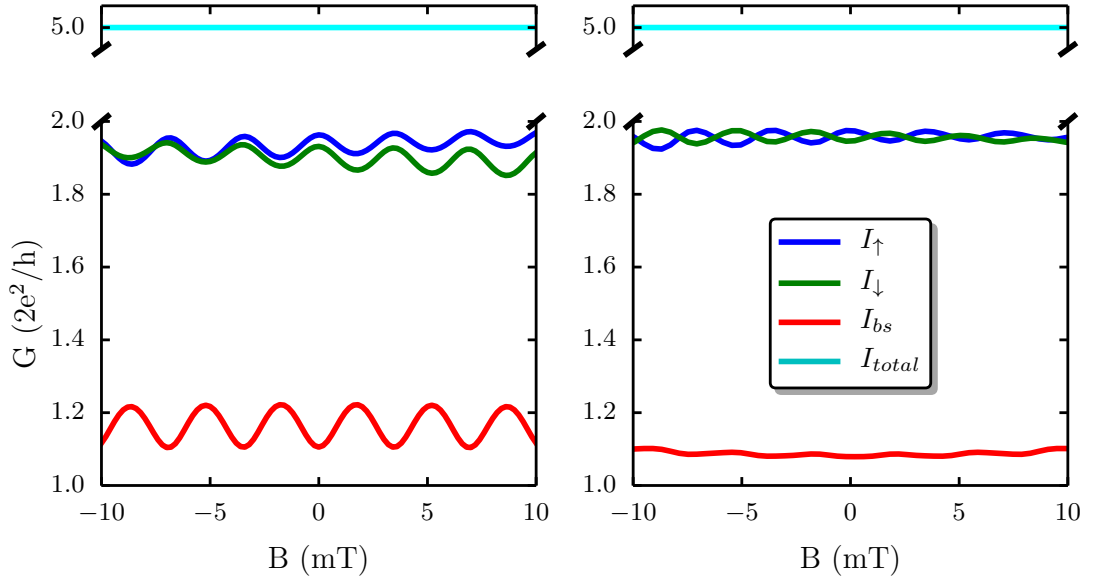


Figure 4.23: Comparison of anti-phase and in-phase regime. Left panel: in-phase oscillations in the SCR. The backscattered signal (red) shows magneto oscillations which indicates that backscattered electrons are encircling the Aharonov-Bohm ring. Right panel: anti-phase oscillations. The magneto oscillations of the backscattered signal are suppressed in the WCR due to the presence of the tunnel coupling in the tunnel-coupled wire.

that electron trajectories are encircling the Aharonov-Bohm ring, as we have discussed in the previous section. Furthermore, one remarks the symmetry of the data with respect to zero magnetic field as we expect from Onsager relations (see equation 2.13). If we now apply a voltage of -8.3 mV to the tunnel-coupled wire (right panel of figure 4.23), we find that the magneto oscillations of the backscattered signal are strongly suppressed, and that both currents oscillate anti-phase with respect to the magnetic field. In order to obtain symmetric anti-phase oscillations, it is not necessary to completely suppress the magneto oscillations of the backscattered signal, however the reduction has to be significant. The less backscattering is present, the more symmetric are the anti-phase oscillations, which is in agreement with observations from experiment [119]. It is rather difficult to estimate a precise number that serves as an upper limit for the amount of *tolerated* oscillating backscattered signal due to the enormous computational cost of such an investigation. However, our data suggests that backscattering, which exceeds few percent of the visibility of the oscillations usually scrambles and shifts the anti-phase oscillations. The amount of backscattered signal strongly depends on the transition from the Aharonov-Bohm ring to the tunnel-coupled wire. To get an idea what is happening we can have a look at the energy landscape of the complete structure for different tunnel gate voltages. Similar to the calculation in the previous section, we now calculate the energy of the symmetric and anti-symmetric state as a function of the spatial position. For each vertical slice in the potential landscape, we create an infinite translational invariant system and calculate

the eigenenergies of the symmetric and anti-symmetric state, similar to what we have conducted before. We plot the result of this calculation in figure 4.24. In the top panel,

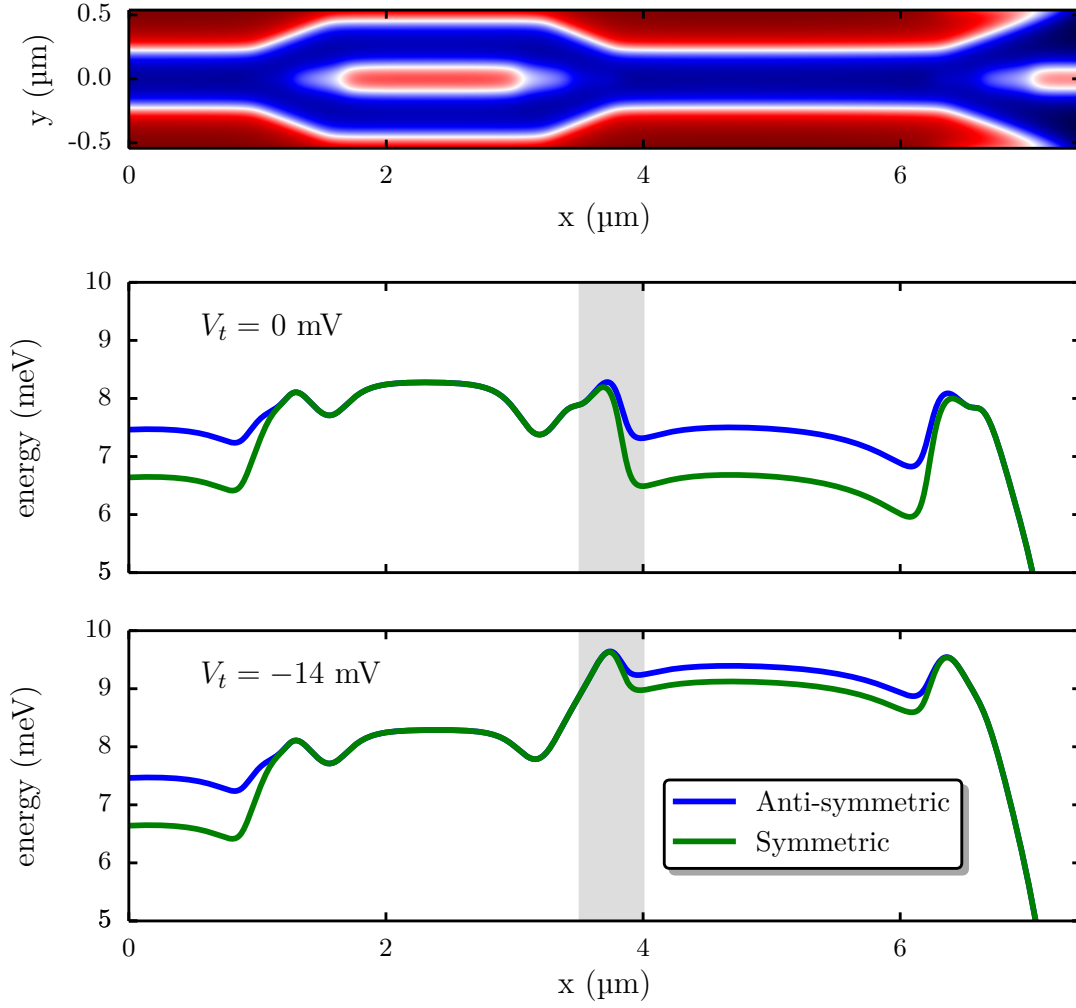


Figure 4.24: Energy of the symmetric and anti-symmetric state as a function of the position inside the device. The two states are degenerate in the Aharonov-Bohm region. The transition from this region into the tunnel-coupled wire (gray region) strongly depends on the voltage of the tunnel-coupled wire and will be discussed in greater detail in figure 4.25.

we show the potential landscape for comparison. In the two bottom panels, we depict the evolution of the energy of the symmetric and anti-symmetric state as a function of the position in the device. On the left, the two states are separated by around 1 meV. Their confinement potential is that of a single quantum wire. At the transition from this wire to the Aharonov-Bohm region, the width of the single wire slightly increases, leading to a drop of the absolute energies. The energies then increase when approaching the two separate arms and become degenerate. At this transition backscattering is rather common, since the onset of the Aharonov-Bohm center gates forms a scattering center for

symmetric wave functions. At the transition to the tunnel-coupled wire, we find a similar but reversed transition at zero tunnel gate voltage, since the confinement potential of the second wire is equivalent to the one of the first wire. The knob, which separates into the upper and lower projection arm also behaves as a scattering center, the energy of the states is decreasing since the confinement potential is decreasing. The bottom panel depicts the situation for a finite tunnel gate voltage of -14 mV. It is important to consider the transition from the Aharonov-Bohm region to the tunnel-coupled wire (gray shaded region in figure 4.24) in greater detail to get a better understanding of the backscattering that is occurring here. We therefore show the difference of the energy of the two states $\Delta E = E_A - E_S$ for different tunnel gate voltages at this transition in figure 4.25 as a function of position. One can clearly see that the energy difference between the two states gets smaller with increasing tunnel gate voltage. We reduce the information

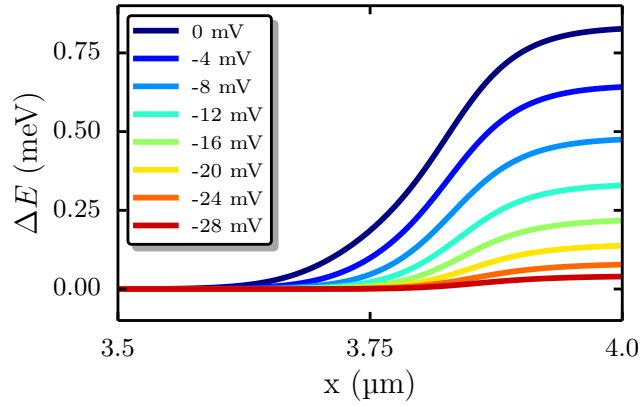


Figure 4.25: Evolution of the energy difference of the symmetric and anti-symmetric state at the transition region from the Aharonov-Bohm ring to the tunnel-coupled wire for different tunnel gate voltages. The higher the tunnel gate, the lesser the separation of these two states.

content of this plot to a single dimension by taking the maximum derivative of ΔE as a function of x and show the data in the top panel of figure 4.26. The negative slope of this curve leads to a rather straightforward interpretation. The larger the energy change at the transition, the more difficult is the matching of the wave functions and the more signal is scattered back. The empirical fact that we can observe a change from in-phase to anti-phase oscillations indicates that a transition is happening when the energy change at this transition becomes small. Nevertheless, the calculated values in figure 4.26 should be seen as a confirmation that a smooth connection of two energy eigenstates reduces backscattering while abrupt changes lead to an increase of the backscattered signal.

Let us now turn back to the SCR. Since the upper and lower currents are oscillating in-phase, the sample behaves as an effective two-terminal device. In this regime, the magneto oscillations are bound to Onsager relations. When attempting to change the wave vector in one arm of the interferometer, this should lead to phase jumps as we have argued in the previous section. To do so, we now change the side gate voltage V_s in the lower arm of the interferometer. At a fixed side gate voltage, we find common

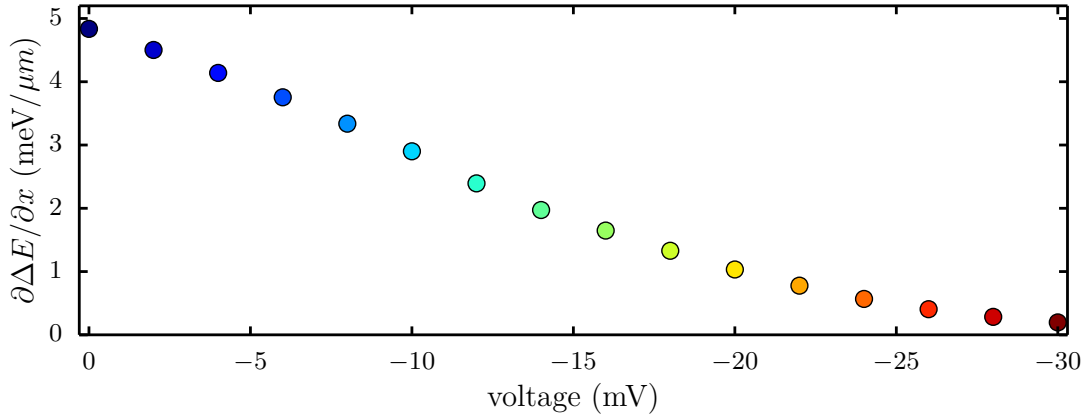


Figure 4.26: Maximum slope of $\partial\Delta E/\partial x$ from figure 4.25. The higher this value, the more backscattering occurs at the transition between the Aharonov-Bohm region and the tunnel-coupled wire. This backscattering leads to electron trajectories that encircle the Aharonov-Bohm ring and this slope has hence to be small for the sample to act as a real two-path interferometer.

Aharonov-Bohm oscillations as it is depicted in the top left panel of figure 4.27. A corresponding experimental data set is depicted in the top right panel. In both plots, the upper (lower) current is represented in blue (green). We find that the two currents in simulations as well as in the experiment are not perfectly identical, which is most likely a geometrical effect. Possible impurities in the real sample can also have an effect on this symmetry, however the effect of impurities has not been studied further. The simulation data corresponding to a side gate sweep for the total transmitted current is depicted in the bottom left panel of figure 4.27, whereas related experimental data is shown in the bottom right panel. Indeed, phase jumps are observed which are associated to the phase rigidity. We find a remarkable resemblance to the experimental data. On the contrary, the absolute values of the side gate voltage differ between simulations and experiment. This difference is due to electron screening which has not been taken into account. To get an estimate of this scaling factor, we compare the pinch-off curves of the simulation and the experiment as we have displayed in figure 4.28. The scaling factor is around 20 and accounts for the difference due to screening effects. Let us now turn to the WCR where a finite tunnel-coupling is induced by the tunnel-coupled wire. As expected from our model, we observe that the two currents are oscillating anti-phase when imposing a finite tunnel barrier in the channel as shown in figure 4.29. Again, experimental data is displayed on the right side whereas simulations are on the left side. For the top figure, we apply a voltage of $V_t = -8.3$ mV which basically corresponds to a single wire regime with a very flat potential at the bottom (see figure 4.13 for comparison).

As we have discussed in the analytical section, the anti-phase oscillations are due to the presence of the symmetric and anti-symmetric state in the split-wire and as a condition, the states have to be transferred smoothly from the Aharonov-Bohm region into the tunnel-coupled wire region. We now follow the same argumentation and state

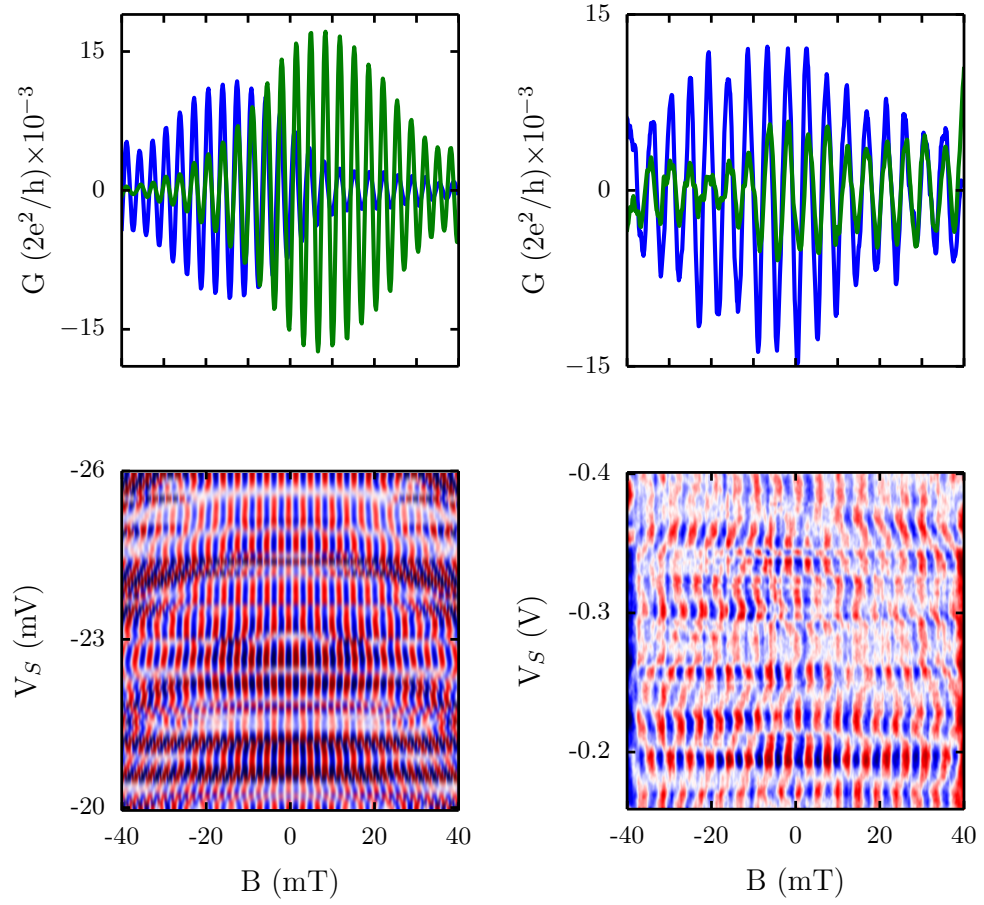


Figure 4.27: Magneto conductance oscillations in the Strong Coupling Regime after subtraction of a smooth background. Left: simulations, right: experimental data. Top: magneto conductance oscillations for a small tunnel gate voltage V_t . The blue (green) curve corresponds to the current in the upper (lower) contact. Both currents are oscillating in-phase. Bottom: 2D colour plot of the magneto conductance oscillations of the total transmitted current (upper - lower) as a function of side gate voltage V_s . Phase jumps due to Onsager relation are clearly observed in the simulated as well as experimental data.

that the difference between the in-phase and the anti-phase oscillations in our microscopic simulations comes from the fact that the symmetric states from both arms of the Aharonov-Bohm interferometer can be smoothly coupled to the symmetric and anti-symmetric modes within the split-wire due to the tunnel-coupled wire that raises the bottom of the potential landscape. From our findings, one could envision a case where a single wire can also induce anti-phase oscillations by carefully shaping its corresponding potential landscape. In this regime we can now induce a smooth phase shift of the Aharonov-Bohm oscillations when sweeping the side gate voltage V_s . This is shown in the bottom panel of figure 4.29. The data again resembles remarkably well the experimental curves. Let us note that the smoothness of the phase shift is sensitive to the symmetry of the gate

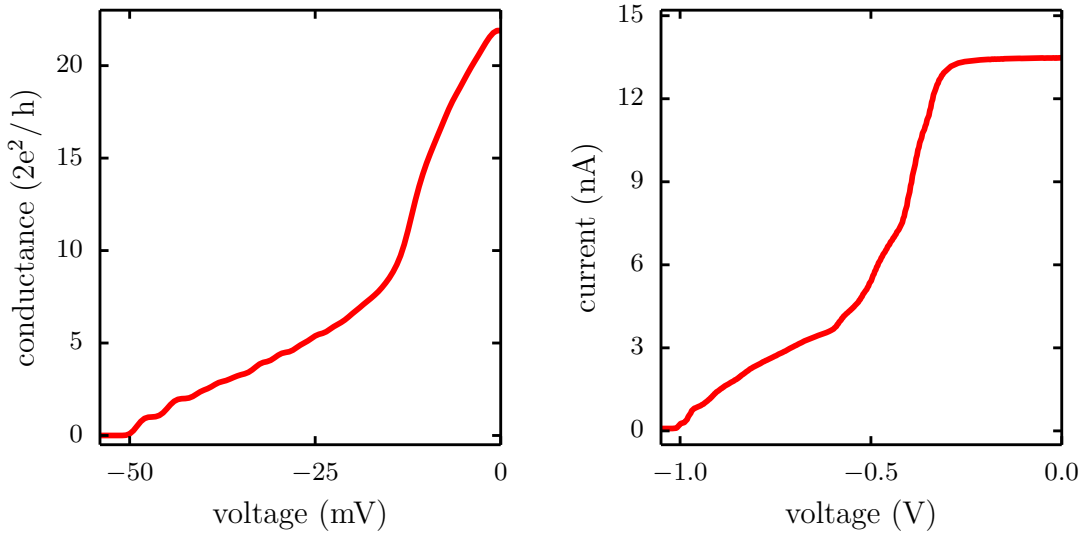


Figure 4.28: Left panel: simulated pinch-off curve of the two outer gates of the right tunnel-coupled wire. Right panel: experimental pinch-off curve of the two outer gates of the tunnel-coupled wire. The comparison of these two curves leads to a scaling factor around 20 that accounts for screening effects.

voltages applied to the individual gates. By inducing an asymmetry the linear shift becomes irregular and the anti-phase oscillations can also shift slightly. The same effect is being observed in experiments [122].

Finally we investigate the conductance oscillations with respect to the tunnel gate voltage in the WCR. This is certainly the most interesting feature of the experiment since it allows to repartition the output current into the upper and lower channel and allows therefore to tune the tunnel-coupled wire into a beam splitter regime. For simplicity, we only inject the current into the upper branch of the Aharonov-Bohm interferometer. This is done experimentally by depleting the tunnel gate on the left side of the Aharonov-Bohm loop and injecting into the upper contact only. For the simulations we follow the same procedure, apply a negative voltage on the left tunnel gate which we have not yet introduced until now and change the lead contact such that it covers only the upper half of the structure. In figure 4.30 we show the simulated as well as the experimental data. A smooth background has been subtracted from both data sets.

While at very small tunnel gate voltage (SCR) the two output currents are basically equal, we observe anti-phase oscillations for both data sets when approaching the WCR. For strongly negative gate voltage the tunnel barrier splits the tunnel-coupled wire into two independent wires. The tunneling probability from the upper into the lower arm becomes zero. Again the correspondence between experiment and simulation is quite remarkable. Having a closer look on the magneto conductance oscillations as a function of the tunnel gate voltage V_t we observe a change in the oscillation frequency when passing from the SCR to the WCR. The corresponding data is displayed in figure 4.31.

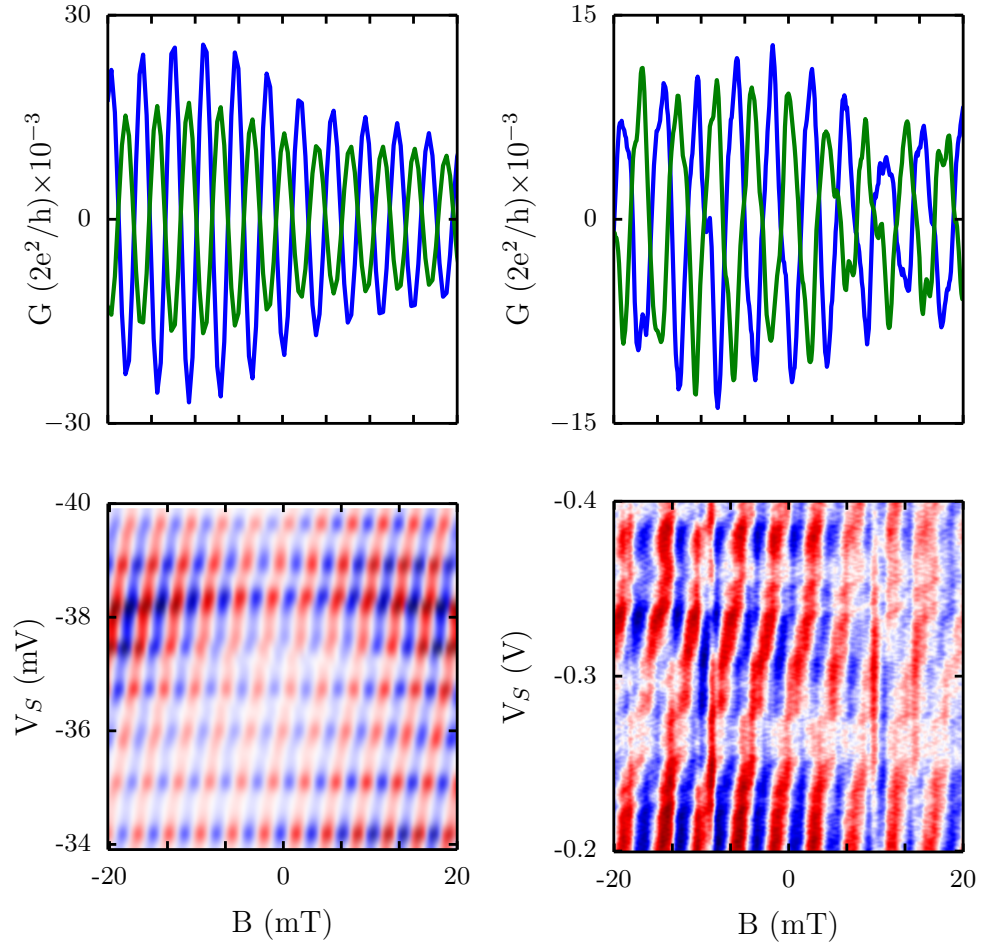


Figure 4.29: Magneto conductance oscillations in the Weak Coupling Regime after subtraction of a smooth background. left: simulations; right: experimental data. Top: magneto conductance oscillations for $V_T = -8.3$ mV. The blue (green) curve corresponds to the current in the upper (lower) contact. Both currents are oscillating anti-phase. Bottom: 2D colour plot of the magneto conductance oscillations of the total transmitted current (upper - lower) as a function of side gate voltage. For both data sets one observes a smooth phase shift of the Aharonov-Bohm oscillations as a function of side gate voltage V_S . This allows to electrically change the phase difference of the two paths by means of the side gate V_S .

For the SCR ($V_t = 0$ V) we observe in-phase oscillations as expected and the oscillation period corresponds simply to the surface area enclosed by the Aharonov-Bohm loop. When increasing the tunnel gate voltage one clearly observes an increase of the number of periods for a given magnetic field range. This implies that the effective Aharonov-Bohm surface area increases. We emphasize this by taking the Fourier transform of the magneto oscillations and by plotting the FFT peak position as a function of the tunnel gate voltage (bottom right panel). One clearly sees an increase of the Fourier peak as a function of tunnel gate voltage as indicated by the dashed line in figure 4.31. This additional surface

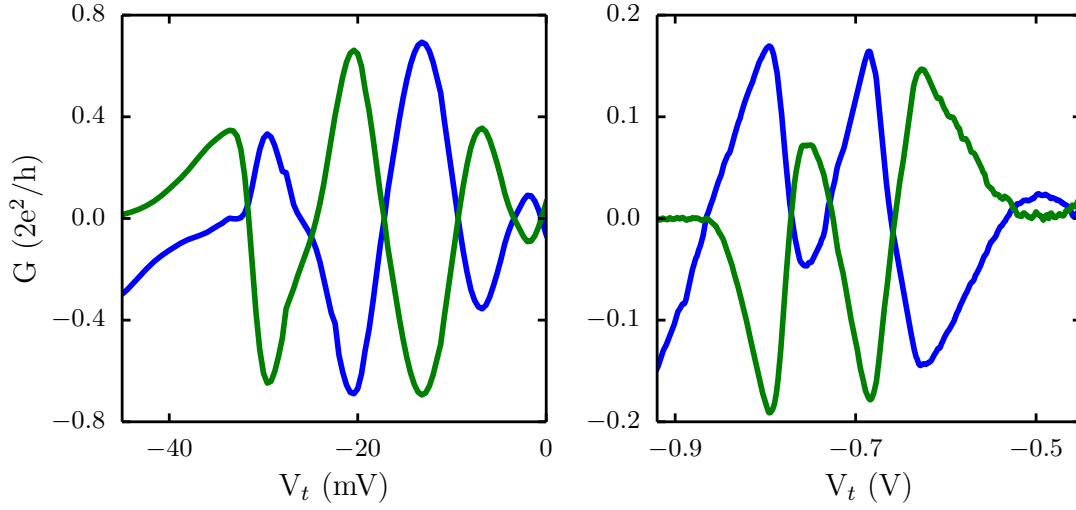


Figure 4.30: Conductance oscillations as a function of tunnel gate voltage after subtraction of a smooth background. left: simulations; right: experimental data. The blue (green) curve corresponds to the current in the upper (lower) contact. Both currents are oscillating anti-phase. The tunnel gate allows to repartition the current into the upper and lower current contact. The tunnel barrier can be tuned into a 50-50 beam splitter condition where the two lines are crossing at zero.

area can only be explained by an additional phase that is acquired between the symmetric and anti-symmetric state in the tunnel-coupled wire. We associate the magnetic field displacement of the wave functions due to the Lorentz force as well as the change of the potential landscape due to the tunnel gate to be responsible for this effect. Note however, that the Lorentz force makes the symmetric and anti-symmetric wave functions more localized in either of the two wires as can be seen in figure 4.18. This reduces the coupling of the two states between the upper and lower wire and as a consequence, the visibility decreases with increasing surface area. This microscopic simulation of the surface area increase corroborate our semi-analytical analysis of the split-wire where we could attribute the magnetic field and tunnel gate dependence to a single parameter, namely Δk , the difference of the wave vectors of the symmetric and anti-symmetric state. These effects could easily be tested with the experimental set-up of ref. [34].

In this chapter we have elaborated a simplified scattering model and conducted realistic simulations of an Aharonov-Bohm interferometer connected to two tunnel-coupled wires. The device behaves as a two-path interferometer similar to the optical Mach-Zehnder interferometer and can be viewed as a flying qubit where the state of the qubit can be manipulated on-the-fly. While our simplified model could account for most experimental observations by assuming suppression of backscattered induced loop trajectories, our numerical simulations of the actual experimental system with realistic parameters can reproduce all of the experimentally observed features as well as suppression of multiple loops in the Aharonov-Bohm ring. We could gain a deep understanding of rather subtle

experimental features. The good agreement between experiment and theory shows, that the physics of the flying qubit is well described within the Landauer-Büttiker scattering formalism. In addition to the interpretation of the experiments, we have shown that Kwant is a powerful open source package than can be a useful tool for quantum device design and signal optimisation. One limitation of the flying qubit is the fact that it used continuous currents to describe the qubit state. A first improvement would be the use of quantized currents. This is already under development by our collaborators [119] where they use pulse-trains of so-called surface acoustic waves (SAW). The second step would be to perform this experiment at the single electron level. This can be achieved by placing quantum dots at the entrance and exit of the structure and transferring the electron by means of a SAW from the one quantum dot to another quantum dot similar to what has been done in [38]. In the following chapter we will introduce the necessary concepts and discuss the first results on such a single electron beam splitter.

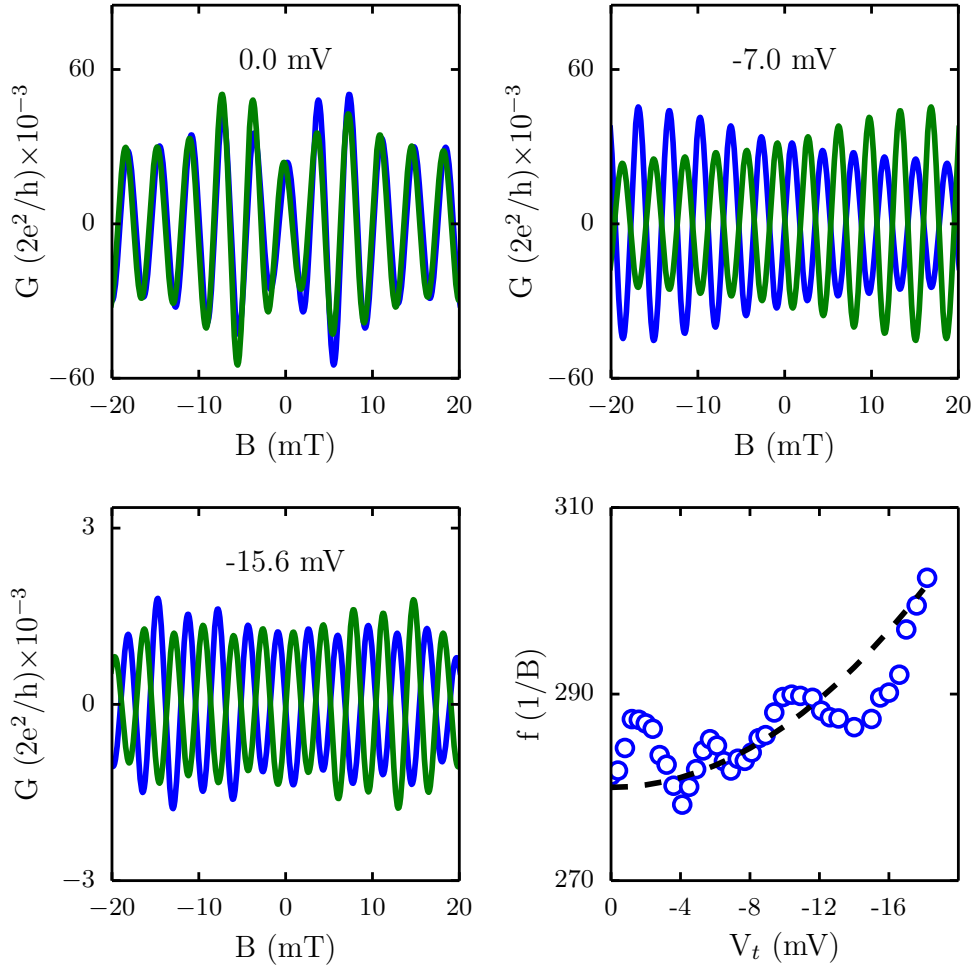


Figure 4.31: Simulations of the evolution of the Aharonov-Bohm conductance oscillations for different values of the tunnel gate voltage V_t . A smooth background has been subtracted from the data. Bottom right panel: frequency of the magneto oscillations (obtained by FFT of the other panels) as a function of V_T . As the tunnel gate voltage is increased the sample undergoes a transition from the SCR into the WCR. Further increase leads to an increase of the Aharonov-Bohm oscillation frequency. This behaviour can be understood as an effective surface area increase of the Aharonov-Bohm ring due to the decreased tunneling rate in the tunnel-coupled wire.

CHAPTER 5

Experiments

So far we have discussed an electronic two-path interferometer where an Aharonov-Bohm ring is connected to a tunnel-coupled wire. The information carrier in this system has been an ensemble of electrons, as we have measured currents at the output of the structure. In the following we will study a tunnel-coupled wire in the single electron regime. After giving the scientific context, we will first of all introduce *quantum dots* to isolate single electrons from their environment. Secondly, we will present the concept of electron transport by means of a *surface acoustic wave* (SAW). We will quickly discuss the cryogenic set-up and show how such samples can be fabricated. At this point, we will introduce the sample design and dimensions. Two different prototypes of the single electron beam splitter have been fabricated during this thesis. We introduce the experimental set-up that has been used for the measurements and present in the end of this chapter the first experimental results of this device.

5.1 The single electron beam splitter

In the late 1950s, Hanbury Brown and Twiss (HBT) have determined the angular size of Sirius by studying the intensity correlations of two identical particles in two independent detectors [126–128]. Their discovery that photons, which are emitted by a thermal boson source, tend to bunch together, stimulated the development of modern quantum optics [129]. Quantum mechanically we can understand this interference in the following way [130]: In figure 5.1 we display the four possible emission and detection processes from two independent points of the source (a,b) to two independent detectors (1,2). The first two processes in panel (i) and panel (ii), where one point source emits two photons to each of the detectors, are distinguishable and do hence not produce any interference. Processes (iii) and (iv) are indistinguishable since it is impossible for the detector to decide from which point source the photon arrived. These amplitudes are coherent and therefore give rise to interference. The Hanbury Brown-Twiss effect is hence a consequence of particle exchange, in this case boson exchange and included in the symmetry of the wave function of the pair of particles. The effect is present for all pairs of identical bosons and can be applied to a variety of fields, for example particle physics [131]. Here, we will focus on the realization of an electronic analog to the Hanbury Brown-Twiss effect. In contrast to particles obeying Bose-Einstein statistics, Fermi-Dirac particles

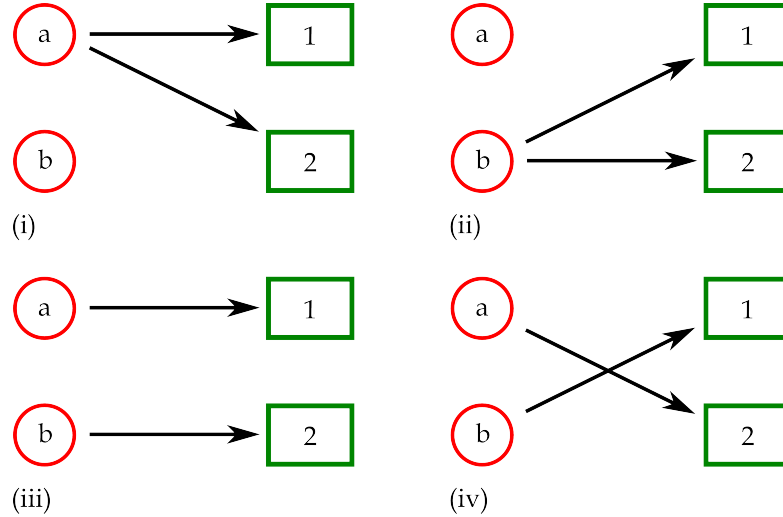


Figure 5.1: Hanbury Brown-Twiss effect. Panel (i)-(iv) show the four independent emission and detection processes. a, b denote light sources, whereas $1, 2$ denote the detectors. The processes (i) and (ii) are distinguishable and do hence not produce any interference. Processes (iii) and (iv) however are indistinguishable since it is impossible for the detector to decide from which point source the photon arrived. These amplitudes are coherent and give therefore rise to interference.

are expected to show anti-bunching, since two indistinguishable fermions must exclude each other by the Pauli principle. One of the major problems when trying to implement an electronic HBT experiment is the low occupation number per mode of the fermionic source [132]. A low degeneracy goes along with low visibility of the anti-correlation signal. Thermal electron sources show a degeneracy of the order of 10^{-12} to 10^{-10} , whereas field emission sources show a degeneracy of the order of 10^{-6} . These limitations could be circumvented in the pioneering works by [133–135]. Olivier et al. [134] have realized a quantum point contact source that served as a single-mode electron emitter with unity occupation number in a high mobility two-dimensional electron gas. Such quantum point contact sources have been studied prior to that [136, 137]. It is important to mention that in these studies it could be shown that the shot noise in such devices is suppressed in the quantum regime. This is a manifestation of the correlation of electrons participating in the current flow through the constriction due to Pauli principle [138] and shows that such emitters indeed have a unity occupation number. The Pauli principle prevents the presence of two electrons at the same position in the electron beam. Oliver et al. could show that the two output current fluctuations of such a ballistic electron beam incident on an electronic beam splitter shows anti-correlations. Similar findings have been reported by Henny et al. [135] in the quantum Hall regime. Furthermore, it has been shown that a HBT experiment can also be conducted with a field emission electron source [139]. The next major development concerning the development of an electronic HBT experiment has been the use of single electronic excitations. It has been shown that a single electron can be injected from a quantum dot into a quantum Hall edge state [108]

and this technique has been used to create the first realization of a Hanbury Brown-Twiss interferometer with single electronic excitations [109]. The next step was to conduct a so-called Hong-Ou-Mandel interferometer [140]. This experiment is rather similar to a HBT experiment, since it is based on the interference of amplitudes but nevertheless differs in the fact that it is an interference phenomenon of two particles incident on a beam splitter. In figure 5.2 we depict all possible trajectories in such a situation. The

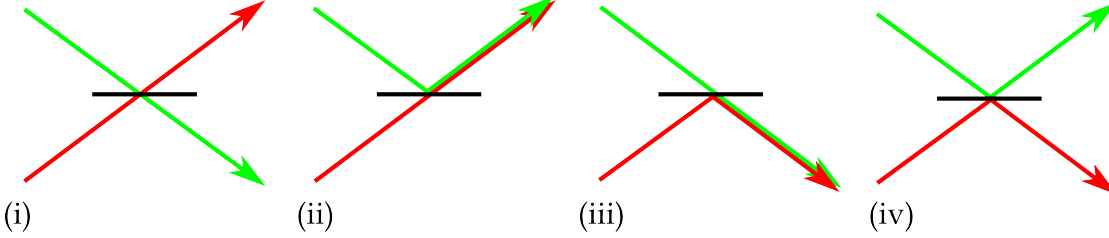


Figure 5.2: Hong-Ou-Mandel interferometer. Two indistinguishable particles are emitted simultaneously onto a 50-50 beam splitter. Panels (i) - (iv) show all possible trajectories. For photons, trajectories (i) and (iv) cancel each other and they tend to bunch together, whereas fermions show the opposite behaviour.

beam splitter is represented by the horizontal black line, whereas the two independent sources have two different colors. Let us consider two incident optical modes described by the annihilation and creation operators \hat{a}, \hat{a}^\dagger and \hat{b}, \hat{b}^\dagger . The beam splitter creates a linear superposition state for the incoming states (here Fock states)

$$\begin{pmatrix} \hat{a} \\ \hat{b} \end{pmatrix} = \frac{1}{\sqrt{2}} \begin{pmatrix} 1 & 1 \\ 1 & -1 \end{pmatrix} \begin{pmatrix} \hat{c} \\ \hat{d} \end{pmatrix} \quad (5.1)$$

We can now calculate the resulting state at the output

$$\hat{a}^\dagger \hat{b}^\dagger |0,0\rangle_{ab} = \frac{1}{2} (\hat{c}^\dagger + \hat{d}^\dagger)(\hat{c}^\dagger - \hat{d}^\dagger) |0,0\rangle_{cd} = \frac{1}{2} (\hat{c}^{\dagger 2} - \hat{d}^{\dagger 2}) |0,0\rangle_{cd} = \frac{1}{\sqrt{2}} (|2,0\rangle_{cd} - |0,2\rangle_{cd}) \quad (5.2)$$

and find that the amplitudes depicted in panel (i) and (iv) of figure 5.2 have interfered destructively. This bunching effect is the manifestation of the symmetrization postulate for bosons and is maximal for the chosen symmetrized beam splitter. For further information about the Hong-Ou Mandel experiment we refer the interested reader to [141]. Fermions show the opposite behavior as amplitudes (ii) and (iii) cancel each other. This experiment has been performed by Bocquillon et al. [91] with electrons and we will briefly address their experimental findings. We display their sample design in panel (a) of figure 5.3. Two electrons are injected simultaneously from the source dots 1 and 2, each into a quantum Hall edge state. They propagate following the indicated directions and collide at the quantum point contact in the center of the figure, which is tuned into beam splitter conditions. If two indistinguishable electrons collide simultaneously at the beam splitter, the noise in the output channels is suppressed because both states are fully occupied without randomness. If two incident electrons appear at different times at the quantum point contact, they would be partitioned randomly and independently,

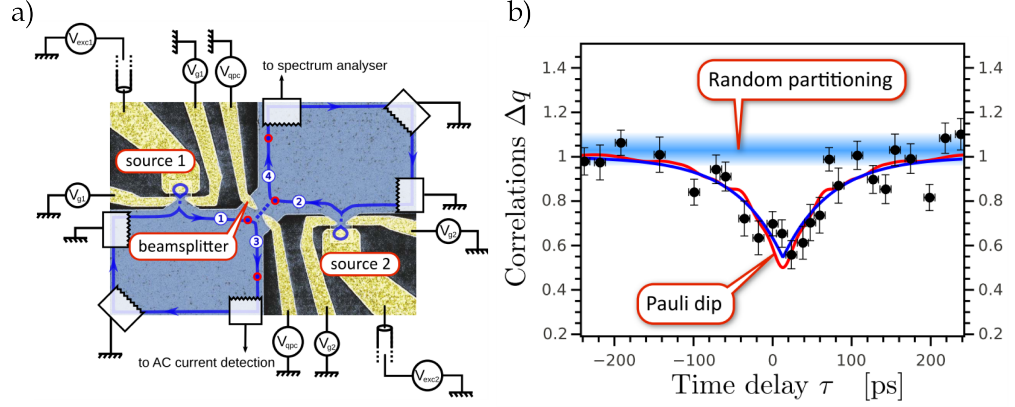


Figure 5.3: Fermionic Hong-Ou Mandel experiment as it has been performed by [91]. Left: false colour SEM image of the sample. The 2DEG is represented in blue. The two quantum dots (source 1 and source 2) act as single electron sources. The electrons are injected into the quantum Hall edge channels, following the indicated trajectories. The quantum point contact in the center of the structure is used as a single-electron beam splitter with a transparency of $T = 1/2$. Right: excess noise of output 4 as a function of the delay τ between the electron/hole emission. At zero time delay, the excess noise shows a dip, which indicates that the two electrons are arriving at the beam splitter simultaneously and show anti-bunching. The level of random partitioning noise is shown as a blue horizontal line.

which would result in noise. The suppression of the noise for a simultaneous arrival now confirms the generation of a two-particle coherent state. The correlations at zero time delay are negative as can be seen in panel (b) of figure 5.3. This is a typical signature of the anti-bunching behavior. In principle, the Pauli dip should go to zero and it is subject to debate, which mechanism, such as decoherence or electron-electron interaction, is responsible for the observed experimental feature. Another impressive experiment has been conducted by Dubois et al. [92]. In their system they made use of so-called Levitons, which are single electronic excitations. In fact, when the Fermi sea is excited with a small Lorentzian pulse, it has been shown that clear single electronic excitations can be created [142]. These excitations were simultaneously sent to a beam splitter and also showed anti-correlations. In this manuscript we will now introduce a third type of system that is capable to study the fermionic behavior of single electrons. We will employ a single electron source that has been developed in our laboratory [38] and combine this technique with an electronic beam splitter, very similar to what we have discussed in the preceding chapters. We will now quickly introduce the necessary concepts, which are needed to understand the experiment, which will be conducted in the end of this chapter.

5.1.1 Quantum dots

So far we have only conceptually mentioned quantum dots as a zero dimensional region in space where electrons can be isolated from their environment. In this manuscript, quantum dots will mainly be used as spinless single electron sources and we will therefore omit the spin degree of freedom from the discussion. Constraining the electron movement in all three spatial directions results in a quantized energy spectrum and quantum dots

can hence be seen as *artificial atoms* [143]. These discrete quantum levels [12, 144–146] can be described by considering the Coulomb charging of the isolated quantum dot island [15]. In 5.5 we show a schematic of a quantum dot.

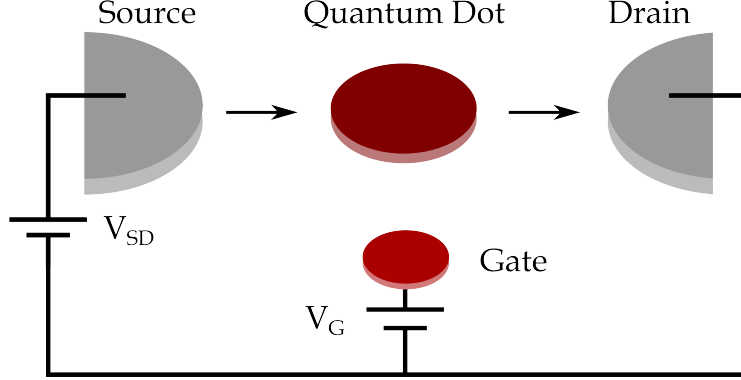


Figure 5.4: Quantum dot schematic. A quantum dot is connected capacitively to a source and a drain contact via tunnel coupling. The electrochemical potential on the quantum dot can be controlled via a gate capacitance.

As the charge is quantized, the number of electrons on the center island (quantum dot) is an integer. Changing the number of charges is associated to a *classical* change in the Coulomb energy of the island expressed in terms of its capacitance C . The electrostatic energy U of the quantum dot can be written as

$$U = -\frac{1}{2}CV^2 \quad (5.3)$$

where $C = C_S + C_D + C_G$ is the total capacitance due to the source (S) and drain (D) contact and the gate (G) and V is the voltage of the island. The number of charges $N \times e$ on the quantum dot can be written as the sum of all the charges on all the surrounding capacitors:

$$-Ne = C_G(V - V_G) + C_S(V - V_S) + C_D(V - V_D) \quad (5.4)$$

and together with equation 5.3 we arrive at the total energy of the quantum dot

$$U(N, V_G) = \frac{(-Ne + C_D V_D + C_S V_S + C_G V_G)^2}{2C} \quad (5.5)$$

We define the chemical potential μ of the quantum dot as the energy needed to add the n -th electron to the island

$$\mu(N, V_G) = U(N) - U(N - 1) = (N - \frac{1}{2})E_c - \frac{C_G}{C}V_G, \quad (5.6)$$

where we have defined the charging energy E_c as the energy separation between two

charge states:

$$\Delta\mu = \mu(N+1) - \mu(N) = \frac{e^2}{C} \equiv E_c \quad (5.7)$$

The proportionality factor C_g/C is called the α -factor or gate lever arm related to the conversion of gate voltage into energy. In order to observe charge quantization, the charging energy has to be larger than the thermal fluctuations $k_B T$. We can get an estimate of this number by approximating the quantum dot by a flat disc with capacitance

$$C_{disc} = 8\varepsilon_r\varepsilon_0 R, \quad (5.8)$$

where ε_r (ε_0) is the dielectric constant of GaAs (vacuum) and R is the radius of the disc. For a realistic size of around $R = 100$ nm, we obtain few meV, whereas 1 meV corresponds to a temperature of 10 K. This is an upper limit for the charging energy, because the presence of the metallic surface gates and the 2DEG increases the total capacitance C . Another condition is that the fluctuation of the electron number on the island due to tunneling has to be less than one over the timescale of measurement. We can get an estimate from

$$\Delta E_c \Delta t = \frac{e^2}{C} R_t C > h, \quad (5.9)$$

where $\Delta t = R_t C$ is the typical time to charge / discharge the island. This sets a lower bound to the tunnel resistance $R_t \gg h/e^2$ and hence to the thickness of the tunnel barriers.

The chemical potential that we have introduced in equation 5.7 plays a crucial role in the transport properties of the quantum dot. In figure 5.5 we display two different

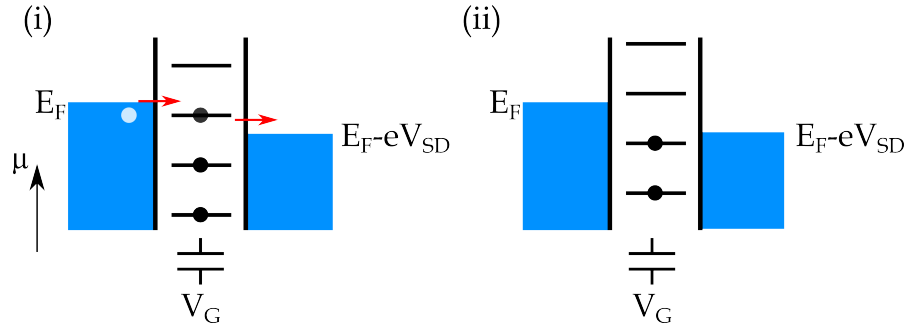


Figure 5.5: Coulomb blockade. When one level is aligned inside the source - drain bias window (left panel), electrons can tunnel through the structure. If no level is available, the charging energy prevents transport through the dot (right panel). This is called the Coulomb blockade.

transport regimes of a quantum dot. In panel (i), the chemical potential has been tuned with the gate voltage V_G such that one state lies within the bias window of the source drain contact. Tunneling is occurring and the conductance in this situation is one, the

electron number of the island is fluctuating by 1, whereas the fluctuation speed depends exponentially on the thickness of the barriers. If no state is available in the bias window as it is depicted in panel (ii), no current through the quantum dot can be recorded, the number of charges on the quantum dot is fix, protected by the charging energy. This is the so-called Coulomb blockade regime. The confinement of the electrons also gives rise to another energy scale which is the single particle level spacing. Unlike the charging energy, this effect is purely quantum and we can get an estimate by considering a particle in a box in two dimensions. The characteristic energy scale is [15]

$$\Delta E = \frac{1}{\pi} \frac{\hbar^2 \pi^2}{m^* L^2} \quad (5.10)$$

and we obtain 0.35 meV for a size of $L = 100$ nm. This value can be as low as several tens of μ eV, whereas 10 μ eV correspond to a temperature of 100 mK. We will come back to single charge detection and measurements of these charge state of a quantum dot in section 6.4. Apart from being able to isolate a single electron from its environment, we need to transport the electrons from the injection quantum dot to the beam splitter and to the detection quantum dot. For this purpose, we make use of a so-called surface acoustic wave.

5.1.2 Surface acoustic waves

Surface acoustic waves (SAW) are elastic vibrations propagating along a surface. Their existence was first demonstrated by Lord Rayleigh in 1885 [147] and are therefore often called Rayleigh waves. First studies of this wave phenomenon have been conducted by geophysicists interested in earthquakes, yet, we will here concentrate on a more delicate electronic application. It has been shown that SAW can be used to transport acoustoelectric current in a 2DEG [148, 149]. As an acoustic wave is propagating on the surface of a piezo-electric heterostructure, it will generate an electric field due to the piezo-electricity of GaAs. This moving potential landscape resembles a train of moving quantum dots and can be used to transport quantized currents [150, 151], where one electron is sitting in each minimum of the moving quantum dots. The quantized current reads $I = e \times f$, where f is the frequency of the SAW. This kind of electron transport takes place in quasi one-dimensional channels and can in principle be used to create flying qubits for quantum computation [152, 153]. These dynamical quantum dots have been extensively studied [154–156] and it has been shown that by combining static quantum dots with dynamical quantum dots it is possible to transport a single isolated electron from one quantum dot to another quantum dot [38, 102]. This forms the starting point of this experiment.

Let us begin with discussing the details of a SAW. In a piezoelectric semiconductor, SAW can be created using a so-called interdigital transducer (IDT) [157]. In figure 5.6 we depict two different types of IDT as they have been fabricated in this thesis. The design in the left (right) panel is called a half-wavelength (quarter-wavelength) resonator due to the single finger spacing with respect to the wavelength λ . A SAW is produced when an rf source is connected to the upper electrode, while the lower electrode is grounded. If this

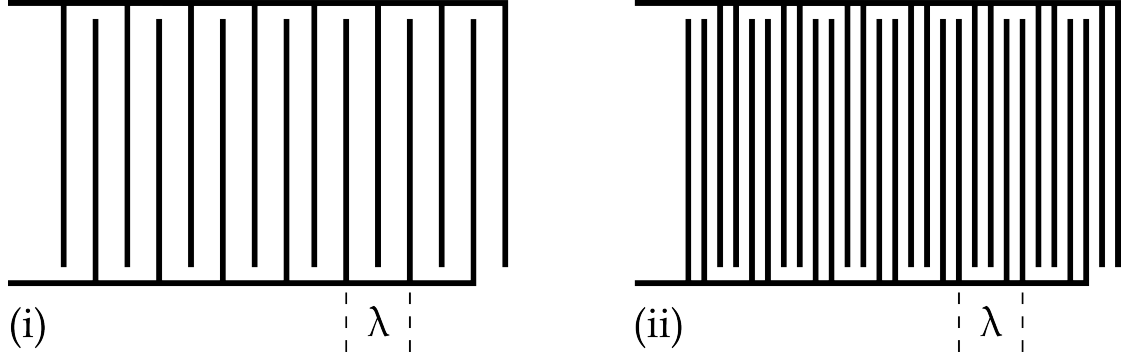


Figure 5.6: Interdigital transducers. Panel (i) shows a half-wavelength interdigital transducer (IDT) and panel (ii) a quarter-wavelength IDT. The nomenclature comes from the finger spacing. If one side of the comb is now excited with a RF source at the structure's resonance frequency, while the other side is connected to ground, such a planar structure will create a surface acoustic wave (SAW). The single finger IDT is simpler in terms of fabrication, however the double finger IDT is superior in terms of SAW potential rise time and energy dissipation inside the IDT structure.

electric field is resonant with the IDT, the electrical energy is converted into a traveling surface wave by piezo-electricity. This is schematically depicted in figure 5.7. We show

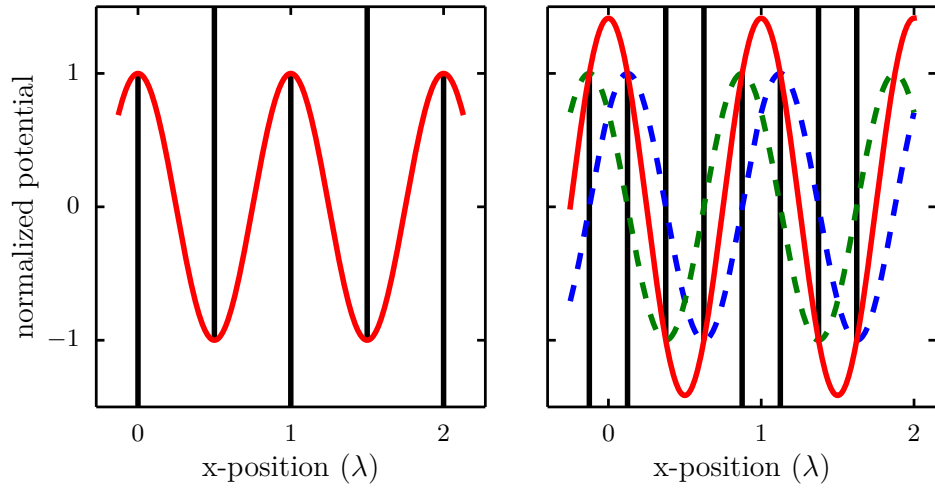


Figure 5.7: Schematic SAW generation by the half (quarter) wavelength IDT in the left (right) panel. The black vertical lines represent the IDT fingers from figure 5.6. The lower (upper) electrodes are positive (negative) at this point of time. The potential of the quarter wavelength IDT adds up, which results in a SAW with higher amplitude, although its wavelength remains unaltered. The red potential is the sum of the green and blue one.

the electric potential created by the two different types of IDT that results in the creation of the SAW. The lower electrode (vertical black fingers) is positive, whereas the upper electrode is negative at this point of time. The quarter wavelength IDT creates a higher

potential, since it adds up the green and blue potential from the individual fingers, and creates hence a SAW with a higher amplitude, compared to the half wavelength IDT. Its wavelength remains unaltered. The resonance frequency f can be calculated from the speed of the SAW $v_{SAW} \approx 2800 \text{ m/s}$ [158] and the periodicity of the IDT, which in our case has been fixed to $\lambda = 1 \mu\text{m}$, via

$$v_{SAW} = \lambda f \quad (5.11)$$

to $f = 2.8 \text{ GHz}$. Both IDT from figure 5.6 will emit SAW in both directions (left and right). However the major difference is the symmetry of the wave generation. The single finger IDT (left panel) is a Bragg mirror in itself. Waves that are generated in its center are reflected back and forth like in a cavity and most of the electrical power is dissipated without creating a propagating wave. This design has been used by [38, 102]. A possible improvement is the double finger IDT (panel ii), which does not show Bragg mirror behavior due to its symmetry and should in principle lead to a higher conversion efficiency of electrical power to propagating SAW power. Let us anticipate that this design has been tested but could not yet found suitable for efficient electron transport, most probably due to an insufficient quality of the fabricated device. This IDT is rather delicate to fabricate since the spacing between single fingers is around 125 nm, unlike in the prior design, where the spacing is twice as big (250 nm).

Nevertheless, further research has to be conducted before any final conclusion can be drawn. In figure 5.8 we show an exaggerated view of the crystal deformation due to the propagation of a SAW. All panels are separated by a constant time interval and show the propagation of such a SAW through the crystal lattice. The atoms of the lattice (crystal) have an elliptic motion. For clarity we have plotted the relative position of the red atom of figure 5.8 in figure 5.9. The direction of motion is counter-clockwise as indicated. The amplitude of the lattice vibrations decreases exponentially with the distance to the surface and the SAW is located within one wavelength λ from the surface of the wafer. The piezo-electric potential that is created by the SAW resembles a train of moving quantum dots 90 nm below the surface. It is important to estimate the *precise* potential landscape that is created by the SAW. For this purpose, we summarize the analytical results of the propagation properties of SAW in GaAs following the procedure presented in [158]. The piezoelectric potential Φ_{SAW} can be expressed as

$$\Phi_{SAW}(x, z, t) = A_{ph}(\tilde{\Phi}_{SAW}(z)e^{i\varphi_{SAW}(x, t)} + \tilde{\Phi}_{SAW}^*(z)e^{-i\varphi_{SAW}(x, t)}) \quad (5.12)$$

where

$$\tilde{\Phi}_{SAW}(z) = i \frac{C}{k_{SAW}} \frac{e_{14}}{\varepsilon \varepsilon_0} ((A_1 e^{-\Omega_R k_{SAW} z - i\phi_R} + A_1^* e^{-\Omega_R^* k_{SAW} z + i\phi_R^*}) + A_2 e^{-k_{SAW} z}) \quad (5.13)$$

and

$$A_1 = \frac{\gamma_R - 2\Omega_R}{\Omega_R^2 - 1} \quad (5.14)$$

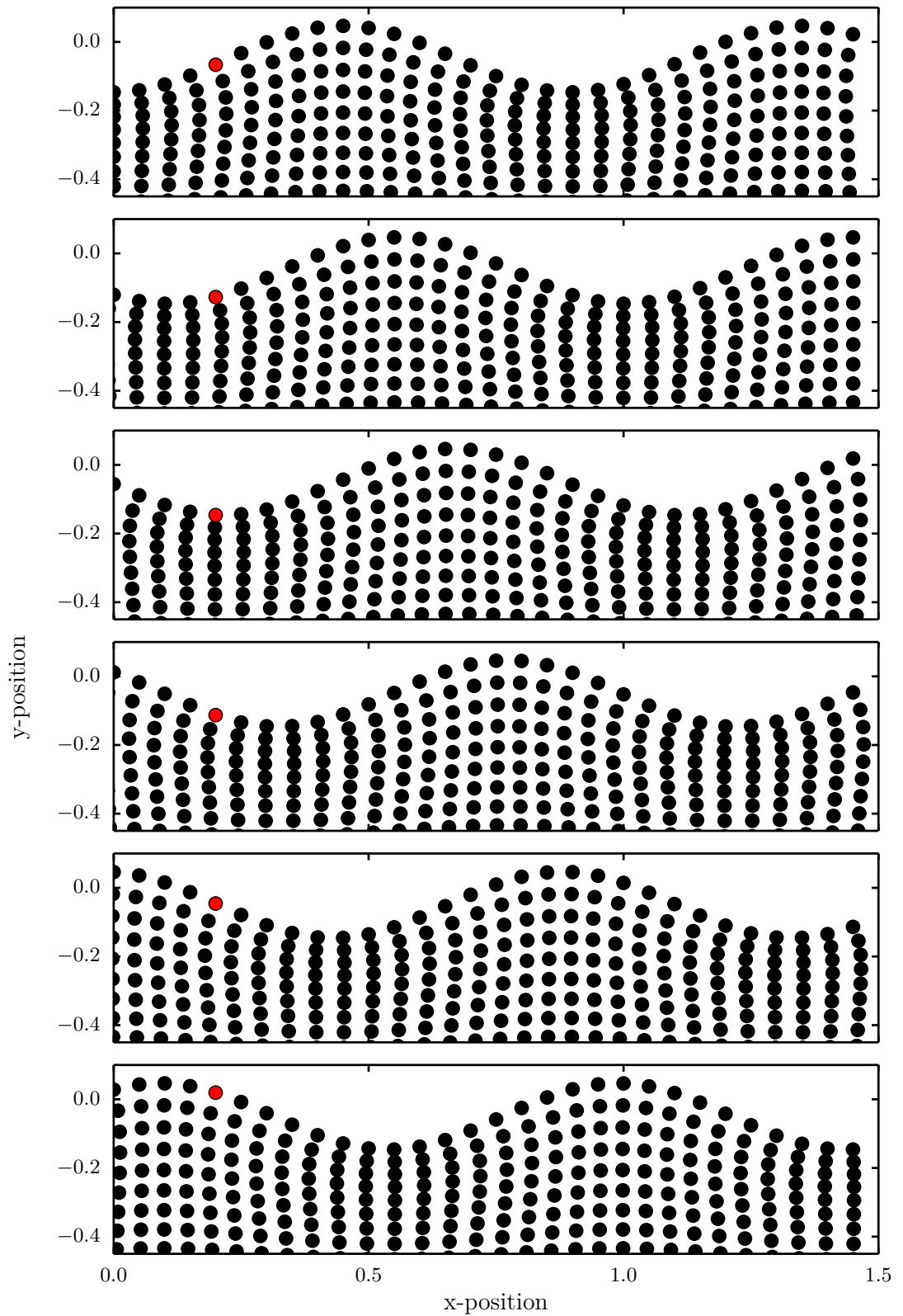


Figure 5.8: Sketch of a surface acoustic wave. Subsequent panels are separated by a constant time interval. The amplitude of the SAW is decreasing exponentially with increasing distance to the surface. The atoms are rotating counter-clockwise on an ellipse, which can be easier seen in figure 5.9, where we show the relative coordinates of the red atom.

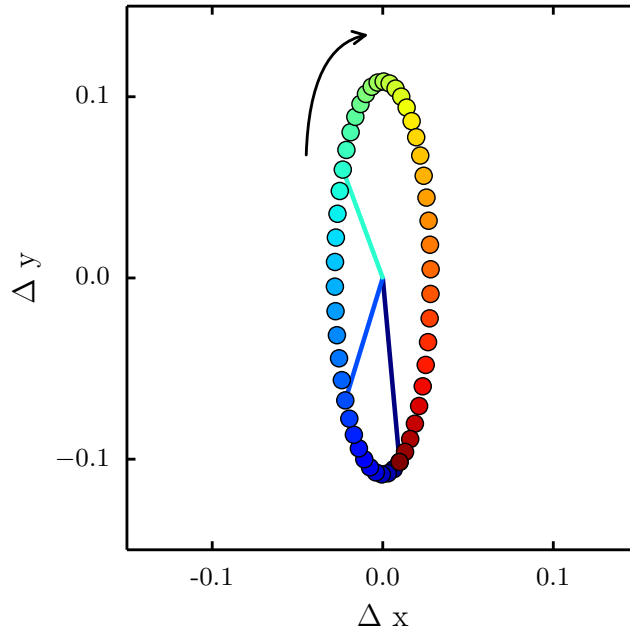


Figure 5.9: Trajectory of one atom in a SAW. The relative movement of the red atom of figure 5.8 is counter-clockwise following an elliptic path. The arrow indicates the direction of movement.

and

$$A_2 = -\frac{1}{1 + \varepsilon^{-1}} (\cos \phi_R + \varepsilon^{-1} \text{Re}(A_1 e^{-i\phi_R}) + \text{Re}(\Omega_R A_1 e^{-i\phi_R})) \quad (5.15)$$

and

$$A_{ph} = \sqrt{\frac{k_{SAW}}{2\rho v_{SAW}^3}} P_t \quad (5.16)$$

and

$$\varphi_{SAW}(x, t) = k_{SAW}x - \omega t \quad (5.17)$$

We summarize the used variables and their respective values in table 5.1.

Table 5.1: Surface acoustic wave parameters (GaAs)

variable	physical meaning	value
ρ	density (kg/m ³)	5316.5 10 ⁶
Ω_R	SAW parameter	0.501+0.480 <i>i</i>
γ_R	SAW parameter	0.676+1.154 <i>i</i>
ϕ_R	SAW parameter	1.050
C	normalization constant	0.457
A_1	amplitude	0.347-0.028 <i>i</i>
A_2	amplitude	-1.362
P_l	linear acoustic power density	20/500 (dBm/nm)=2 10 ⁵ (W/m)
A_{ph}	power dependent mode amplitude	7.1 10 ⁻⁵
$k_{SAW} = \frac{2\pi}{\lambda}$	wave vector (m ⁻¹)	6.3 10 ⁶
v_{SAW}	SAW velocity (m/s)	2863
ε	permittivity GaAs	10.89 ^a
ε_0	permittivity vacuum (F/m)	8.854 10 ⁻¹²
t	time	0
$\omega = 2\pi f$	angular frequency (rad/s)	1.8 10 ¹⁰
e_{14}	piezoelectric constant (C/m ²)	-0.16 [159]

^a <http://www.ioffe.ru/SVA/NSM/Semicond/AlGaAs/>

With equations 5.12 - 5.17 we are now able to quantitatively estimate the potential landscape created by the SAW as it is seen by the electrons in the 2DEG 90 nm below the surface. We plot this result in figure 5.10. We find a peak-peak value of around 60 meV. This value should be taken as an upper limit for the real peak-peak value, since our calculations omit screening effects and moreover, neither the number of fingers, which would increase this value, nor the losses due to reflection of the rf-power at the entrance of the IDT, which would decrease this value, have been taken into account. This propagating electrostatic potential can now be seen as moving quantum dots and we can calculate the energy spacing and wave functions in such a quantum dot. We will therefore assume that the damping of the SAW is negligible and the potential constant over the time of the flight. Let us first simplify the potential seen by the electrons by writing

$$V(x) = eV_{max} \cos((k_{SAW} - \frac{\lambda}{2})x), \quad (5.18)$$

where e is the electronic charge and $V_{max} = 60$ meV. We can develop the potential around a minimum

$$V(x) = -eV_{max} + \frac{2e\pi^2 V_{max} x^2}{\lambda^2} + O(x^3). \quad (5.19)$$

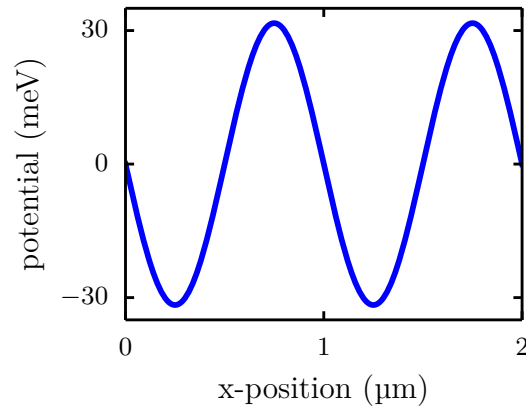


Figure 5.10: Calculated electrostatic potential created from the SAW from equations 5.12-5.17. The peak-peak value is around 60 meV, which should be seen as an upper limit of the real potential.

For this potential it is straight forward to solve the one-dimensional Schrödinger equation where its Hamiltonian reads

$$H = -\frac{\hbar^2}{2m^*} \frac{d^2}{dx^2} + \frac{1}{2}kx^2. \quad (5.20)$$

$m^* = 0.067 \times m_0$ is the effective mass of the electrons in the 2DEG. Neglecting constant terms we identify

$$k = \frac{4e\pi^2 V_{max}}{\lambda^2} \quad (5.21)$$

and calculate the eigenenergies.

$$E(n) = \hbar\omega(n + \frac{1}{2}) \quad (5.22)$$

where n is the quantum number of the n -th energy level and $\omega = \sqrt{k/m^*}$. The energy level separation $\hbar\omega = 1.6$ meV. The wave functions are given by

$$\Psi(n, x) = N_n H_n(\sqrt{\alpha}x) e^{-\frac{\alpha x^2}{2}}, \quad (5.23)$$

where $H_n(x)$ are the Hermite polynomials,

$$\alpha = \sqrt{\frac{m^*k}{\hbar^2}} \quad (5.24)$$

and

$$N_n = \left(\frac{\alpha}{\pi}\right)^{1/4} \left(\frac{1}{2^n n!}\right)^{1/2} \quad (5.25)$$

is the normalization constant. We can go one step further and now calculate the overlap of the wave functions of two electrons sitting in two different minima, propagating with v_{SAW} and arriving at a time δt at the beam splitter. This time delay will not be tunable in the sample that we are going to present, since only one SAW is available for the propagation of both electrons. We will come back to this point in the outlook. For the calculation it is straightforward to assume a time delay between two different SAW and we will therefore conduct this calculation since it nicely shows the expected output of such an experiment. The overlap can be written as

$$\langle \psi_1 | \psi_2 \rangle = \int_0^\infty \psi(0, x) \psi(0, x + v_{SAW} \delta t) dx. \quad (5.26)$$

From this we can now compute the probability $P(1,1)$ that the two particles exit in different outputs [91]

$$P(1,1) = \frac{1}{2}(1 + |\langle \psi_1 | \psi_2 \rangle|^2) \quad (5.27)$$

The result is shown in figure 5.11. This is the typical curve one should obtain for electronic anti-bunching due to the Fermi statistics of the electrons. This is one of the experiments that can be envisioned with two electrons in two distinct minima of dynamical quantum dots arriving simultaneously at an electronic 50-50 beam splitter. We have now introduced the necessary concepts for the realization of a single electron beam-splitter. A sophisticated nano-fabrication is necessary to realize prototypes where such experiments can be conducted and we will therefor introduce the major steps of the nanofabrication process.

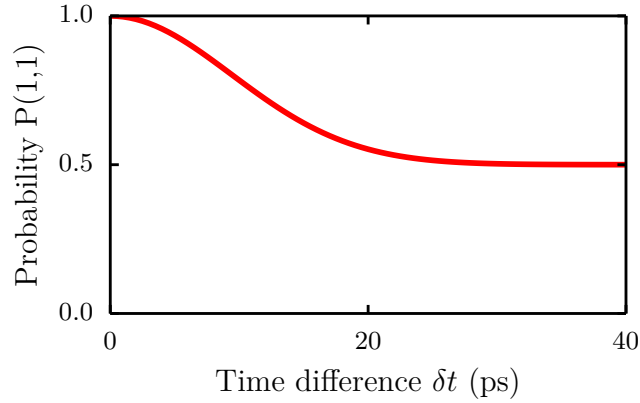


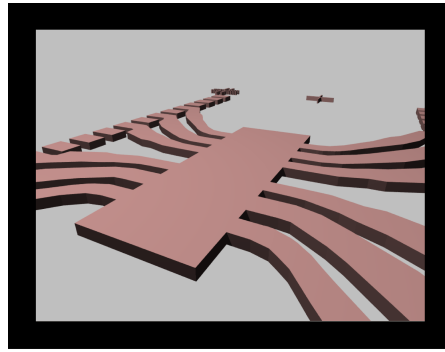
Figure 5.11: Coincidence counts at different outputs as a function of the difference of the arrival time. At zero time delay, the probability of measuring the fermions in two distinct detectors reaches one.

5.2 Device fabrication

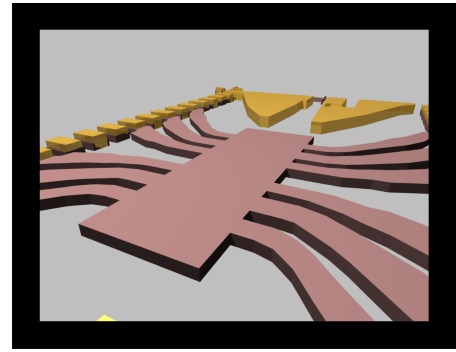
Prototyping is a widely used technique in research as well as in industry. Since these procedures are difficult to develop and standard procedures rare, we will here briefly detail the fabrication process that has been used in this thesis. In the end of this section, we will discuss the fabricated sample design with respect to the concepts that we have introduced in the first part of this chapter. Most samples were fabricated on $9 \times 9 \text{ mm}^2$ pieces of a GaAs/AlGaAs heterostructure, where we could place 8 identical prototypes. The wafer that has been used had a charge carrier density of $n_e = 2.7 \cdot 10^{11} \text{ cm}^{-2}$ and a mobility of $\mu = 1 \times 10^6 \text{ cm}^2 \text{ V}^{-1} \text{ s}^{-1}$. The fabrication process consists of five major steps, which are shown in figure 5.12. **The first step** (panel a) is the definition of the mesa. The mesa defines the geometry where the 2DEG is situated, the rest of the wafer has been etched down below the 2DEG by chemical etching. After spin-coating the wafer with S1805 (6000 rpm, 6000 acc, 30s, 115°C for 1 minute), the mesa has been defined using laser lithography. Development of the resist was done in Microdev:H₂O (1:1) for 1 min. The wet etching was done using the so-called Piranha solution H₂SO₄:H₂O₂:H₂O (5:1:25) with an etch rate of around 100 nm/15s. The acid volume proportions refer to a 40% H₂O₂ and a 98% H₂SO₄ solution. The peroxide acts as the oxidizing agent while the sulfuric acid dissolves the resulting oxide. Stopping the etching process is done with deionized H₂O. There are two important things to note: first, the order of mixing is H₂O, then H₂SO₄ and finally H₂O₂. The mixing is a highly exothermic chemical reaction and mixing a highly concentrated Piranha is only possible while cooling the mixing Becher. The acid decays quickly (hours) after preparation, should be tested on plain GaAs structures before employment on expensive heterostructures and the H₂O₂ concentration is crucial for a successful etching. Deviations from the suggested concentrations can lead to unetched places on the wafer. **The second step** (panel b) is the creation of ohmic contacts. The actual geometry is defined by laser-lithography as explained above. For this step we evaporate the following metal layers:

5 nm Ni + 60 nm Ge + 120 nm Au + 10 nm Ni + 30 nm Au

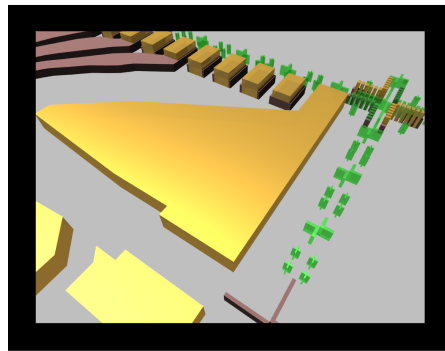
Afterwards, the structure is annealed at 450°C for 1 minute. This allows the metals to diffuse into the mesa and to make contact to the 2DEG. Germanium acts as a dopant, enhances the conductivity at the interface and most importantly reduces the Schottky-barrier between the metal and the semiconductor. Common ohmic contacts are of the order of several hundreds of Ohm. **In the third step** we define alignment crosses by means of laser lithography and metal evaporations (20 Ti + 100 Au) as can be seen in panel (c) of figure 5.12 (green marks). This step has to be done separately since the annealing from the previous step smears out the alignment crosses and it is difficult to align and center the fine gate structure in the next step. **In the fourth step**, the fine structure is written (panel c). This includes the gate structure (panel e) as well as the IDT (panel f). For this purpose we make use of a so-called masker, which is a 100 kV electron beam lithography machine (Jeol JBX 6300 FS) with an interferometric stage for alignment. The machine provides resolutions down to several tens of nanometers. Working at such high acceleration voltage, the electron beam does not induce damage to the 2DEG, which is sitting 90 nm below the surface [160]. The used write field sizes of this



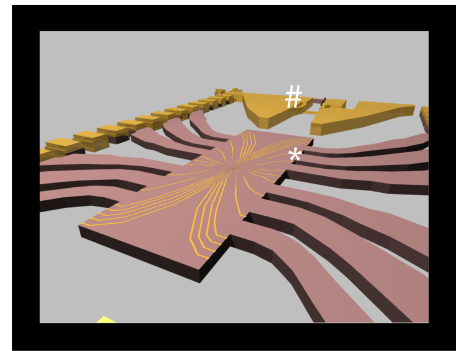
(a) Mesa



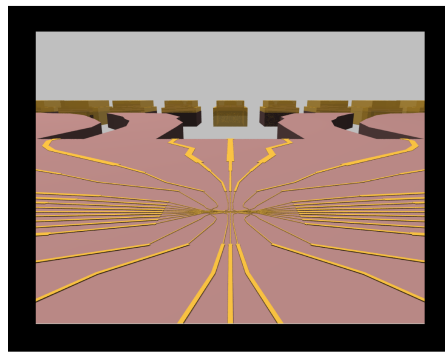
(b) Ohmic Contacts



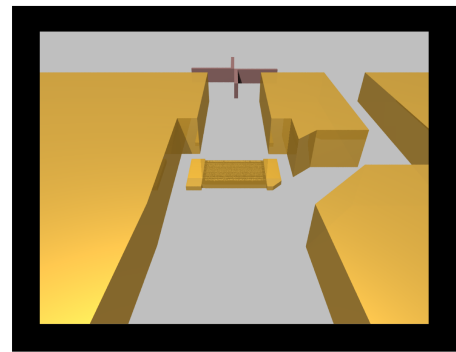
(c) Alignment Crosses



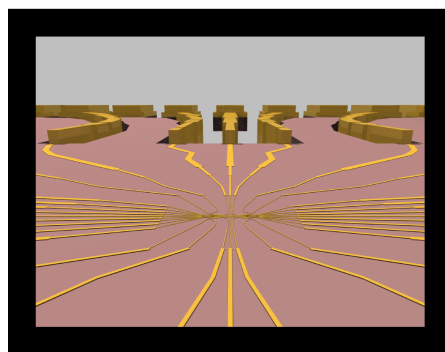
(d) Electron beam lithography



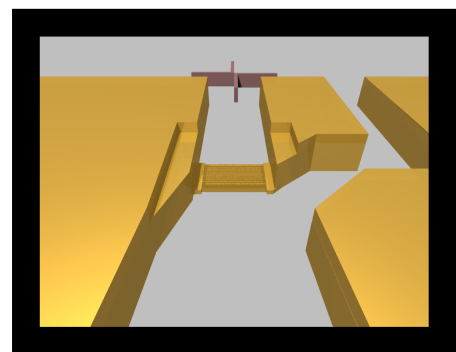
(e) Center from viewpoint *



(f) IDT from viewpoint #



(g) Center: laser lithography



(h) IDT: laser lithography

Figure 5.12: Fabrication steps. 3D render of the different fabrication steps. The process is detailed in the text.

machine are a square with $62.5\text{ }\mu\text{m}$ and $500\text{ }\mu\text{m}$ length. The smallest structures should be centered within these squares to avoid focus problems due to electron beam deflection. After development of the PMMA (4%) resist in MIBK:IPA for 1 minute, $5\text{ nm Ti} + 20\text{ nm Au}$ is evaporated. Lift off is done in NMP with the use of the smallest ultrasonic power possible for few seconds. It has become common practice to leave the sample in NMP for few hours after the application of ultrasonic power, since this guarantees that the sample surface is completely free from organic compounds. **In the last step**, the gates structure and the IDT are connected to their respective bonding pads via *large* gates that have again been defined using laser lithography. The evaporated metal $20\text{ nm Ti} + 100\text{ nm Au}$ should surpass the etched mesa depth. Corresponding images can be found in panels (g) and (h) of figure 5.12. After fabrication, the individual samples were

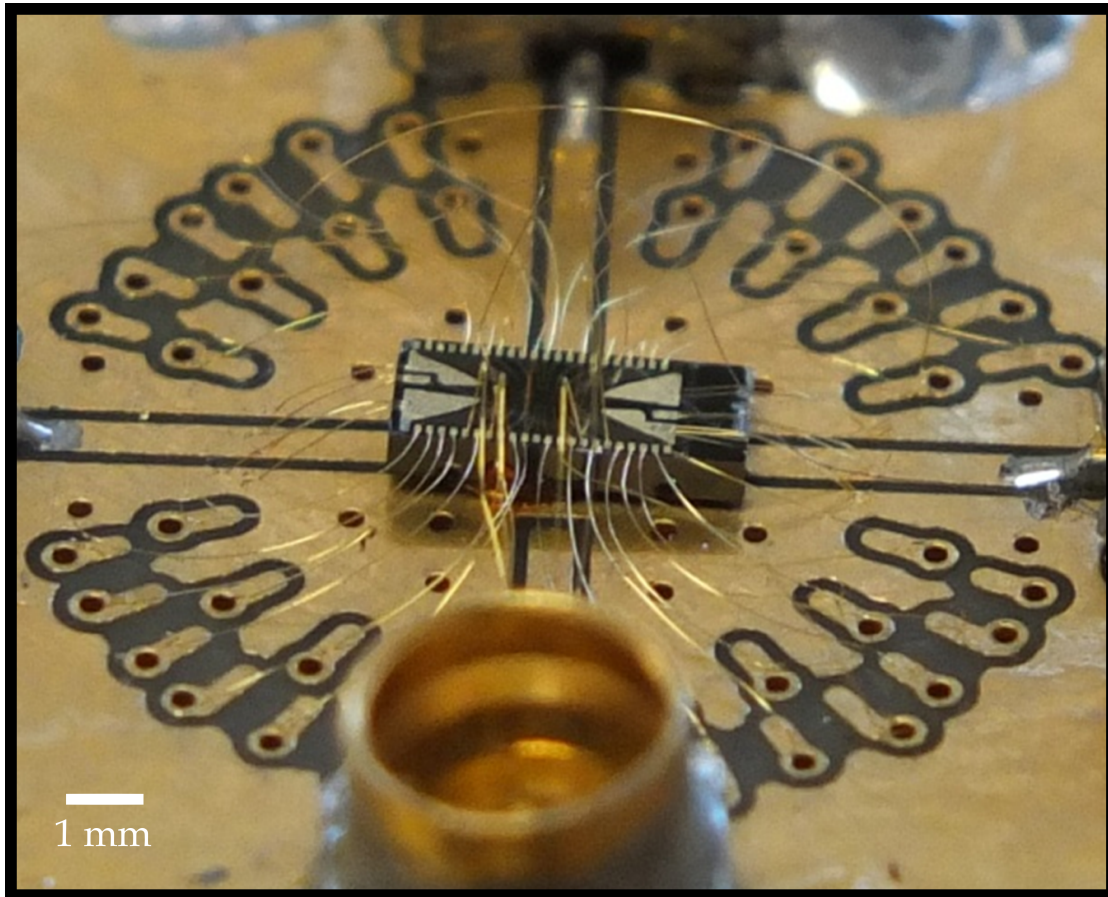
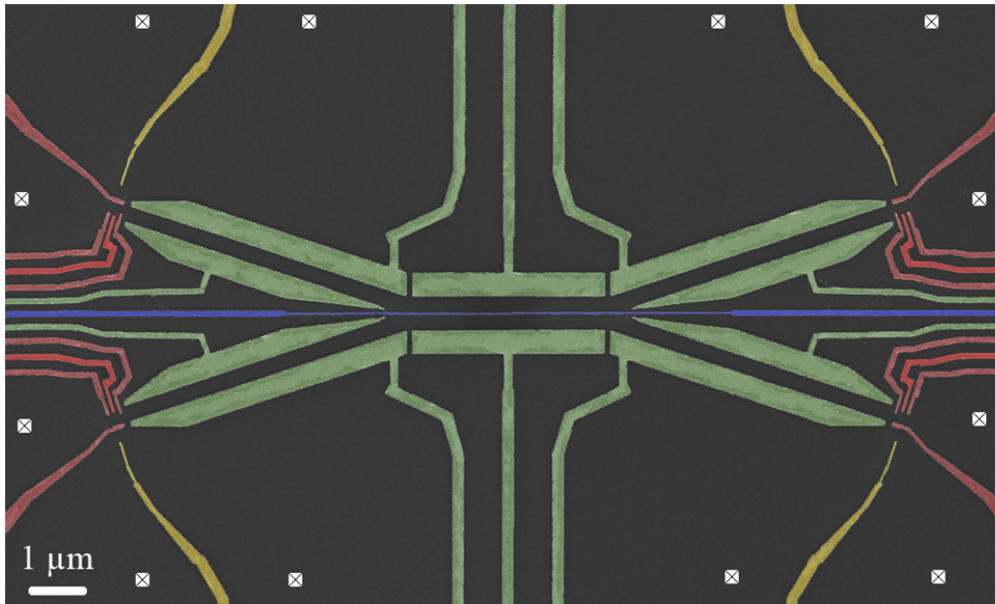


Figure 5.13: Bonding. The sample is glued on the sample holder, which consists of 40 DC measurement lines and 4 rf connectors (SMP). Bonding was done with a manual gold wire bonding machine.

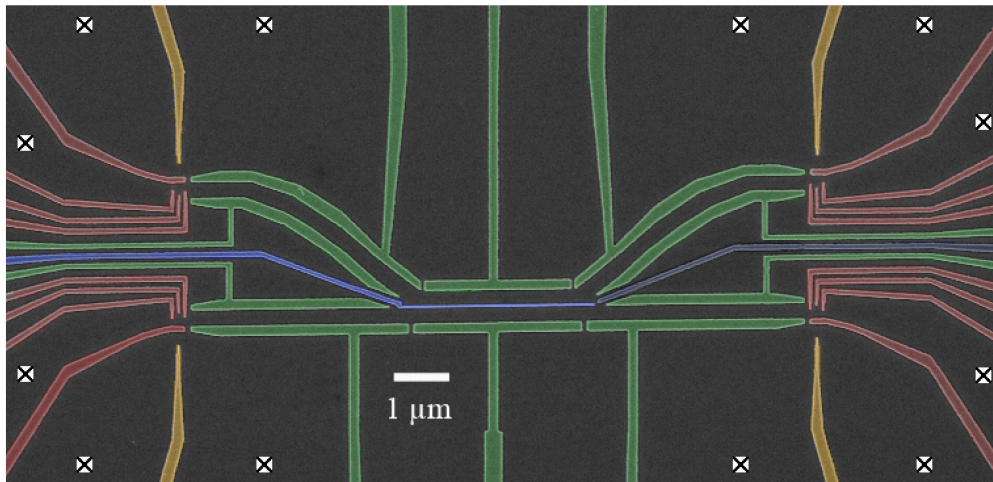
separated with a diamond cutter, while being covered with resist to protect them from dust, glued on the sample holder and bonded as can be seen in figure 5.13.

We have fabricated two prototypes during this thesis, both which are displayed in figure 5.14. The first device is point symmetric with respect to its center. The tunnel-coupled

wire separates the structure into one identical upper and one identical lower part. IDT have been fabricated on each side of the structure (not displayed), such that each side can independently serve as injection or reception, although only one IDT could be connected at a time due to space limitations in the cryogenic set-up. The red gates show the four different quantum dots that were used to isolate single electrons from their environment. The gates will be commonly referred to as reservoir gate, plunger gate and channel gate (from left to right). Green gates form the one-dimensional channel for the propagation, which is 300 nm wide. The yellow gates form the quantum point contacts that will serve as charge sensors in the following. In the best fabrication run, we could obtain a tunnel gate with a width of 60 nm over a distance of roughly 6 μm . The crossed boxes represent ohmic contacts. The sample is rather elegant to tune, as the parameter space can be reduced to four identical subspaces. Every quantum dot behaves similar, apart from the impurity concentration in the surrounding areas. Nevertheless, assuming maximum available resolution and common pinch-off voltages around -1.5 V , the maximum amount of different gate configurations (the parameter space) is as big as 10^{118} . The injection in the prototype is inclined, that is the direction of the SAW (vertical) is not parallel to the tunnel barrier between the injection quantum dots and the channel. This complication has been overcome in the second prototype, which can be seen in panel (b) of figure 5.14. All injection and projections are done parallel to the propagation direction of the SAW as in the original experiment [38]. Furthermore, the tunnel gate has been split into two part for greater tunability and less risk of electric discharge. The size of the channel gates has also been reduced to reduce possible damping effects of the SAW due to their weight. We will now detail the measurement set-up that has been used to characterize these two devices.



(a) Prototype I



(b) Prototype II

Figure 5.14: False color SEM images of the fabricated prototypes. Two different prototypes have been fabricated to realize the single electron beam splitter. Surface gates are colored, whereas the 2DEG is in gray. In both designs, electrons can be sent and caught from either side of the structure. Prototype I is point symmetric whereas in prototype II we have focused on making the transition between a quantum dot and the channel as straight as possible, similar to the original experiment [38].

5.3 Experimental set-up

The measurement set-up consists of two parts. On the one hand it consists of the cables that connects the low temperature stage with the room temperature end of the cryostat and on the other hand it consists of the electronic set-up that is used for the electrical manipulation. At the beginning of this thesis, a total of 12 DC connections had been installed in the used cryostat *Melusine*. Due to the complexity of the sample design, it was necessary to upgrade its complete electrical installation. Cabling is a rather time consuming and delicate task and we will briefly mention the important details here. In

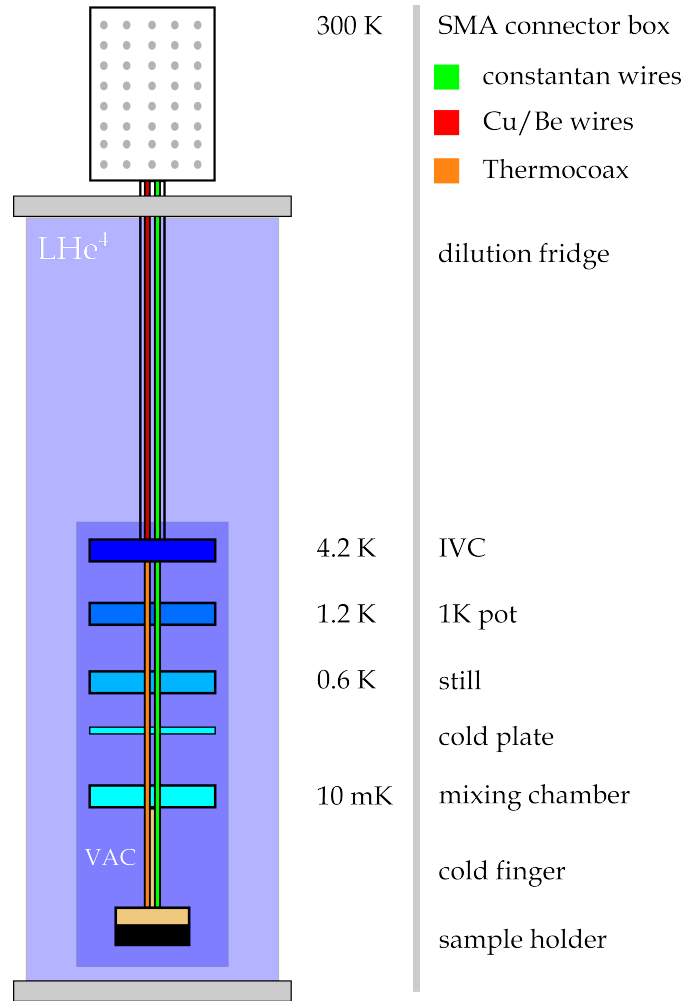


Figure 5.15: Cabelling of the cryostat. The cryostat has been equipped with 30 DC Constantan wires that are filtered with Eccosorb [161] and 12 coaxial lines consisting of Cu/Be coaxial lines between room temperature and 4 K that are then connected to Thermocoax coaxial cables at low temperatures for filtering purpose.

fig 5.15 we display a sketch of the dilution cryostat with the installed cables. The SMA connector box as well as the sample holder have space for 42 DC connections, which are split into Constantan DC and coaxial DC lines. The Constantan wires are filtered

using Eccosorb [161], whereas the coaxial lines consist of Cu/Be coaxial lines between room temperature and 4 K and are then connected to Thermocoax coaxial cables at low temperatures for filtering purpose. The wires are thermally anchored at the different thermal stages and the connections to the cold finger are designed such that the cold finger can be detached. These connectors are not depicted here. Furthermore the sample holder is equipped with four rf-connections (not displayed). The rf-lines consist of high temperature stainless steel silver coated lines between room temperature and 4 K and below, of niobium superconducting coax lines down to the mixing chamber. The base temperature with all DC wires installed is 8 mK and increases to 13 mK with the installed rf-wires.

In figure 5.16 we display a schematic of the experimental set-up that has been used for the electric manipulation of the samples. A LabVIEW program is used to control all

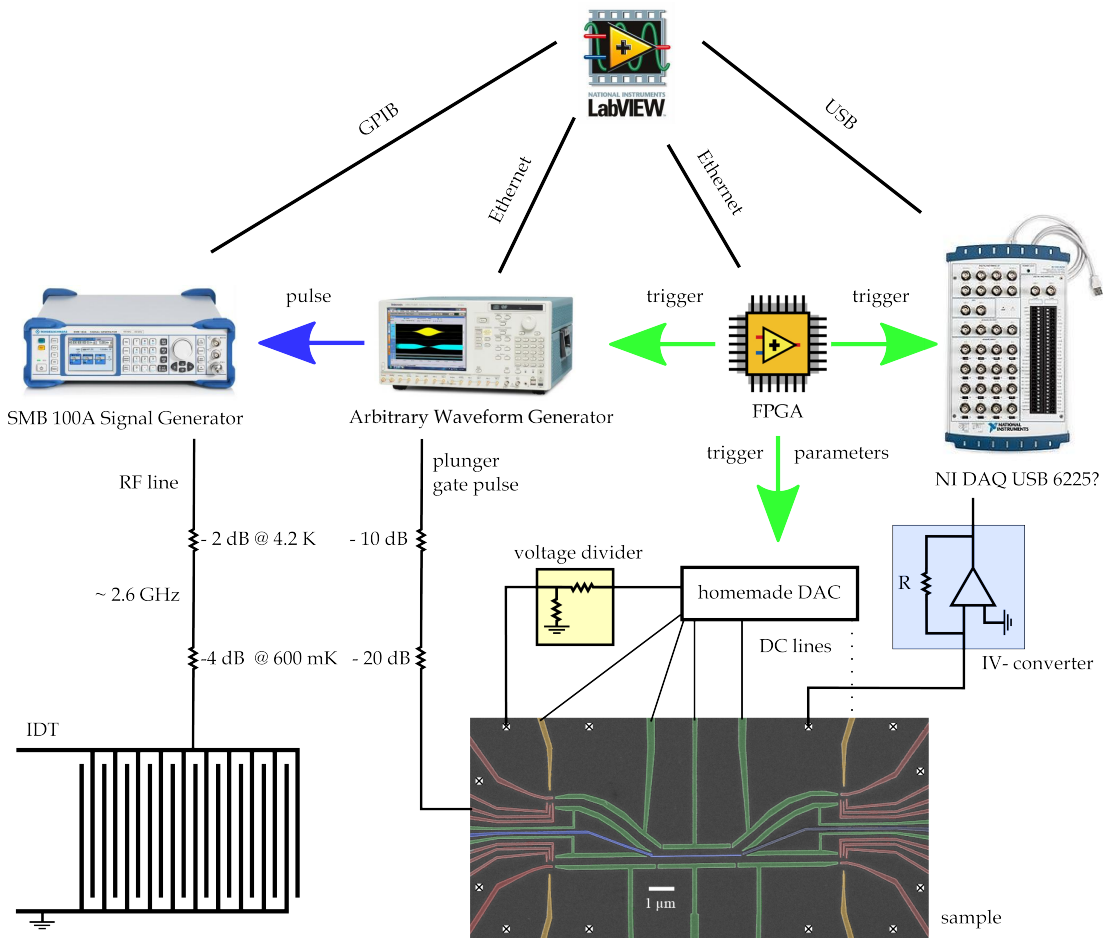


Figure 5.16: Experimental set-up. The gate voltages can be applied via a homemade DAC that is connected to a FPGA and controlled via a LabVIEW software. The IDT is actuated by a rf-signal generator that is triggered by an arbitrary waveform generator. Currents are measured using homemade current amplifiers that are measured with a NI DAQ USB board.

the different instruments. The IDT is actuated with a microwave signal generator R&S

SMB 100A. This device covers a frequency spectrum from 9 kHz to 6 GHz with a power level ranging from $-145 \text{ dBm} = 3.162 \text{ aW}$ to $30 \text{ dBm} = 1 \text{ W}$. The device has mainly been used with an external trigger from the arbitrary waveform generator (AWG) such that pulse trains of the order of 100 ns could be created. The rf-output of this device has been fed through two attenuation states ($-2 \text{ dB} @ 4.2 \text{ K}$ and $-4 \text{ dB} @ 600 \text{ mK}$) to one comb of the IDT whereas the other comb has been connected to the cold ground of the sample holder. One output of the AWG has also been connected to the each plunger gate of the injection quantum dots to be able to apply a ns-pulse in order to inject the two electrons simultaneously into the same minimum of SAW. The used AWG is a Tektronix 7122B with a sampling rate of 12 GS/s and a peak-peak value of 2.5 V. It is triggered by a field-programmable gate array (FPGA) that has been programmed via LabVIEW using the Xilinx compiler. The FPGA is integrated into a National Instruments Single Board RIO 9612 embedded control and acquisition device. The board has one hundred 44 MHz digital input/outputs, grouped per port of 10 I/Os. The FPGA micro controller takes care of the communication between the computer and the instruments and synchronization. It sends the commands to the homemade digital-to-analog converters (DACs) which have a range of $\pm 5 \text{ V}$. These voltages can be changed within 16 μs although the rise time is limited to 300 mV/ μs . The DACs have a resolution of 16 bits (150 μV). Their noise level is 25 nV/ $\sqrt{\text{Hz}}$. On the one hand, the DACs are used to control the bias of the electronic reservoirs and are hence connected to the ohmic contacts via a voltage divider (usually 1/1000). On the other hand, the DACs are connected to the surface gates to control their electrostatic potential and to tune the potential landscape. The measurement signal is a current that is recorded by homemade IV-converters. These devices are based on a Texas Instruments TLC2201 operational amplifier. Its band pass varies from 8 kHz to 1.4 kHz, while changing its feedback resistor from 10^6 to 10^9 Ohm (R in figure 5.16). These resistors have a Johnson-current noise of 129 fA/ $\sqrt{\text{Hz}}$ to 4.07 fA/ $\sqrt{\text{Hz}}$. The operational amplifier has a maximum voltage noise at 1 Hz of 1 μV , leading to an upper limit of 1 pA/ $\sqrt{\text{Hz}}$ and 1 fA/ $\sqrt{\text{Hz}}$, with respect to the feedback resistors. The signal from the homemade IV-converters are measured with a 16-bit National Instruments data acquisition board (NI DAQ USB 6229) with a sampling rate of 250 kS/s, which has to be divided by the number of used acquisition channels.

CHAPTER 6

Experimental results and outlook

In this chapter we will present the experimental results that we have obtained during this thesis. First, we characterize the SAW with a vector network analyzer (VNA) and afterwards with the aid of a SAW current measurement. Furthermore we use a quantum dot to characterize the moving quantum dots generated by the SAW. Next, we will show, how a quantum point contact can be used as a single electron charge sensor and introduce the stability diagram of a quantum dot. Furthermore, we will explain how to control the tunnel barriers in such a quantum dot. We will then discuss meta stable charge states high above the Fermi energy of the reservoirs and show how to control their life-time. In the end, we will see how all these techniques can be used to transfer an electron from one quantum dot to another quantum dot.

All techniques that we are using for the single electron transfer have become well established in our lab. Nevertheless, the combination of this highly reliable single electron source with a tunnel-coupled wire comes along with the need of a certain sophistication when tackling the problem. Incorporating this tunnel barrier with two electron sources and receptors increases dramatically the number of electric gates and the number of ohmic contacts. From an experimentalist's point of view, it is straightforward to overcome this size issue, simply by installing more electrical connections into the cryostat and by using an appropriate amount of stable voltage sources, current amplifiers and radio frequency sources. However, the more complex a system is, the more subject it is to vulnerability and the longer it takes to develop *the* sample.

Most results which are shown in the following section have been obtained from the first prototype. This device allowed us to gain valuable information about design flaws concerning single electron injection into channels that are not perfectly aligned with the SAW propagation direction. Electrons were most likely lost during the injection process into the reservoir as we will see in the end of this chapter. The bad performance of the interdigital transducers of the first prototype has motivated a non-negligible experimental effort to improve the SAW creation efficiency. All samples that had been equipped with IDT prior to this manuscript had been fabricated in collaboration with Tokyo university. During this manuscript, the fabrication technology was transferred to the local fabrication

facilities, i.e. the Nanofab in Institut Neel and the PTA technology platform in the CEA. All IDT VNA measurements shown in the following section have been conducted on test samples and design details will be given accordingly. The comparison of the half wave length and quarter wave length resonator has been done on Japanese devices at the same time with the improvement of the local fabrication process. The first prototype had only been equipped with double finger IDT. For the second prototype we have chosen to pursue a mixed strategy, i.e. both types of IDT for different reasons. On the one hand, the fabrication of single finger IDT is more reliable and a single finger IDT has been used in the original experiment [38]. On the other hand, the bandwidth of single finger IDT is limited to around 10 MHz, whereas the bandwidth of double finger IDT can go up to 200 MHz. The latter are therefore superior in terms of SAW potential rise time and are most probably the long term choice of IDT for this project.

The design of the second prototype eliminates most of the design faults of the first prototype however further research will need to be conducted to validate this statement. One problematic point in particular is the total number of 43 contacts of prototype 1 and 2 and the resulting density of the electrical gates leaving the device vulnerable to electric shock and complicating the fabrication procedure. In addition, only 42 contact pads were available on the most advanced chip carrier that we are using to date. To circumvent this peculiar problem, we have chosen to interconnect several ohmic contacts at low temperatures, giving rise to less tuneability and less stability.

One possible solution to the mentioned issues would be to optimize and limit the number of electrical contacts. It is for this precise reason that we propose a third prototype, which reduces the complexity of the given device while keeping its functionality and tuneability intact. The design of the third prototype has become possible due to advancements of the algorithm which has been presented in section 3.3. It is now possible to directly convert the GDSII stream format files into pythonic gate objects and immediately calculate the electrostatic landscape seen by the electrons 90 nm below the surface. Such calculations are platform independent and only take a few seconds, which allows for a fast feedback optimization cycle, i.e. numerically sweeping several gates, analyzing obtainable potential landscapes and adjusting the geometry of the gates to obtain the desired performance. Let us start with the characterization of surface acoustic waves.

6.1 Surface acoustic wave characterization

Surface acoustic waves (SAW) are created by inducing earthquake-like waves [147] in the piezo-electric substrate of GaAs by applying an oscillating rf-field on the interdigital transducers (IDT), being situated on the sample's surface. The objective of these measurements now is to determine the exact resonance frequency of the SAW and to prove that the IDT are working properly. First characterizations can be conducted at room temperature, whereas a precise determination of the amplitude of the moving potential landscape resembling moving quantum dots has to be carried out at low temperatures.

We display the SEM images of a quarter wave length resonator and a half wave length resonator in figure 6.1. The left panels show the single finger resonator with a finger spacing of 250 nm, whereas the double finger resonator in the right panels has a finger spacing of 125 nm. The fingers for both designs are 60 μm long, ensuring a homogeneous

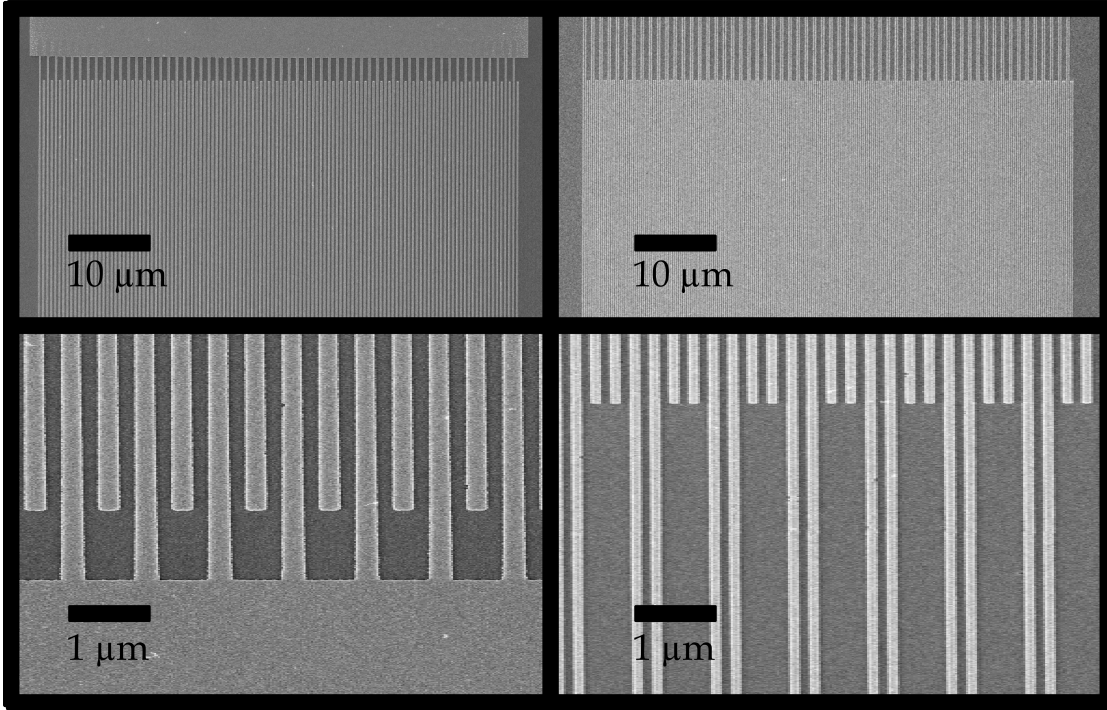


Figure 6.1: SEM pictures of the IDT. Top left: single finger IDT; Bottom left: single finger zoom; Top right: double finger; Bottom right: double finger zoom. One finger of the single finger IDT is 250 nm wide, one finger of the double finger IDT is 125 nm wide. The samples have been fabricated in the PTA, Grenoble. The fingers for both designs are 60 μm long. The fabrication yield of both structures exceeds 95% with minor fluctuations of the finger thickness of ± 5 nm.

wave front of a distance larger than the sample size. The fabrication yield of both structures exceeds 95% with minor fluctuations of the finger thickness of ± 5 nm. Let us focus first on the quarter wavelength resonator. All samples are equipped with two IDT on each side of the structure and we can therefore measure the transmitted signal between these two devices. Due to the rather large bandwidth of such double finger IDT (40 to 200 MHz, depending on the fabrication run), a mismatch of the resonance frequency within the bandwidth does not disturb the measurement of the transmission signal. For the measurement, we connect both IDT to a vector network analyzer (R&S ZVL) with a spectrum ranging from 9 kHz to 6 GHz and record the transmitted signal as it is depicted in figure 6.2. Our data contains two beating signals. The first visible oscillation has a frequency spacing of around 100 MHz and corresponds to reflections at the end of the used rf-lines due to bad impedance matching and imperfect calibrations. This signal is hence not of interest. The second oscillation has a frequency spacing of 8 MHz and we associate it to the generation of SAW. To confirm that this frequency spacing indeed corresponds to the IDT, we can calculate the separation of the two IDT [37]. An elegant way to do so is to take the FFT of the transmitted signal and multiply it by the velocity of the SAW ($v_{SAW} = 2800$ m/s). Our data suggests that the two IDT are separated by 350 μm ,

as can be seen in the bottom panel of figure 6.2. The actual distance between these two IDT was $300\text{ }\mu\text{m}$ and the discrepancy between these two values can be understood from the simple fact that signal generation and reflection is not happening at the outermost fingers of the IDT, but rather inside the IDT structure. The additional $25\text{ }\mu\text{m}$ are well in between the sample borders. The resonance frequency of this IDT is around 2.5 GHz . No significant dip can be seen in a reflection measurement and a precise determination of the resonance frequency is rather difficult using a transmission measurement between two IDT. However, our data provides a clear confirmation that both IDT are working properly, due to the existence of the beating signal in the transmission. A reflection measurement alone cannot give sufficient information about a double finger IDT and it is hence indispensable to equip such devices with two double finger IDT. A series of such measurements has been done for testing and optimization purpose. Most double finger IDT, which have been characterized in this thesis, only show an extremely small power dissipation in reflection of maximal 0.5 dB . For convenience, we display the obtained data for two good double finger IDT in the left panel of figure 6.3. The top left panel shows their transmission signal, whereas the reflection signal is depicted in the bottom left panel. Although the resonance dip is clearly visible in this dataset (red curve in the bottom left panel), we have to note, that the data has been taken at room temperature, knowing the transmitted signal between the IDT with a well-calibrated VNA. Cooling down to low temperature commonly scrambles this calibration and disallows for a proper reflection measurement with the needed precision. Both IDT have similar transmitted signals, while the reflection dip for the black curve in the bottom panel of figure 6.3 is almost invisible. With this method it is rather difficult to obtain a precise value of the center resonance frequency, however the frequency range is a good starting point for the measurements that will be carried out in the two following subsections. Before characterizing the double finger IDT with a different method let us now turn to single finger IDT. The characterization is following the same procedure as explained above. In the right panels of figure 6.3 we display the obtained data. The top right panel shows the transmitted signal whereas the bottom panel the reflected signal. Maximum energy conversion occurs around 2.67 GHz , the bandwidth is smaller compared to the double finger IDT and around 10 MHz . Single finger IDT can easily be tested in reflection without a second IDT. The smaller bandwidth of the single finger IDT leads to a longer rise time of the induced electrostatic potential landscape, which is the main advantage of the double finger IDT. At the same time, the smaller dip in reflection of the double finger IDT goes along with lower power consumption of the device, limiting heating effects at cryogenic temperatures. The difference in the reflection peak can be understood by the following argument. Waves that are reflected inside the single finger IDT from two neighboring electrodes have a phase difference of 2π due to the finger spacing of $\lambda/2$, leading to constructive interference inside the IDT. On the contrary, the spacing of two neighboring electrodes in a double finger IDT is $\lambda/4$, leading to a phase difference of π and hence destructive interference. The double finger IDT reduces the acoustic reflections inside the structure and therefore the dissipated power. The purpose of the SAW is to transport electrons across the structure which is why we now turn to the SAW current measurement at low temperatures.

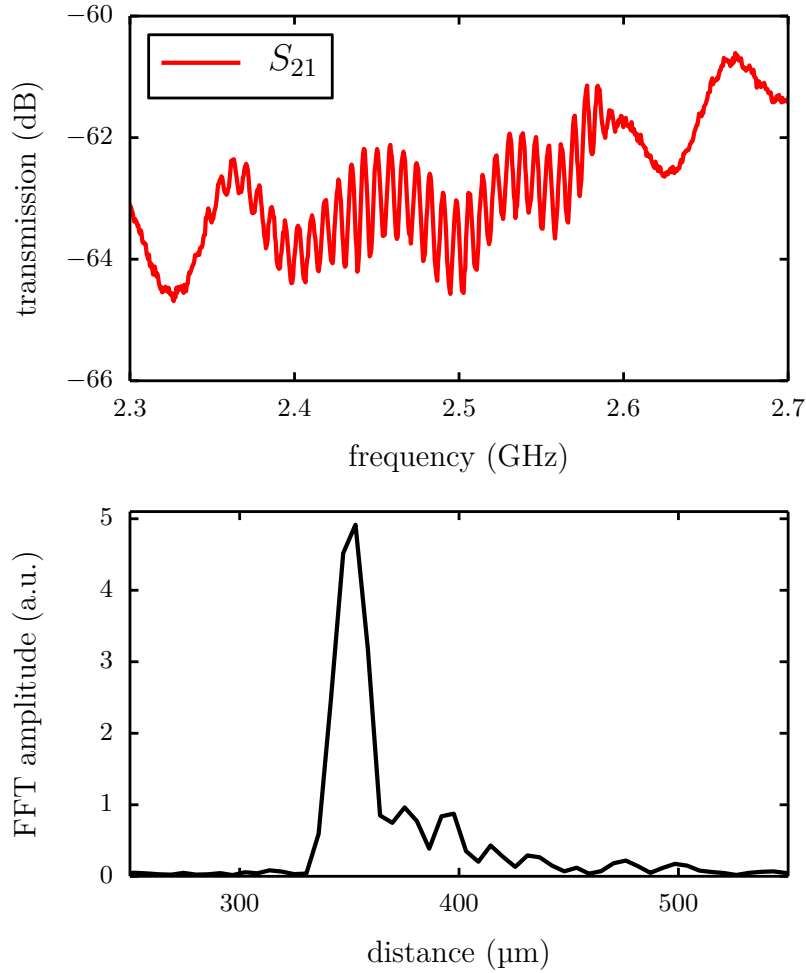


Figure 6.2: Transmission of two IDTs. In the top panel we depict the transmitted signal between two double finger IDT. The slow beating signal is due to line reflections in the measurement set-up whereas the fast oscillating signal is due to the IDT. The lower panel is the FFT of the top panel, taking into account the SAW velocity. From the FFT peak we can extract the distance of the IDT, which is in good agreement with the sample design. The actual distance between these two IDT, measured with SEM, was 300 μm and the discrepancy between the SEM and the FFT value can be understood from the simple fact that signal generation and reflection is not happening at the outermost fingers of the IDT, but rather inside the IDT structure.

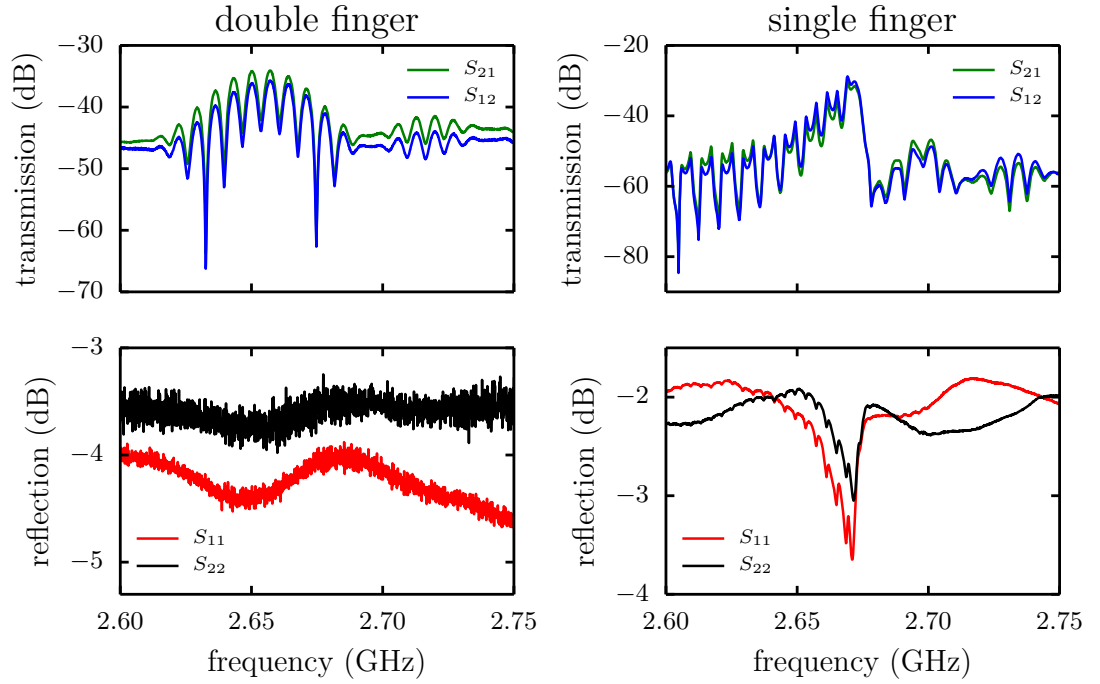


Figure 6.3: Transmission and reflection of double and single finger IDT. Top left panel shows the transmission of two double finger IDT at 300 K, whereas the bottom left panel shows the obtained reflection signal. The measurement set-up was calibrated prior to data acquisition. The transmission of two single finger IDT is shown in the top right panel whereas their respective reflection curves are in the bottom right panel. The resonance frequency of single finger IDT can be taken from the minimum dip in the reflected signal. The beatings are most probably due to reflections of the SAW on the sample.

6.2 SAW current measurement

As we have mentioned earlier, SAW can be used to transport acoustoelectric currents in a 2DEG [148, 149]. Before going into detail about the measurements, let us quickly turn to the measurement set-up. Generation of SAW is done by applying rf-power to the IDT at the resonance frequency, which we have determined in the previous measurement. The generation of acoustoelectric current is a bit more delicate than the measurement of the power spectrum of the IDT. Due to an imperfect impedance matching of the IDT rf-circuit, there are different points to consider. A part of the rf-signal is reflected back into the cable coming from the top of the cryostat, which is of no further interest. Another part of the rf-signal gets airborne [162] and couples capacitively to the 2DEG. This can lead to a parasitic current alongside to the acoustoelectric current of interest. In addition, this parasitic signal can be of the same order of magnitude as the SAW signal and can, in the worst case of an IDT with low conversion efficiency, completely overlay the measurement signal. In order to diminish this effect, we have installed a rf-shield on top of the sample holder as can be seen in figure 6.4. The image on the left displays the (empty) sample holder, which is screwed into the cold finger at the bottom part of the cryostat. The flexible rf-cables are used to connect to the female SMP connectors of the

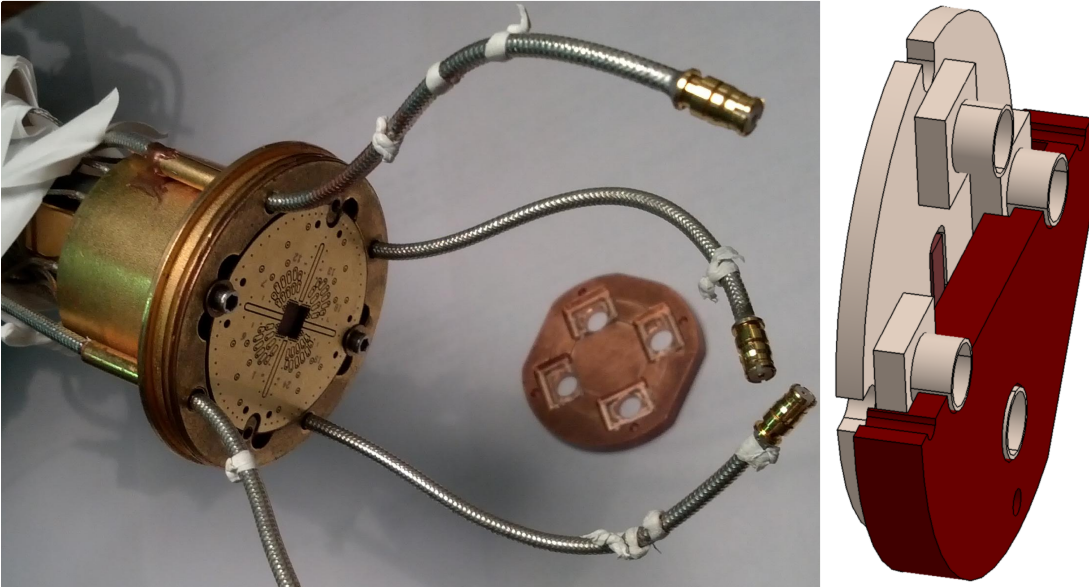


Figure 6.4: Sample holder rf-shielding. The left image shows the chip carrier, which is screwed into the cold finger at the bottom part of the cryostat. The rf-shield is made out of copper and can be seen in the background. The right image is a technical drawing with a cut of the rf-shield along the center axis. The shield has been placed as close as possible above the sample ($800\text{ }\mu\text{m}$) to capture the parasitic rf-signal which gets airborne at the IDT and does not contribute to the creation of SAW.

chip carrier, which can be seen in the technical drawing. A copper rf-shield has been constructed (background of left image), which can be screwed on top of the chip carrier as close as $800\text{ }\mu\text{m}$ above the sample. At the same time, the sample is embedded in a

hole in the center of the chip carrier to align its height with the height of the coplanar waveguides for the IDT. The right image shows a technical drawing of the rf-shield, which is cut along its center line for display purpose. We remark that the bonding wires (not displayed) must not touch the rf-shield for obvious reasons, which is a rather trivial task with a total number of 86 bondings per sample.

Despite the fact that our sample design is neither aimed nor optimized for the detection

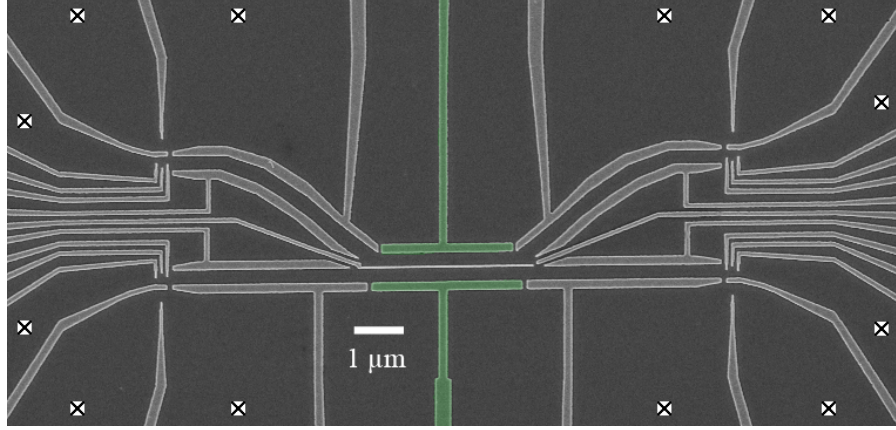


Figure 6.5: SAW current measurement device configuration. A SAW is sent from the left through a one-dimensional channel formed by the two green center gates, carrying an acoustoelectric current over the barrier. The respective bias between the two sides is set to zero, whereas the SAW induced current is recorded via a current amplifier connected to one of the ohmic contacts on the right side.

of quantized SAW currents, we can nevertheless use several gates to form a quasi one-dimensional channel over which the electrons can be transported in order to test the SAW generation. It is important to note that the one-dimensional channel has to be depleted to prevent normal current flow, however, the onset of the potential barrier that is formed must not exceed a certain slope in the direction of SAW propagation. In the limiting case of a step-like barrier it is easy to imagine that the electrons traveling in the SAW minima cannot maintain their position and are reflected back on arrival at the potential barrier. A smooth barrier is hence worthwhile and can be obtained by a clever choice of gates and experimental fine-tuning of the barrier. One possibility is to use the two green center gates of the structure as it is shown in figure 6.5, however other gate combinations are possible. We pinch the center gates of our structure and connect two opposed ohmic contacts, whereas we put their respective bias to zero. A train of SAW, induced by a double finger IDT, with a duty cycle of 1:100 at 5 MHz is sent on the quasi one-dimensional channel and the output current is recorded. The duty cycle is important in order to prevent heating effects of the 2DEG which can lead to a parasitic current that overlaps the signal of interest. In figure 6.6 we display the results of both, double finger (left panel) and single finger (right panel) IDT. The channel is pinched 30 mV below the pinch-off value. The pinch-off curves for both, single finger and double finger IDT tests, are displayed in the bottom panel of figure 6.7. In this curve, the upper and lower channel gate are pinched simultaneously. At low input power (red curves), the induced

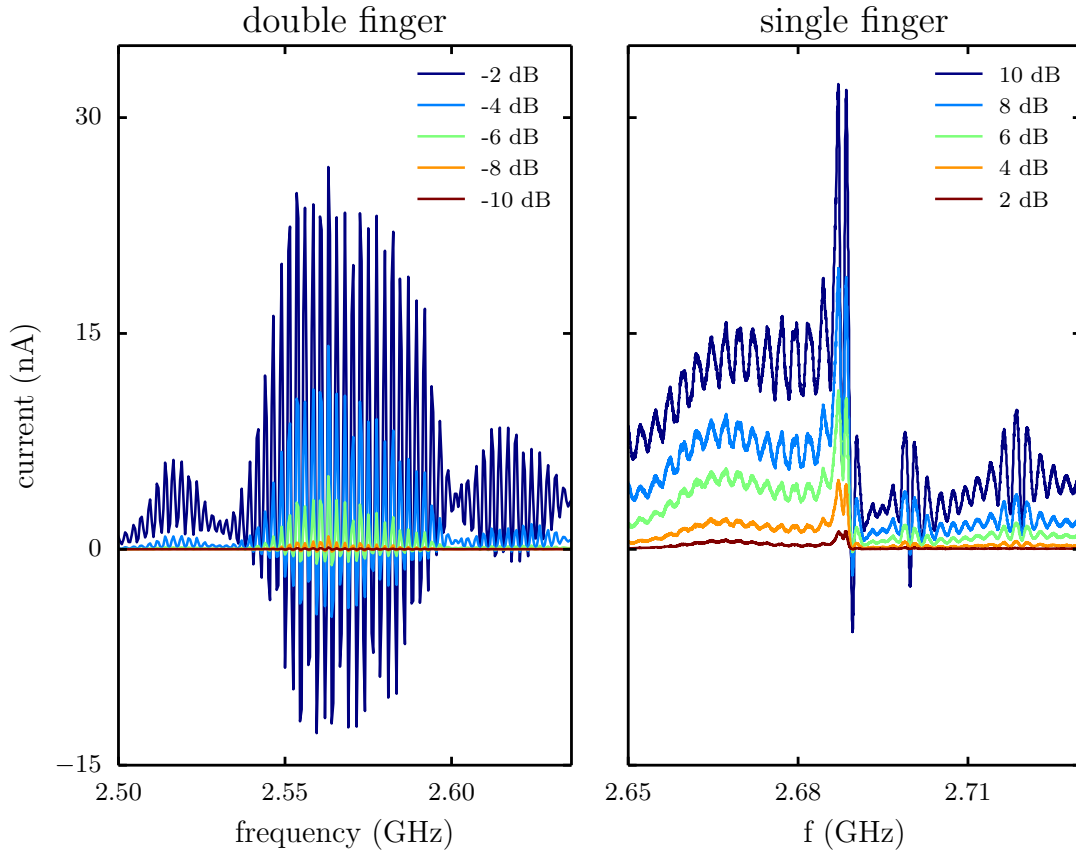


Figure 6.6: SAW current measurement. In both panels, the green gates of figure 6.5 are pinched just below their pinch-off value. Their respective pinch-off curves can be seen in the bottom panels of figure 6.7. The frequency of the SAW is swept at different input powers (color scale). No current is visible at low input power, whereas we find current peaks emerging at the resonance frequency with increasing power level.

SAW is too weak to transport acoustoelectric current across the one-dimensional channel. With increasing rf-power we find current peaks emerging at the resonance frequency of the SAW. We display five different input powers for both devices. At high rf-power, heating effects induce thermal currents, lifting the background of the measurement as can be seen in the blue curves, the SAW resonances are still nicely visible. This measurement allows to estimate the power dependence of the SAW on the current. It should be noted that from the power dependence one cannot directly deduce the amplitude of the SAW potential, since the absolute current value being transported depends strongly on the shape of the potential barrier of the one-dimensional channel. In order to test this behavior, we pinch the center channels at different values below its pinch-off value of -0.64 V (-0.79 V) for the double (single) finger IDT and plot this dependency in the top panel of figure 6.7. The data confirms our above statement. Both resonators show that for every 10 mV of potential rise, around 1 dBm of additional input power has to be

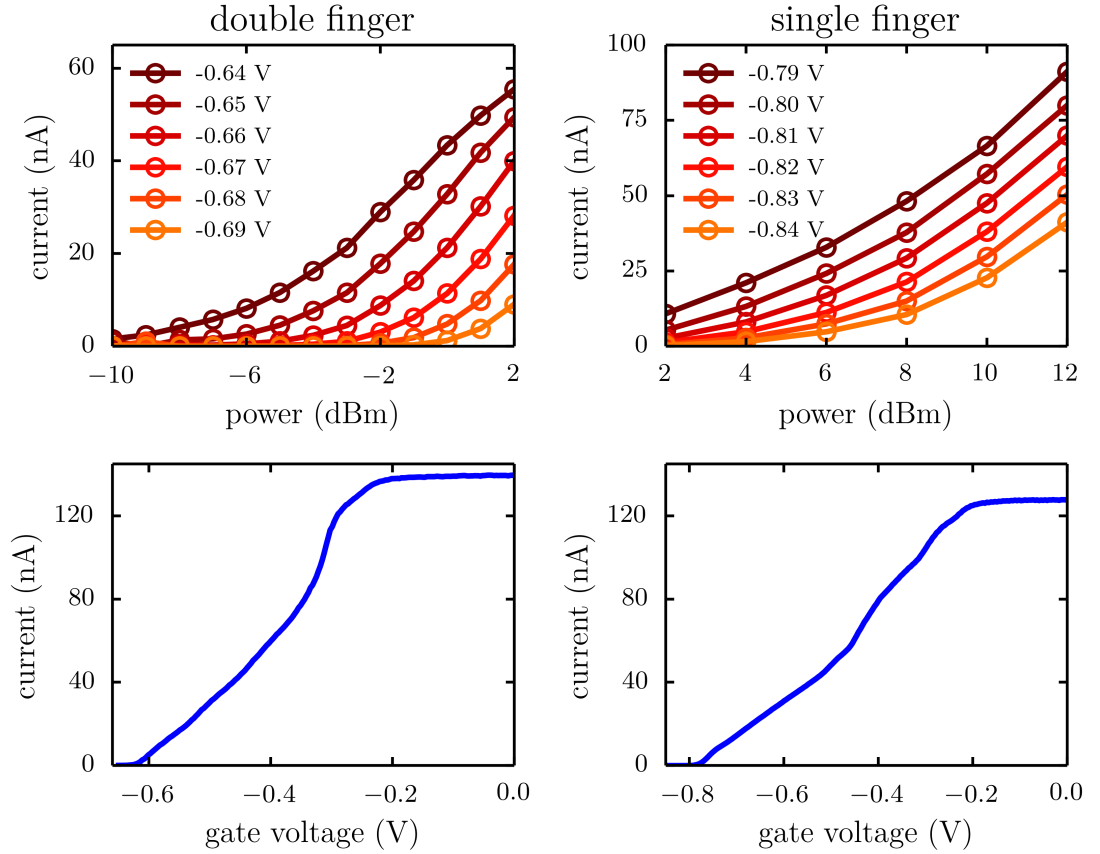


Figure 6.7: SAW current dependence on the pinch voltage. Top panel: acoustoelectric current at the resonance frequency as a function of input power at different pinch voltages. At zero rf-radiation, the gates are pinched at -0.64 V (-0.79 V) for the double (single) finger IDT as can be seen in the bottom left (right) panel. The higher the one-dimensional channel lies in energy, the more SAW amplitude and hence rf-power is needed to transport the current through the constriction.

applied to obtain similar current levels. A rough estimate in the approximately linear region between -4 dBm and 2 dBm (8 dBm and 12 dBm) suggests that an increase of the potential barrier by around 0.5 meV can be compensated by an input power increase of 1 dBm. The difference in applied rf-power between the single finger and the double finger IDT might be explained by the difference in the pinch-off values, leading to a difference in the potential barrier and therefore higher rf-power for the single finger IDT. In order to obtain a more precise and even absolute value of the amplitude of the SAW, we now make use of a quantum dot and study the influence of a SAW on its energy levels.

6.3 SAW influence on a quantum dot

A good way to estimate the amplitude of the oscillating electric field that is created by the SAW is to study its influence on the energy levels of a quantum dot [163]. In the

Coulomb blockade regime, transport through the quantum dot is only possible, if an energy level lies inside the source-drain bias window as can be seen in the first panel of figure 6.8. As an oscillating electric field is generated by continuous SAW radiation, the energy levels oscillate sinusoidally in time and the energy window through which the electrons can tunnel, spreads out as depicted in the second panel. Since the energy

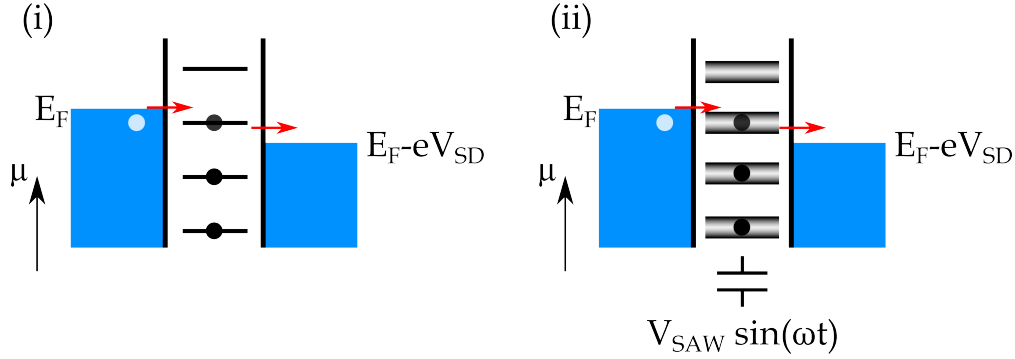


Figure 6.8: SAW induced energy level broadening. The electric potential generated by the SAW can be seen as a plunger gate voltage modulation of the chemical potential of the quantum dot. This broadens the conductance window and allows to measure and calibrate the amplitude of the generated oscillating electric field by measuring the conductance peaks depending on the SAW transducer power.

levels spend more time near the extrema of the oscillations, the conductance peak will split into two extrema, as indicated by the color gradient of the energy levels. Knowing the gate lever arm (α -factor) we can then directly determine the amplitude of the SAW potential from the splitting of the peaks at a given transducer power. The amplitude of the SAW induced electric field is related to the transducer input power via the relation

$$A_{p-p}[eV] = \frac{2}{\alpha} \times 10^{\frac{P[dBm] - P_0}{20}}. \quad (6.1)$$

A_{p-p} is the peak-peak amplitude of the SAW potential, α the gate lever arm, P the incident power of the transducer and P_0 a fit parameter accounting for all power losses. We plot the results of the double (single) IDT in the top (bottom) right panel of figure 6.9. The top (bottom) left panels shows the Coulomb peaks for the double (single) finger IDT of the used quantum dots, i.e. vertical cuts of the color plots at -30 dBm. The peak broadening is limited by temperature at this input power. For the quantum dot of the double finger IDT, three Coulomb peaks are clearly visible, the position of a forth peak at a gate voltage of around -670 mV is faint. Due to the size of the quantum dot used together with the single finger IDT, only one Coulomb peak could be observed. The right panels of figure 6.9 show the power dependence of these peaks. At low input power (-30 dBm) no peak broadening is visible, whereas the splitting becomes clearly resolvable around -20 dBm in both cases. The dotted lines are fits making use of equation 6.1. The negative current values of the double finger IDT are not completely understood and associated with parasitic effects due to high rf-power and hence of no further interest. The crossings of the dotted lines give a first good value for SAW potential, since at these

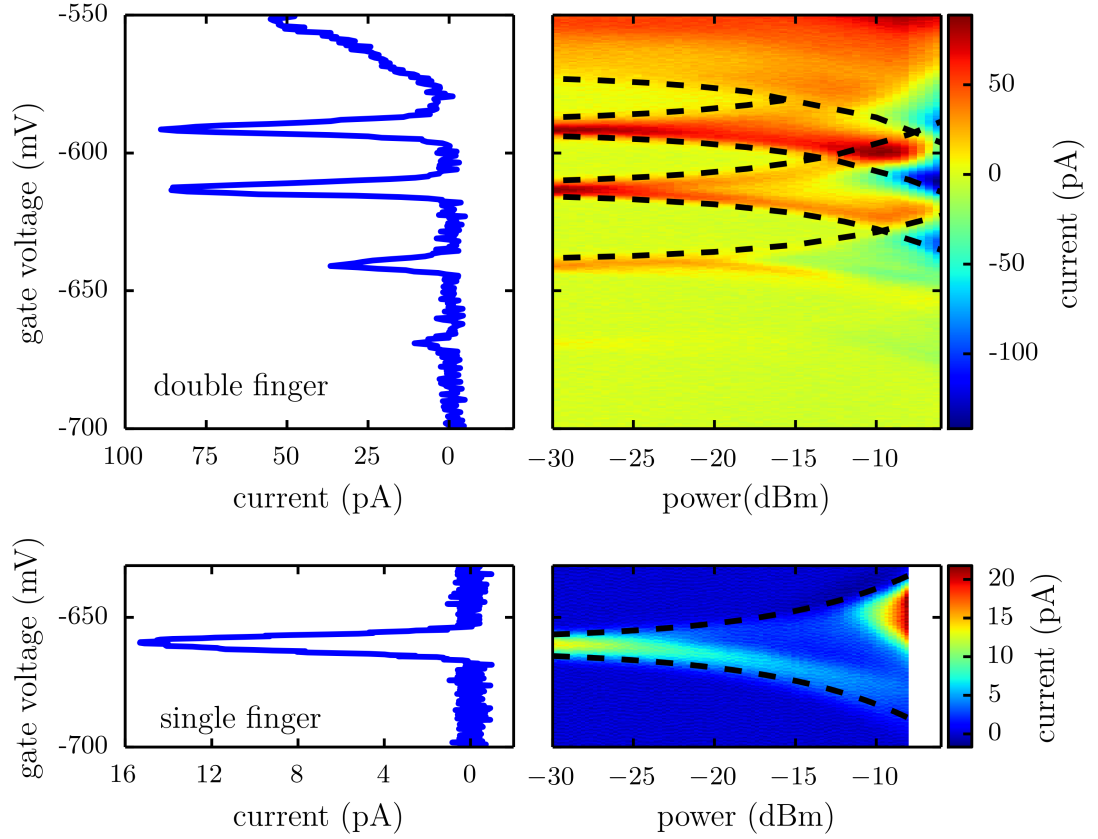


Figure 6.9: SAW induced Coulomb peak splitting. Top (bottom) left panel: Coulomb peaks of the quantum dots used for the double (single) finger IDT. These vertical cuts are taken at -30 dBm. Top (bottom) right panel: Coulomb peak splitting as a function of applied SAW power at the resonance frequency for a double (single) finger IDT. Three Coulomb peaks are clearly visible for the double finger IDT. Due to the size of the quantum dot, only one Coulomb peak is visible for the single finger IDT. In both cases, the peaks start splitting around -20 dBm. The dotted lines are fits following equation 6.1. At the intersections of the split Coulomb peaks, the SAW potential has the same amplitude as the charging energy between the quantum dot levels.

points, two neighboring levels are broadened such that they overlap and their energy difference is hence the amplitude of the induced SAW potential. For simplicity, we plot the obtained data from all tested IDT in figure 6.10. For comparison, we also depict the performance of the IDT used in [38]. We find that single finger IDT and double finger IDT have similar performance in terms of created SAW potential.

Since single finger IDT are simpler to fabricate, they seem to be the better choice, however we note, that as soon as the SAW rise time is of importance, double finger IDT are the better choice due to their larger bandwidth. The diminished internal reflections of the double finger IDT also limit heating effects of the sample. Concerning our device fabrication, we have decided to pursue both approaches, since the yield of

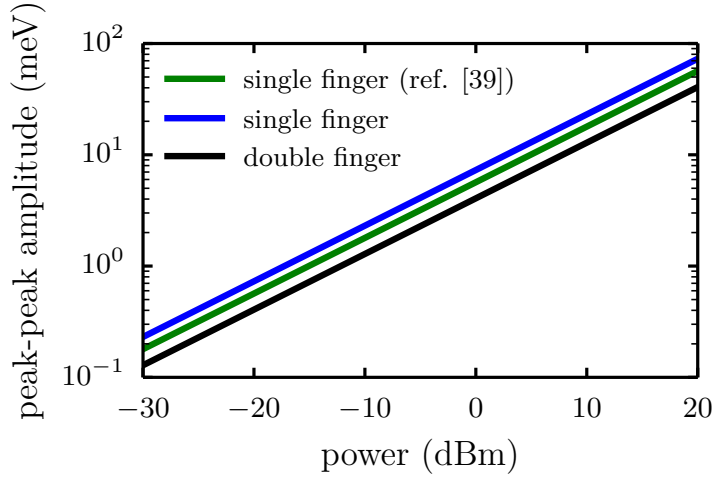


Figure 6.10: Comparison of single and double finger IDT. Extracted fits following equation 6.1 from the Coulomb peak splitting of figure 6.9 for single and double finger IDT. We also display the performance of the IDT from [38] for comparison. Single and double finger IDT show a similar performance in terms of SAW potential amplitude.

both fabrication processes exceeds 95% for most fabrication runs. For convenience we also plot the frequency dependence of the double (single) finger Coulomb peak at around -640 mV (-660 mV) in the left (right) bottom panel of figure 6.11 at a fixed input power of -20 dBm. The other Coulomb peaks show a similar dependence and are hence omitted. In the top panels, we display a horizontal cut following the dotted lines in the lower panels. The Coulomb peak broadenings resemble well and confirm the SAW current measurements in the one-dimensional channel (figure 6.6). The resonances inside the peak are interferences with the reflected SAW from the second IDT on the sample. We could further analyze this behavior by taking the FFT of the obtained frequency spectrum and multiplying with the SAW velocity, similar to our argumentation in section 6.1.

So far we have shown three complimentary methods to characterize the IDT and to analyze the created SAW by extracting the SAW amplitude as a function of the applied SAW power. Let us now investigate the next ingredient of the single electron beam-splitter and introduce single electron charge sensing with the aid of a quantum point contact.

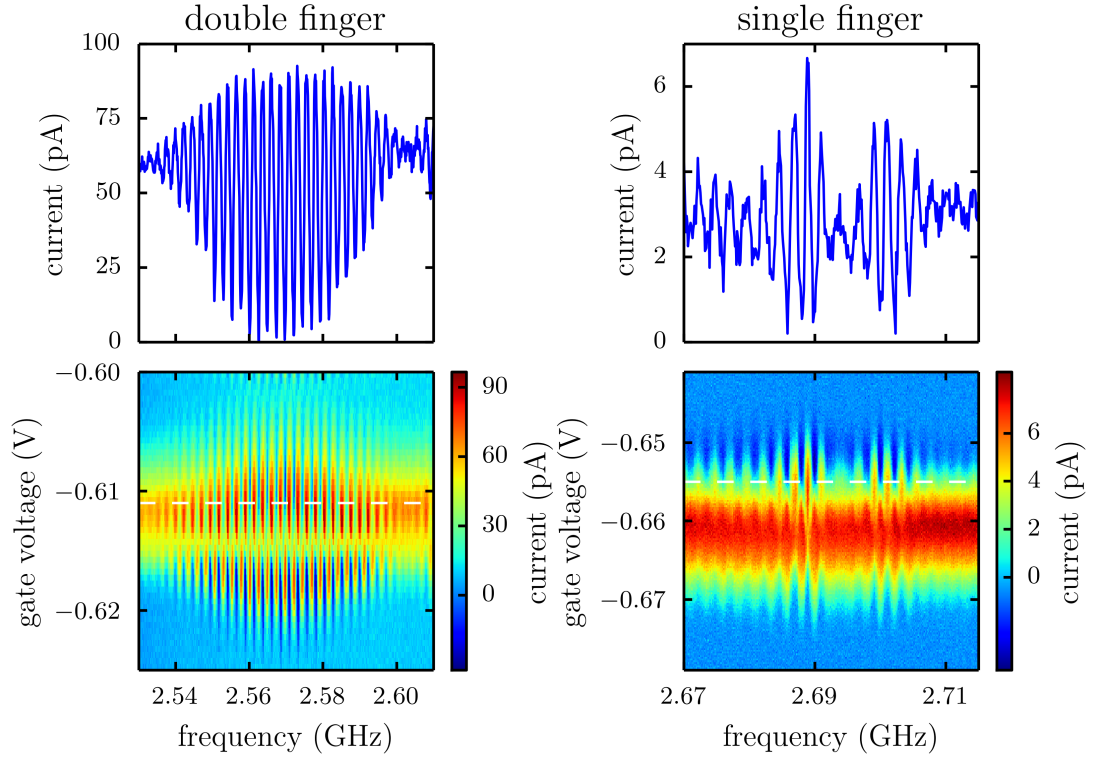


Figure 6.11: Frequency dependence of SAW induced Coulomb peak splitting. Bottom panel: Coulomb peak splitting of a double (left) and single (right) finger IDT around the resonance frequency at a constant rf-power of -20 dBm. Off-resonance, no splitting appears. While sweeping through the resonance, the Coulomb peak is split confirming the data from the SAW current measurement from figure 6.6. The top panels are horizontal cuts following the dotted lines. The interference pattern is due to interference of the SAW being reflected at the second IDT on the sample.

6.4 Stability diagrams

Having determined the precise frequency of our SAW and characterized the SAW amplitude, we can now turn to the characterization of the quantum dots. For this purpose, we will first show how the quantum point contact, which we have discussed in section 3.3, can serve as a single electron charge sensor [16–18]. In figure 6.12 we display a typical gate configuration to form a quantum dot in the few electron regime (red gates), which is coupled to a quantum point contact in close proximity (yellow gate). The quantum point contact forms a short one-dimensional constriction for the electrons. Close to its pinch-off value, the quantum point contact is highly sensitive to changes in the electrostatic environment, i.e. the presence or absence of a single electron in the neighboring quantum dot. We depict one measurement curve in figure 6.13. In this specific case, an impurity is close to the quantum point charge sensor, leading to Fabry-Perot resonances. This enhances the QPC sensitivity, since a small change in voltage, leads to a big alteration in current. The change in current through this constriction is on the order of several hundred pA,

when an electron is leaving or entering the quantum dot [39]. As an example, we display the current through the QPC as a function of the gate V_R from figure 6.12 in the few electron regime in figure 6.14.

As this gate voltage is swept to more negative values, the size of the quantum dot is

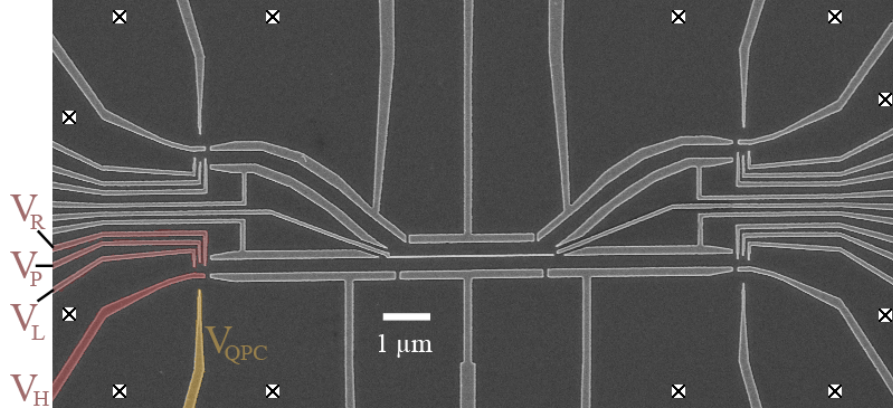


Figure 6.12: Quantum dot with quantum point contact charge sensor. Typical gate configuration of a quantum dot (red gates) coupled to a quantum point contact (QPC) (yellow gate). The current which is passing through the quantum point contact constriction is sensitive to a change in the electron number of the adjacent quantum dot and can hence be used as a charge sensor.

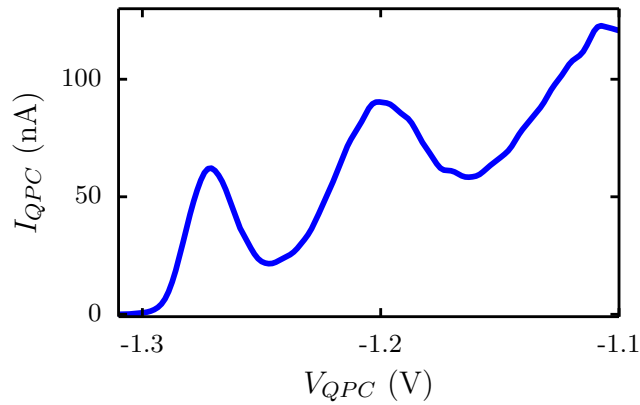


Figure 6.13: Quantum point contact charge sensor pinch-off. Close to its pinch-off, the quantum point contact is highly sensitive to changes in the electrostatic environment and can hence be used as a charge sensor. In this particular case, an impurity is close to the QPC, leading to Fabry-Perot resonances, enhancing its sensitivity, though limiting its working range.

shrinking and electrons are pushed out into the reservoir. Such an electron tunneling event goes along with a diminished electrostatic environment of the quantum point contact and leads hence to an increase of the current through the QPC. In figure 6.14 we display six events of electrons leaving the quantum dot, however we postpone to comment on the total number of electrons at this stage. The background which is decreasing linearly

with a more negative gate voltage can simply be explained by the increase of the gate potential which has a non-negligible influence on the QPC width. Since this background does not contain any information about the actual number of electrons, we derive the measured current with respect to the applied gate voltage leading to the bottom panel of figure 6.14. We can now use this charge sensing technique to characterize the quantum dots in greater detail.

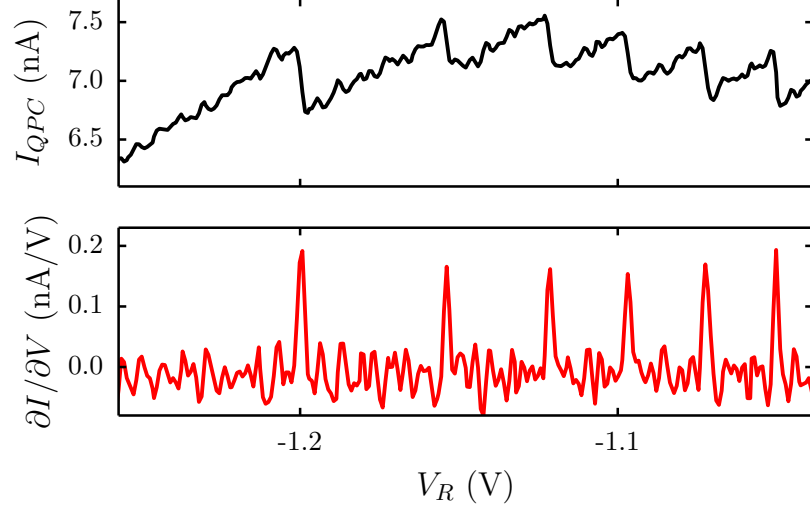


Figure 6.14: Quantum point contact charge sensor. When sweeping the gate V_R of the quantum dot (see figure 6.12 for comparison) to more negative values, electrons leave the quantum dot towards the reservoir, which can be seen as jumps in the current through the quantum point contact in the top panel. Removing an electron from the quantum dot lowers the electrostatic environment of the QPC and the constriction widens, hence the current through the constriction increases. The background is due to the influence of the gate voltage on the QPC. For convenience, we derive the signal with respect to the gate voltage to remove this background as displayed in the bottom panel.

6.5 Single electron regime and metastable states

We now turn to the characterization of the four different quantum dots of our structure. We concentrate on the quantum dot, which is highlighted in figure 6.12. Due to the device symmetry, all dots show similar performance, and their separate discussion can be omitted. For tuning purpose, we set a fixed gate voltage on the horizontal gate V_H and set the plunger gate V_P to zero. This gate is not obligatory to form the quantum dot, however it is of avail for tuning the chemical potential of the quantum dot or applying short ns-pulses to the structure. We obtain a so-called stability diagram when sweeping V_L (see figure 6.12) and stepping V_R . A typical diagram is shown in figure 6.15. Each blue line corresponds to the derivative of a current jump, analog to what we have presented above in figure 6.14. At very negative voltages on both gates, we observe a region without additional events (bottom left), which we can attribute to an empty quantum dot. If we now decrease V_R at a fixed V_L of say $V_L = -1.4$ V, we can count the number electrons

inside the quantum dot starting from zero as it is shown in figure 6.15. In this case, all blue lines are parallel, since we are working with a single quantum dot with only one connection to the reservoir. The situation gets more complex when increasing the number of coupled quantum dots [164, 165]. An interesting feature now is the onset of statistical

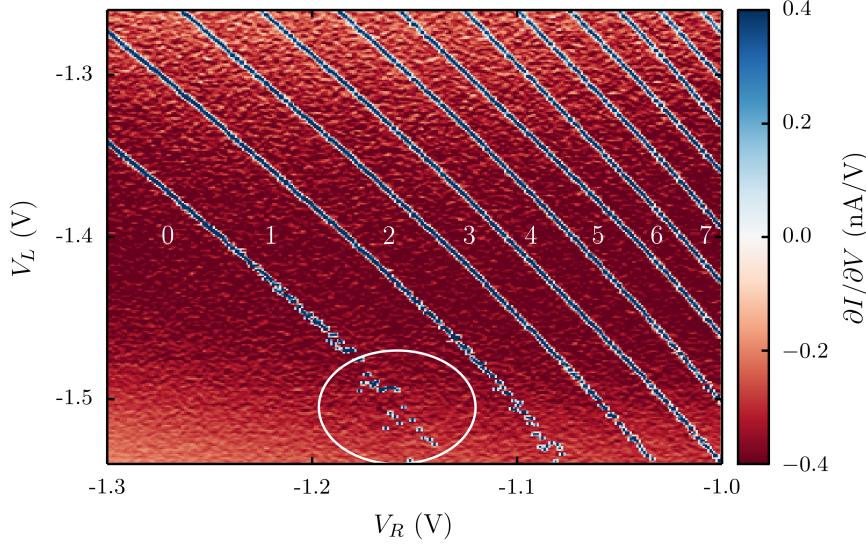


Figure 6.15: Stability diagram of a quantum dot. In the bottom left region, at very negative gate voltages, the quantum dot is empty. Going to more positive voltages, we cross the blue lines and fill up the quantum dot one by one starting from zero electrons. The white circle now indicates, where statistical tunneling events can be observed. This is due to the fact that the tunnel rate of the barrier between the quantum dot and the reservoir gets comparable to the measurement time, which is of the order of kHz.

events, indicated by the white circle in figure 6.15. At a high negative voltage of V_L , the barrier towards the reservoir gets thicker and hence its associated tunneling time larger. As this time gets comparable with or larger than the time it takes to measure the QPC, which is of the order of ms, the statistical nature of the tunneling process can be observed. Obviously, the stronger the barrier, the longer the electrons stay in the quantum dot before tunneling out. For further investigation, we have a closer look on the sweep parameters. In the left panel of figure 6.16, we display the measurement of the quantum dot in the same experimental regime, however the gate voltage configuration differs slightly. The sweep is conducted from more positive values of V_L to more negative values of V_L , whereas V_R is stepped after each sweep. The sweep direction is indicated by the black arrow. For comparison, this is the same kind of sweep as we have shown beforehand in figure 6.15. In the left panel, we find again statistical events due to the slow enough barrier towards the reservoir. The thicker the barrier, the longer the electron life-time, the more shifted are the statistical events towards negative values of V_L . Note, that these events are not exclusive for a quantum dot population of one electron only. After each sweep, the gate voltage V_L is initialized with the maximum speed of the DACs, which is 2 μ s. At the end of each sweep, the electrons have tunneled out of the

quantum dot and the quantum dot is initialized in the top region at low negative values of V_L , where the barrier towards the reservoir is thin and electrons can enter. We now change the sweep direction of the quantum dot and show the resulting measurement in the right panel of figure 6.16. Here, V_L is swept to more positive values, indicated by the black arrow. First, we remark that the color of the lines on the top of the figure are inverted. Blue lines correspond to electrons leaving the quantum dot, whereas red lines correspond to electrons entering the quantum dot. In the left (right) panel, the quantum dot is loaded (empty) at the beginning of the sweep and electrons are leaving (entering) the quantum dot when pushing V_L to more negative (positive) values. The color of the background has also changed, which can be understood by looking again at figure 6.14. When pushing the gate voltage more positive (negative), the background has a positive (negative) slope, leading after derivation to a positive (negative) constant, resulting in the color blue (red). Secondly, we point out that the endpoint of a sweep is

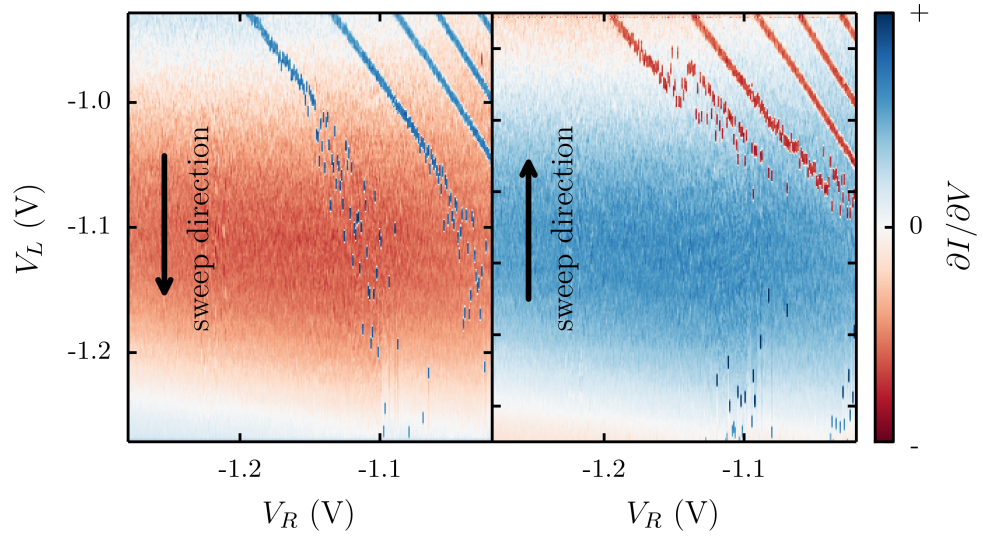


Figure 6.16: The sweep direction influences the stability-diagram due to a different initialization of the quantum dot at the beginning of the sweep. When sweeping the left gate to more negative values, the statistical events occur when the time to tunnel to the reservoir is comparable to the measurement time as discussed above. At the end of each sweep, the quantum dot is empty. On the contrary, when sweeping the left gate to more positive value, the quantum dot is filled with electrons at the end of each sweep, the number depending on the right gate voltage. When the barrier towards the reservoir is slow enough, the initialization of the sweep, which is done in $2\mu\text{s}$ allows to keep the electrons in a metastable position. Such electrons are leaving the quantum dot when lowering again the left gate voltage as can be seen as blue dots in the bottom right part of the figure.

different depending on the sweep direction. When sweeping to more positive values (right panel), we end up on the top of the figure and starting from $V_R = -1.2\text{ V}$, at least one electron is loaded at the end of the sweep. The reinitialization pulse of $2\mu\text{s}$ now brings the quantum dot, along with this loaded electron(s) into a metastable state, i.e. as soon as the barrier towards the reservoir gets thick enough, the electrons are being kept inside

the quantum dot even after this pulse. Such metastable states are characterized by being strongly disconnected from the reservoirs and sitting above the Fermi energy in a local minimum of the potential landscape. In figure 6.16 we find that around $V_R = -1.1$ V, the electrons stay inside the dot until they tunnel out (dark blue events on the bottom) when lowering V_L during the sweep. At a voltage of $V_L \approx -1.0$ V, the electrons can re-enter the quantum dot and the red line is shifted to more positive values due to the barrier thickness. We have now found a way, to load electrons into the quantum dot and to move them into a position high above the Fermi energy into a metastable state. Instead of only using the sweep-initialization pulse of the DAC, we can now engineer a time-resolved loading procedure with gate pulses and study the electron in different positions above the Fermi energy. This is the favorable technique to bring the electron close to the one-dimensional channel, into which we would like to inject the electrons later on.

In order to observe the electrons leaving the quantum dots induced by SAW, we have to be able to control the electron life-time. For this purpose, let us now turn to time resolved measurements and show how we can use voltage pulses to position the quantum dot on the charge stability diagram and how to control the life-time of the electrons in the metastable quantum dot. To ascertain that the quantum dot is empty, we begin our sequence in A, as shown in figure 6.17. The quantum dot is then loaded by moving the left gate to B and allowing an electron to enter. We then move to the metastable position C and wait. We measure the current while moving the gate V_L as it is depicted in figure 6.18. From A to B, the measured current increases, since we are lowering

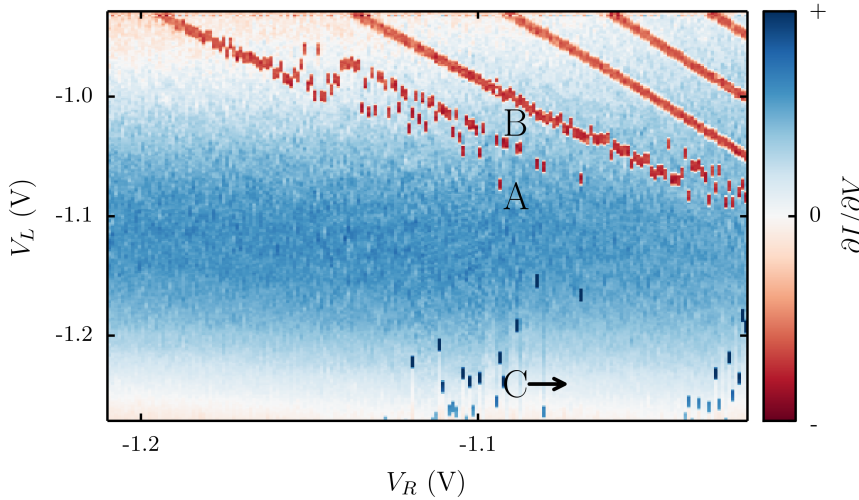


Figure 6.17: Electron loading sequence. We empty the quantum dot at A, pulse the gate V_L to B to load one electron and then push it into the metastable state C. The arrow indicates the step that has been used in figure 6.19 to control the electron life-time.

the gate voltage V_L , which influences and opens the adjacent QPC. An electron enters the quantum dot at position B, however we do not resolve the entering process, since the barrier at this point is too fast for our measurement set-up. When moving from

B to C, the total current inside the QPC drops, since V_L is more negative. The QPC has been adapted prior to this measurement to an optimal working point at position C to have optimal resolution when the electrons are leaving the quantum dot in the metastable state. We wait 500 ms in position C in order to study the electron life-time in this position. In figure 6.18, we show several of such time resolved measurement

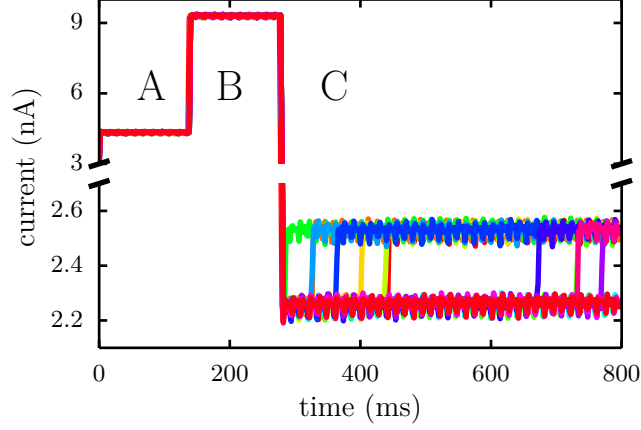


Figure 6.18: Electron escape in the metastable state. The quantum dot is initialized with zero electrons in position A (see figure 6.17 for comparison). The gate V_L is then pushed to position B to load an electron, however this loading process is happening at a timescale that cannot be resolved by our measurement set-up. The quantum dot is then pushed into the metastable position C, where we wait 500 ms in order to observe the electrons that are leaving the quantum dot. A current level of 2.2 nA corresponds to one loaded electron, while a current level of 2.5 nA corresponds to zero electrons.

curves. The value of 2.2 nA corresponds to an electron being inside the quantum dot in the metastable state, a current level of 2.5 nA indicates that the electron has left. For the green curve, the electron has either left the quantum dot while being brought into the metastable position or on a timescale smaller than one measurement point (3 ms). For all other traces, we can measure the time that the electron stays in the metastable position and averaging over multiple of such traces will give us an idea about the average life-time of the electron. To further investigate this behavior, we add an additional gate movement to this gate movement sequence. In addition to the gate movement of V_L from points A to B to C, which we have conducted in figure 6.18, we add an additional movement of V_R as indicated by the black arrow in figure 6.17. This allows to change the size of the quantum dot and hence the electron life-time. We record 100 of such traces and plot their averaged curves for different values of the gate V_R in figure 6.19. The dotted lines correspond to an exponential fit, from which we get the average life-time of the electrons, which is depicted in the bottom panel of this figure. The color code in the bottom panel corresponds to the averaged traces in the top panel. In this measurement we achieve electron life-times up to 200 ms, however the limits of the life-time of metastable charge states have not been investigated further.

So far we have shown, how to isolate a single electron from its environment with the aid

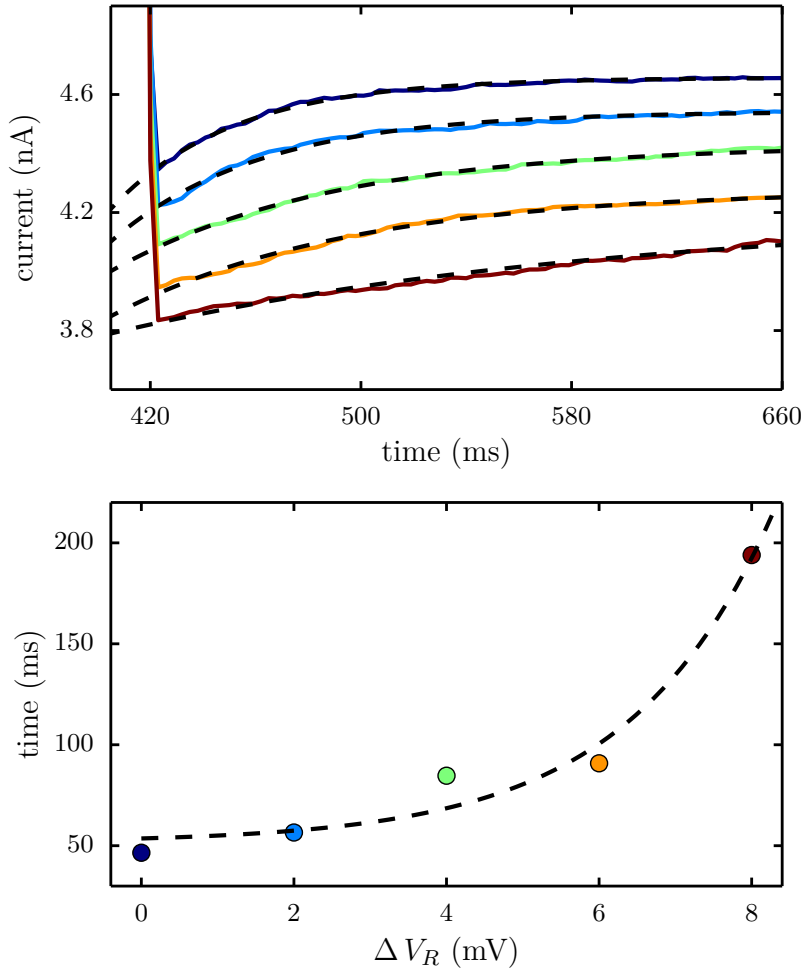


Figure 6.19: Electron life-time in the metastable state. The life-time can be obtained by averaging over multiple single electron escape events, in this case 100. The dotted lines are exponential fits, whereas the average life-time for different values of the right quantum dot gate is shown in the bottom panel of this figure.

of a quantum dot and how to control the life-time of an electron at the time scales of our measurements in a metastable position. The metastable position now is important since it brings the electron close to the one-dimensional channel. It is now possible to send a SAW in order to pick-up the electron and to transfer it through the one-dimensional channel into the interaction region of the sample and to catch it in one of the two reception quantum dots on the other side. For this purpose, we repeat the above gate movement sequence and put the electron into a metastable state with a life-time of 200 ms. In addition, we send a SAW at the resonance frequency of 2.616 GHz with an amplitude of 26 dBm when the electrons are in the metastable state close to the one-dimensional channel. The measurement result is depicted in figure 6.20. Multiple traces are displayed

on the horizontal axis of this figure. The orange color represents the initialization with zero electrons (position A of figure 6.17), whereas the red color corresponds to the current level of one loaded electron (position B). The metastable state with a life-time of 200 ms is in blue. We remark, that not all electrons could be kept during the preparation of the metastable state, as we have discussed above. These events already have green color at a time of 360 ms. Other events could be loaded efficiently (blue color at 360 ms), however the electron have escaped the metastable state, before the SAW was sent. The SAW is sent at 420 ms. The number of electrons of all remaining metastable quantum dot changes to zero when sending the SAW. This clearly shows, that the electrons have left their metastable state induced by SAW. The next step now is to prepare the reception quantum dots in a position to stop the electrons that are propagating on the SAW, however the design of the first prototype did not allow for such a measurement as we will see in the following section.

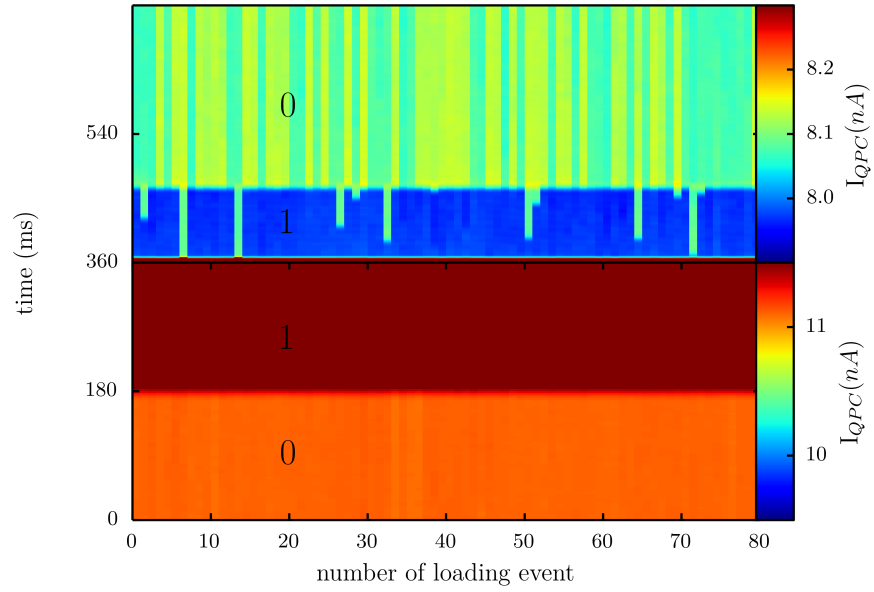


Figure 6.20: Electron sending efficiency. The x-axis shows different events. The quantum dot is initialized with zero electrons (orange, position A in figure 6.17). One electron is loaded (red) and pushed into a metastable state (blue) with a life-time of around 200 ms. A SAW is sent at 420 ms, which empties the quantum dot reliably.

6.6 Comparison and outlook

The techniques, which we have presented in the last section have been verified, optimized and are being standardized. It has been possible to test all tools and ingredients throughout this thesis which are necessary to realize the single electron beam-splitter, however the device fabrication did not work in favor to combine all concepts in one working device. The measurement curve which should have been observed for electron transfer is the following: after preparing one injection quantum dot on the left with one electron in a metastable position, we send a SAW burst of several hundred nanoseconds. Looking

at the time trace of the injection quantum dot, we observe that the electron is leaving the dot simultaneously with the SAW burst as it is depicted in figure 6.21. The black

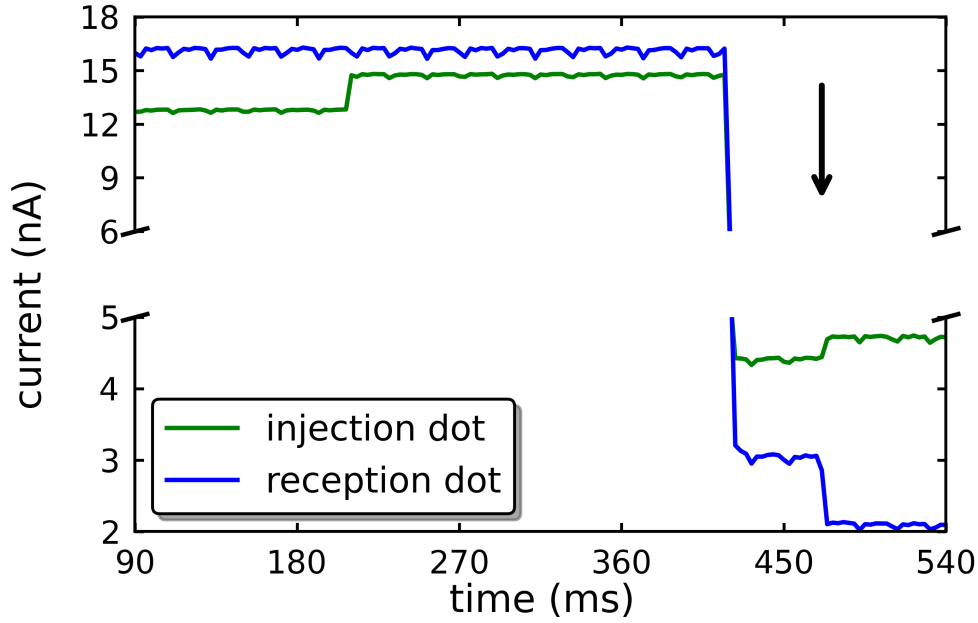


Figure 6.21: Electron transfer. The injection quantum dot is prepared with one electron in a metastable position close to the one-dimensional channel. The electron escapes the dot mediated by the SAW burst and is captured in the reception dot. This is the typical curve one expects for single electron transfer mediated by surface acoustic waves.

arrow indicates the moment of the SAW burst. In the same time, we have prepared the reception quantum dot with zero electrons and raised its right barrier in order to catch the electron that is traveling on the SAW. The data which should be obtained looks exactly like the blue curve in figure 6.21, where an electron is entering one reception quantum dot at the moment of the SAW burst, however this figure does not contain the complete picture. After tens of thousands of sending events, only one single electron could be received in one of the reception dots, and this curve could never be reproduced. The caught electron is most likely an electron, which has been stuck somewhere in the channel and not the electron which had been injected from the left quantum dot.

The rf-power needed to empty the injection quantum dot has been as high as 26 dBm and since no electron could be transferred, we concluded that this first prototype did not fulfill the necessary requirements for the single electron transfer. As quickly mentioned above, one difficulty has been the performance of its double finger IDT. In support of this argument, we depict the representative transmission spectrum of this particular IDT in the left panel of figure 6.22 and confront it with a good IDT in the right panel. Both VNA measurements have been taken in the same experimental conditions at 4.2 K and we clearly see that the improved IDT (right panel) has a ten times higher transmission signal than the IDT from the first sample run. This IDT performance has led to a time

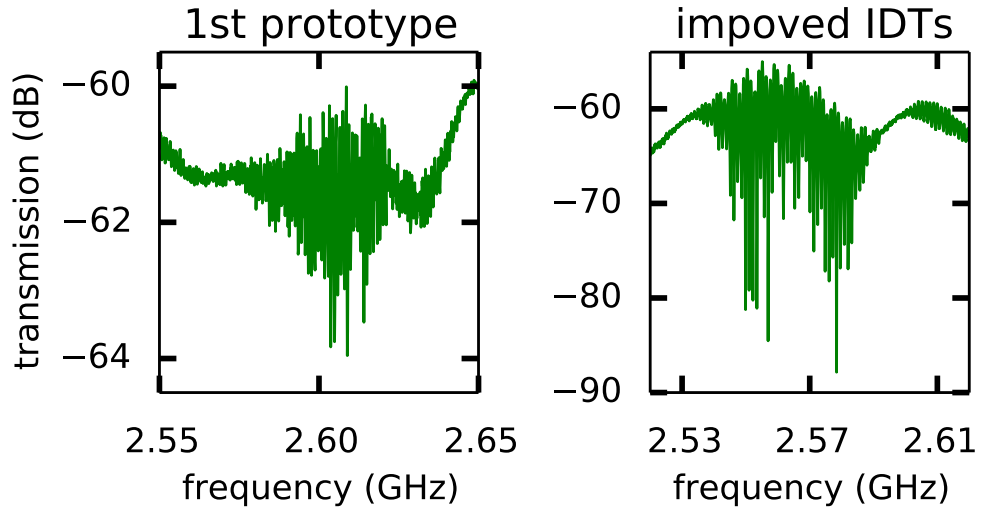


Figure 6.22: Comparison of the performance of the double finger IDT from the first prototype (left) panel to the improved IDT. The improved IDT shows a ten times higher transmission signal. This poor performance of the IDT of the first prototype led to a big experimental effort to improve their fabrication procedure.

consuming experimental effort to improve the IDT design and fabrication process, as we have discussed in this beginning of this chapter.

Another issue of the first prototype had been the question if the electron injection into the angled channel works as good as what has been reported with straight channels [38, 102]. To answer this question, but also in the spirit for future device structure design, we have developed a new and powerful tool to calculate potential landscapes on-the-fly and in the following we will make use of the developed tools to have a closer look at this particular problem. In figure 6.23(b) we plot the calculated potential landscape of the first prototype, whereas we show the corresponding SEM image of the surface gates in figure 6.23(a).

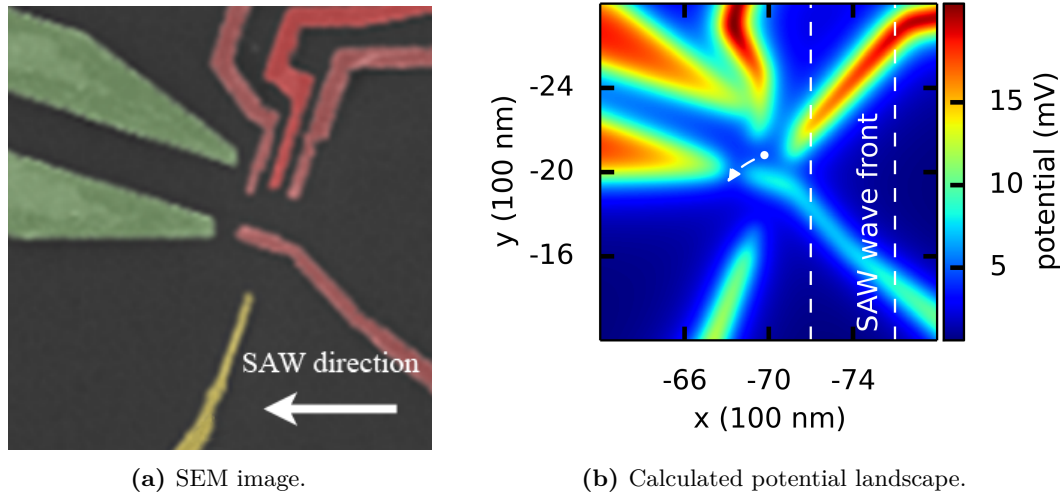


Figure 6.23: Injection quantum dot of the first prototype. Based on the fabricated gate structure (left panel: false colour SEM image), we have calculated the electrostatic potential landscape seen by the electrons 90 nm below the surface (right panel). The calculation indicates an unwanted tunnel barrier towards the reservoir between the lower channel gate (green) and the quasi horizontal quantum dot gate (red), giving a possible explanation, why electron transfer in this structure had not been possible. The same potential is depicted in greater detail in figure 6.24.

Different gate voltage configurations have been tested, however one feature in the potential landscape could not be suppressed. In between the lower left channel gate (green) and the horizontal quantum dot gate (red), there seems to be a small opening, which in principle could allow electrons to exit the quantum dot into the reservoirs. The electron is represented as a white dot in the potential minimum formed by the gates, its possible escape path is indicated by the white arrow, the SAW wave front is shown incoming from the right side of the structure. To get a better view on this effect, we display the calculated potential differently in figure 6.24. The SAW propagation direction follows precisely the direction of the blue potential lines, the wave front is indicated by the parallel black lines. The electron (black dot), while being dragged inside a SAW minimum first sees the rise of the potential barrier due to the lower channel gate. Instead of taking the red path towards the one-dimensional channel, this opening provides a more favorable path (black arrow), which lies lower in energy and allows the electron to escape towards the reservoir. This argumentation line is based purely on numerical calculations, however it provides a possible explanation, why the electrons in the first prototype could never be received, however it was possible to empty the first quantum dot induced by SAW pulses (see figure 6.20 for comparison).

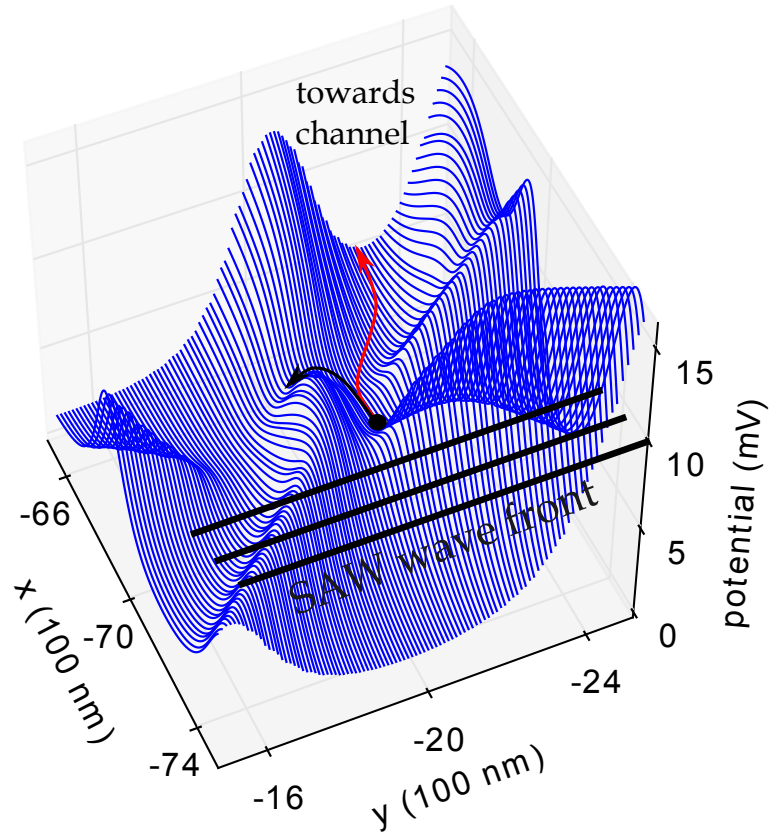


Figure 6.24: Potential of the injection quantum dot of the first prototype in 3D. Three dimensional view of the injection region of the first prototype. The SAW wave front is shown as black parallel lines, i.e. the SAW propagation follows the direction of the blue lines. An electron sitting in the potential minimum in the center of the figure, which is about to tunnel into the moving quantum dots from the SAW, faces the potential rise of the lower left channel gate. This potential rise most probably pushes the electron to leave the structure via the reservoir to left (black arrow) instead of following the channel on the right (red arrow).

This problem has led to the development of the second prototype, which solves the issue of a non-straight injection. Let us have a closer look at the potential landscape of the second prototype, which is displayed in figure 6.25. The left panel shows a SEM image of the gate structure, whereas the right panel shows the calculated potential landscape. The electron sits in the potential minimum in the center of the structure, indicated by the white dot in the left panel. The SAW is arriving from the right. To get a better view on the potential landscape, we also show a three dimensional view in figure 6.26. In this figure, the electron is represented as a black dot. The transition into the channel is smooth compared to the potential landscape presented for the angled injection. Although a similar dip in the potential landscape between the channel gate and the horizontal quantum dot gate is observed, the electron will already have passed this *hole* and will be protected by the confinement potential of the channel, without having the possibility to escape into the reservoir. Although the argumentation line presented above is purely based on numerical simulations and geometrical considerations, it is clear that an electron injection parallel with the SAW propagation direction is the favorable choice of injection.

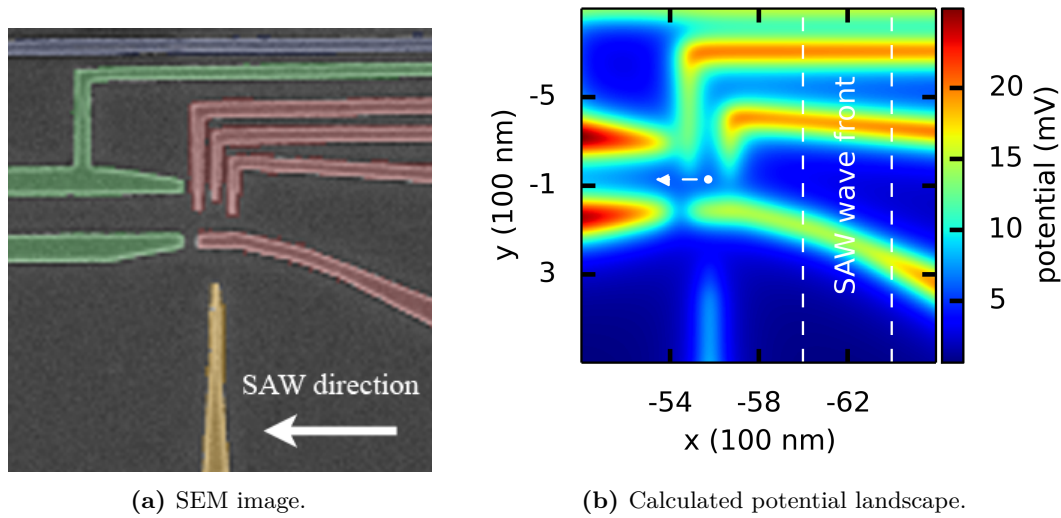


Figure 6.25: Injection quantum dot of the second prototype. Based on the fabricated gate structure (left panel: false colour SEM image), we have calculated the electrostatic potential landscape seen by the electrons 90 nm below the surface (right panel). Compared to the angled electron injection, a straight channel allows to inject the electron into the one-dimensional channel. The same potential is depicted in greater detail in figure 6.26.

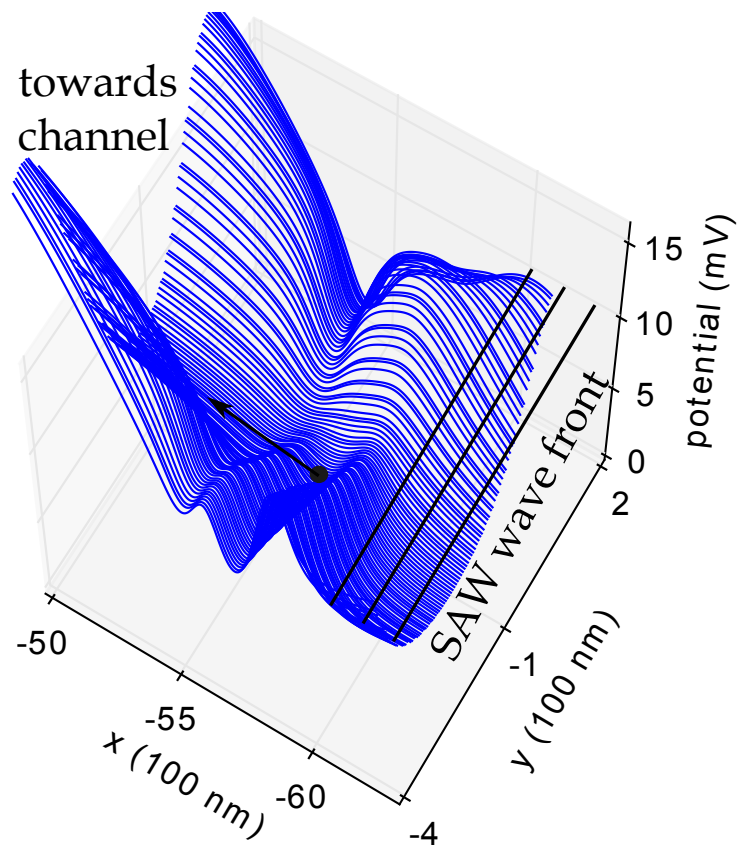


Figure 6.26: Potential of the injection quantum dot of the second prototype in 3D. The electron (black dot) can follow the direction of the SAW and injection into the one-dimensional channel is straight forward.

We will now propose a third design, which can be used to study single electrons on-the-fly inside a tunnel-coupled wire. Instead of isolating different electrons in different quantum dots and letting them propagate towards the interaction region in different SAW minima, we can also directly initialize the system in a double quantum dot-like structure inside the tunnel-coupled wire. For this purpose, we changed the design of the structure such that the injection of single electrons into the tunnel-coupled wire will be done from the side instead of from the front of the propagation channel. We have designed and optimized the device structure with the help of the potential calculator and show the obtained gate structure in figure 6.27. The two circular gates on the top and the bottom part of the structure serve as injection quantum dots. Into each dot, electrons can be loaded via the right reservoir gate and each quantum dot is coupled to the interaction region via a QPC that is formed between its adjacent channel confinement gate and the thin horizontal gates, forming a constriction of 100 nm. Another QPC is coupled to the left quantum dot gate for charge sensing. Each quantum dot has a total of four gates, including the gate of the horizontal QPC with is formed with the respective channel gate. This QPC allows to control the coupling to the channel. For a structure with 4 quantum dots and tunnel-coupled wire, we obtain a total of 35 electrical contacts, including ohmic contacts, reducing the complexity of the structure by 20%. Concerning the electron pick-up into the SAW, a straight channel is preferred, as we have already discussed for prototype two. One point we have not yet mentioned is the potential barrier in between the quantum dot and the channel, which is raised due to the quantum dot gate close to the channel (see most left red gate in figure 6.23(a) for comparison). As we have discussed in the SAW current measurement (see section 6.1), the smoother the potential rise, the less SAW power is needed to pick-up and to transfer an electron. The prototype is designed such that the electrons can be confined close to the injection quantum dots by simply increasing the size of the top and bottom channel gate. For clarity, we plot a slice along the white dotted line in the left panel of figure 6.28 in the right panel. We find that a potential minimum and hence a quantum dot is formed in the region of interest. The design not only has fewer gates, the interaction region is also completely translation invariant. As we have seen in the discussion of the flying qubit, the transition from the Aharonov-Bohm ring into the tunnel-coupled wire plays a crucial role on the actual state of the device. Avoiding such rather abrupt changes in the potential landscape allows the study of the tunneling behavior of flying electrons in the tunnel-coupled wire. No potential broadening goes along with no excitation of the electronic wave function into higher states and eliminates therefore another source of error. One possible excitation mechanism however remains, which is the pick-up process of the electron into the moving quantum dots. Nevertheless, it should be feasible to reduce the needed SAW power due to the optimized transition towards the channel, which can be seen as another advantage of this third prototype.

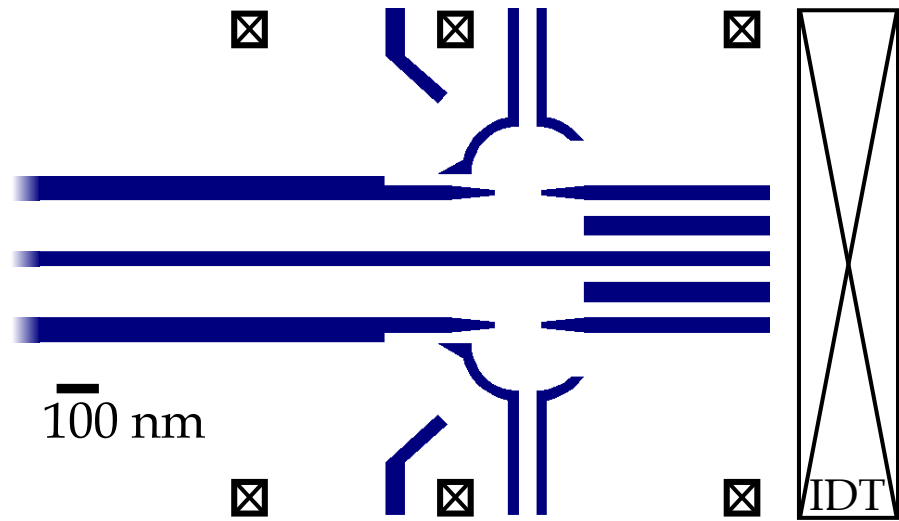


Figure 6.27: Gate structure of the third prototype. The image shows the right edge of the structure, since this is where injection and reception of the electrons will take place. The center region is translation invariant as indicated by the fading gates. The length of this interaction region can be adjusted at will. The depicted gates can serve as injection and reception. Electrons can be loaded from the top and bottom side into the interaction region. In this image, the SAW propagates to the left.

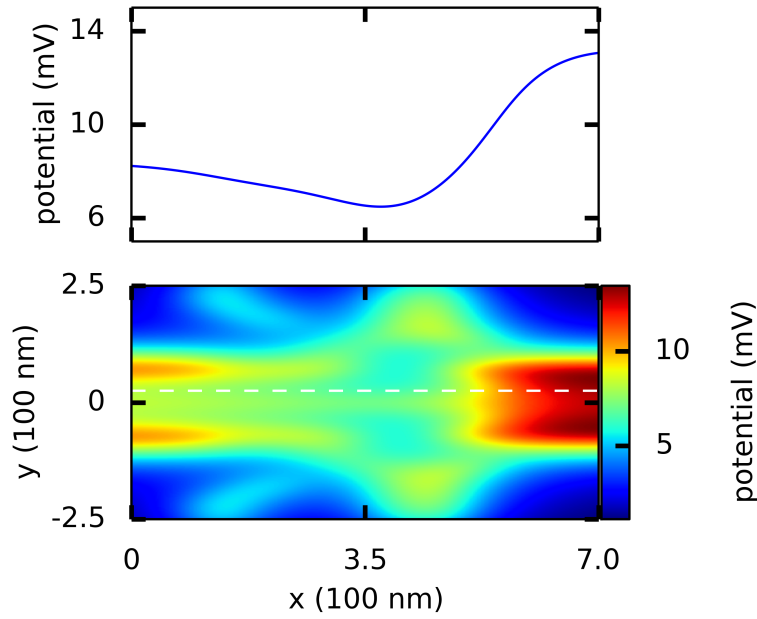


Figure 6.28: Potential landscape of the third prototype. The bottom panel shows the calculated potential landscape of the third prototype. The extension of the center tunnel-coupled wire can be seen on the left side, whereas the SAW stopping potential is on the right (red bulk). The quantum dots are formed in the center of the structure, whereas the coupling between the two upper and the two lower dots is bigger than the inter-dot-coupling in this configuration. The top panel is a slice along the white dotted line showing the position of the potential minimum along the x-direction.

CHAPTER 7

Conclusion

Many building blocks are needed to construct a working quantum computer and the community is getting closer to achieving this highly ambitious experimental goal. Being able to reliably control and use quantum information for computation, would be another breakthrough in computer science similar to the development of the transistor, which has led to unimaginable technological progress in less than a century of time. Today's physicists are facing the challenge of exploiting any possible two-level system that can serve as a quantum information carrier. Quantum states have to be prepared reliably, their time evolution has to be controlled and their measurement needs to be carefully designed. Apart from the storage and manipulation of such qubits, the question of coherent exchange of information, i.e. coupling coherent states to other coherent states has been raised and is under vivid investigation. Exchange of information can be done by coupling different systems to exchange particles, like photons or cooper-pairs or by directly transporting the particle that carries the quantum information from one place to another.

The goal of this thesis has been to study and manipulate electrons, while they are propagating through a designed structure and to gain knowledge about their quantum state. We have been pursuing two different approaches. First, the manipulation of ballistic electrons in an electronic two-path interferometer and second, the combination of a single electron source with an electronic beam-splitter. The first project has been carried out in collaboration with Tokyo university. We could show, that an Aharonov-Bohm interferometer coupled to a tunnel-coupled wire is a real two-path interferometer and that the phase of the electron can be fully controlled by electrostatic gates, making it a very promising example of a flying electron qubit. The absence and presence of electrons in the upper and lower arm of the interferometer defines a quantum state, which can be manipulated on-the-fly, simply by adjusting the electrostatic environment of the electrons, i.e. changing electrostatic gate voltages. We have developed a sophisticated numerical model to understand all the subtle effects that are taking place in this structure. This analysis has only been possible due the advancements by our collaborators from the CEA in the field of numerical quantum transport, which allowed us to dramatically increase the numerical sample size and to simulate the precise experimental conditions with the help

of a computation cluster. With the aid of these calculations, we could understand the working principle of the flying qubit in detail and reproduce all the experimental findings. We figured out, that the tunnel-coupled wire not only controls the repartitioning of the electrons into the upper and lower channel of the tunnel-coupled wire, but also its role for the propagation of the electronic modes at the interface between the Aharonov-Bohm ring and the tunnel-coupled wire. Depending on the tunnel barrier, two experimental regimes can be obtained. In the first regime, a lot of signal is scattered back into the Aharonov-Bohm ring arm on the opposite side, leading to encircling electron paths and scrambling the real two-path interferometry. We could show, that in the second regime this backscattering is strongly suppressed and the device can be operated as a flying qubit. In this regime, it is possible to tune the phase of the electrons in the Aharonov-Bohm ring, simply by changing a confinement gate voltage of the ring. Furthermore, the tunnel-coupled wire allows to repartition the ballistic electrons between the upper and lower path of the tunnel-coupled wire. These two features allow to access every state on the Bloch-sphere of the flying qubit by carefully adjusting the gate voltages. We note that even though we neglected Coulomb interaction, the experimental features could be nicely reproduced, however more research and calculations will have to be conducted to gather more knowledge about the role of Coulomb interactions in such a system. We have proposed an additional measurement with the flying qubit, which is the effective surface area increase due to the presence of the tunnel-coupled wire, which can be studied in the near future. The device is suitable for a variety of different measurements, like the measurement of the transmission phase of a quantum dot in the Kondo regime, placed inside one of the arms of the Aharonov-Bohm interferometer and will most likely be used to study spin-flip scattering in the future.

The second project of this thesis has been the combination of the surface acoustic wave single electron source, which has been developed in our lab prior to this thesis and its combination with the same electronic beam splitter, which we have used in the tunnel-coupled wire of the flying qubit. Since only one electron would be interacting with the tunnel-coupled wire, the visibility of the tunneling events should be close to 100%. Once the tunnel barrier is tuned as a beam splitter, i.e. 50% probability for the electron to be measured in the upper channel and 50% of probability to be measured in the lower channel, the device can serve as a measurement platform for quantum optics experiments with electrons, i.e. one can send two electrons simultaneously onto the beam splitter and study their interactions. The structure can be seen as a flying double quantum dot and could also be used to study the transport of electron spin, similar to what our group is pursuing in the single flying quantum dot structures, however we have omitted the discussion of electron spin in this manuscript. We have been able to study the required techniques, needed to build such a device. We have successfully characterized and optimized the interdigital transducers (IDT), which are needed to create the flying quantum dots in our structure. We could compare single finger and double finger IDT in terms of induced electric potential and found to our surprise that both designs have comparable performance in terms of amplitude. Nevertheless, the bandwidth of double finger IDT is larger, leading to faster surface acoustic wave rise times. To further improve

the IDT fabrication, we propose the use of nano-imprint lithography for the interdigital transducers as it clearly enhances the device quality, paving the way for high frequency SAW applications. Surface gates in GaAs/AlGaAs heterostructures together with the isolation of single electrons in the 2DEG is a well-established technology in our field. However, the designed gate structures has had the highest number of electrical contacts so far in our lab. The first prototype has to be seen as a proof of principle that even such highly dense structures are feasible and taking into account further progress in nanofabrication technology, even more complicated structures can be envisioned. The total number of electrical contacts has also lead to a time-consuming update of the electrical set-up of the used cryostat Melusine. At the same time, other technologies are also being studied by the community, to reduce the amount of electrical connections using multiplexing techniques. The second prototype has been close to being ready for measurement at the end of this manuscript, however with ongoing issues of the delicate e-beam masker, final efforts have come to grief.

A positive side effect of the software, which has been developed to study the transport properties of the flying qubit, has been the development of an algorithm capable of quickly calculating the potential landscapes that are created by surface gates. The emerged piece of software now allows even unfamiliar users to test their surface gate design by calculating obtainable potential landscapes. This should in principle help optimizing the sample development for all different kind of experiments and support experience-based sample design. A third prototype with a slightly less dense gate structure has been developed guided by this piece of code and will hopefully inspire future generations of students to further push in a similar direction. The single electron beam splitter for quantum optics experiments in solid state systems based on what has been presented in this thesis is by all means achievable and further experiments are currently being carried out.

Bibliography

- [1] R. P. Feynman: ‘Simulating physics with computers’, *International Journal of Theoretical Physics* **21** (1982), 467–488, DOI: [10.1007/BF02650179](https://doi.org/10.1007/BF02650179) (see pp. [2](#), [10](#)).
- [2] T. D. Ladd, F. Jelezko, R. Laffamme, Y. Nakamura, C. Monroe, and J. L. O’Brien: ‘Quantum computers’, *Nature* **464** (2010), 45–53, DOI: [10.1038/nature08812](https://doi.org/10.1038/nature08812) (see pp. [2](#), [3](#), [10](#)).
- [3] P. Shor: ‘Polynomial-Time Algorithms for Prime Factorization and Discrete Logarithms on a Quantum Computer’, *SIAM Review* **41** (1999), 303–332, DOI: [10.1137/S0036144598347011](https://doi.org/10.1137/S0036144598347011) (see pp. [2](#), [10](#)).
- [4] David P. DiVincenzo: ‘Quantum Computation’, *Science* **270** (1995), 255–261, DOI: [10.1126/science.270.5234.255](https://doi.org/10.1126/science.270.5234.255) (see pp. [2](#), [10](#)).
- [5] J. I. Cirac and P. Zoller: ‘Quantum Computations with Cold Trapped Ions’, *Phys. Rev. Lett.* **74** (1995), 4091–4094, DOI: [10.1103/PhysRevLett.74.4091](https://doi.org/10.1103/PhysRevLett.74.4091) (see pp. [2](#), [10](#)).
- [6] V. Bouchiat, D. Vion, P. Joyez, D. Esteve, and M. H. Devoret: ‘Quantum coherence with a single Cooper pair’, *Physica Scripta* **1998** (1998), 165, DOI: [10.1238/Physica.Topical.076a00165](https://doi.org/10.1238/Physica.Topical.076a00165) (see pp. [2](#), [10](#)).
- [7] M. H. Devoret, A. Wallraff, and J. M. Martinis: ‘Superconducting Qubits: A Short Review’, *ArXiv e-prints* (2004), arXiv: [cond-mat/0411174](https://arxiv.org/abs/cond-mat/0411174) [[cond-mat.mes-hall](#)] (see pp. [2](#), [10](#)).
- [8] M. H. Devoret and R. J. Schoelkopf: ‘Superconducting Circuits for Quantum Information: An Outlook’, *Science* **339** (2013), 1169–1174, DOI: [10.1126/science.1231930](https://doi.org/10.1126/science.1231930) (see pp. [2](#), [10](#)).
- [9] W. H. Zurek: ‘Decoherence and the transition from quantum to classical’, *Physics Today* **44** (1991), 36–44, DOI: [10.1063/1.881293](https://doi.org/10.1063/1.881293) (see pp. [2](#), [10](#)).
- [10] E. Knill: ‘Quantum computing with realistically noisy devices’, *Nature* **434** (2005), 39–44, DOI: [10.1038/nature03350](https://doi.org/10.1038/nature03350) (see pp. [3](#), [11](#)).
- [11] Daniel Loss and David P. DiVincenzo: ‘Quantum computation with quantum dots’, *Phys. Rev. A* **57** (1998), 120–126, DOI: [10.1103/PhysRevA.57.120](https://doi.org/10.1103/PhysRevA.57.120) (see pp. [3](#), [11](#)).

- [12] S. Tarucha, D. G. Austing, T. Honda, R. J. van der Hage, and L. P. Kouwenhoven: ‘Shell Filling and Spin Effects in a Few Electron Quantum Dot’, *Phys. Rev. Lett.* **77** (1996), 3613–3616, DOI: [10.1103/PhysRevLett.77.3613](https://doi.org/10.1103/PhysRevLett.77.3613) (see pp. 3, 11, 89).
- [13] S. Tarucha, T. Honda, D.G. Austing, Y. Tokura, K. Muraki, T.H. Oosterkamp, J.W. Janssen, and L.P. Kouwenhoven: ‘Electronic states in quantum dot atoms and molecules’, *Physica E: Low-dimensional Systems and Nanostructures* **3** (1998), 112–120, DOI: [10.1016/S1386-9477\(98\)00225-2](https://doi.org/10.1016/S1386-9477(98)00225-2) (see pp. 3, 11).
- [14] M. Ciorga, A. S. Sachrajda, P. Hawrylak, C. Gould, P. Zawadzki, S. Jullian, Y. Feng, and Z. Wasilewski: ‘Addition spectrum of a lateral dot from Coulomb and spin-blockade spectroscopy’, *Phys. Rev. B* **61** (2000), R16315–R16318, DOI: [10.1103/PhysRevB.61.R16315](https://doi.org/10.1103/PhysRevB.61.R16315) (see pp. 3, 11).
- [15] L. P. Kouwenhoven, D. G. Austing, and S. Tarucha: ‘Few-electron quantum dots’, *Reports on Progress in Physics* **64** (2001), 701, DOI: [10.1088/0034-4885/64/6/201](https://doi.org/10.1088/0034-4885/64/6/201) (see pp. 3, 11, 89, 91).
- [16] M. Field, C. G. Smith, M. Pepper, D. A. Ritchie, J. E. F. Frost, G. A. C. Jones, and D. G. Hasko: ‘Measurements of Coulomb blockade with a noninvasive voltage probe’, *Phys. Rev. Lett.* **70** (1993), 1311–1314, DOI: [10.1103/PhysRevLett.70.1311](https://doi.org/10.1103/PhysRevLett.70.1311) (see pp. 4, 11, 120).
- [17] J. M. Elzerman, R. Hanson, J. S. Greidanus, L. H. Willems van Beveren, S. De Franceschi, L. M. K. Vandersypen, S. Tarucha, and L. P. Kouwenhoven: ‘Few-electron quantum dot circuit with integrated charge read out’, *Phys. Rev. B* **67** (2003), 161308, DOI: [10.1103/PhysRevB.67.161308](https://doi.org/10.1103/PhysRevB.67.161308) (see pp. 4, 11, 120).
- [18] L. M. K. Vandersypen, J. M. Elzerman, R. N. Schouten, L. H. Willems van Beveren, R. Hanson, and L. P. Kouwenhoven: ‘Real-time detection of single-electron tunneling using a quantum point contact’, *Applied Physics Letters* **85** (2004), 4394–4396, DOI: [10.1063/1.1815041](https://doi.org/10.1063/1.1815041) (see pp. 4, 11, 120).
- [19] J. M. Elzerman, R. Hanson, L. H. Willems van Beveren, B. Witkamp, L. M. K. Vandersypen, and L. P. Kouwenhoven: ‘Single-shot read-out of an individual electron spin in a quantum dot’, *Nature* **430** (2004), 431–435, DOI: [10.1038/nature02693](https://doi.org/10.1038/nature02693) (see pp. 4, 11).
- [20] J. R. Petta, A. C. Johnson, J. M. Taylor, E. A. Laird, A. Yacoby, M. D. Lukin, C. M. Marcus, M. P. Hanson, and A. C. Gossard: ‘Coherent Manipulation of Coupled Electron Spins in Semiconductor Quantum Dots’, *Science* **309** (2005), 2180–2184, DOI: [10.1126/science.1116955](https://doi.org/10.1126/science.1116955) (see pp. 4, 11).
- [21] F. H. L. Koppens, C. Buizert, K. J. Tielrooij, I. T. Vink, K. C. Nowack, T. Meunier, L. P. Kouwenhoven, and L. M. K. Vandersypen: ‘Driven coherent oscillations of a single electron spin in a quantum dot’, *Nature* **442** (2006), 766–771, DOI: [10.1038/nature05065](https://doi.org/10.1038/nature05065) (see pp. 4, 11).
- [22] R. Hanson, L. P. Kouwenhoven, J. R. Petta, S. Tarucha, and L. M. K. Vandersypen: ‘Spins in few-electron quantum dots’, *Rev. Mod. Phys.* **79** (2007), 1217–1265, DOI: [10.1103/RevModPhys.79.1217](https://doi.org/10.1103/RevModPhys.79.1217) (see pp. 4, 11).

- [23] R. Ionicioio, G. Amaratunga, and F. Udrea: ‘Quantum Computation With Ballistic Electrons’, *International Journal of Modern Physics B* **15** (2001), 125–133, DOI: [10.1142/S0217979201003521](https://doi.org/10.1142/S0217979201003521) (see pp. 4, 12).
- [24] Yang Ji, Yunchul Chung, D. Sprinzak, M. Heiblum, D. Mahalu, and Hadas Shtrikman: ‘An electronic Mach-Zehnder interferometer’, *Nature* **422** (2003), 415–418, DOI: [10.1038/nature01503](https://doi.org/10.1038/nature01503) (see pp. 4, 12, 48, 49).
- [25] L. V. Litvin, H.-P. Tranitz, W. Wegscheider, and C. Strunk: ‘Decoherence and single electron charging in an electronic Mach-Zehnder interferometer’, *Phys. Rev. B* **75** (2007), 033315, DOI: [10.1103/PhysRevB.75.033315](https://doi.org/10.1103/PhysRevB.75.033315) (see pp. 4, 12).
- [26] Preden Roulleau, F. Portier, P. Roche, A. Cavanna, G. Faini, U. Gennser, and D. Mailly: ‘Direct Measurement of the Coherence Length of Edge States in the Integer Quantum Hall Regime’, *Phys. Rev. Lett.* **100** (2008), 126802, DOI: [10.1103/PhysRevLett.100.126802](https://doi.org/10.1103/PhysRevLett.100.126802) (see pp. 4, 12, 50).
- [27] P. Roulleau, F. Portier, P. Roche, A. Cavanna, G. Faini, U. Gennser, and D. Mailly: ‘Noise Dephasing in Edge States of the Integer Quantum Hall Regime’, *Phys. Rev. Lett.* **101** (2008), 186803, DOI: [10.1103/PhysRevLett.101.186803](https://doi.org/10.1103/PhysRevLett.101.186803) (see pp. 4, 12, 50).
- [28] P. Roulleau, F. Portier, P. Roche, A. Cavanna, G. Faini, U. Gennser, and D. Mailly: ‘Tuning Decoherence with a Voltage Probe’, *Phys. Rev. Lett.* **102** (2009), 236802, DOI: [10.1103/PhysRevLett.102.236802](https://doi.org/10.1103/PhysRevLett.102.236802) (see pp. 4, 12).
- [29] P.-A. Huynh, F. Portier, H. le Sueur, G. Faini, U. Gennser, D. Mailly, F. Pierre, W. Wegscheider, and P. Roche: ‘Quantum Coherence Engineering in the Integer Quantum Hall Regime’, *Phys. Rev. Lett.* **108** (2012), 256802, DOI: [10.1103/PhysRevLett.108.256802](https://doi.org/10.1103/PhysRevLett.108.256802) (see pp. 4, 12, 50).
- [30] A. Yacoby, M. Heiblum, D. Mahalu, and Hadas Shtrikman: ‘Coherence and Phase Sensitive Measurements in a Quantum Dot’, *Phys. Rev. Lett.* **74** (1995), 4047–4050, DOI: [10.1103/PhysRevLett.74.4047](https://doi.org/10.1103/PhysRevLett.74.4047) (see pp. 4, 12, 50).
- [31] E. Buks, R. Schuster, M. Heiblum, D. Mahalu, V. Umansky, and H. Shtrikman: ‘Measurement of Phase and Magnitude of the Reflection Coefficient of a Quantum Dot’, *Phys. Rev. Lett.* **77** (1996), 4664–4667, DOI: [10.1103/PhysRevLett.77.4664](https://doi.org/10.1103/PhysRevLett.77.4664) (see pp. 4, 12, 50).
- [32] J. A. del Alamo and C. C. Eugster: ‘Quantum field effect directional coupler’, *Applied Physics Letters* **56** (1990), 78–80, DOI: [10.1063/1.102657](https://doi.org/10.1063/1.102657) (see pp. 4, 12, 50).
- [33] N. Tsukada, A. D. Wieck, and K. Ploog: ‘Proposal of novel electron wave coupled devices’, *Applied Physics Letters* **56** (1990), 2527–2529, DOI: [10.1063/1.102877](https://doi.org/10.1063/1.102877) (see pp. 4, 12, 50, 59).
- [34] Michihisa Yamamoto, Shintaro Takada, Christopher Bäuerle, Kenta Watanabe, Andreas D. Wieck, and Seigo Tarucha: ‘Electrical control of a solid-state flying qubit’, *Nat Nano* **7** (2012), 247–251, DOI: [10.1038/nnano.2012.28](https://doi.org/10.1038/nnano.2012.28) (see pp. 4, 12, 51, 55, 58, 69, 81).

- [35] C. W. Groth, M. Wimmer, A. R. Akhmerov, and X. Waintal: ‘Kwant: a software package for quantum transport’, *ArXiv e-prints* (2013), arXiv: [1309.2926 \[cond-mat.mes-hall\]](#) (see pp. [4](#), [12](#), [23](#), [26](#), [28](#)).
- [36] Tobias Bautze, Christoph Süssmeier, Shintaro Takada, Christoph Groth, Tristan Meunier, Michihisa Yamamoto, Seigo Tarucha, Xavier Waintal, and Christopher Bäuerle: ‘Theoretical, numerical, and experimental study of a flying qubit electronic interferometer’, *Phys. Rev. B* **89** (2014), 125432, DOI: [10.1103/PhysRevB.89.125432](#) (see pp. [4](#), [12](#), [48](#)).
- [37] P. Utke, J. Bindslev Hansen, P.E. Lindelof, C.B. Sorensen, and K. Gloos: ‘Single-Electron Transport Driven by Surface Acoustic Waves: Moving Quantum Dots Versus Short Barriers’, English, *Journal of Low Temperature Physics* **146** (2007), 607–627, DOI: [10.1007/s10909-006-9285-6](#) (see pp. [5](#), [12](#), [109](#)).
- [38] Sylvain Hermelin, Shintaro Takada, Michihisa Yamamoto, Seigo Tarucha, Andreas D. Wieck, Laurent Saminadayar, Christopher Bäuerle, and Tristan Meunier: ‘Electrons surfing on a sound wave as a platform for quantum optics with flying electrons’, *Nature* **477** (2011), 435–438, DOI: [10.1038/nature10416](#) (see pp. [5](#), [12](#), [47](#), [82](#), [88](#), [91](#), [93](#), [102](#), [103](#), [108](#), [118](#), [119](#), [130](#)).
- [39] S. Hermelin: ‘Transport d’un électron unique dans des nanostructures’, PhD thesis, Université de Grenoble, 2011 (see pp. [5](#), [12](#), [121](#)).
- [40] B. Bertrand: ‘Single electron spin transfer (todo)’, PhD thesis, Université de Grenoble, 2011 (see pp. [5](#), [12](#)).
- [41] K. v. Klitzing, G. Dorda, and M. Pepper: ‘New Method for High-Accuracy Determination of the Fine-Structure Constant Based on Quantized Hall Resistance’, *Phys. Rev. Lett.* **45** (1980), 494–497, DOI: [10.1103/PhysRevLett.45.494](#) (see pp. [13](#), [37](#)).
- [42] E. F. Schubert: ‘Delta doping of III–V compound semiconductors: Fundamentals and device applications’, *Journal of Vacuum Science & Technology A* **8** (1990), 2980–2996, DOI: [10.1116/1.576617](#) (see p. [13](#)).
- [43] L. J. van der Pauw: ‘A method of measuring specific resistivity and Hall effect of discs of arbitrary shape’, *Philips Research Reports* **13** (1958), 1–9 (see p. [14](#)).
- [44] L. J. van der Pauw: ‘A method of measuring the resistivity and Hall coefficient on lamellae of arbitrary shape’, *Philips Research Reports* **20** (1958), 220–224 (see p. [14](#)).
- [45] C. Davisson and L.H. Germer: ‘The Scattering of Electrons by a Single Crystal of Nickel’, *Nature* **119** (1927), 558–560, DOI: [10.1038/119558a0](#) (see p. [16](#)).
- [46] C.J. Davisson: ‘The diffraction of electrons by a crystal of nickel’, *Bell System Technical Journal, The* **7** (1928), 90–105, DOI: [10.1002/j.1538-7305.1928.tb00342.x](#) (see p. [16](#)).
- [47] Louis-Victor de Broglie: ‘Recherches sur la theorie des quanta’, PhD thesis, Annales de Physique - 10e Serie - Tome III, 1925 (see p. [16](#)).

- [48] Claus Jönsson: ‘Elektroneninterferenzen an mehreren künstlich hergestellten Feinspalten’, German, *Zeitschrift für Physik* **161** (1961), 454–474, DOI: [10.1007/BF01342460](https://doi.org/10.1007/BF01342460) (see p. 16).
- [49] Claus Jönsson: ‘Electron Diffraction at Multiple Slits’, *American Journal of Physics* **42** (1974), 4–11, DOI: [10.1119/1.1987592](https://doi.org/10.1119/1.1987592) (see p. 16).
- [50] P. G. Merli, G. F. Missiroli, and G. Pozzi: ‘On the statistical aspect of electron interference phenomena’, *American Journal of Physics* **44** (1976), 306–307, DOI: [10.1119/1.10184](https://doi.org/10.1119/1.10184) (see p. 16).
- [51] A. Tonomura, J. Endo, T. Matsuda, and T. Kawasaki: ‘Demonstration of single-electron buildup of an interference pattern’, *Am. J. Phys.* **57** (1989), 117–120, DOI: [10.1119/1.16104](https://doi.org/10.1119/1.16104) (see p. 16).
- [52] G. Möllenstedt and H. Düker: ‘Fresnelscher Interferenzversuch mit einem Biprisma für Elektronenwellen’, *Naturwissenschaften* **42** (1955), 41–41, DOI: [10.1007/BF00621530](https://doi.org/10.1007/BF00621530) (see p. 16).
- [53] R. P. Feynman, R. Leighton, and M. Sands: *The Feynman Lectures on Physics*, Second, vol. 3, Addison-Wesley, 1965, DOI: [10.1063/1.3051743](https://doi.org/10.1063/1.3051743) (see p. 17).
- [54] Y. Aharonov and D. Bohm: ‘Significance of Electromagnetic Potentials in the Quantum Theory’, *The Physical Review* **115** (1959), 485–491, DOI: [10.1103/PhysRev.115.485](https://doi.org/10.1103/PhysRev.115.485) (see p. 18).
- [55] A. Tonomura, T. Matsuda, R. Suzuki, A. Fukuhara, N. Osakabe, H. Umezaki, J. Endo, K. Shinagawa, Y. Sugita, and H. Fujiwara: ‘Observation of Aharonov-Bohm Effect by Electron Holography’, *Phys. Rev. Lett.* **48** (1982), 1443–1446, DOI: [10.1103/PhysRevLett.48.1443](https://doi.org/10.1103/PhysRevLett.48.1443) (see p. 18).
- [56] R. A. Webb, S. Washburn, C. P. Umbach, and R. B. Laibowitz: ‘Observation of h/e Aharonov-Bohm Oscillations in Normal-Metal Rings’, *Phys. Rev. Lett.* **54** (1985), 2696–2699, DOI: [10.1103/PhysRevLett.54.2696](https://doi.org/10.1103/PhysRevLett.54.2696) (see p. 18).
- [57] R. Landauer: ‘Spatial variation of currents and fields due to localized scatterers in metallic conduction’, *IBM Journal of Research and Development* **1** (1957), 223–231, DOI: [10.1147/rd.13.0223](https://doi.org/10.1147/rd.13.0223) (see p. 19).
- [58] R. Landauer: ‘Spatial variation of currents and fields due to localized scatterers in metallic conduction’, *IBM Journal of Research and Development* **32** (1988), 306–316, DOI: [10.1147/rd.323.0306](https://doi.org/10.1147/rd.323.0306) (see p. 19).
- [59] R. Landauer: ‘Electrical resistance of disordered one-dimensional lattices’, *Philosophical Magazine* **21** (1970), 863–867, DOI: [10.1080/14786437008238472](https://doi.org/10.1080/14786437008238472) (see p. 19).
- [60] M. Büttiker, Y. Imry, R. Landauer, and S. Pinhas: ‘Generalized many-channel conductance formula with application to small rings’, *Phys. Rev. B* **31** (1985), 6207–6215, DOI: [10.1103/PhysRevB.31.6207](https://doi.org/10.1103/PhysRevB.31.6207) (see p. 19).
- [61] M. Büttiker: ‘Symmetry of Electrical Conduction’, *IBM J. Res. Dev.* **32** (1988), 317–334, DOI: [10.1147/rd.323.0317](https://doi.org/10.1147/rd.323.0317) (see p. 19).

- [62] Daniel S. Fisher and Patrick A. Lee: ‘Relation between conductivity and transmission matrix’, *Phys. Rev. B* **23** (1981), 6851–6854, DOI: [10.1103/PhysRevB.23.6851](https://doi.org/10.1103/PhysRevB.23.6851) (see pp. 19, 26).
- [63] S. Douglas Stone and Aaron Szafer: ‘What is Measured when You Measure a Resistance; The Landauer Formula Revisited’, *IBM J. Res. Dev.* **32** (1988), 384–413, DOI: [10.1147/rd.323.0384](https://doi.org/10.1147/rd.323.0384) (see p. 19).
- [64] Supriyo Datta: *Electronic Transport in Mesoscopic Systems (Cambridge Studies in Semiconductor Physics and Microelectronic Engineering)*, Cambridge University Press, 1997, DOI: [10.1017/CB09780511805776](https://doi.org/10.1017/CB09780511805776) (see pp. 19, 26).
- [65] E. Rutherford: ‘The Scattering Of α and β Particles By Matter and the Structure of the Atom’, *Philosophical Magazine* **21** (1911), 669–688, DOI: [10.1080/14786440508637080](https://doi.org/10.1080/14786440508637080) (see p. 19).
- [66] E. D. Bloom, D. H. Coward, H. DeStaebler, J. Drees, G. Miller, L. W. Mo, R. E. Taylor, M. Breidenbach, J. I. Friedman, G. C. Hartmann, and H. W. Kendall: ‘High-Energy Inelastic e-p Scattering at 6° and 10°’, *Phys. Rev. Lett.* **23** (1969), 930–934, DOI: [10.1103/PhysRevLett.23.930](https://doi.org/10.1103/PhysRevLett.23.930) (see p. 19).
- [67] M. Breidenbach, J. I. Friedman, H. W. Kendall, E. D. Bloom, D. H. Coward, H. DeStaebler, J. Drees, L. W. Mo, and R. E. Taylor: ‘Observed Behavior of Highly Inelastic Electron-Proton Scattering’, *Phys. Rev. Lett.* **23** (1969), 935–939, DOI: [10.1103/PhysRevLett.23.935](https://doi.org/10.1103/PhysRevLett.23.935) (see p. 19).
- [68] Jun John Sakurai: *Modern Quantum Mechanics*, Revised, Addison-Wesley Publishing Company, 1994, DOI: [10.1119/1.14491](https://doi.org/10.1119/1.14491) (see p. 20).
- [69] D.J. Griffiths: *Introduction to quantum mechanics*, Pearson Prentice Hall, 2005 (see p. 20).
- [70] M. Büttiker: ‘Absence of backscattering in the quantum Hall effect in multiprobe conductors’, *Phys. Rev. B* **38** (1988), 9375–9389, DOI: [10.1103/PhysRevB.38.9375](https://doi.org/10.1103/PhysRevB.38.9375) (see pp. 21, 50).
- [71] B. J. van Wees, H. van Houten, C. W. J. Beenakker, J. G. Williamson, L. P. Kouwenhoven, D. van der Marel, and C. T. Foxon: ‘Quantized conductance of point contacts in a two-dimensional electron gas’, *Phys. Rev. Lett.* **60** (1988), 848–850, DOI: [10.1103/PhysRevLett.60.848](https://doi.org/10.1103/PhysRevLett.60.848) (see pp. 21, 32–34).
- [72] N.W. Ashcroft and N.D. Mermin: *Solid state physics*, Saunders College, 1976 (see pp. 21, 70).
- [73] K. Kazymyrenko and X. Waintal: ‘Knitting algorithm for calculating Green functions in quantum systems’, *Phys. Rev. B* **77** (2008), 115119, DOI: [10.1103/PhysRevB.77.115119](https://doi.org/10.1103/PhysRevB.77.115119) (see pp. 22, 25).
- [74] Patrick A. Lee and Daniel S. Fisher: ‘Anderson Localization in Two Dimensions’, *Phys. Rev. Lett.* **47** (1981), 882–885, DOI: [10.1103/PhysRevLett.47.882](https://doi.org/10.1103/PhysRevLett.47.882) (see p. 25).

- [75] D. J. Thouless and S. Kirkpatrick: ‘Conductivity of the disordered linear chain’, *Journal of Physics C: Solid State Physics* **14** (1981), 235, DOI: [10.1088/0022-3719/14/3/007](https://doi.org/10.1088/0022-3719/14/3/007) (see p. 25).
- [76] A. MacKinnon: ‘The calculation of transport properties and density of states of disordered solids’, English, *Zeitschrift für Physik B Condensed Matter* **59** (1985), 385–390, DOI: [10.1007/BF01328846](https://doi.org/10.1007/BF01328846) (see p. 25).
- [77] C. Caroli, R. Combescot, P. Nozieres, and D. Saint-James: ‘Direct calculation of the tunneling current’, *Journal of Physics C: Solid State Physics* **4** (1971), 916, DOI: [10.1088/0022-3719/4/8/018](https://doi.org/10.1088/0022-3719/4/8/018) (see p. 25).
- [78] Yigal Meir and Ned S. Wingreen: ‘Landauer formula for the current through an interacting electron region’, *Phys. Rev. Lett.* **68** (1992), 2512–2515, DOI: [10.1103/PhysRevLett.68.2512](https://doi.org/10.1103/PhysRevLett.68.2512) (see p. 25).
- [79] L.V. Keldysh: ‘Diagram technique for nonequilibrium processes’, *Zh. Eksp. Teor. Fiz.* **47** (1964), 1515–1527 (see p. 25).
- [80] Supriyo Datta: ‘Nanoscale device modeling: the Greens function method’, *Superlattices and Microstructures* **28** (2000), 253–278, DOI: [10.1006/spmi.2000.0920](https://doi.org/10.1006/spmi.2000.0920) (see p. 25).
- [81] A. Pecchia, G. Penazzi, L. Salvucci, and A. Di Carlo: ‘Non-equilibrium Green’s functions in density functional tight binding: method and applications’, *New Journal of Physics* **10** (2008), 065022, DOI: [10.1088/1367-2630/10/6/065022](https://doi.org/10.1088/1367-2630/10/6/065022) (see p. 25).
- [82] A. Martinez, N. Seoane, A.R. Brown, and A. Asenov: ‘A detailed 3D-NEGF simulation study of tunnelling in n-Si nanowire MOSFETs’, *Silicon Nanoelectronics Workshop (SNW), 2010*, 2010, 1–2, DOI: [10.1109/SNW.2010.5562591](https://doi.org/10.1109/SNW.2010.5562591) (see p. 25).
- [83] Chien-Liang Chen, Ching-Ray Chang, and Branislav K. Nikolic: ‘Quantum coherence and its dephasing in the giant spin Hall effect and nonlocal voltage generated by magnetotransport through multiterminal graphene bars’, *Phys. Rev. B* **85** (2012), 155414, DOI: [10.1103/PhysRevB.85.155414](https://doi.org/10.1103/PhysRevB.85.155414) (see p. 25).
- [84] Benoit Gaury, Joseph Weston, Matthieu Santin, Manuel Houzet, Christoph Groth, and Xavier Waintal: ‘Numerical simulations of time-resolved quantum electronics’, *Physics Reports* **534** (2014), 1–37, DOI: [10.1016/j.physrep.2013.09.001](https://doi.org/10.1016/j.physrep.2013.09.001) (see p. 26).
- [85] John H. Davies, Ivan A. Larkin, and E. V. Sukhorukov: ‘Modeling the patterned two-dimensional electron gas: Electrostatics’, *Journal of Applied Physics* **77** (1995), 4504–4512, DOI: [10.1063/1.359446](https://doi.org/10.1063/1.359446) (see p. 31).
- [86] D. A. Wharam, T. J. Thornton, R. Newbury, M. Pepper, H. Ahmed, J. E. F. Frost, D. G. Hasko, D. C. Peacock, D. A. Ritchie, and G. A. C. Jones: ‘One-dimensional transport and the quantisation of the ballistic resistance’, *Journal of Physics C: Solid State Physics* **21** (1988), L209, DOI: [10.1088/0022-3719/21/8/002](https://doi.org/10.1088/0022-3719/21/8/002) (see p. 32).

- [87] M. Büttiker: ‘Quantized transmission of a saddle-point constriction’, *Phys. Rev. B* **41** (1990), 7906–7909, DOI: [10.1103/PhysRevB.41.7906](https://doi.org/10.1103/PhysRevB.41.7906) (see p. 32).
- [88] H. van Houten, C.W.J. Beenakker, and B.J. van Wees: *Chapter 2: Quantum Point Contacts*, ed. by Mark Reed, vol. 35, Elsevier, 1992, 9–112, DOI: [10.1016/S0080-8784\(08\)62392-3](https://doi.org/10.1016/S0080-8784(08)62392-3) (see p. 32).
- [89] M. A. Topinka, B. J. LeRoy, S. E. J. Shaw, E. J. Heller, R. M. Westervelt, K. D. Maranowski, and A. C. Gossard: ‘Imaging Coherent Electron Flow from a Quantum Point Contact’, *Science* **289** (2000), 2323–2326, DOI: [10.1126/science.289.5488.2323](https://doi.org/10.1126/science.289.5488.2323) (see p. 37).
- [90] B. J. LeRoy, M. A. Topinka, R. M. Westervelt, K. D. Maranowski, and A. C. Gossard: ‘Imaging electron density in a two-dimensional electron gas’, *Applied Physics Letters* **80** (2002), 4431–4433, DOI: [10.1063/1.1484548](https://doi.org/10.1063/1.1484548) (see p. 37).
- [91] E. Bocquillon, V. Freulon, J.-M Berroir, P. Degiovanni, B. Plaçais, A. Cavanna, Y. Jin, and G. Fève: ‘Coherence and Indistinguishability of Single Electrons Emitted by Independent Sources’, *Science* **339** (2013), 1054–1057, DOI: [10.1126/science.1232572](https://doi.org/10.1126/science.1232572) (see pp. 37, 50, 87, 88, 98).
- [92] J. Dubois, T. Jullien, F. Portier, P. Roche, A. Cavanna, Y. Jin, W. Wegscheider, P. Roulleau, and D. C. Glatthli: ‘Minimal-excitation states for electron quantum optics using levitons’, *Nature* **502** (2013), 659–663, DOI: [10.1038/nature12713](https://doi.org/10.1038/nature12713) (see pp. 37, 88).
- [93] M. Ya. Azbel: ‘Eigenstates and properties of random systems in one dimension at zero temperature’, *Phys. Rev. B* **28** (1983), 4106–4125, DOI: [10.1103/PhysRevB.28.4106](https://doi.org/10.1103/PhysRevB.28.4106) (see p. 41).
- [94] Weige Xue and P. A. Lee: ‘Two-dimensional resonant tunneling’, *Phys. Rev. B* **38** (1988), 3913–3917, DOI: [10.1103/PhysRevB.38.3913](https://doi.org/10.1103/PhysRevB.38.3913) (see p. 41).
- [95] P.L. McEuen, B.W. Alphenaar, R.G. Wheeler, and R.N. Sacks: ‘Resonant transport effects due to an impurity in a narrow constriction’, *Surface Science* **229** (1990), 312–315, DOI: [10.1016/0039-6028\(90\)90896-G](https://doi.org/10.1016/0039-6028(90)90896-G) (see p. 42).
- [96] C.G. Smith, M. Pepper, H. Ahmed, J.E.F. Frost, D.G. Hasko, R. Newbury, D.C. Peacock, D.A. Ritchie, and G.A.C. Jones: ‘One dimensional electron tunneling and related phenomena’, *Surface Science* **228** (1990), 387–392, DOI: [10.1016/0039-6028\(90\)90334-5](https://doi.org/10.1016/0039-6028(90)90334-5) (see p. 42).
- [97] A. Wallraff, D. I. Schuster, A. Blais, L. Frunzio, R.-S. Huang, J. Majer, S. Kumar, S. M. Girvin, and R. J. Schoelkopf: ‘Strong coupling of a single photon to a superconducting qubit using circuit quantum electrodynamics’, *Nature* **431** (2004), 162–167, DOI: [10.1038/nature02851](https://doi.org/10.1038/nature02851) (see p. 47).
- [98] F. Jelezko, T. Gaebel, I. Popa, A. Gruber, and J. Wrachtrup: ‘Observation of Coherent Oscillations in a Single Electron Spin’, *Phys. Rev. Lett.* **92** (2004), 076401, DOI: [10.1103/PhysRevLett.92.076401](https://doi.org/10.1103/PhysRevLett.92.076401) (see p. 47).

- [99] H. Bernien, B. Hensen, W. Pfaff, G. Koolstra, M. S. Blok, L. Robledo, T. H. Taminiau, M. Markham, D. J. Twitchen, L. Childress, and R. Hanson: ‘Heralded entanglement between solid-state qubits separated by three metres’, *Nature* **497** (2013), 86–90, DOI: [10.1038/nature12016](https://doi.org/10.1038/nature12016) (see p. 47).
- [100] A. Imamoglu, S. Fält, J. Dreiser, G. Fernandez, M. Atatere, K. Hennessy, A. Badolato, and D. Gerace: ‘Coupling quantum dot spins to a photonic crystal nanocavity’, *Journal of Applied Physics* **101**, 081602 (2007), DOI: [10.1063/1.2722724](https://doi.org/10.1063/1.2722724) (see p. 47).
- [101] W. B. Gao, P. Fallahi, E. Togan, J. Miguel-Sanchez, and A. Imamoglu: ‘Observation of entanglement between a quantum dot spin and a single photon’, *Nature* **491** (2012), 426–430, DOI: [10.1038/nature11573](https://doi.org/10.1038/nature11573) (see p. 47).
- [102] R. P. G. McNeil, M. Kataoka, C. J. B. Ford, C. H. W. Barnes, D. Anderson, G. A. C. Jones, I. Farrer, and D. A. Ritchie: ‘On-demand single-electron transfer between distant quantum dots’, *Nature* **477** (2011), 439–442, DOI: [10.1038/nature10444](https://doi.org/10.1038/nature10444) (see pp. 47, 91, 93, 130).
- [103] I. Neder, M. Heiblum, Y. Levinson, D. Mahalu, and V. Umansky: ‘Unexpected Behavior in a Two-Path Electron Interferometer’, *Phys. Rev. Lett.* **96** (2006), 016804, DOI: [10.1103/PhysRevLett.96.016804](https://doi.org/10.1103/PhysRevLett.96.016804) (see p. 50).
- [104] I. Neder, N. Ofek, Y. Chung, M. Heiblum, D. Mahalu, and V. Umansky: ‘Interference between two indistinguishable electrons from independent sources’, *Nature* **448** (2007), 333–337, DOI: [10.1038/nature05955](https://doi.org/10.1038/nature05955) (see p. 50).
- [105] H. le Sueur, C. Altimiras, U. Gennser, A. Cavanna, D. Mailly, and F. Pierre: ‘Energy Relaxation in the Integer Quantum Hall Regime’, *Phys. Rev. Lett.* **105** (2010), 056803, DOI: [10.1103/PhysRevLett.105.056803](https://doi.org/10.1103/PhysRevLett.105.056803) (see p. 50).
- [106] E. Weisz, H. K. Choi, M. Heiblum, Yuval Gefen, V. Umansky, and D. Mahalu: ‘Controlled Dephasing of an Electron Interferometer with a Path Detector at Equilibrium’, *Phys. Rev. Lett.* **109** (2012), 250401, DOI: [10.1103/PhysRevLett.109.250401](https://doi.org/10.1103/PhysRevLett.109.250401) (see p. 50).
- [107] Eugene V. Sukhorukov and Vadim V. Cheianov: ‘Resonant Dephasing in the Electronic Mach-Zehnder Interferometer’, *Phys. Rev. Lett.* **99** (2007), 156801, DOI: [10.1103/PhysRevLett.99.156801](https://doi.org/10.1103/PhysRevLett.99.156801) (see p. 50).
- [108] G. Feve, A. Mahe, J.-M. Berroir, T. Kontos, B. Placais, D. C. Glattli, A. Cavanna, B. Etienne, and Y. Jin: ‘An On-Demand Coherent Single-Electron Source’, *Science* **316** (2007), 1169–1172, DOI: [10.1126/science.1141243](https://doi.org/10.1126/science.1141243) (see pp. 50, 86).
- [109] E. Bocquillon, F. D. Parmentier, C. Grenier, J.-M. Berroir, P. Degiovanni, D. C. Glattli, B. Placais, A. Cavanna, Y. Jin, and G. Fève: ‘Electron Quantum Optics: Partitioning Electrons One by One’, *Phys. Rev. Lett.* **108** (2012), 196803, DOI: [10.1103/PhysRevLett.108.196803](https://doi.org/10.1103/PhysRevLett.108.196803) (see pp. 50, 87).
- [110] Guangzhao Xu, Min Yang, and Ping Jiang: ‘A theoretical investigation on the quantum field effect directional coupler’, *Journal of Applied Physics* **74** (1993), 6747–6753, DOI: [10.1063/1.355072](https://doi.org/10.1063/1.355072) (see p. 50).

- [111] A. Yacoby, R. Schuster, and M. Heiblum: ‘Phase rigidity and $h/2e$ oscillations in a single-ring Aharonov-Bohm experiment’, *Phys. Rev. B* **53** (1996), 9583–9586, DOI: [10.1103/PhysRevB.53.9583](https://doi.org/10.1103/PhysRevB.53.9583) (see p. 50).
- [112] David W. Keith, Christopher R. Ekstrom, Quentin A. Turchette, and David E. Pritchard: ‘An interferometer for atoms’, *Phys. Rev. Lett.* **66** (1991), 2693–2696, DOI: [10.1103/PhysRevLett.66.2693](https://doi.org/10.1103/PhysRevLett.66.2693) (see p. 50).
- [113] R. Schuster, E. Buks, M. Heiblum, D. Mahalu, V. Umansky, and Hadas Shtrikman: ‘Phase measurement in a quantum dot via a double-slit interference experiment’, *Nature* **385** (1997), 417–420, DOI: [10.1038/385417a0](https://doi.org/10.1038/385417a0) (see p. 50).
- [114] E. Buks, R. Schuster, M. Heiblum, D. Mahalu, and V. Umansky: ‘Dephasing in electron interference by a which-path detector’, *Nature* **391** (1998), 871–874, DOI: [10.1038/36057](https://doi.org/10.1038/36057) (see p. 51).
- [115] Yang Ji, M. Heiblum, D. Sprinzak, D. Mahalu, and Hadas Shtrikman: ‘Phase Evolution in a Kondo-Correlated System’, *Science* **290** (2000), 779–783, DOI: [10.1126/science.290.5492.779](https://doi.org/10.1126/science.290.5492.779) (see p. 51).
- [116] Yang Ji, M. Heiblum, and Hadas Shtrikman: ‘Transmission Phase of a Quantum Dot with Kondo Correlation near the Unitary Limit’, *Phys. Rev. Lett.* **88** (2002), 076601, DOI: [10.1103/PhysRevLett.88.076601](https://doi.org/10.1103/PhysRevLett.88.076601) (see p. 51).
- [117] M. Avinun-Kalish, M. Heiblum, O. Zarchin, D. Mahalu, and V. Umansky: ‘Crossover from mesoscopic to universal phase for electron transmission in quantum dots’, *Nature* **436** (2005), 529–533, DOI: [10.1038/nature03899](https://doi.org/10.1038/nature03899) (see p. 51).
- [118] M. Zaffalon, Aveek Bid, M. Heiblum, D. Mahalu, and V. Umansky: ‘Transmission Phase of a Singly Occupied Quantum Dot in the Kondo Regime’, *Phys. Rev. Lett.* **100** (2008), 226601, DOI: [10.1103/PhysRevLett.100.226601](https://doi.org/10.1103/PhysRevLett.100.226601) (see p. 51).
- [119] S. Takada: ‘Coherent Control and Phase Measurement in Electron Quantum Interferometer’, PhD thesis, Department of Applied Physics, University of Tokyo, 2013 (see pp. 51, 52, 69, 74, 82).
- [120] R. Baltin, Y. Gefen, G. Hackenbroich, and H.A. Weidenmüller: ‘Correlations of conductance peaks and transmission phases in deformed quantum dots’, *The European Physical Journal B - Condensed Matter and Complex Systems* **10** (1999), 119–129, DOI: [10.1007/s100510050835](https://doi.org/10.1007/s100510050835) (see p. 51).
- [121] Jun Kondo: ‘Resistance Minimum in Dilute Magnetic Alloys’, *Progress of Theoretical Physics* **32** (1964), 37–49, DOI: [10.1143/PTP.32.37](https://doi.org/10.1143/PTP.32.37) (see p. 51).
- [122] S. Takada, C. Bäuerle, M. Yamamoto, K. Watanabe, S. Hermelin, T. Meunier, A. Alex, A. Weichselbaum, J. von Delft, A. Ludwig, A. D. Wieck, and S. Tarucha: ‘Transmission Phase in the Kondo Regime Revealed in a Two-Path Interferometer’, *Phys. Rev. Lett.* **113** (2014), 126601, DOI: [10.1103/PhysRevLett.113.126601](https://doi.org/10.1103/PhysRevLett.113.126601) (see pp. 51, 55, 69, 79).

- [123] Herbert Kroemer and Hiroshi Okamoto: ‘Some Design Considerations for Multi-Quantum-Well Lasers’, *Japanese Journal of Applied Physics* **23** (1984), 970, DOI: [10.1143/JJAP.23.970](https://doi.org/10.1143/JJAP.23.970) (see p. 59).
- [124] Amnon Yariv, Chris Lindsey, and Uri Sivan: ‘Approximate analytic solution for electronic wave functions and energies in coupled quantum wells’, *Journal of Applied Physics* **58** (1985), 3669–3672, DOI: [10.1063/1.335726](https://doi.org/10.1063/1.335726) (see p. 59).
- [125] W. Y. Mak, F. Sfigakis, K. Das Gupta, O. Klochan, H. E. Beere, I. Farrer, J. P. Griffiths, G. A. C. Jones, A. R. Hamilton, and D. A. Ritchie: ‘Ultra-shallow quantum dots in an undoped GaAs/AlGaAs two-dimensional electron gas’, *Applied Physics Letters* **102**, 103507 (2013), DOI: [10.1063/1.4795613](https://doi.org/10.1063/1.4795613) (see p. 71).
- [126] R. Hanbury Brown and R. Q. Twiss: ‘A Test of a New Type of Stellar Interferometer on Sirius’, *Nature* **178** (1956), 1046–1048, DOI: [10.1038/1781046a0](https://doi.org/10.1038/1781046a0) (see p. 85).
- [127] R. Hanbury Brown and R. Q. Twiss: ‘Interferometry of the Intensity Fluctuations in Light. I. Basic Theory: The Correlation between Photons in Coherent Beams of Radiation’, *Royal Society of London Proceedings Series A* **242** (1957), 300–324, DOI: [10.1098/rspa.1957.0177](https://doi.org/10.1098/rspa.1957.0177) (see p. 85).
- [128] R. Hanbury Brown and R. Q. Twiss: ‘Interferometry of the Intensity Fluctuations in Light II. An Experimental Test of the Theory for Partially Coherent Light’, *Royal Society of London Proceedings Series A* **243** (1958), 291–319, DOI: [10.1098/rspa.1958.0001](https://doi.org/10.1098/rspa.1958.0001) (see p. 85).
- [129] E. M. Purcell: ‘The Question of Correlation between Photons in Coherent Light Rays’, *Nature* **178** (1956), 1449–1450, DOI: [10.1038/1781449a0](https://doi.org/10.1038/1781449a0) (see p. 85).
- [130] G. Baym: ‘The Physics of Hanbury Brown-Twiss intensity interferometry: From stars to nuclear collisions’, *Acta Phys. Polon.* **B29** (1998), 1839–1884, arXiv: [nuc1-th/9804026](https://arxiv.org/abs/nuc1-th/9804026) [nuc1-th] (see p. 85).
- [131] Gerson Goldhaber, Sulamith Goldhaber, Wonyong Lee, and Abraham Pais: ‘Influence of Bose-Einstein Statistics on the Antiproton-Proton Annihilation Process’, *Phys. Rev.* **120** (1960), 300–312, DOI: [10.1103/PhysRev.120.300](https://doi.org/10.1103/PhysRev.120.300) (see p. 85).
- [132] M.P. Silverman: ‘On the feasibility of observing electron antibunching in a field-emission beam’, *Physics Letters A* **120** (1987), 442–446, DOI: [10.1016/0375-9601\(87\)90106-X](https://doi.org/10.1016/0375-9601(87)90106-X) (see p. 86).
- [133] R. C. Liu, B. Odom, Y. Yamamoto, and S. Tarucha: ‘Quantum interference in electron collision’, *Nature* **391** (1998), 263–265, DOI: [10.1038/34611](https://doi.org/10.1038/34611) (see p. 86).
- [134] William D. Oliver, Jungsang Kim, Robert C. Liu, and Yoshihisa Yamamoto: ‘Hanbury Brown and Twiss-Type Experiment with Electrons’, *Science* **284** (1999), 299–301, DOI: [10.1126/science.284.5412.299](https://doi.org/10.1126/science.284.5412.299) (see p. 86).
- [135] M. Henny, S. Oberholzer, C. Strunk, T. Heinzel, K. Ensslin, M. Holland, and C. Schönenberger: ‘The Fermionic Hanbury Brown and Twiss Experiment’, *Science* **284** (1999), 296–298, DOI: [10.1126/science.284.5412.296](https://doi.org/10.1126/science.284.5412.296) (see p. 86).

- [136] M. Reznikov, M. Heiblum, Hadas Shtrikman, and D. Mahalu: ‘Temporal Correlation of Electrons: Suppression of Shot Noise in a Ballistic Quantum Point Contact’, *Phys. Rev. Lett.* **75** (1995), 3340–3343, DOI: [10.1103/PhysRevLett.75.3340](https://doi.org/10.1103/PhysRevLett.75.3340) (see p. 86).
- [137] A. Kumar, L. Saminadayar, D. C. Glatthli, Y. Jin, and B. Etienne: ‘Experimental Test of the Quantum Shot Noise Reduction Theory’, *Phys. Rev. Lett.* **76** (1996), 2778–2781, DOI: [10.1103/PhysRevLett.76.2778](https://doi.org/10.1103/PhysRevLett.76.2778) (see p. 86).
- [138] Th. Martin and R. Landauer: ‘Wave-packet approach to noise in multichannel mesoscopic systems’, *Phys. Rev. B* **45** (1992), 1742–1755, DOI: [10.1103/PhysRevB.45.1742](https://doi.org/10.1103/PhysRevB.45.1742) (see p. 86).
- [139] Harald Kiesel, Andreas Renz, and Franz Hasselbach: ‘Observation of Hanbury Brown-Twiss anticorrelations for free electrons’, *Nature* **418** (2002), 392–394, DOI: [10.1038/nature00911](https://doi.org/10.1038/nature00911) (see p. 86).
- [140] C. K. Hong, Z. Y. Ou, and L. Mandel: ‘Measurement of subpicosecond time intervals between two photons by interference’, *Phys. Rev. Lett.* **59** (1987), 2044–2046, DOI: [10.1103/PhysRevLett.59.2044](https://doi.org/10.1103/PhysRevLett.59.2044) (see p. 87).
- [141] C. Texier: *Mécanique quantique - Cours et exercices corrigés: Cours et exercices corrigés*, Dunod, 2011 (see p. 87).
- [142] Leonid S. Levitov, Hyunwoo Lee, and Gordey B. Lesovik: ‘Electron counting statistics and coherent states of electric current’, *Journal of Mathematical Physics* **37** (1996), 4845–4866, DOI: [10.1063/1.531672](https://doi.org/10.1063/1.531672) (see p. 88).
- [143] M.A. Kastner: ‘Artificial Atoms’, *Physics Today* **46** (1993), 24–31, DOI: [10.1063/1.881393](https://doi.org/10.1063/1.881393) (see p. 89).
- [144] A. T. Johnson, L. P. Kouwenhoven, W. de Jong, N. C. van der Vaart, C. J. P. M. Harmans, and C. T. Foxon: ‘Zero-dimensional states and single electron charging in quantum dots’, *Phys. Rev. Lett.* **69** (1992), 1592–1595, DOI: [10.1103/PhysRevLett.69.1592](https://doi.org/10.1103/PhysRevLett.69.1592) (see p. 89).
- [145] Bo Su, V. J. Goldman, and J. E. Cunningham: ‘Observation of Single-Electron Charging in Double-Barrier Heterostructures’, *Science* **255** (1992), 313–315, DOI: [10.1126/science.255.5042.313](https://doi.org/10.1126/science.255.5042.313) (see p. 89).
- [146] Stephanie M. Reimann and Matti Manninen: ‘Electronic structure of quantum dots’, *Rev. Mod. Phys.* **74** (2002), 1283–1342, DOI: [10.1103/RevModPhys.74.1283](https://doi.org/10.1103/RevModPhys.74.1283) (see p. 89).
- [147] Lord Rayleigh: ‘On Waves Propagated along the Plane Surface of an Elastic Solid’, *Proceedings of the London Mathematical Society* **s1-17** (1885), 4–11, DOI: [10.1112/plms/s1-17.1.4](https://doi.org/10.1112/plms/s1-17.1.4) (see pp. 91, 108).
- [148] J. M. Shilton, D. R. Mace, V. I. Talyanskii, M. Y. Simmons, M. . Pepper, A. C. Churchill, and D. A. Ritchie: ‘Experimental study of the acoustoelectric effects in GaAs-AlGaAs heterostructures’, *Journal of Physics: Condensed Matter* **7** (1995), 7675, DOI: [10.1088/0953-8984/7/39/010](https://doi.org/10.1088/0953-8984/7/39/010) (see pp. 91, 113).

- [149] J. M. Shilton, D. R. Mace, V. I. Talyanskii, Yu Galperin, M. Y. Simmons, M. Pepper, and D. A. Ritchie: ‘On the acoustoelectric current in a one-dimensional channel’, *Journal of Physics: Condensed Matter* **8** (1996), L337, DOI: [doi:10.1088/0953-8984/8/24/001](https://doi.org/10.1088/0953-8984/8/24/001) (see pp. 91, 113).
- [150] V. I. Talyanskii, J. M. Shilton, M. Pepper, C. G. Smith, C. J. B. Ford, E. H. Linfield, D. A. Ritchie, and G. A. C. Jones: ‘Single-electron transport in a one-dimensional channel by high-frequency surface acoustic waves’, *Phys. Rev. B* **56** (1997), 15180–15184, DOI: [10.1103/PhysRevB.56.15180](https://doi.org/10.1103/PhysRevB.56.15180) (see p. 91).
- [151] V. I. Talyanskii, J. M. Shilton, J. Cunningham, M. Pepper, C. J. B. Ford, C. G. Smith, E. H. Linfield, D. A. Ritchie, and G. A. C. Jones: ‘Quantized current in one-dimensional channel induced by surface acoustic waves’, *Physica B: Condensed Matter* **249–251** (1998), 140–146, DOI: [10.1016/S0921-4526\(98\)00086-6](https://doi.org/10.1016/S0921-4526(98)00086-6) (see p. 91).
- [152] C. H. W. Barnes, J. M. Shilton, and A. M. Robinson: ‘Quantum computation using electrons trapped by surface acoustic waves’, *Phys. Rev. B* **62** (2000), 8410–8419, DOI: [10.1103/PhysRevB.62.8410](https://doi.org/10.1103/PhysRevB.62.8410) (see p. 91).
- [153] Roberta Rodriguez, Daniel K. L. Oi, Masaya Kataoka, Crispin H. W. Barnes, Toshio Ohshima, and Artur K. Ekert: ‘Surface-acoustic-wave single-electron interferometry’, *Phys. Rev. B* **72** (2005), 085329, DOI: [10.1103/PhysRevB.72.085329](https://doi.org/10.1103/PhysRevB.72.085329) (see p. 91).
- [154] M. Kataoka, R. J. Schneble, A. L. Thorn, C. H. W. Barnes, C. J. B. Ford, D. Anderson, G. A. C. Jones, I. Farrer, D. A. Ritchie, and M. Pepper: ‘Single-Electron Population and Depopulation of an Isolated Quantum Dot Using a Surface-Acoustic-Wave Pulse’, *Phys. Rev. Lett.* **98** (2007), 046801, DOI: [10.1103/PhysRevLett.98.046801](https://doi.org/10.1103/PhysRevLett.98.046801) (see p. 91).
- [155] M. R. Astley, M. Kataoka, C. J. B. Ford, C. H. W. Barnes, D. Anderson, G. A. C. Jones, I. Farrer, D. A. Ritchie, and M. Pepper: ‘Energy-Dependent Tunneling from Few-Electron Dynamic Quantum Dots’, *Phys. Rev. Lett.* **99** (2007), 156802, DOI: [10.1103/PhysRevLett.99.156802](https://doi.org/10.1103/PhysRevLett.99.156802) (see p. 91).
- [156] M. Kataoka, M. R. Astley, A. L. Thorn, D. K. L. Oi, C. H. W. Barnes, C. J. B. Ford, D. Anderson, G. A. C. Jones, I. Farrer, D. A. Ritchie, and M. Pepper: ‘Coherent Time Evolution of a Single-Electron Wave Function’, *Phys. Rev. Lett.* **102** (2009), 156801, DOI: [10.1103/PhysRevLett.102.156801](https://doi.org/10.1103/PhysRevLett.102.156801) (see p. 91).
- [157] R. M. White and F. W. Voltmer: ‘Direct Piezoelectric Coupling To Surface Elastic Waves’, *Applied Physics Letters* **7** (1965), 314–316, DOI: [10.1063/1.1754276](https://doi.org/10.1063/1.1754276) (see p. 91).
- [158] Mauricio M. de Lima Jr. and Paulo V. Santos: ‘Modulation of photonic structures by surface acoustic waves’, *Reports on Progress in Physics* **68** (2005), 1639, DOI: [10.1088/0034-4885/68/7/R02](https://doi.org/10.1088/0034-4885/68/7/R02) (see p. 93).

- [159] S. Adachi: ‘GaAs, AlAs, and $\text{Al}_x\text{Ga}_{1-x}\text{As}$: Material parameters for use in research and device applications’, *Journal of Applied Physics* **58** (1985), 1–29, DOI: [10.1063/1.336070](#) (see p. 96).
- [160] D.D. Smith, T. Fink, W.D. Braddock, and M.-L. Saunders: ‘RTA removal of E-beam-induced damage in GaAs-AlGaAs heterostructures as determined by magnetotransport characterization’, *Journal of Electronic Materials* **19** (1990), 757–760, DOI: [10.1007/BF02655246](#) (see p. 99).
- [161] Soumen Mandal, Tobias Bautze, Remi Blinder, Tristan Meunier, Laurent Saminadayar, and Christopher Bäuerle: ‘Efficient radio frequency filters for space constrained cryogenic setups’, *Review of Scientific Instruments* **82**, 024704 (2011), DOI: [10.1063/1.3543736](#) (see pp. 104, 105).
- [162] J. Filipiak, L. Solarz, and G. Steczko: ‘Surface Acoustic Wave Vibration Sensor Electronic System’, *Acta Physica Polonica A* **120** (2011), 598–603 (see p. 113).
- [163] R. J. Schneble, M. Kataoka, C. J. B. Ford, C. H. W. Barnes, D. Anderson, G. A. C. Jones, I. Farrer, D. A. Ritchie, and M. Pepper: ‘Quantum-dot thermometry of electron heating by surface acoustic waves’, *Applied Physics Letters* **89**, 122104 (2006), DOI: [10.1063/1.2346372](#) (see p. 116).
- [164] J. R. Petta, A. C. Johnson, C. M. Marcus, M. P. Hanson, and A. C. Gossard: ‘Manipulation of a Single Charge in a Double Quantum Dot’, *Phys. Rev. Lett.* **93** (2004), 186802, DOI: [10.1103/PhysRevLett.93.186802](#) (see p. 123).
- [165] Romain Thalineau, Sylvain Hermelin, Andreas D. Wieck, Christopher Bäuerle, Laurent Saminadayar, and Tristan Meunier: ‘A few-electron quadruple quantum dot in a closed loop’, *Applied Physics Letters* **101**, 103102 (2012), DOI: [10.1063/1.4749811](#) (see p. 123).
- [166] Charles Kittel: *Introduction to Solid State Physics*, 6th, John Wiley & Sons, Inc., 1986, DOI: [10.1016/0016-0032\(53\)90624-3](#) (see p. 164).

List of Figures

2.1	GaAs/AlGaAs heterostructure with band structure	14
2.2	Transport regimes	15
2.3	Electronic interference experiments	17
2.4	Tomomura experiment	18
2.5	Scattering matrix	20
2.6	Tight-binding square lattice	23
3.1	Examples of different tight-binding lattices	26
3.2	Low-level tight-binding system	28
3.3	Conductance as a function of energy	29
3.4	Dispersion relation	30
3.5	Electrostatic gate definition	31
3.6	QPC: gatestructure	33
3.7	QPC: simulation vs. experiment	33
3.8	QPC: different geometries	34
3.9	QPC: convergence test	36
3.10	QPC: wave functions	38
3.11	Aharonov-Bohm interferometer	38
3.12	Aharonov-Bohm oscillations	39
3.13	First two propagating modes in the Aharonov-Bohm ring	41
3.14	Series quantum point contacts	42
3.15	Resonant tunneling	42
3.16	Fabry-Perot resonances	43
3.17	Software architecture	44
4.1	Mach-Zehnder interferometer	48
4.2	Electronic Mach-Zehnder interferometer	49
4.3	Electronic Mach-Zehnder interferometer - experimental data	49
4.4	Flying qubit sample	51
4.5	Flying qubit oscillations vs. magnetic field	52
4.6	Electron trajectories in the WCR and the SCR	53
4.7	Phase jumps vs. linear phase shift	54
4.8	Flying qubit oscillations vs. tunnel gate	55

4.9	Qubit rotations	57
4.10	Flying qubit schematic	58
4.11	Electron trajectories	59
4.12	Graphical representation of equation 4.19	62
4.13	Split-wire potential	64
4.14	Wave functions in the split-wire	64
4.15	Dispersion relation	65
4.16	Semi-analytical results	66
4.17	Conductance oscillations vs. tunnel gate voltage (semi-analytical)	67
4.18	Confinement potential under magnetic field	68
4.19	Potential landscape of different split-wire geometries	70
4.20	Surface area increase for different split-wire geometries	71
4.21	Flying qubit gate structure implementation	72
4.22	Flying qubit potential landscape	73
4.23	Comparison anti-phase / in-phase regime	74
4.24	Spatial evolution of the energy of the symmetric and anti-symmetric state	75
4.25	Spatial evolution of the energy difference of the symmetric and anti-symmetric state	76
4.26	Maximum slope of $\partial\Delta E/\partial x$	77
4.27	In-phase oscillations	78
4.28	Simulated pinch-off curves of the flying qubit	79
4.29	Anti-phase oscillations	80
4.30	Conductance oscillations vs. tunnel gate voltage (numerical)	81
4.31	Surface area increase	83
5.1	Hanbury Brown-Twiss effect	86
5.2	Hong-Ou-Mandel interferometer	87
5.3	Fermionic Hong-Ou Mandel experiment	88
5.4	Quantum dot schematic	89
5.5	Coulomb blockade	90
5.6	Interdigital transducers	92
5.7	IDT visualization	92
5.8	Surface acoustic wave	94
5.9	Trajectory of one atom in a SAW	95
5.10	Electrostatic potential from the SAW	97
5.11	Fermionic anti-bunching	98
5.12	Fabrication steps	100
5.13	Bonding	101
5.14	Fabricated prototypes	103
5.15	Cabelling	104
5.16	Experimental set-up	105
6.1	SEM pictures of IDT	109
6.2	Transmission of two IDTs	111

6.3	Transmission and reflection of double and single finger IDT	112
6.4	Sample holder rf-shielding	113
6.5	SAW current measurement device configuration	114
6.6	SAW current measurement	115
6.7	SAW current dependence on the pinch voltage	116
6.8	SAW induced energy level broadening	117
6.9	Coulomb peak splitting: power dependence	118
6.10	Comparison of single and double finger IDT	119
6.11	Coulomb peak splitting: frequency dependence	120
6.12	Quantum dot with quantum point contact charge sensor.	121
6.13	Quantum point contact charge sensor pinch-off	121
6.14	Quantum point contact charge sensor	122
6.15	Stability diagram: single electron regime	123
6.16	Stability diagram: sweep direction	124
6.17	Electron loading sequence	125
6.18	Electron escape in the metastable state	126
6.19	Electron life-time in the metastable state	127
6.20	Electron sending efficiency	128
6.21	Electron transfer	129
6.22	First prototype: poor IDT performance	130
6.23	First prototype: injection quantum dot	131
6.24	First prototype: injection quantum dot (3D)	132
6.25	Second prototype: injection quantum dot	133
6.26	Second prototype: injection quantum dot (3D)	134
6.27	Third prototype: gate structure	136
6.28	Third prototype: potential landscape	137
A.1	A single lead contact	163
A.2	quantum network	165

List of Tables

3.1	Comparison of different lattice constants	35
5.1	Surface acoustic wave parameters (GaAs)	96

APPENDIX A

Appendix

A.1 Leads

Let us discuss a single lead contact. Several leads can always be considered as a combination of single leads and considering a single lead is hence sufficient. It is important to choose a proper notation and orientation for the lead.

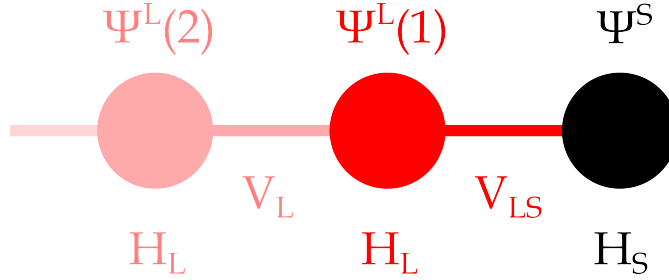


Figure A.1: Details are given in the text.

In figure A.1 we display the simplest case of a tight-binding system being connected to a single lead. The black dot corresponds to the typically large scattering region S, which in this case consists of one site. We enumerate the leads starting from the scattering region. This labeling leads to a semi-infinite tridiagonal Hamiltonian. This will become clear if we look at the left-hand side (LHS) of the Schrödinger equation

$$H\Psi = \begin{pmatrix} \ddots & V_L & & \\ V_L^\dagger & H_L & V_L & \\ & V_L^\dagger & H_L & V_{LS} \\ & & V_{LS}^\dagger & H_S \end{pmatrix} \begin{pmatrix} \vdots \\ \Psi^L(2) \\ \Psi^L(1) \\ \Psi^S \end{pmatrix} \quad (\text{A.1})$$

From this it is comprehensive, that H_S is the Hamiltonian matrix of the central scattering region, which is typically quite large. H_L is the usually much smaller projection of the lead Hamiltonian inside one unit cell of the lead while V_L connects one unit cell of the lead to the next. V_{LS} is the hopping from the system to the leads. The wave

functions are labeled correspondingly, as it can also be seen in figure A.1. The potential $U(x)$ of the semi-infinite lead is invariant under a translation of the lattice constant a in x-direction:

$$U(x) = U(x + a) \quad (\text{A.2})$$

We can also rephrase this equation in terms of a translational operator $\hat{T}(a)$:

$$\hat{T}(a)U(x) = U(x + a) = U(x) \quad (\text{A.3})$$

In the one-electron approximation [166], the wave function may be expressed as a Fourier series summing over all possible values of the wave vector

$$\Psi(x) = \sum_k C(k)e^{ikx} \quad (\text{A.4})$$

and is hence a superposition of plane waves. As a first conclusion we find that due to the translational invariance of the leads, the general form of the wave function in them is a superposition of plane waves. The eigenstates of the leads are equivalent to the eigenstates of the Translation operator, since the translation operator commutes with the system Hamiltonian.

$$[T, H] = 0 \quad (\text{A.5})$$

We can quickly verify this:

$$\hat{T}(a)\hat{H}(x)\Psi(x) = \hat{H}(x + a)\Psi(x + a) = \hat{H}(x)\Psi(x + a) = \hat{H}(x)\hat{T}(a)\Psi(x) \quad (\text{A.6})$$

We remark that this is valid only for the case of a periodic Hamiltonian. The eigenstates of the translation operator in the lead now take the form

$$\phi_n(j) = (\lambda_n)^j \chi_n, \quad (\text{A.7})$$

such that they obey the Schrödinger equation

$$(H_L + V_L \lambda_n^{-1} + V_L^\dagger \lambda_n) \chi_n = E \chi_n. \quad (\text{A.8})$$

j is a index of the unit cell of the lead. χ_n is the n-th eigenvector, and λ_n the n-th eigenvalue. Now we state that normalizability requires that $|\lambda_n| \leq 1$. Modes with $|\lambda_n| < 1$ are evanescent and decay, whereas the rest of the modes ($|\lambda_n| = 1$) is propagating and

$$\lambda_n = e^{ik_n} = 1 \quad (\text{A.9})$$

which leads to

$$k_n = n * 2\pi, \quad (\text{A.10})$$

with $n \in \mathbb{N}$. The propagating modes are normalized according to the expectation value of the particle current, such that

$$\langle I \rangle \equiv \text{Im} \langle \phi_n(j) | V_L | \phi_n(j-1) \rangle = \pm 1 \quad (\text{A.11})$$

Usually, the probability current in qm looks like

$$j = \frac{\hbar}{m} \text{Im}(\Psi^* \nabla \Psi) \quad (\text{A.12})$$

to arrive at the upper expression I can imagine doing something like

$$T(a) = \exp(-ia\hat{p}/\hbar) = \exp(-a\nabla) \quad (\text{A.13})$$

which comes from the definition of the translation operator with the help of the momentum operator \hat{p} , but These modes can now be sorted into incoming ones $\phi_n^{in}(\langle I \rangle = +1)$, outgoing ones ($\phi_n^{out}(\langle I \rangle = -1)$) and evanescent ones $\phi_n^{ev}(\langle I \rangle = 0)$ The scattering states in the leads take the form

$$\Psi_n(i) = \phi_n^{in}(i) + \sum_m S_{mn} \phi_m^{out}(i) + \sum_p \tilde{S}_{pn} \phi_p^{ev}(i) \quad (\text{A.14})$$

i labels again the i -unit cell away from the scattering region. S_{mn} labels the scattering matrix and we can write the scattering wave function inside the system

$$\Psi_n(0) = \phi_n^S \quad (\text{A.15})$$

A.2 Analytical model

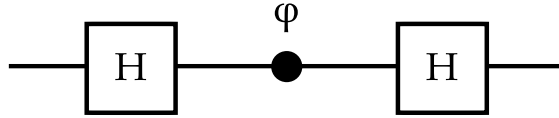


Figure A.2: Quantum network diagram. A Hadamard gate is followed by a phase shift gate and followed by a Hadamard gate. From this representation we can calculate the transfer matrix of the tunnel-coupled wire.

As briefly mentioned in section 4.3, the transfer matrix of the tunnel-coupled wire can also be obtained more elegantly. We describe all elements of the Mach-Zehnder interferometer as a quantum network diagram of elementary quantum operations as can be seen in figure A.2. The depicted quantum logic gates are the Hadamard gate

$$H = \frac{1}{\sqrt{2}} \begin{pmatrix} 1 & 1 \\ 1 & -1 \end{pmatrix} \quad (\text{A.16})$$

and the phase shift gate

$$P_\varphi = \begin{pmatrix} 1 & 0 \\ 0 & e^{i\varphi} \end{pmatrix} \quad (\text{A.17})$$

with $\varphi = (k_A - k_S)L$ being the phase difference accumulated in the tunnel-coupled wire. Putting everything together, we obtain

$$\begin{aligned}
 t_{tw} &= HP_\varphi H \\
 &= \frac{1}{\sqrt{2}} \begin{pmatrix} 1 & 1 \\ 1 & -1 \end{pmatrix} \begin{pmatrix} 1 & 0 \\ 0 & e^{i\varphi} \end{pmatrix} \frac{1}{\sqrt{2}} \begin{pmatrix} 1 & 1 \\ 1 & -1 \end{pmatrix} \\
 &= e^{i\frac{\varphi}{2}} \begin{pmatrix} \cos \varphi/2 & -i \sin \varphi/2 \\ -i \sin \varphi/2 & \cos \varphi/2 \end{pmatrix}.
 \end{aligned} \tag{A.18}$$

We have arrived at equation [4.18](#).

Publications

Scientific publications

1. SOUMEN MANDAL, **Tobias Bautze**, REMI BLINDER, TRISTAN MEUNIER, LAURENT SAMINADAYAR AND CHRISTOPHER BÄUERLE: ‘Efficient radio frequency filters for space constrained cryogenic setups’. *Review of Scientific Instrument* (2011), 024704.
2. SOUMEN MANDAL, **Tobias Bautze**, OLIVER A. WILLIAMS, CECILE NAUD, ETIENNE BUSTARRET, FRANCK OMNES, PIERRE RODIERE, TRISTAN MEUNIER, CHRISTOPHER BÄUERLE AND LAURENT SAMINADAYAR: ‘The Diamond Superconducting Quantum Interference Device’. *ACS Nano* (2011), Vol.5, No.9, pp. 7144-7148.
3. SOUMEN MANDAL, **Tobias Bautze** AND CHRISTOPHER BÄUERLE: ‘Superconductivity in Nanostructured Boron-doped Diamond and its Application to Device Fabrication’. *Nanodiamond* (2013), 31, p. 385.
4. **Tobias Bautze**, SOUMEN MANDAL, OLIVER A. WILLIAMS, PIERRE RODIERE, TRISTAN MEUNIER AND CHRISTOPHER BÄUERLE: ‘Superconducting nano-mechanical diamond resonators’. *Carbon* (2014), 72, 100-105.
5. **Tobias Bautze**, CHRISTOPH SUSSMEIER, SHINTARO TAKADA, CHRISTOPH GROTH, TRISTAN MEUNIER, MICHIHISA YAMAMOTO, SEIGO TARUCHA, XAVIER WAIN TAL AND CHRISTOPHER BÄUERLE: ‘Theoretical, numerical, and experimental study of a flying qubit electronic interferometer’. *Physical Review B* (2014), 89 (12), 125432.

Acknowledgments

I would like to express my deep gratitude to my PhD supervisor, Christopher Bäuerle, for accepting me as his PhD student and for guiding me throughout the years that we have spent together. His knowledge and intuition are impressive, I appreciate his ability to take decisions in setting high goals for a research project. Thank you for keeping the expectations high, for teaching me the art of scientific expression and for sharing your incredible work ethics. Perfection is not attainable, but if we chase perfection we can catch excellence. I do enjoy a perfect timing, support for different ideas, resourceful discussions, patience and high reading speed. Thank you for exploring the realm of possibilities together. Thanks for all the comments, corrections and suggestions. So long, and thanks for all the skills.

I express my sincere gratitude to Xavier Waintal, Hartmut Buhmann, Gwendal Fève, Denis Feinberg and Christoph Texier for accepting to be part of my jury, for their time, suggestions, corrections, inspiration and their critical mind.

I am grateful of having had the opportunity to discuss with Tarucha-sensei and Yamamoto-sensei and to work together with Takada-san.

I have met a variety of people in France: professors, colleagues, scientists, engineers, students, friends, athletes, musicians, nerds, geeks and politicians and I would like to thank all of them equally for rendering my French experience perfect. To make things a little bit more interesting, I have used a trivial sorting algorithm to change the order of appearance:

I would like to thank Tony Motakis, Sabine Andergassen, Zahi Essa, Alexander Grimm, Argel Estrada, Thierry Morigault, Sebastian Klemmt, Nahuel Montebianco, Anja Backen, Audrey Genwald, Christoph Süßmeier, Benoit Bertrand, Cécile Naud, Eddy Collin, Gaëtan Harter, Marc Ganzhorn, Johanna Seidemann, Étienne Dumur, Antoine Delmas, Giada Ghezzi, Clément Fevrier, Pierre Nowak, Sébastien Dufresnes, Thierry Crozes, Gwénaëlle Julie, Frans Schotsch, Rodolph Kreutz, Thierry Fournier, Giovanni Vinai, Johanna Seidemann, Marian Marx, Raphael Fascio, John Landers, Nicolas Roch, Ioan Chioar, Candice Thomas, Farida Veliev, Pierre Perrier, Martial Defoort, Pascal Maro-

tel, Preeti Felix, Anna Vianelli, Eric Montredon, Sven Rohr, Anne Laffilhe, Florence Villani, Guillaume Forestier, Tristan Meunier, Bruno Fernandez, Andreas Wieck, Yvan Denis, Thomas Lavocat, Stefan Thiele, Catherina Tomba, Olivier Crauste, Eva Dupont-Ferrier, Jean-francois Motte, Christophe Hoarau, Katrin Zimmermann, Soumen Mandal, Sebastien Pairis, Klaus Hasselbach, Stephanie Monfront, Pierre-andré Mortemousque, Izabella Petrykiewicz, Abdelkarim Ferhat, Francois Forget, Andrew Burgess, Alexandru Romanescu, Tingting Zou, Hani Sherry, Sylvain Hermelin, Yannick Baines, Romain Thalineau, Dipankar Kalita, Bruno Kung, Alina Radu-Pralong, Christoph Blanc, Viviana Herrera, Konstantinos Rogdakis, Marine Schott, Dibyendu Hazra, Olivier Arcizet, Logi Olgeirsson, Olivier Buisson, Fabio Pistolesi, Lukas Worschech, Gregoire Roussely, Hanno Flentje, Vivien Thiney, Oleg Yuschuk, Yann Perrin, Christoph Groth, Bernard Marie-Amiot, Romain Brunet, Mathias Solana, Henri Rodenas, Julien Korinman, Thomas Dancoisne and many more.

Thank you for all the support at the Néel Institut !

I express my deep gratitude for my funding from the Nanosciences Fondation !

Herzlichen Dank an meine Familie für all die Unterstützung, obgleich es nicht immer offensichtlich war an was ich denn gerade arbeitete. Danke Matthias, Julia, Lea, Emil, Frank und Marianne Bautze. Besonderer Dank gilt Kristin Kredel für das schöne gemeinsame Leben, das uns bevorsteht. Ebenfalls herzlichen Dank an all meine Freunde aus der Heimat !

Many people do an amazing job and often there is no room for appreciation. I would like to raise attention to Guido van Rossum and John Hunter who deserve my gratitude. Thanks for inspiration, Craig Venter and Richard Dawkins. Thank you Matthias Pospiech for the L^AT_EXtemplate.

If **you** are reading this thesis, feel free to contact me via tobiasbautze replace yahoo dot de.